University of Strathclyde Glasgow

A Revised Biomechanical Model of Frequency Filtering and Transmission in the Field Cricket (Gryllinae) Ear and Host–Parasitoid Interactions

PhD Thesis

Brendan Latham

Bioacoustics Group, Centre for Ultrasonic Engineering
Electronic and Electrical Engineering
University of Strathclyde, Glasgow

Supervisors:

Dr Andrew Reid
Dr Joseph Jackson
Prof. James Windmill

August 7, 2025

Magna opera Domini exquisita in omnes voluntates eius

Psalm 111:2
Inscribed over the entrance to the Cavendish Laboratory,
in Latin for the original laboratory (1874),
in English for the second (1974),
University of Cambridge.

“Great are the works
of the LORD, studied
by all who delight in them.”

This doctoral thesis is dedicated to my parents,
whose steadfast support since the earliest days
of my passion for the natural world
made all this possible,
and to my sister,
Mairi.

This thesis is the result of the author's original research. It has been composed by the author and has not been previously submitted for examination which has led to the award of a degree.

Signed: Brendan Latham

Date: August 7, 2025

Acknowledgements

First and foremost, I would like to express my deep gratitude to my three supervisors: Prof. James Windmill, Dr Joseph Jackson, and Dr Andrew Reid.

Joe, thank you for being an outstanding primary supervisor from the inception of this project. You welcomed me warmly into the lab (and over zoom during lockdown) and fostered an environment that was both intellectually stimulating and fun. I'm also grateful for those football sessions in the park.

James, this project would not have begun without your leadership. Thank you for securing the initial funding and position, and for backing my somewhat last-minute application to the UK–Canada scheme. I am especially thankful for your graciousness during the more stressful phases of this journey.

To Andy, who became my primary supervisor after Joe's move to Australia, thank you for being a consistent and generous source of guidance and friendship from the outset. Even before officially joining the supervisory team, your technical expertise and status as Wizard of the Lab made your familiarity with the equipment invaluable.

To both Joe and Andy, I particularly enjoyed our supervision meetings where a question from me about physical acoustics would lead to an enthusiastic explanation at the whiteboard. Those moments remind me of an opening line from *Acoustic Systems in Biology* by Neville H. Fletcher: *"I do not mean to imply by this that all biologists are unsophisticated"*. Thank you both for significantly strengthening this work with your interdisciplinary physics–engineering insights, and for putting up with this life scientist in your midst.

I would also like to give special thanks to Dr Jonathan Williams, our resident expert in all things micro-CT. I hugely valued our impromptu, somewhat geeky, science chats. The spontaneity of our scientific rapport was both encouraging but also very helpful to the strength of this research – to which you directly contributed when brought onto the co-authorship of the coupled membranes work.

Many others made important contributions to the success of this research. Prof. Nathan Bailey of the University of St Andrews – thank you for

letting me leave your lab with some of your *T. commodus* specimens. Prof. Fernando Montealegre-Z of the University of Lincoln – thanks for our email exchange on bushcricket auditory anatomy.

Across the Atlantic, I owe sincere thanks to Prof. Andrew Mason at the University of Toronto Scarborough. Thank you for your warm and relaxed welcome to a new lab and country, and for the opportunity to experience a lab focused primarily on biology. I especially enjoyed the fieldwork in the Albertan woods – searching for *Cyphoderris* at night in bear country with only headtorches! Working in the field alongside Terrance Chang and Subaen Ravinthiran was a hugely enjoyable highlight. It's good we weren't eaten.

I am also grateful to Andrew for arranging my visit to the sister lab in Minnesota. Prof. Norman Lee and Jimena Dominguez, it was an enormous pleasure and highlight visiting your lab at St. Olaf College. Thank you both for your kind welcome and for collaborating with me. I am proud of our work. Also, the baseball game was great.

At the University of Strathclyde's workshop, I'd like to thank Alex Ward, now retired, who fabricated the custom platform for the laser vibrometer. Thanks also to Colin Campbell for assisting with 3D printing of anatomical specimens – (Watch this space?).

On a more personal note, I want to acknowledge all my colleagues, including Geo, Ehsan, and Matt. I also want to acknowledge Walter Galbraith, a highly valued colleague who sadly passed away shortly after fully retiring, just weeks before the submission of this thesis. I always loved bumping into Walter and exchanging a hello.

During the course of this PhD, I lived with four flatmates, though never all at once. Three of them got married immediately after moving out (not sure what that says). Iain, Simon, Tim, and most recently Josef – thank you for being the best flatmates. A special thanks to Tim, my longest-standing flatmate, thanks for your friendship.

Finally, I want to express my deepest love and gratitude to my family, and my thanks to God for them. Thank you to my parents for your unwavering love and support always. Thank you to Andrew and Rhona for our Glasgow camaraderie, and for our friendship and fellowship. Thank you to Mairi and Conor for being an inspiration and for those joyous visits to your flat during the Inverness write-up season. And my thanks and love to Helen and Hannes, along with Olivia, Lachlan, and now wee baby Brendan

Brendan Latham

Abstract

The field cricket (subfamily Gryllinae) auditory pathway is characterised by its unique peripheral anatomy and well-characterised neurophysiological and behavioural organisation, establishing it as an important model in behavioural neuroscience, particularly neuroethology. Males produce a highly pure-toned calling song centred around 5 kHz, which females use for phonotactic localisation with exceptional directional sensitivity, resolving sound source position to within 1° of the frontal axis – comparable to human hearing. This acuity arises from a distinct configuration of three sound inputs per ear: one external and two internal via the acoustic trachea. Gryllinae anatomy is further distinguished by asymmetric peripheral structures, comprising a large, thin posterior tympanal membrane (PTM), a smaller, thicker anterior tympanal membrane (ATM), and a cavity-like anterior tracheal branch (ATB) decoupled from the ATM. Auditory neurons are arranged tonotopically along the dorsal membrane of the ATB, enabling discrimination between calling and courtship song frequencies. While the neurophysiological and behavioural stages are well understood, the initial biomechanical stage remains unresolved.

Two key questions persist: the mechanism underlying sharp frequency tuning and how PTM vibrations are transmitted to the auditory sensilla. Although the PTM is established as the primary acoustic input and has been extensively studied using laser Doppler vibrometry (LDV), reported frequency responses are inconsistent and often insufficient to explain sharp neuronal tuning near the calling song frequency. This has led to the longstanding hypothesis of an additional mechanical filter between the tympanum and sensilla. Competing explanations for transmission include mechanical coupling to internal tracheal structures, as well as airflow- and sound pressure–based mechanisms within the air-filled tracheal branches. Consequently, both filtering and transmission remain incompletely understood.

To address these problems, this research employs an integrated experimental and computational approach combining three complementary techniques not previously applied to this system. Scanning LDV maps PTM

vibration amplitude across the membrane and captures phase information beyond conventional single-point measurements. X-ray micro-computed tomography (micro-CT) provides non-invasive three-dimensional reconstructions of internal auditory structures, enabling 3D morphometric analysis and surpassing traditional 2D sectioning techniques. Finite element analysis (FEA), informed by micro-CT data, simulates the mechanical behaviour of internal components under acoustic stimulation.

The results establish a revised biomechanical model of the Gryllinae peripheral auditory system. In contrast to recent single-point LDV studies, the PTM exhibits two vibrational optima at 6 kHz and 14 kHz. Phase analysis indicates that the higher-frequency peak corresponds to the intrinsic resonance of the membrane, whereas the lower-frequency peak reflects a driven response arising from coupling with a second resonator, supporting the second filter hypothesis. X-ray micro-CT and FEA identify the dorsal membrane of the posterior tracheal branch (DM-PTB) as the probable 6 kHz resonator. In addition, a previously overlooked structure, termed here the dividing membrane (DivM), is identified; it possesses its own resonant frequency and amplifies vibrational energy. Simulations further suggest frequency-dependent, membrane-driven ATB deformation. Together, both frequency filtering and sound transmission arise from a chain of mechanically coupled, successively tuned membranes extending from the PTM through the DM-PTB and DivM to the ATB supporting the auditory neurons.

This framework reconciles discrepancies between tympanal and neuronal tuning and clarifies the mechanisms underlying filtering and transmission in the peripheral auditory pathway, emphasising that the PTM should not be considered in isolation but as part of a coupled system. It also indicates relevance to bioinspired applications, particularly in microelectromechanical systems (MEMS) diaphragm microphones used in smartphones and hearing aids. This relevance is underscored by the ear of the parasitoid fly *Ormia ochracea*, which is likewise tuned to the Gryllinae calling song and has already inspired multiple MEMS microphone patents.

In addition to this biomechanical study, this research examines host–parasitoid interactions between field crickets and *O. ochracea*. By manipulating larval load and recording host cricket sex and size, this work shows that in-host resource competition determines developmental outcomes, influencing both fly offspring number and individual fitness. A protocol for maintaining laboratory colonies of *O. ochracea* is presented, recommending a one-larva regime and validating the commercially available field cricket *Acheta domesticus*, although not a natural host, as a viable model host.

Keywords: Biomechanics, Bioacoustics, Gryllinae, *Ormia ochracea*, X-ray micro-CT imaging, finite element analysis, laser Doppler vibrometry

List of Publications

The research presented in this thesis has also been published in three peer-reviewed articles in high-impact journals. These include two lead-author original research papers and one second-author review article. These papers correspond to Appendices B–D.

2025

J. A. Dominguez†, B. **Latham†**, L. C. Mongui, A. Rossinow, Y. Xiong, B. V. Schmidt, Q. Vu, B. L. Torres-Lopez, P. A. Henderson, A. C. Mason, N. Lee, "Resource competition affects developmental outcomes of the acoustic parasitoid fly *Ormia ochracea*," *Annals of the Entomological Society of America*, 2025.
doi: 10.1093/aesa/saaf018

- **† "Co-first authors contributed equally to this work"**

2024

B. **Latham**, A. Reid, J. C. Jackson-Camargo, J. A. Williams, and J. F. Windmill, "Coupled membranes: a mechanism of frequency filtering and transmission in the field cricket ear evidenced by micro-computed tomography, laser Doppler vibrometry and finite element analysis," *Journal of the Royal Society Interface,* vol. 21, no. 214, 2024.
doi: 10.1098/rsif.2023.0779

2023

L. Díaz-García, B. **Latham**, A. Reid, and J. Windmill, "Review of the applications of principles of insect hearing to microscale acoustic engineering challenges," *Bioinspiration & Biomimetics,* vol. 18, no. 5, 2023.
doi: 10.1088/1748-3190/aceb29

List of Abbreviations

AMT	Air Motion Transformer
AN1	Ascending Neuron 1
AN2	Ascending Neuron 2
ARF	Auditory Receptor Fibre
ATB	Anterior Tracheal Branch
ATM	Anterior Tympanal Membrane
BS1–3	Beam Splitter 1–3
CF	Carrier Frequency
CS	Contralateral Spiracle
DA	Distal Aperture
DivM	Dividing Membrane
DM-ATB	Dorsal Membrane of the Anterior Tracheal Branch
DM-PTB	Dorsal Membrane of the Posterior Tracheal Branch
FEA	Finite Element Analysis
FFT	Fast Fourier Transform
FRF	Frequency Response Function
GLMM	Generalised Linear Mixed-effects Model
HMDS	Hexamethyldisilazane

IPD	Interaural Phase Difference
LDV	Laser Doppler Vibrometry
MEMS	Microelectromechanical Systems
Micro-CT	X-ray Micro-Computed Tomography Imaging
OCT	Optical Coherence Tomography
PA	Proximal Aperture
PTA	Phosphotungstic Acid
PTB	Posterior Tracheal Branch
PTM	Posterior Tympanal Membrane
SD	Standard Deviation
SEM	Standard Error of the Mean
SPL	Sound Pressure Level
TO	Tympanal Organ
VW-ATB	Ventral Wall of the Anterior Tracheal Branch
VW-PTB	Ventral Wall of the Posterior Tracheal Branch

Contents

List of Figures

Chapter 1

Introduction

1.1 Scope of this Research

This research investigates frequency filtering and signal transmission in the peripheral auditory system of the field cricket (family Gryllidae, subfamily Gryllinae). The location of the Gryllinae ear within the proximal prothoracic tibia is shown in Figure 1.1B, highlighted by a red square. Unless otherwise stated, this core biomechanical investigation should be assumed to be the primary focus throughout this research. The results of this main project are presented in Chapters 3 and 4 and are also reported in a 2024 peer-reviewed, first-author paper in the *Journal of the Royal Society Interface* (Appendix C) [1].

In addition to this primary focus, a secondary investigation examines larval development of the parasitoid fly *Ormia ochracea* (family Tachinidae, subfamily Tachininae, tribe Ormiini) within the field cricket host *Acheta domesticus* (Figure 1.1C). The results of this Ormiini investigation are presented in Chapter 5 and are also reported in a 2025 peer-reviewed, co-first-author paper in the *Annals of the Entomological Society of America* (Appendix B) [2].

The thematic link between the primary and secondary components of this research is sound reception in insects, specifically sensitivity to the 4–5 kHz carrier frequency (CF) of the male Gryllinae calling song [3]. This cross-study link is illustrated in Figure 1.1, where the calling song frequency is represented by Panel A. Female crickets (Figure 1.1B) use this frequency cue

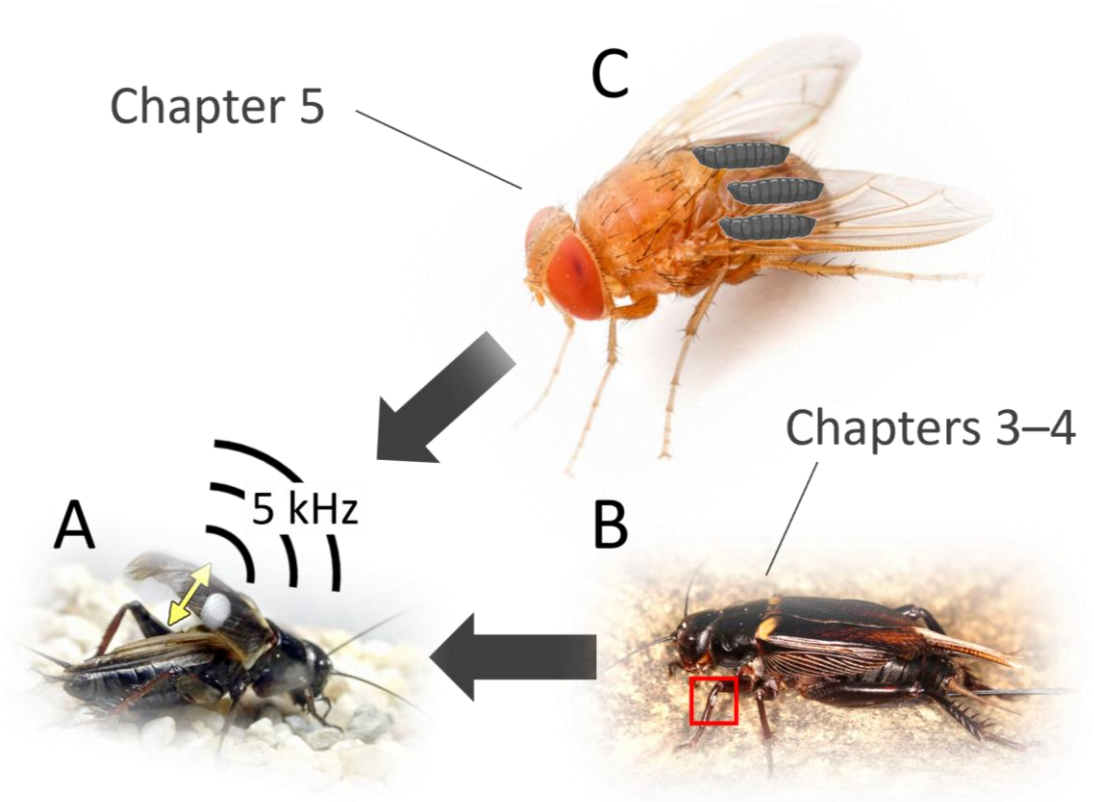

Figure 1.1 | The Gryllinae calling song carrier frequency underlies both auditory biomechanics and parasitoid ecology. (A) The thematic link between the primary and secondary projects is tuning to the carrier frequency of the male field cricket's calling song, produced by forewing stridulation and typically centred around 5 kHz. Image adapted from [4]. **(B)** Female Gryllinae use this conspecific frequency cue to orient phonotactically towards the male, using ears located in the foreleg tibiae (red square). The primary research investigates how this and other spectral components are biomechanically filtered and transmitted in the first stage of the auditory pathway. Photograph: Holger Krisp (Wikimedia Commons, CC BY 3.0). **(C)** Gravid (larvae-carrying) *Ormia ochracea* flies are parasitoids that 'eavesdrop' on the same Gryllinae song frequency to locate field crickets phonotactically and parasitise the host with their larvae. The secondary project investigates how host traits and larval competition within the cricket influence fly offspring development, using *Acheta domesticus* as a host. Photograph: © Salvador Vitanza.

to locate singing males (Figure 1.1A) [5, 6]. However, the peripheral biomechanics within the ear responsible for filtering [7-12] and transmitting [7, 10, 13-15] this frequency, as well as other spectral components (including the

11–16 kHz courtship song CF [16]), remain unresolved. This gap constitutes the primary research problem addressed here.

In certain regions of North America, a parasitoid fly belonging to the tachinid family, *Ormia ochracea* (Figure 1.1C), exploits this same calling song from various Gryllinae species [17]. Gravid (larvae-carrying) female flies, while in flight, use the dominant 4–5 kHz frequency of the male cricket's song to locate crickets, which they target as hosts for larval development [18]. How *O. ochracea* larval development is influenced by resource competition within the host, and by host traits such as cricket size and sex, remains incompletely understood – particularly in manually infested *Acheta domesticus* hosts. This gap constitutes the secondary research problem addressed here.

1.2 **Novelty of the Biomechanics Study**

The ear of the field cricket is notable for its remarkable sound-source localisation accuracy on level with that of humans [6], achieved via three sound inputs per ear [19]. The Gryllid ear also exhibits an instance among insects of 'tonotopy', with auditory neurons arranged along a low to high frequency gradient as in the human cochlea [20]. The field cricket is further well known for its unusually pure-toned calling song [21], produced by stridulation of the forewings [22] transmitted with a single carrier frequency between 4–5 kHz [3].

The field cricket auditory pathway is sharply tuned to the calling song carrier frequency at both the behavioural [5, 6] and neurophysiological [20, 23, 24] levels. The female's phonotactic localisation of the male's position prior to mating is sharply tuned to the 4–5 kHz frequency [5, 6]. The predictable nature of this phonotactic behaviour, which can be correlated with underlying neural pathways, has established the field cricket auditory pathway as a valuable model system in the field of behavioural neuroscience (specifically, neuroethology) [25]. At the biophysical stage of the auditory pathway, the principal focus of this thesis, the posterior tympanal membrane (PTM) is the essential first link of the path of transmission [5, 7, 14, 26]. Nevertheless, there has remained considerable discrepancies as to the exact *vibrational response* of the PTM (**research gap 1**).

Prior to the neurophysiological and behavioural stages is the biophysical stage. The biophysical stage consists of two ears, one in each of the two front legs, at the proximal end of the tibia leg segment. Each of these ears has two tympana. The larger tympanum, the PTM, is regarded as the primary sound receiver of the Gryllinae ear [5, 7, 14, 26]. Despite decades of study, the mechanism of *frequency filtering* in the peripheral auditory system remains unresolved [7-12]. How the cricket's ear achieves its sharp frequency tuning at this initial biophysical stage (including but not necessarily limited to the PTM) is not yet clear (**research gap 2**).

Moreover, early studies show a mismatch between broad tuning of the posterior tympanum and the sharp tuning of the sensory neurons [7, 8], prompting speculations of a 'second filter' somewhere between the PTM and the sensilla to account for this mismatch [8, 10, 12, 26]. Prior to this present work [1], recent studies suggested the PTM–sensilla mismatch is even greater than previously thought, thus renewing attention to the longstanding 'second filter hypothesis' [12, 27]. However, the anatomy of this region between the PTM and the sensilla is complex [15, 23, 28-30], and how the PTM vibrations are *transmitted* through this anatomy to the sensors has remained enigmatic [15] (**research gap 3**).

As such, the region between the PTM and the auditory neurons is predicted to support both an unknown transmission pathway and a yet unidentified mechanism of secondary filtering. However, a limiting factor to the understanding of the functional anatomy of this PTM–sensilla region, as well as of insect acoustical systems in general, is the historic reliance on traditional two-dimensional anatomical techniques restricted to sectioned material [23, 28, 31]. Such 2D techniques not only limit our understanding of the *3D spatial relationships* among auditory structures but also limit the degree of *3D morphometric data*, such as the volume or thickness of a structure (**research gap 4**).

These four research gaps outlined above correspond to the primary research aims of this thesis. Each aim has been addressed through the first application of the following techniques to this system:

- Multi-point *scanning* laser Doppler vibrometry (LDV)
- LDV phase recordings
- X-ray micro-computed tomography (micro-CT)
- Finite element analysis (FEA)

The four primary research aims of this research are therefore as follows:

Aim 1: To resolve the *vibrational profile* of the Gryllinae posterior tympanal membrane (Chapter 3).

Aim 2: To uncover the hypothesised mechanism of *secondary frequency filtering* within the peripheral auditory system of the field cricket, including any filtering occurring downstream of the posterior tympanum (Chapter 4).

Aim 3: To identify the mechanical *transmission pathway* between the posterior tympanal membrane and the auditory neurons (Chapter 4).

Aim 4: To employ X-ray micro-CT imaging for *direct 3D volumetric reconstruction* and to perform *3D morphometric analysis* of the field cricket's internal ear structures (Chapter 4).

1.3 Importance of the Biomechanics Study

Why research insect acoustics? Insects, the most biodiverse taxon on Earth, represent over half of all known animal species [32], offering an unparalleled source of microscale acoustical mechanisms. Tympanal (eardrum) systems, for example, are widespread across vertebrate phyla yet exhibit a relatively conserved layout: two ears positioned on either side of the head leading to an inner ear. In contrast, among invertebrates, only insects possess tympanal ears, yet insects far surpass vertebrates in their diversity of ear design [33]. The tympanal ear among insects is thought to have evolved independently at least 19 times [34], despite only a small proportion of insects exhibiting tympanal hearing [33]. Examples include the one-eared praying mantis [35],

‘wing ears’ on lacewings [36], and ‘neck ears’ on the tachinid fly [37]. Given that an estimated 80% of insects remain to be described [32], there are surely more auditory systems to be discovered. Therefore, for researchers interested in uncovering novel microscale mechanisms for sound reception and processing, the field of insect acoustics offers unparalleled opportunities for discovery.

For engineers, insect ears have already proven to directly inspire the invention of new acoustic sensor technologies. For example, the number of engineering patents from engineering labs around the world based directly on the ear of the parasitoid fly *Ormia ochracea* today numbers in the double figures [38]. In addition, the locust tympanum [39], the *Achroia* moth ear [40], the trichoid sensilla of caterpillars [41] are among the other insect acoustical mechanisms directly inspiring engineered sensors today.

The tympanal ear, whether in vertebrates or insects, is essentially a stretched diaphragm over a chamber that vibrates in response to changes in air pressure either side [42]. The design of the tympanal ear is therefore curiously analogous to human made diaphragm microphones, and one of the technologies that is especially a beneficiary of insect acoustics is in fact the microelectromechanical systems (MEMS) microphone. The insect-inspired MEMS microphone is the same type of microphone used in today’s smartphones and hearing aids [43]. Another potential technology avenue for applying bioinspiration from insect structures is the fast-growing field of acoustic metamaterials [44]. As acoustic technologies further miniaturise and engineers seek to compact improved specifications within ever smaller form factors, insect ears will continue to be a valuable reference for tomorrow’s technologists.

Consider the *O. ochracea* fly. In 1975, a life scientist conducting a behavioural experiment confirmed the fly’s phonotactic ability, without any reference to potential engineering applications [18]. This discovery raised a new biophysical question: the fly locates male field crickets by eavesdropping on their calling songs, laying its larvae on the host, which then develop internally before emerging, pupating, and then hatching as adult flies.

However, its tympanal membranes are only 520 µm apart [45], while the cricket's song carries at a frequency of around 5 kHz, corresponding to a wavelength of approximately 7 cm – far larger than the fly's entire body. This physical mismatch makes it seemingly impossible for the fly to localise sound with such precision, comparable to human hearing, using conventional mechanisms.

To investigate this problem, interdisciplinary research involving biologists, physicists, and engineers uncovered a novel mechanical solution: a see-saw-like structure known as the tympanal or intertympanal bridge, which amplifies interaural differences [37] (Figure 1.2A). Only after these biological and biophysical insights was the mechanism then adopted by engineering laboratories around the world – in China [46], Japan [47], Taiwan [48], the USA [49-53], and the UK (particularly at the University of Strathclyde [54, 55]). Drawing directly on the fly's tympanal bridge mechanism, these engineering teams developed MEMS microphone designs that have demonstrated significantly enhanced performance [46-55] (e.g., Figure 1.2B).

Why research Gryllinae acoustics? (1) The field cricket ear is extremely small [15], the ear-proper in the prothoracic tibia being around 1 mm by 0.5 mm in size; (2) the ear is known to be sharply tuned to a low frequency of around 5 kHz (6.86 cm wavelength) [5, 6, 24, 56]; (3) and yet it still maintains a rare capability of tonotopic frequency decomposition [20, 57]; (4) as well as demonstrating hyperacute sound-source localisation comparable to humans [6]. All of this is achieved in a system both unique in its anatomical layout [15, 23, 28-30] but also largely unresolved in how the biophysical structures filter those frequencies [7-12] and transmit the signal [7, 10, 13-15]. Given the precedent already established by previous biophysical discoveries from other insect ears (e.g., Figure 1.2), this thesis, in helping to solve these problems, could precipitate new bioinspiration solutions.

Furthermore, the Gryllinae acoustical system is now an important model for the field of behavioural neuroscience (neuroethology), with implications for human medicine. An integral part of the field cricket's importance as a neuroethological model [25] is its frequency tuning at each stage of the

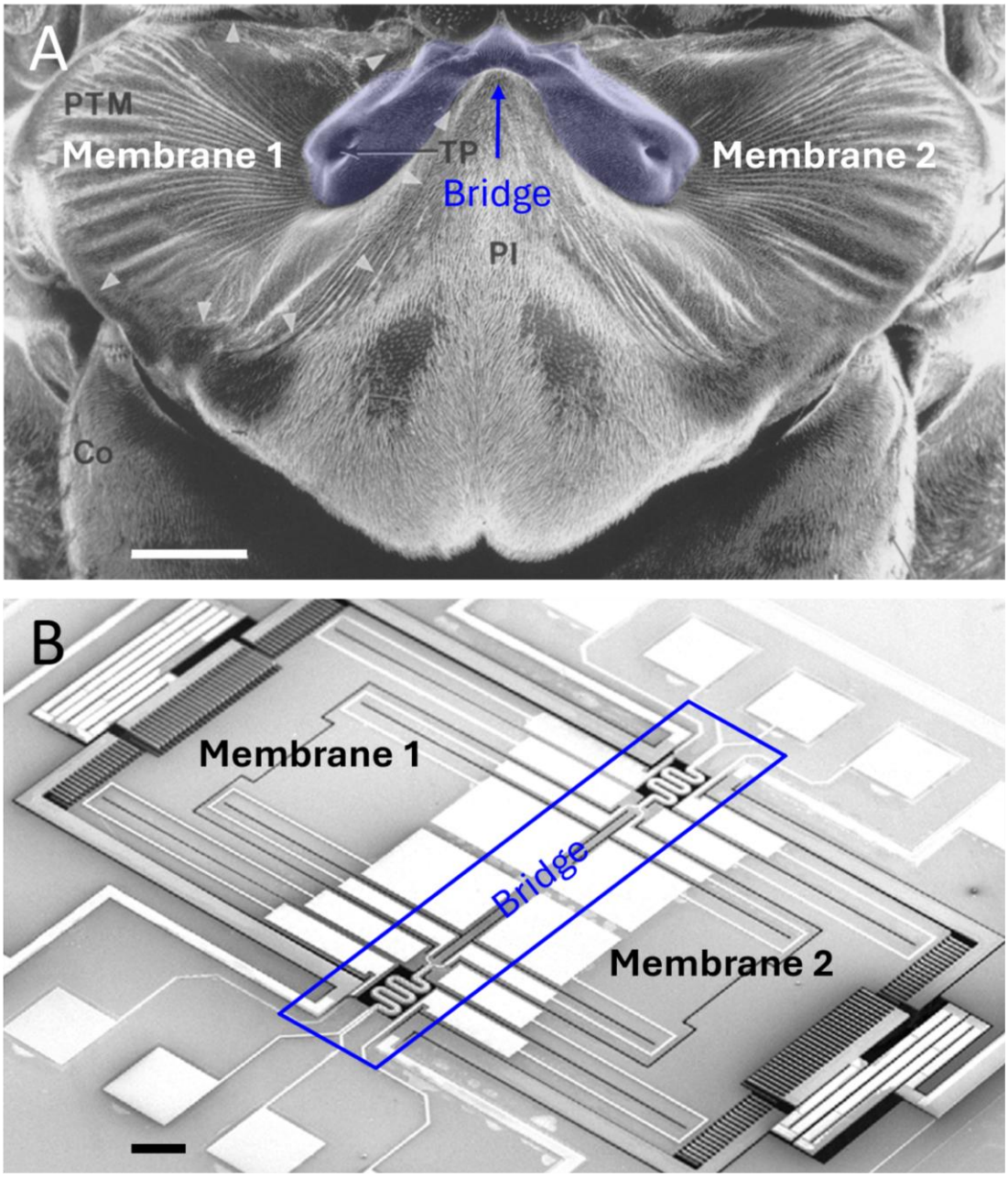

Figure 1.2 | Insect ears inspire novel acoustic micro-sensor technologies. The ear of the *Ormia ochracea* fly serves as an example of how insect acoustics can directly inspire novel engineering solutions. This fly ear was found to consist of two tympanal membranes coupled by an intermediary bridge, and this unique mechanism has since directly inspired the design of microelectromechanical systems (MEMS) microphones. **(A)** Scanning electron micrograph of the *O. ochracea* ear, with the two membranes and the intermediary bridge highlighted. Adapted from [37]. **(B)** An *Ormia*-inspired MEMS microphone developed at the University of Strathclyde, with the *Ormia* analogues highlighted: two membranes (diaphragms) and an intermediary bridge. Adapted from [58]. *Scale bars:* 200 μm.

auditory pathway [11]. Yet the biophysical source of the downstream neuroethology is far less clear, and neuroethologists do not know how the peripheral anatomy is causing the effects they study (Stefan Schöneich, personal communication). By bringing renewed clarity to the biophysical processes at the source of the auditory pathway, this thesis may also contribute to the contextualisation of our understanding of this valuable neuroethology model.

1.4 **Conferences, Awards, Outreach**

In addition to three peer-reviewed publications in high-impact journals, this PhD project produced the following other deliverables, listed below.

1.4.1 Conferences

- **2023**
  - I. Invertebrate Sound and Vibration (ISV) Conference 2023, Lincoln, UK. *"Coupled membranes: possible analogue of mammalian ear bones found in the field cricket ear"*. (Poster presentation). (Abstract).
- **2022**
  - II. 14th International Congress of Neuroethology 2022, Lisbon, Portugal. *"Auditory mechanics and morphometry of an insect's tracheal vesicles"*. (Poster presentation). (Abstract).
  - III. 14th SINAPSE (Scottish Imaging Network: A Platform for Scientific Excellence) Annual Scientific Meeting 2022, Glasgow, UK. *"Micro-CT reveals morphometrics and mechanical properties in an insect's auditory vesicles"*. (Oral presentation).
  - IV. 4th Doctoral School Multidisciplinary Symposium (DSMS) 2022, University of Strathclyde, UK. (Oral presentation).
- **2021**
  - V. 3rd Doctoral School Multidisciplinary Symposium (DSMS) 2021, University of Strathclyde, UK. (Oral presentation).

1.4.2 Awards

- **2024**
  - *Images of Research 2024* competition, University of Strathclyde, 'Highly Commended' [59].
- **2023**
  - *UK-Canada Globalink Doctoral Exchange Scheme 2023* [60]. Funding awarded by UKRI and Mitacs based on a submitted research proposal (Appendix A).
  - Material from this awarded research proposal appears in Chapter 3 of this thesis.
- **2022**
  - *3 Minute Thesis 2022* competition, University of Strathclyde, 2022 finalist [61].

1.4.3 Outreach

- **2024**
  - *Glasgow Science Festival 2024* stall, April 2024 [62].
- **2022**
  - Clydeview Academy invited talks to secondary school (S5) pupils, June 2022
  - *Pint of Science 2022* invited talk, May 2022 [63].

1.5 **Contributions and Collaborations**

This work comprises independently led research conducted within the Bioacoustics Group at the Centre for Ultrasonic Engineering, University of Strathclyde, Department of Electronic and Electrical Engineering. The research was funded through a Student Excellence Award (SEA) Studentship under an EPSRC Doctoral Training Partnership, alongside a competitively awarded secondment to the University of Toronto funded by Mitacs and UKRI.

The primary body of work was conducted at the University of Strathclyde. All experiments were conceived, designed, and executed by the

thesis author. This included laser Doppler vibrometry (LDV) experiments and X-ray micro-computed tomography (micro-CT) imaging and analysis. The thesis author also provided the micro-CT-informed geometry for finite element analysis (FEA), defined the material properties for the finite element models, and directed the overall FEA simulation framework. The FEA simulations themselves were implemented by Dr Andrew Reid.

This work was supported by several key collaborations. The project was initially supervised by Dr Joseph Jackson and Prof. James Windmill, with Dr Reid – originally a co-author on early outputs – later assuming the role of primary supervisor. Dr Jonathan Williams, also a co-author, contributed particularly through expertise in X-ray micro-CT. Statistical analysis of the 3D micro-CT thickness data was initially conducted by the thesis author; however, the final iteration of this analysis, as reported in the associated publication [1], was performed by Dr Williams. A theoretical component on natural resonance and driving forces (Section 2.3.3) draws on supplementary material authored by Dr Reid.

This body of work resulted in a first-author peer-reviewed publication (2024) [1] and associated conference presentations.

A second major component of the research arose from a competitively awarded UKRI–Mitacs funded *UK-Canada Globalink Doctoral Exchange Scheme* secondment to the University of Toronto, supervised by Prof. Andrew Mason. During this placement, the thesis author independently conceived and executed a series of preliminary experiments investigating *Ormia ochracea* larval development across different species of cricket hosts.

Given the overlap with ongoing work in the Lee Lab at St. Olaf College (Prof. Norman Lee), this led to a three-laboratory three-country collaboration and a 2025 peer-reviewed publication for which the thesis author is one of two first-authors [2]. Within this collaborative project, the thesis author contributed to conceptualisation and data collection and subsequently assumed a lead-author role.

1.6 **The Sensory Modality of Hearing**

Sensory modalities may be considered to follow a sequence of three broad stages: biomechanical, neurophysiological, and behavioural (Figure 1.3). Across sensory modalities, that of *hearing* has certain unique advantages. One of these is 360° perception of the organism's environment. Unlike vision which requires a direct line of transmittance between source and receiver, sound can travel in all directions, refract around obstacles, and travel through them. This can be invaluable to an organism: consider for example a female bushcricket (also known as a katydid) in dense tropical vegetation listening to the calling song of a male far away and singing from behind numerous complex obstacles (leaves, branches, trees, etc.), yet nevertheless being able to orient towards and locate the calling male.

Another advantage of hearing is its unparalleled capacity for information-rich communication. Sound signals can convey complex, real-time information, whereas communication via pheromones, for example, is slower and typically holds less information. An acoustic signal, such as a mating call, can communicate a remarkable breadth of detail, including species identification [64], individual identity [65], sexual maturity [66], and even the health of the caller [67]. This breadth is possible because an auditory signal can rapidly modulate multiple components of sound simultaneously, including frequency, amplitude, and temporal pattern.

1.7 **Fundamentals of Physical Acoustics**

Sound is a 'wave' because alternating compressions and rarefactions form a repeating pattern as they propagate (Figure 1.4). A wave may be understood as the organised propagation of a disturbance through space [68]. This can be visualised using a helical spring: a localised compression produces alternating regions of compression and rarefaction that propagate along its length. Similarly, vibrating vocal cords cause air particles to oscillate parallel to wave travel, defining a *longitudinal wave* (e.g., Figure 1.4), which characterises most acoustic signalling.

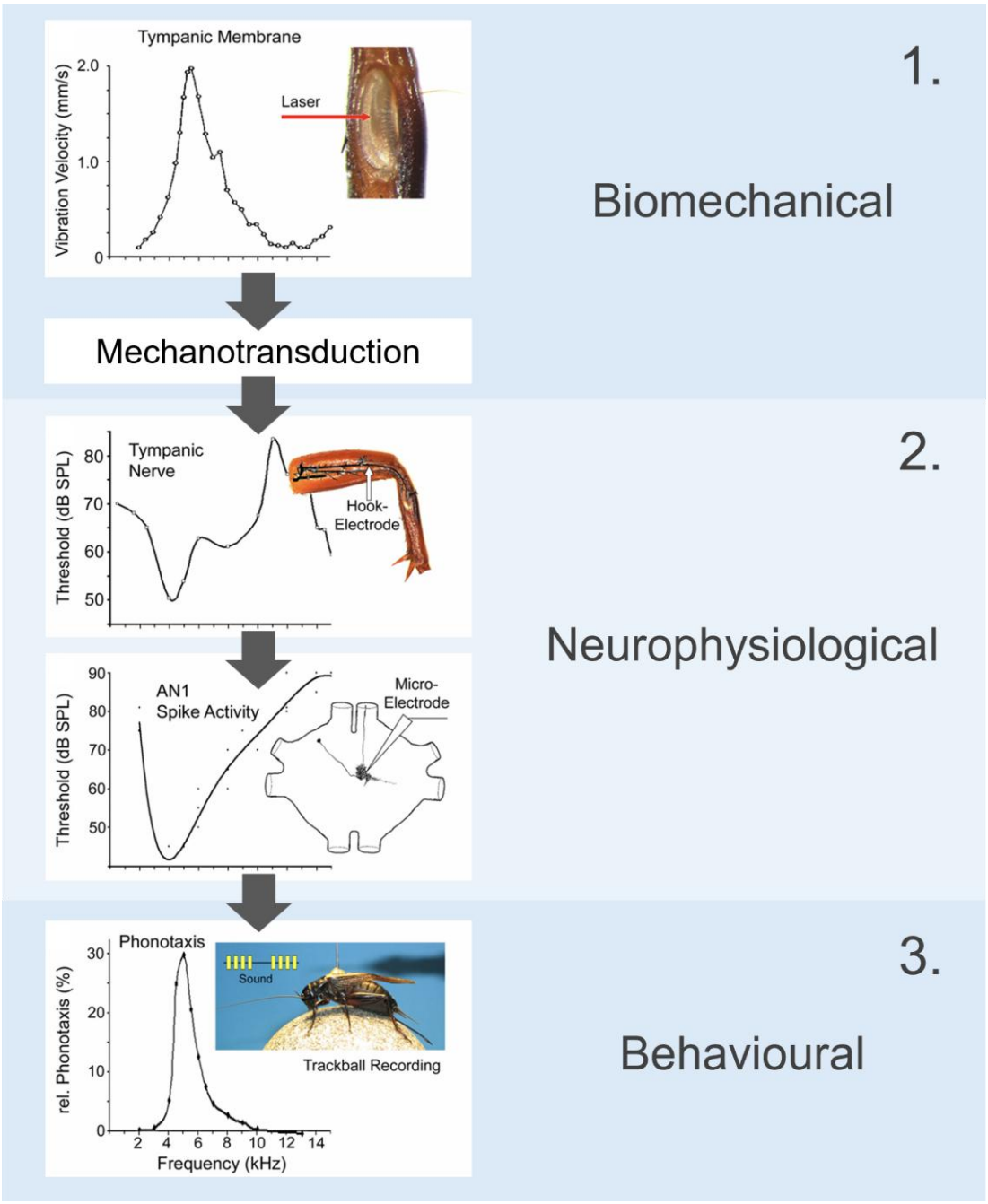

Figure 1.3 | Sensory pathways follow three sequential stages. Illustrated here using the example of frequency filtering in the auditory pathway of the field cricket (adapted from [11]). Across sensory modalities such as vision, touch, and hearing, processing typically progresses through three stages: **(1)** a biomechanical stage, in which mechanical structures deform in response to a stimulus, followed by mechanotransduction that converts this motion into an electrical signal; **(2)** a neurophysiological stage, in which the signal is transmitted through neural networks to a central processing centre, typically the brain; and **(3)** a behavioural stage, in which the processed information elicits an appropriate behavioural response.

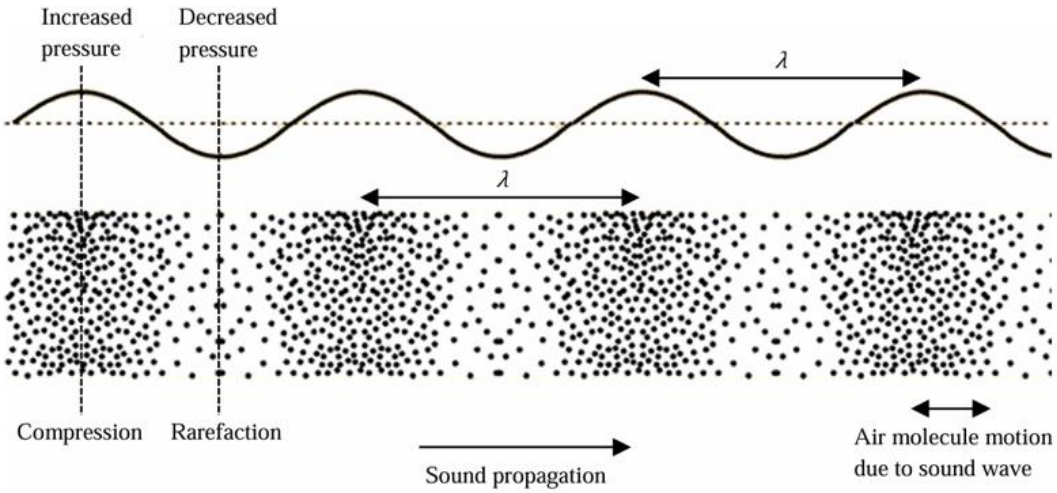

Figure 1.4 | Sound waves propagate through alternating compressions and rarefactions. Sound consists of vibrations travelling through a medium (solid, liquid, or gas) via alternating regions of compression (increased molecular density and pressure) and rarefaction (decreased density and pressure), as illustrated here. These fluctuations result from the displacement of molecules by a vibrating source (e.g., the forewings of a male field cricket), initiating a chain of collisions that propagates through the medium. Although the sound wave moves directionally away from the source, individual molecules oscillate back and forth around their equilibrium positions. In the top part of the figure, molecular density is plotted against distance to produce a characteristic waveform, with peaks corresponding to compressions and troughs to rarefactions. The wavelength (λ) represents the distance between successive compressions or rarefactions. Figure from [39].

For airborne signals, wave motion typically aligns with the biomechanical source (e.g., vocal cords). In substrate-borne signalling (e.g., an ant tapping), the wave remains longitudinal but travels in a different plane to the source motion.

A longitudinal waveform shows peaks (compressions) and troughs (rarefactions) (Figure 1.4). The y-axis represents pressure (Pa) or particle velocity (m/s), and the x-axis time (s) or position (m). The example shown in Figure 1.4 is *sinusoidal*, producing a pure tone with constant frequency and amplitude.

Transverse waves, where particle motion is perpendicular to wave travel, are rare in vibroacoustics but occur in systems like spider webs [69].

Bioacoustic signals are *travelling waves*, with energy moving through a medium; this is distinct from *shoaling waves*, though the term is often used interchangeably. Shoaling waves, often referred to as travelling waves, enable ‘tonotopy’ across taxa (Section 1.9; [70]).

A *standing wave* forms when two waves of equal frequency travel in opposite directions, producing nodes (no movement) and antinodes (maximum movement). Nodes result from *destructive interference*; antinodes from *constructive interference*, which doubles amplitude [12, 71-73]. Standing waves can therefore amplify signals, as in resonating chambers like mole cricket burrows [74].

A sound wave’s structure and behaviour can be described by its key properties: frequency, amplitude, wavelength, and phase.

Frequency is the number of complete oscillations (cycles of compression and rarefaction) per second, measured in Hertz (Hz). One hertz equals one cycle per second; for example, a 5,000 Hz (5 kHz) signal completes 5,000 cycles each second. Frequency determines pitch and is central to species-specific communication in insects, such as mating calls used to recognise conspecifics.

Hearing ranges vary across organisms. The human audible spectrum spans 20 Hz to 20 kHz; frequencies above this are ultrasonic, and below 20 Hz are infrasonic. Many insects, such as *Galleria mellonella*, detect only ultrasonic frequencies, aiding predator avoidance (e.g., bats) [75], while others, such as Gryllinae crickets, span both audible and ultrasonic ranges (spanning 500 Hz to 42 kHz) [76].

Amplitude describes the magnitude of a sound wave. It may refer to particle motion – measured as maximum velocity (m/s) or displacement (m) – or to pressure variation, measured as deviation from ambient pressure (Pa). In terms of perceived loudness, amplitude is expressed in decibels (dB). It enables organisms to distinguish between near and distant sound sources.

Wavelength is the distance between successive compressions or rarefactions, measured in metres (m), and is inversely proportional to frequency (longer wavelength = lower frequency). This is important for

directionality: some insects, particularly orthopterans, process low frequencies with wavelengths longer than their body size, requiring alternative localisation mechanisms [19].

Phase is a wave's position in its cycle relative to another, measured in degrees (°), with one full cycle equal to 360°. A phase shift occurs when this position changes while frequency remains constant. A key example is the interaural phase difference (IPD), the phase difference between sounds arriving at each ear due to source position. Many animals, notably field crickets [12, 71-73], use IPD as part of their directional hearing systems.

In nature, frequency, amplitude, wavelength, and phase can all be modulated, allowing acoustic signals to convey complex information.

1.8 **Mechanotransduction and the Insect Chordotonal Organ**

Mechanotransduction is the process by which mechanical stimuli, such as pressure, stretch, or vibration, are converted into electrical signals, using sensory cells (or complexes of cells) called mechanoreceptors. Mechanotransduction therefore acts as the transition between the biomechanical and neurophysiological stages of sensory systems (Figure 1.3). All mechanoreceptors consist of three broad features: (1) a structure that deforms in response to mechanical force, (2) mechanically gated ion channels that open due to this deformation to allow ion flow, and (3) a sensory neuron that generates an electrical impulse called an action potential when the ion concentration reaches a threshold [77].

In understanding mechanotransduction in insect acoustics, vertebrate – especially mammalian – auditory mechanoreception serves as a valuable comparative model that helps illuminate underlying principles and guide interpretation of the less well-characterised insect system. This approach is known as comparative biology.

The mechanoreceptors known as hair cells are found in the ears of all major groups of terrestrial vertebrates – including amphibians, reptiles, birds, and mammals (Figure 1.5A). In the mammalian ear, each hair cell is embedded within supporting cells located between the basilar membrane and the tectorial

membrane, extending from one to the other. Near the tectorial membrane, the hair cell features a cluster of hair-like projections known as stereocilia, which emerge from the supporting tissue. These projections are arranged in a staircase-like pattern, varying in length from shortest to tallest, and are surrounded by a potassium-rich fluid called endolymph in mammals. This staircase organisation of stereocilia, as well as their role in sound detection, is conserved across non-mammalian vertebrates [78, 79]. While much of the following discussion is applicable to vertebrate ears in general, it focuses specifically on the mammalian hair cell.

When sound vibrations cause the mammalian basilar membrane to move, it pushes the stereocilia against the tectorial membrane, which causes the stereocilia to bend.

The stereocilia are physically linked by thin filaments called tip links. When a taller stereocilium tilts, it pulls on the mechanically gated ion channel of its neighbouring shorter stereocilium via its tip link. This allows positively charged K^+ and some calcium (Ca^{2+}) ions to rush into the cell, making its internal environment more positively charged.

This tip-link mechanism and ion influx is conserved among vertebrates. The cell's internal voltage increases, usually from around –60 mV to a threshold of about –40 mV. At this point, additional ion channels (voltage gated ion channels) at the base of the hair cell, near an associated neuron, open and allow an influx of more Ca^{2+} ions. This causes the hair cell to release chemical signals called neurotransmitters to the neuron. Synaptic transmission between hair cells and sensory neurons is also a general vertebrate feature [79].

The sensory neuron is surrounded by a different fluid, called 'perilymph', that is high in sodium (Na^+) ions. When a receptor on the surface of the neuron binds to the incoming neurotransmitter, an ion gate opens and Na^+ flows into the cell, changing the neuron's voltage from around –70 mV to a threshold of about –55 mV. This threshold triggers the opening of more Na^+ channels in a chain reaction, leading to a rapid influx of Na^+ and a rise in voltage to around +30 mV. This very sudden change is called an action potential, or neuron firing, and it moves like a wave down the neuron's long axon. All the axons from the

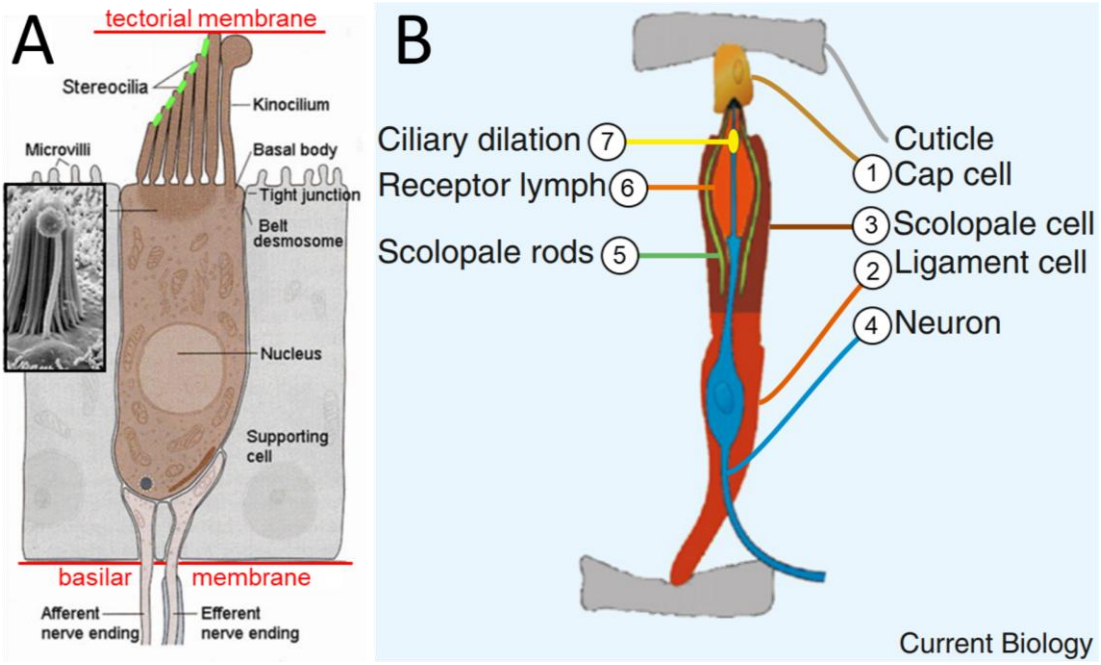

Figure 1.5 | Auditory mechanoreceptors convert vibrations into electrical signals. A generalised schematic of a vertebrate hair cell is shown in **(A)**, adapted to illustrate the mammalian basilar and tectorial membranes (red). In the vertebrate ear, stereocilia are arranged in a staircase-like pattern and interconnected by tip links (green), such that when a taller stereocilium moves, it pulls on its shorter neighbour, opening mechanically gated ion channels. Inset shows an image of stereocilia from the ear of a frog. Adapted from [78]. **(B)** The chordotonal organ, found in insect ears, responds mechanically to sound by connecting two cuticular structures (often one being the tympanum) and detecting their relative movement. Shown here is a single scolopidium, the functional unit of the chordotonal organ, which is here labelled according to its description in the main text: 1. cap cell; 2. ligament cell; 3. scolopale cell; 4. neuron; 5. scolopale rods; 6. receptor lymph; 7. ciliary dilation. Adapted from [80].

ear join to form the auditory (or cochlear) nerve, which communicates the electrical signal to the brain [79].

Chordotonal organs are mechanoreceptors found in insects and crustaceans [81]. Chordotonal organs are found across insect taxa and occur throughout the insect body, including in the joints of the legs and wings. They detect mechanical movement and are mostly used for proprioception, as well as vibration sensing and hearing [80].

The sensory unit of the chordotonal organ is the scolopidium. A chordotonal organ may consist of a single scolopidium that contains only one sensory neuron (as in the notodontid moth tympanal ear) or may be composed of several thousand scolopidia each of which comprises up to four sensory neurons (such as in the Johnston's organ of the mosquito ear) [80].

Each scolopidium is a complex of cells with each subunit performing a different role in the process of mechanotransduction, as illustrated with subunits numbered and labelled in Figure 1.5B. Typically, the (1) *cap cell* (a type of 'attachment cell') secures the scolopidium to the vibrating structure, while the (2) *ligament cell* anchors the other end of the scolopidium to a more stable substrate [82]. However, this orientation can be reversed, with the cap cell attaching instead to the stable structure, such as in cicadas and mantids [83]. In insect tympanal systems the vibrating structure is often the tympanum itself; however, in some insects, as in other auditory systems (e.g. the basilar membrane in mammals), the receptor instead couples to intermediary structures that transmit motion from the sound-receiving membrane to the mechanoreceptors. In the Gryllinae tympanal organ, cap cells attach scolopidia to one end of the 'cellular mass', a tent-like structure suspended by ligaments from the internal exocuticular wall of the leg [15].

Adjacent and proximal to the cap cell is the (3) *scolopale cell***,** into which the dendritic cilium of the (4) *neuron* extends. The cilium is surrounded by the (5) *scolopale rods*. Within the scolopale cell is a fluid called (6) *receptor lymph*, which has been hypothesised to be high in K^+ ions [84]. The cilium likely deforms in response to sound-induced mechanical stimulus, and this mechanical force has been proposed to be that of *stretch* [85]. Multiple sites along the cilium are candidate sites for mechanically gated ion channels, including the (7) *ciliary dilation* [86].The exact nature of the mechanically gated ion channels used in insect auditory receptors, and how they permit K^+ influx, remains unclear [87]. However, Warren and Matheson [87] used 'patch-clamp' recordings from locust auditory neurons and chemically activated two dendritic membrane proteins near the ciliary dilation, 'Nanchung' and 'Inactive', using the insecticide pymetrozine. This produced a sustained current matching the

natural sound-evoked response, and subsequent sound stimulation caused no further change, suggesting the channels were already fully open. They therefore propose that the Nanchung-Inactive protein complex may either constitute, or form part of, the mechanically gated ion channel employed in insect chordotonal organs.

1.9 **Tonotopy**

The organisation of distinct frequency sensitivities across auditory neurons is broadly termed *tonotopy*. In insect chordotonal organs, the auditory neurons within scolopidia respond preferentially to specific frequencies [20].

Tuning of insect auditory neurons could arise from purely mechanical processes – i.e., from the physical properties of the sound-receiving apparatus (such as the tympanum or antenna) and their associated structures – or from neurophysiological processes within the sensilla themselves, or from a combination of both. Recent evidence, particularly from the locust Müller's organ, suggests that tuning in insect auditory chordotonal organs is likely achieved primarily if not solely through mechanical means [34].

Tuning is plotted as a threshold or tuning curve, which shows the minimum sound intensity (amplitude) required to evoke an action potential in a neuron at different frequencies. The neuron is most sensitive, meaning the lowest sound intensity at which the neuron can fire, at a particular point or range within the frequency spectrum. Tuning may be sharp, as exhibited in the Gryllinae AN1 interneuron, where the neuron is highly selective and responds best to only a narrow range of frequencies, or broad as in the field cricket's AN2 interneuron, where the neuron fires optimally across a wider range [24].

In some insects, all auditory neurons may be tuned to similar frequencies, as is the case in many moths, such as owlet moths (family Noctuidae), which possess two auditory neurons. These moths do not communicate acoustically but detect and respond to the ultrasonic echolocation calls of predatory bats [88]. Orthopterans operating in acoustically complex environments [33], exhibit different sensory neurons tuned to different frequencies, allowing discrimination of spectra from

predators and those from conspecific signals such as calling and courtship songs [57, 89].

Frequency discrimination requires multiple auditory neurons to respond to different frequencies. This differential tuning arises when neurons attach to mechanical structures that vary in their properties – for example in thickness or width – causing different regions to vibrate maximally at different frequencies. This frequency-specific maximal displacement of a point on a substrate, if coupled to a sensory neuron, can in turn mechanically stimulate that neuron independently, thus tuning the cell to a single frequency. Thus, 'tonotopy', from the Greek *tonos* ('frequency') and *topos* ('place'), can also be described as *place-based frequency decomposition*.

Tonotopy often involves a 'travelling wave', a phenomenon enabling frequency decomposition across diverse taxa, from humans [90, 91] to bushcrickets [92, 93] and locusts [94], and suggested in crickets [11]. In both the mammalian basilar membrane and the bushcricket crista acustica, a wedge-shaped membrane provides the morphological gradient that supports the travelling wave, which shoals along the membrane, increasing in amplitude while slowing, and reaching maximal displacement at a frequency-specific location [90-93].

In contrast to vertebrates, tonotopic systems are rarer in invertebrates yet show greater diversity. Given this diversity and our comparatively limited understanding of these systems, invertebrate tonotopy offers potential for novel discovery. Insect tonotopy may be categorised into two types, *cochlea-like tonotopic systems* and *tympanal tonotopic systems*. Both are exemplified by the bushcricket and the locust, respectively, as illustrated in Figure 1.7.

1.9.1 Cochlea-like Tonotopic Systems in Insects

The ear of the bushcricket (also known as katydids; family Tettigoniidae, infraorder Tettigoniidea) has been compared to the mammalian cochlea [93] (Figure 1.6A), as has the field cricket ear [15] (Figure 1.6B), although crickets – while also within the suborder Ensifera – are distinct from bushcrickets. The bushcricket's auditory system mirrors key functions of the mammalian middle

and inner ear. Each of the bushcricket's two tympana include a small rigid tympanal plate. The tympanum and tympanal plate act like a seesaw. Sound makes the tympanum vibrate, and because it is connected to the smaller tympanal plate around a pivot point (a fulcrum), the two rock back and forth like a lever. The large movement of the tympanum is converted into a smaller but stronger push at the tympanal plate, which helps drive vibrations into the fluid-filled acoustic vesicle (Figure 1.7B), where the resulting fluid motion deflects the dorsal cuticle of the anterior tracheal branch supporting the *crista acustica* organ (Figure 1.7A). These deflections travel along the dorsal cuticle as a travelling wave, bending the crista acustica and mechanically stimulating the tonotopically arranged auditory sensilla attached [93].

This lever-based amplification facilitates the transfer of sound energy from air into fluid, much like the small bones of the middle ear in mammals relay sound to the cochlea. Vibrations in the bushcricket's acoustic vesicle generating a travelling wave along the crista acustica and selectively stimulating the linearly arranged sensilla according to pitch is analogous to the frequency mapping of the mammalian cochlea and its basilar membrane [93].

The most noticeable characteristic of the bushcricket crista acustica is its tapered shape and orderly arrangement of sensilla (Figure 1.7A). The 25 or so sensory neurons are tonotopically arranged along the wedge-shaped crista acustica from low frequency tuned cells at its widest point (tuned from about 6 kHz) to those tuned to higher frequencies at the narrower tip (up to and above 50 kHz) [95]. These sensors lie on a thin wall of a cuticular cavity, the anterior tracheal branch. Their dendrites project dorsally, and each connects to a cap cell which is itself attached to a thin sheet that covers the entire organ, the tectorial membrane (Figure 1.7B). The size gradient of these cap cells is correlated with the tonotopy. However, the correlation is not sufficient to account for the full resolution of frequencies represented. The tonotopy of the crista acustica may therefore require another morphological gradient such as features of the neurons themselves [96]. A travelling wave starts at the distal, narrow end of the crista acustica and travels proximally. Low frequency sounds

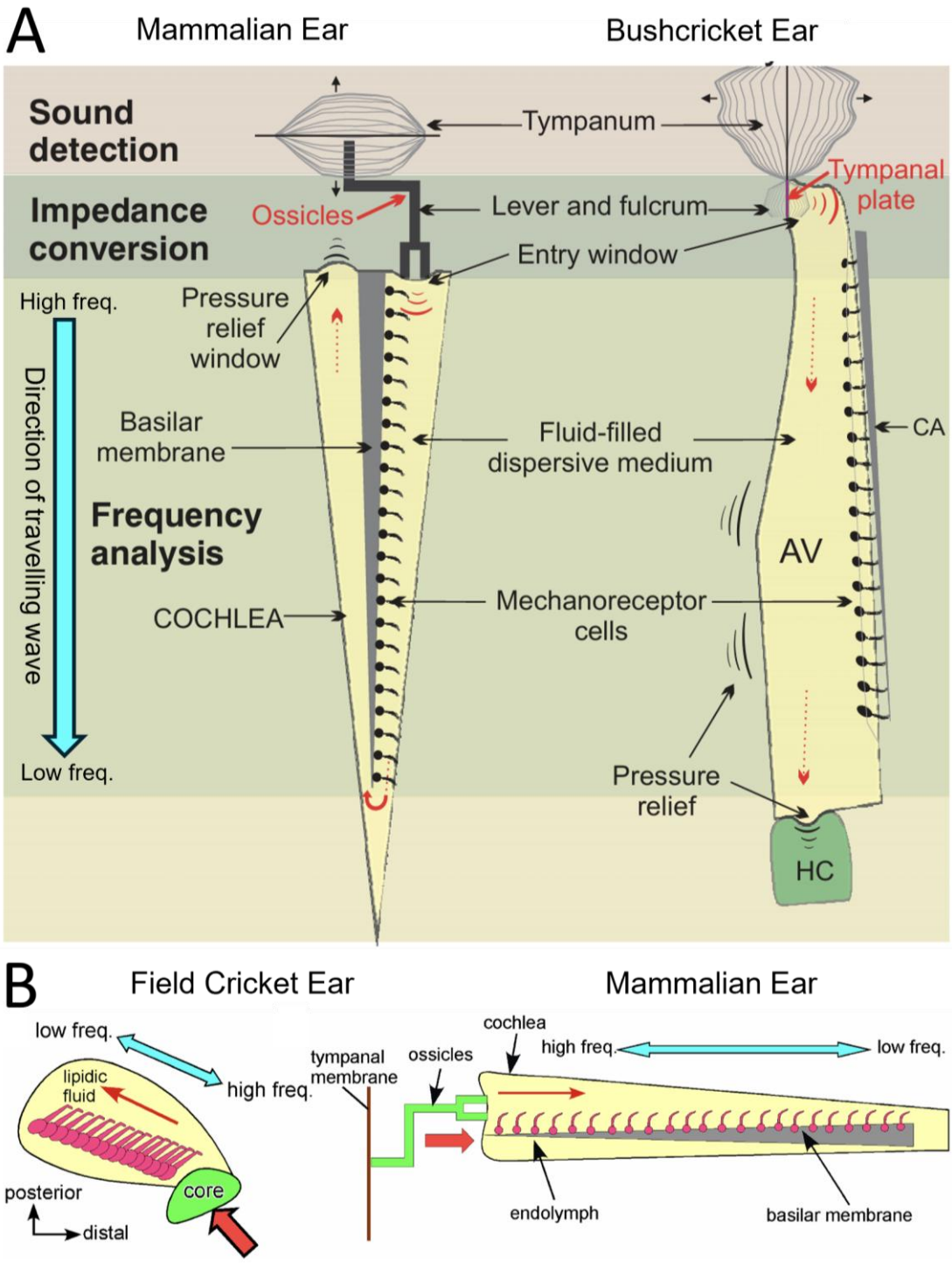

Figure 1.6 | Insect ears reveal mechanisms analogous to those in the well-characterised mammalian ear. Certain insect ears have been directly compared by researchers to the human–mammalian ear. **(A)** The bushcricket ear (right) exhibits middle and inner ear functionality analogous to that of mammals (left) [93]. **(B)** In the Gryllinae ear (left), the epithelial core in the suspensorium may serve a lever-like function similar to the ear bones (ossicles) of the mammalian ear (right) [15].

Insect *cochlear* tonotopy

Bushcricket

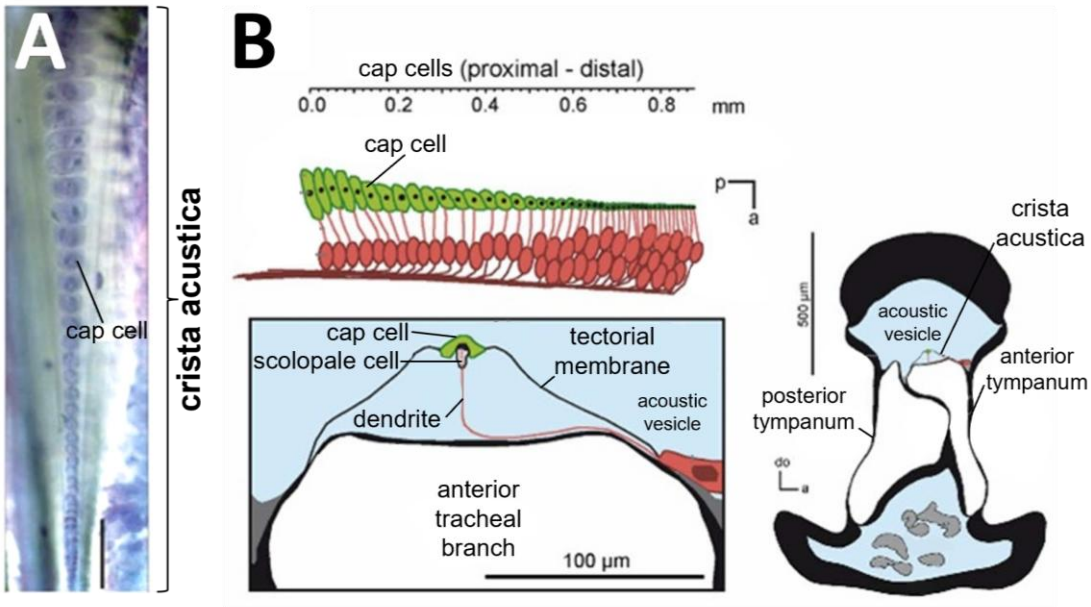

Insect *tympanal* tonotopy

Locust

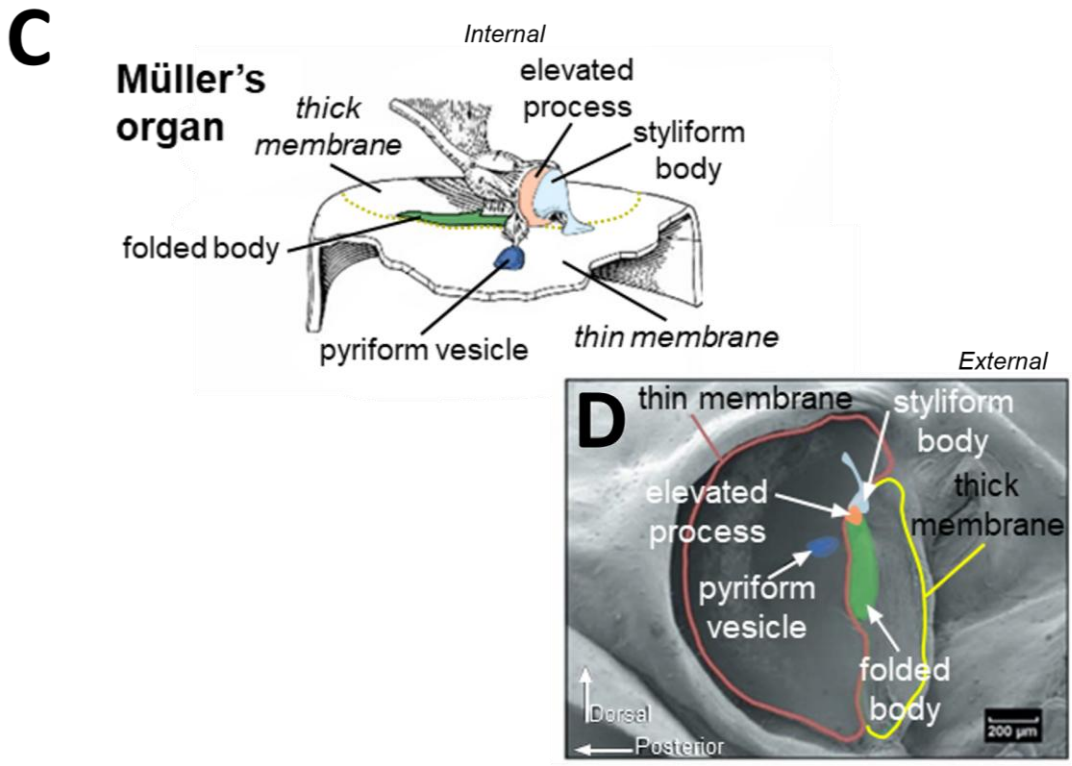

Figure 1.7 | Insect tonotopy occurs in cochlear and tympanal forms. Adapted from Díaz-García, Latham et al. (2023) [70]. Tonotopic systems in insects can be broadly categorised into two types: cochlea-like **(A,B)** and tympanal **(C,D)**. **(A,B)** In bushcrickets, as in mammals, tonotopy occurs in a 'middle ear'. In bushcrickets, this organ is called the *crista acustica* and is functionally analogous to the mammalian cochlea. **(A)** Photograph of the wedge-shaped *crista acustica* [92]. **(B)** Illustration showing the morphological gradient of the *crista acustica* [96]. **(C,D)** In contrast, locusts do not exhibit a separate middle and inner ear; tonotopy occurs directly on the sound-receiving structure, the tympanum itself, which consists of the thin and thick membranes. On the underside of the tympanum, scolopidia of Müller's organ attach to four distinct morphological regions: the folded body, the styliform body, the elevated process, and the pyriform vesicle. **(C)** Illustration of Müller's organ and the *internal* surface of the locust tympanum, adapted from [97]. Outline of thick membrane is approximate. **(D)** Annotated scanning electron micrograph of the *external* surface of the locust tympanum, adapted from [94]. Positions of styliform body and elevated process approximate.

travel further towards the wider end, while high-frequency sounds stop closer to the narrow distal end [92].

1.9.2 Tympanal Tonotopic Systems in Insects

In what may be categorised as tympanal tonotopic systems (see Figure 1.7C,D), known in the locust [94] and in the cicada [98], the tympanum, responsible for sound capture, is also the structure responsible for frequency decomposition. Both functions occur at the same substrate (in contrast to cochlea-like systems). This dual functionality requires the eardrums to be unusually complex, and indeed the locust tympanal membrane may be the most sophisticated tympanum.

Unlike bushcrickets and crickets (suborder Ensifera), locusts (suborder Caelifera) have only one tympanum per ear. Locusts therefore possess two tympana in total, one on each lateral side of their first abdominal segment. The locust tympanum is morphologically heterogeneous, consisting of the thin membrane and the thick membrane. Each of these membranes also contains specialised cuticular structures: the thin membrane contains the *pyriform*

vesicle, while the thick membrane contains the *folded body* (Figure 1.7C,D). In addition, two further structures occur near the transitional boundary between the thin and thick membranes [99]: the *elevated process* and the *styliform body* (Figure 1.7C,D) [94, 97, 99].

These four structures serve as attachment sites for three groups [87] of mechanoreceptor neurons forming *Müller's organ* (Figure 1.7C). The organ comprises approximately 60–80 scolopidia [100] distributed across these three groups. Each group is tuned to a distinct frequency band: the folded body (1.5–3 kHz), styliform body (around 3.5 kHz), elevated process (3.5–4 kHz), and pyriform vesicle (10–14 kHz) [100].

When the locust tympanum is stimulated with sound, a travelling wave is initiated in the thin membrane and propagates across the tympanum, with maximal vibration occurring at different regions depending on the input frequency. At high frequencies, motion of the thick membrane becomes very small relative to that of the thin membrane – The travelling wave converges near the high-frequency attachments and rapidly attenuates upon reaching the thicker cuticle. In this way, sound energy is spatially distributed across the tympanum, producing a frequency-dependent mechanical decomposition of high and low frequencies [94].

1.10 The Four Main Types of Insect Auditory Receptor

Vibroacoustic apparatus among insects may be categorised into four broad types [82].

Tympanal Organ and Johnston’s Organ

The distinction between the sound pressure and particle velocity components of sound underlies two major types of auditory receptors in insects [42]. Both are sensitive to airborne signals.

First, (1) the *tympanal organ*, the chordotonal organ of tympanal systems, occurs in seven of the approximately 30 insect orders, including Lepidoptera (especially moths) and Orthoptera (grasshoppers, bushcrickets, and crickets), and detects the pressure component of sound. In moths,

tympanal hearing is typically associated with detecting ultrasonic echolocation calls from predatory bats. Among orthopterans, tympanal hearing is unusually widespread compared with the other six orders, reflecting their extensive use of complex intraspecific acoustic communication [33].

Second, (2) *Johnston's organ*, present in insects such as mosquitoes [101] and fruit flies [102], detects the particle velocity component of sound [82].

The tympanal ear (which contains the tympanal organ) and the antennal ear (which contains Johnston's organ in the pedicel of the antenna) detect different sound components because of their mechanical structure [42].

Tympanal ears (Figure 1.8A) detect sound pressure using a thin membrane called the tympanum stretched over an air-filled cavity. The membrane vibrates when pressure on one side changes relative to the other. This design makes tympanal ears highly sensitive and well suited for *far-field* detection, meaning regions distant from the sound source where pressure dominates and particle velocity is relatively small.

In contrast, antennal ears (Figure 1.8B) detect particle velocity through the movement of the antenna caused by the viscous drag from air particle motion generated by nearby sounds. Each antenna bears an appendage called the arista, which has fine extensions. The shape and stiffness of the arista mechanically tune antennal motion to be most sensitive at particular frequencies, such as the wingbeats of other mosquitoes. As the antenna moves, the scolopidia of Johnston's organ near the antennal base are mechanically stimulated. Antennal ears are especially effective in the *near-field* – areas close to the sound source, typically less than one wavelength – where particle motion is strong but decays rapidly with distance [42].

Trichoid Sensilla and Subgenual Organ

Two other major categories of auditory receptors are more common across the Insecta and detect airflow and substrate-borne vibrations.

The third type is (3) *trichoid sensilla*, hair-like structures abundant on the external surface of the animal. They detect airflow and occur, for example,

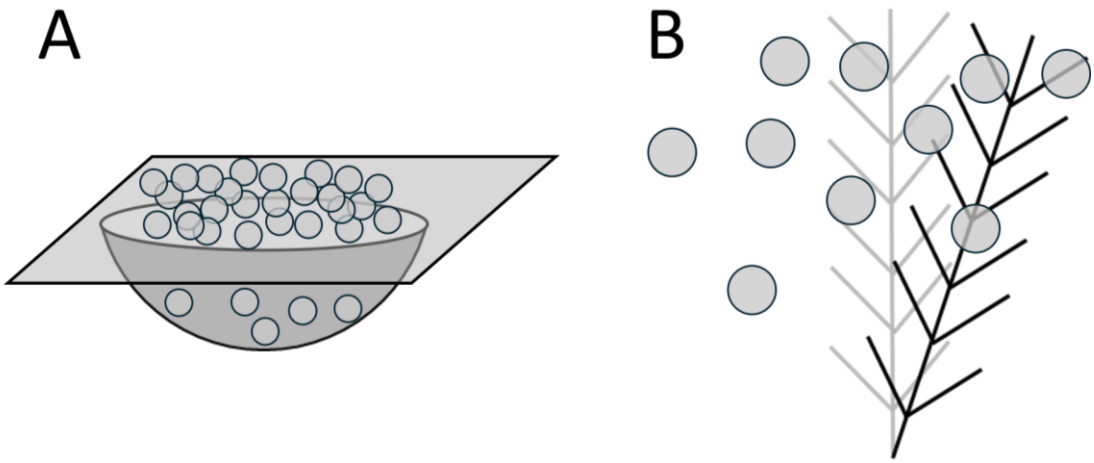

Figure 1.8 | Insect ears detect sound via pressure and particle velocity mechanisms. Among insect ears that detect airborne signals, there are two broad categories corresponding to sensitivity to distinct components of a sound signal, its sound pressure and its particle velocity. **(A)** *Sound pressure ears*, found in moths, cicadas, locusts, and others, use a tympanum, typically backed by an air-filled cavity, that oscillates in response to changes in sound pressure on either side. These ears are sensitive in the 'far-field' and tend to allow the animal to detect sounds from much greater distances. **(B)** *Particle velocity ears*, found for example in mosquitoes and fruit flies, use their antennae, with scolopidia at the base forming the Johnston's organ, to move through viscous drag in response to the back-and-forth motion of air molecules. These ears function in the 'near-field', typically at distances less than one wavelength. Figure adapted from [42].

on the anal cerci of crickets. These mechanisms have inspired prototype hair-like sensors in engineering [41].

The fourth type is (4) the *subgenual organ*, which, like trichoid sensilla, is widely distributed among insects [103]. The subgenual organ detects substrate-borne vibrations. In Gryllinae crickets, a subgenual organ is present in each of the six leg tibiae, including within the two fore tibiae where the tympanal organ is also located.

1.11 Overview of Gryllinae Peripheral Auditory Anatomy

In the present study, anatomical description of the Gryllinae peripheral auditory system follows standard nomenclature (Figure 1.9). *Peripheral* here means outside the central nervous system (i.e., before the downstream *central* auditory system). *Dorsal* and *ventral* denote upper and lower surfaces; *anterior* and *posterior*, front and rear. Along appendages, *proximal* refers to positions closer to the midline of the body and *distal* to positions further away. *Ipsilateral* and *contralateral* indicate the same or opposite side of the body respectively. *Apposed* describes structures lying flush against one another. *Afferent* pathways carry sensory signals to the central nervous system; *efferent* pathways carry signals away from it.

Field crickets (Gryllinae), together with Tettigoniidae (bushcrickets), belong to the suborder Ensifera within the order Orthoptera. Ensiferans possess two ears, each located in the proximal region of the prothoracic tibiae, just distal (below) to the tibio-femoral joint (the ‘knee’) (Figures 1.9B and 1.11). Each ear comprises two tympana, the anterior tympanal membrane (ATM) and the posterior tympanal membrane (PTM), positioned opposite each other on either side of the tibia segment [15, 23] (Figures 1.9B and 1.11). Running within each leg is the acoustic trachea, an air-filled tube connecting the ear to external sound openings, the acoustic spiracles (Figure 1.9A), located on the thorax and equipped with cuticular flaps to regulate sound entry (Figure 2.3). Each ear therefore receives both external sound at the tympanal surface and internal sound transmission via the ipsilateral spiracle [19] (Figure 1.9A). Distally, at the level of the ear, the leg trachea bifurcates into two branches, separated by a cuticular septum: the anterior tracheal branch (ATB) and posterior tracheal branch (PTB) [15, 19, 23, 104] (Figure 1.9B).

In Gryllinae, the two ears are acoustically coupled. The left and right tracheae meet centrally within the thorax, with the medial septum at the midline marking the junction between the two halves of the system [104] (Figure 1.9A). The field cricket acoustic trachea, with its four inputs – two spiracular and two tympanal – thus forms an ‘H’ shape (Figure 1.10). This arrangement allows each ear to receive three inputs: external sound, ipsilateral spiracular input,

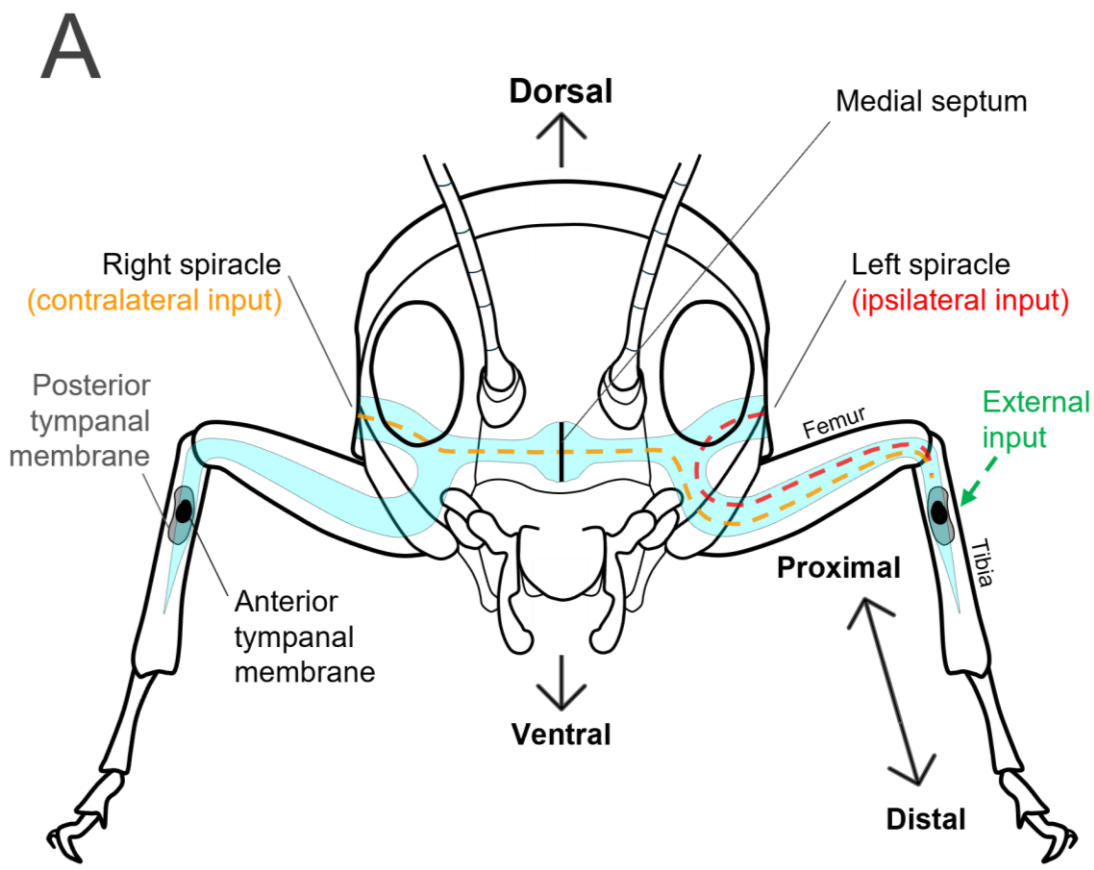
A
Dorsal
Medial septum
Right spiracle
(contralateral input)
Left spiracle
(ipsilateral input)
Posterior
tympanal
membrane
Femur
External
input
Tibia
Proximal
Anterior
tympanal
membrane
Ventral
Distal

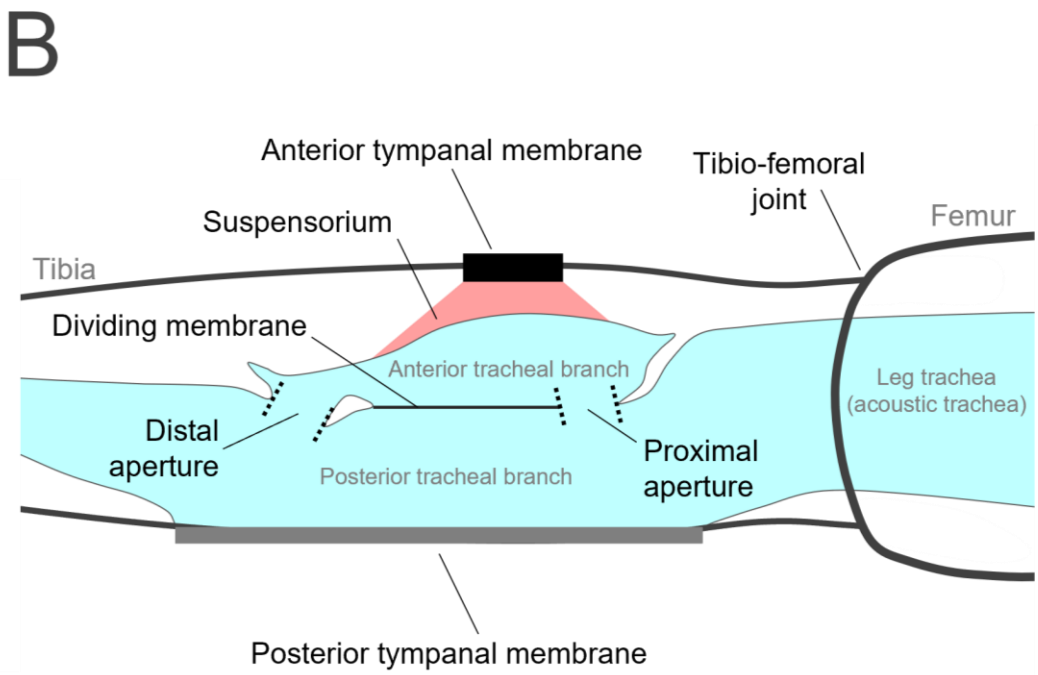
B
Anterior tympanal membrane
Tibio-femoral
joint
Femur
Suspensorium
Tibia
Dividing membrane
Anterior tracheal branch
Leg trachea
(acoustic trachea)
Distal
aperture
Posterior tracheal branch
Proximal
aperture
Posterior tympanal membrane

Figure 1.9 | Field cricket peripheral auditory anatomy is defined by three sound inputs and asymmetry. (A) Each ear of the field cricket receives three sound inputs. Sound reaches the external surface of the posterior tympanal membrane (green), as well as its internal surface via the ipsilateral spiracle (red) and the contralateral spiracle (orange). According to the phase-shift hypothesis, at the carrier frequency of the male calling song, the phases of the two internal pathways combine and interact with the phase of the external input. This interaction amplifies tympanal motion at that frequency, thereby enhancing interaural (between-ear) differences and improving directional acuity toward the male's position. **(B)** Asymmetry in the tympana and tracheal branches is a defining feature of Gryllinae peripheral auditory anatomy. In contrast to other ensiferans, the anterior tympanal membrane is considerably smaller and thicker than the posterior tympanal membrane. The anterior tracheal branch is cavity-like rather than continuous with the leg trachea and connects to the posterior tracheal branch via two small apertures. Additionally, the anterior tympanum is not directly coupled to the anterior branch but is separated from it by a tissue layer known as the suspensorium.

and contralateral spiracular input, such that the Gryllinae ear functions as a three-input system [19] (Figure 1.9A).

Functionally, this system operates as a pressure-gradient receiver rather than as a pressure-difference receiver. Tympanal membranes respond to the difference in sound pressure across their two surfaces; however, in Gryllinae both sides of the membrane are acoustically driven, with sound arriving externally and via the acoustic trachea. This means that membrane motion is determined by the relative phase and amplitude of these inputs rather than by comparison to a fixed internal reference [42].

Directional sensitivity arises through phase-shift tuning. Phase-shift directional tuning in field crickets arises because each tympanum is driven by multiple sound inputs that arrive with different phases, which are mechanically summed before any neural processing. Sound reaches the posterior tympanum externally and internally via the ipsilateral and contralateral spiracles through the acoustic tracheal system (Figure 1.9A). These internal pathways introduce frequency-dependent phase delays, particularly for the contralateral input, due to propagation along the trachea and passage through

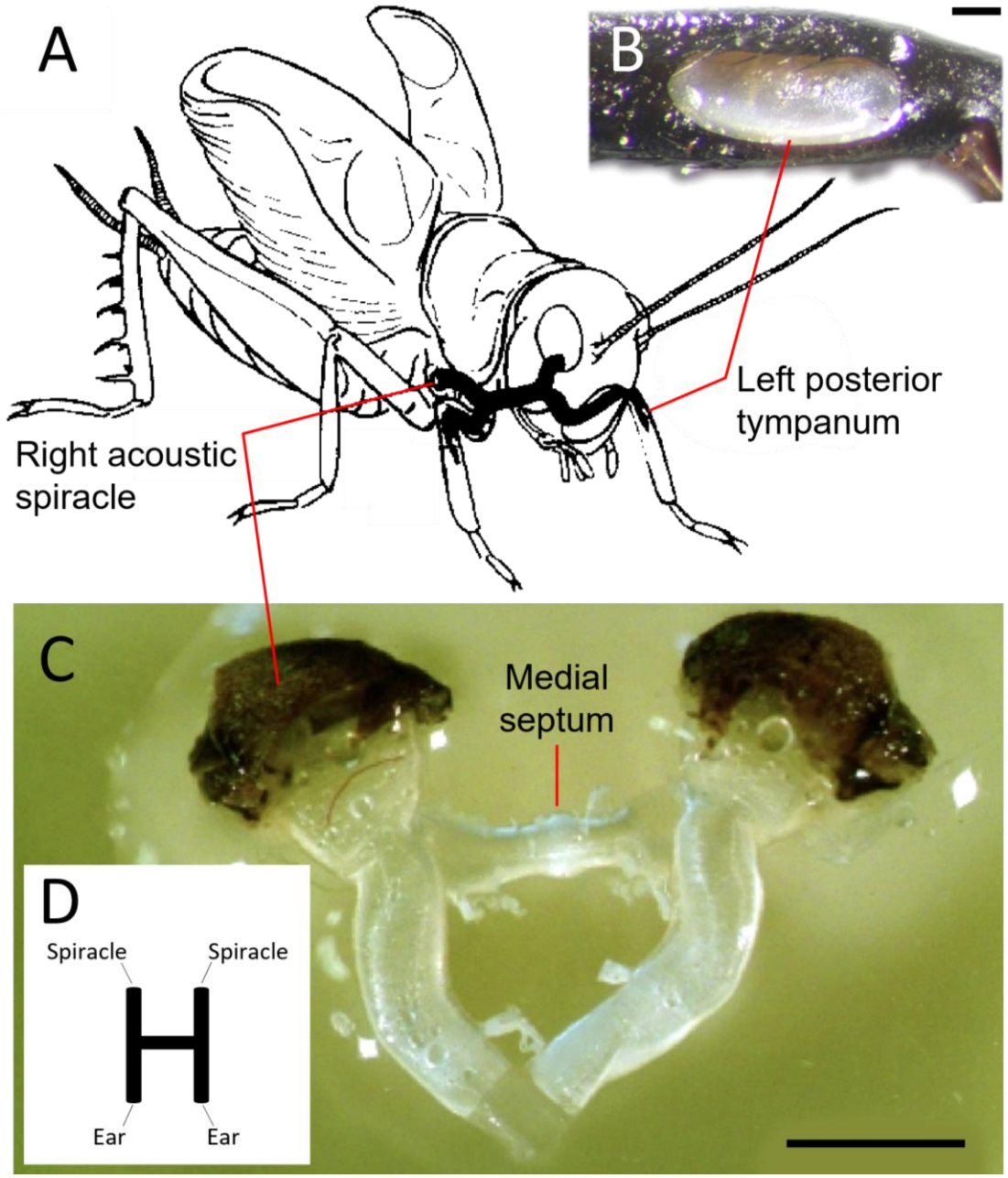

Figure 1.10 | The field cricket acoustic trachea forms an H-shaped connection between ears and spiracles. The field cricket's two ears are connected by an internal hollow tube known as the acoustic trachea, which is also connected to two openings, the acoustic spiracles. Together, these form the four ends of the H-shaped acoustic trachea. **(A)** Schematic adapted from [71] illustrating the acoustic trachea. **(B)** A photograph from this thesis of a left posterior tympanal membrane, immediately behind which, inside the leg, is the acoustic trachea. *Scale bar:* 200 µm. **(C)** A photograph of a dissected acoustic trachea adapted from [104], also showing the medial septum. *Scale bar:* 1000 µm. **(D)** Simple schematic. **(A-C)** *Gryllus bimaculatus*.

the medial septum [71]. At the tympanum, all inputs are effectively summed (vector superposition), so their phase relationships determine whether they reinforce or cancel each other. When inputs are out of phase (e.g. external 'push' coinciding with internal 'pull'), they add constructively and drive large tympanal vibrations; when they are in phase, they partially cancel, reducing vibration [12]. The key hypothesis is that this mechanism is not equally effective at all frequencies but is instead tuned by the physical properties of the tracheal system such that, at particular frequencies – around the 4–5 kHz carrier frequency of the male calling song – the phase relationships between external, ipsilateral, and contralateral inputs become optimal. At these frequencies, phase differences are transformed into maximal amplitude differences between the two ears, greatly enhancing directional sensitivity [73]. In other words, the geometry and acoustics of the tracheal system are thought to set the frequencies at which effective phase interactions occur, and these frequencies are hypothesised to coincide with the biologically relevant calling song, allowing the peripheral system to amplify directional cues specifically where they are behaviourally needed.

A distinguishing feature of Gryllinae anatomy compared to other ensiferans such as bushcrickets is the pronounced asymmetry between the tympana (Figures 1.9B and 1.11B,C). The ATM is small and thick (approximately 250 × 150 μm and 20 μm thick), whereas the PTM is large, thin, and kidney-bean shaped (approximately 900 × 300 μm and 5 μm thick) [23, 27] (Figure 1.11B,C).

The tracheal branches are likewise asymmetric (Figure 1.9B). This again is a distinguishing feature of Gryllinae compared to more arboreal Ensifera: Eneopterinae [27], Oecanthinae [105], Tettigoniidae [106], and Hagloidea [107]. Unlike these taxa, the field cricket ATB is the smaller of the two branches. This cross-taxa size difference is apparent in Figure 1.12, adapted from [27], which presents tibial cross-sections from four Eneopterinae species (Panels B–E) alongside that of a Gryllinae species, *G. bimaculatus*

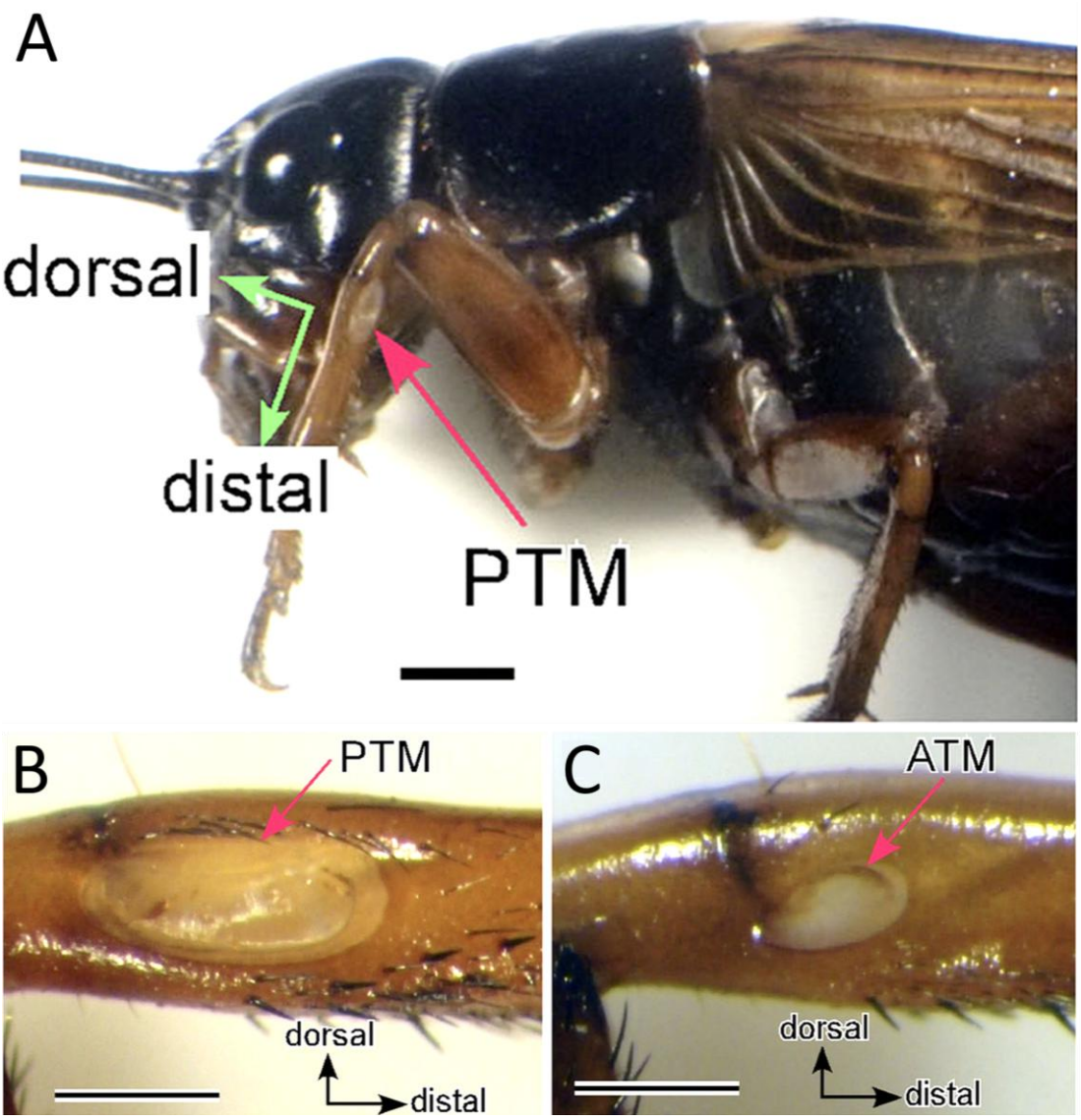

Figure 1.11 | Gryllinae ears exhibit a larger posterior tympanum and a smaller anterior tympanum. Light microscopy images of the **(A, B)** posterior tympanal membrane (PTM) and **(C)** anterior tympanal membrane (ATM) in *Gryllus bimaculatus*, adapted from [15]. The PTM is large and thin, whereas the ATM is smaller and thicker, reflecting pronounced asymmetry between the two tympana. *Scale bars:* **(A)** 1 mm; **(B, C)** 0.5 mm.

(Panel A). The Gryllinae ATB also forms more of an enclosed cavity, with only two small openings [15, 29] connecting it to the posterior branch (Figure 1.9B).

These openings, termed here the proximal aperture (PA) and distal aperture (DA) [1] (Figure 1.9B), are absent in other ensiferans, which typically

exhibit openly bifurcated leg tracheae with both branches continuous with the main lumen, unlike Gryllinae where the ATB is distinctly cavity-like. This structural distinctiveness of the Gryllinae may explain why previous anatomical investigation [15] refer to each typically termed ‘branch’ as a ‘vesicle’, a term suggesting a more closed geometry.

The most significant distinction however may be that unlike in these other ensiferans, where both tympana are directly apposed to their respective tracheal branches, the field cricket’s ATB is anatomically separated from any direct mechanical input from the tympana (Figures 1.9B and 1.12). In other ensiferans both tympana are directly apposed to their respective tracheal branches. Gryllinae, in contrast, show an anterior branch and an anterior tympanum separated by a region of tissue traditionally termed the *suspensorium* [31] (Figure 1.13). In Figure 1.12A, the *G. bimaculatus* ATM lies distinctly apart from the ATB, in contrast to the direct physical connection seen in the four Eneopterinae species (Figure 1.12B–E). Figure 1.12A shows labelled and highlighted in red the suspensorium.

The suspensorium separating the ATM from the ATB is more complex than historically assumed [15, 28]. It comprises multiple components, including the *epithelial core*, *basement membrane*, *epithelial cell layers*, and *labyrinth-like frameworks* [15] (Figure 1.13).

The tympanal organ (TO) (Figures 1.12A and 1.13) forms the final step of the peripheral auditory system prior to mechanotransduction. It contains approximately 70 auditory receptor neurons [23], arranged tonotopically [20]. These neurons are associated with the ATB; their cell bodies lie along its dorsal external surface, while their dendritic processes connect to a cellular mass by attachment cells. The cellular mass is itself suspended from the internal exocuticular ceiling by ligaments and is enclosed by a covering membrane, forming a tent-like cavity containing the fluid-filled chamber in which the majority of the sensilla dendrites are immersed [15] (Figure 1.13).

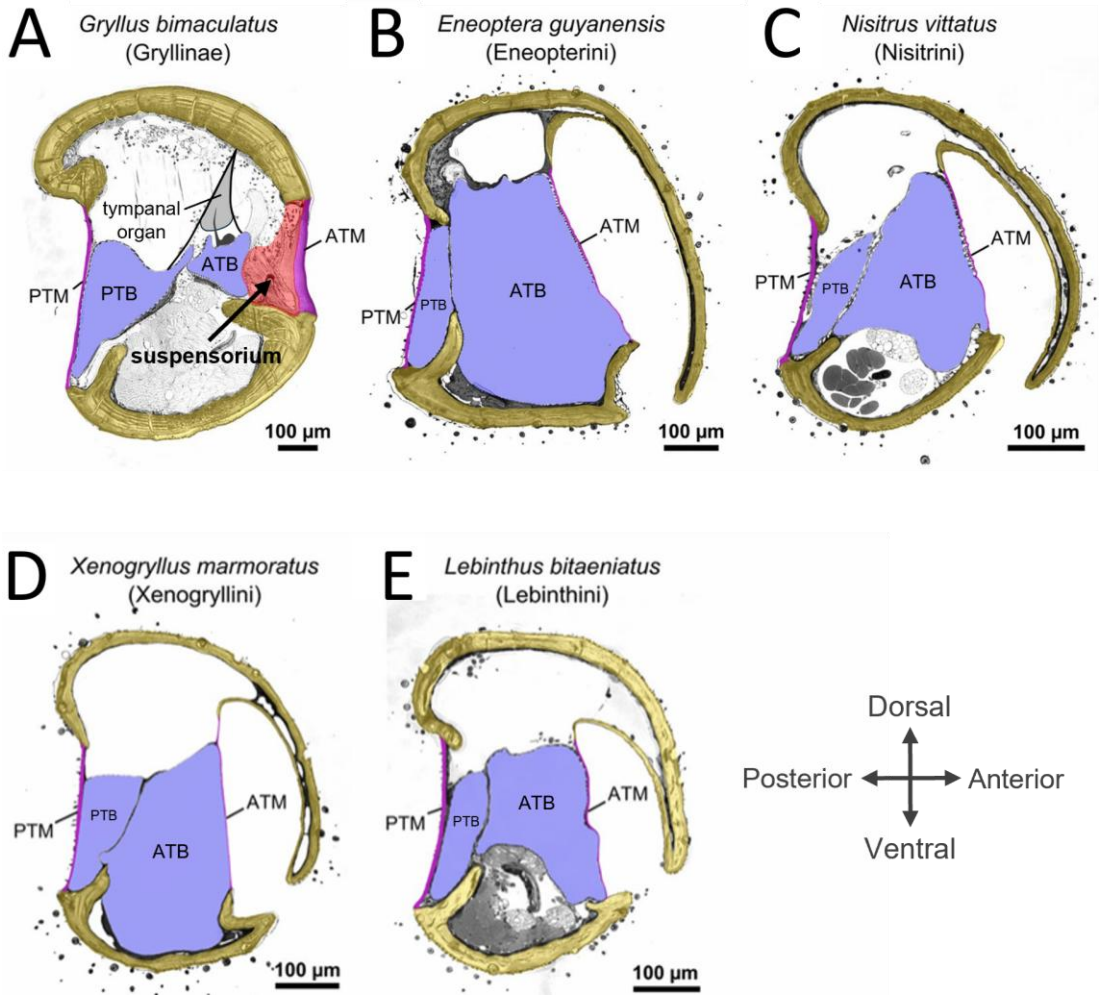

Figure 1.12 | Gryllinae ears show a decoupled anterior tympanum unlike those of other Gryllidae. Coloured light microscopy photographs from [27] showing cross-sectional slices through the prothoracic tibia of five species from the family Gryllidae: **(A)** one representative of the subfamily Gryllinae, and **(B–E)** four representatives of the subfamily Eneopterinae. **(A)** In the Gryllinae species, the anterior tympanal membrane (ATM) is not connected to the anterior tracheal branch (ATB) but is instead separated by a tissue region traditionally referred to as the 'suspensorium'. Additionally, the ATM in Gryllinae is notably thicker and smaller than the posterior tympanal membrane (PTM). The ATB is also substantially smaller than the posterior tracheal branch (PTB), whereas in the other Gryllidae species the ATB is the larger of the two branches. In all Eneopterinae species, both the ATB and PTB are in direct contact with their respective tympanal membranes, whereas in Gryllinae only the PTB contacts the posterior tympanum. Panel A has been adapted to highlight the Gryllinae suspensorium in red and to illustrate the approximate position of the tympanal organ.

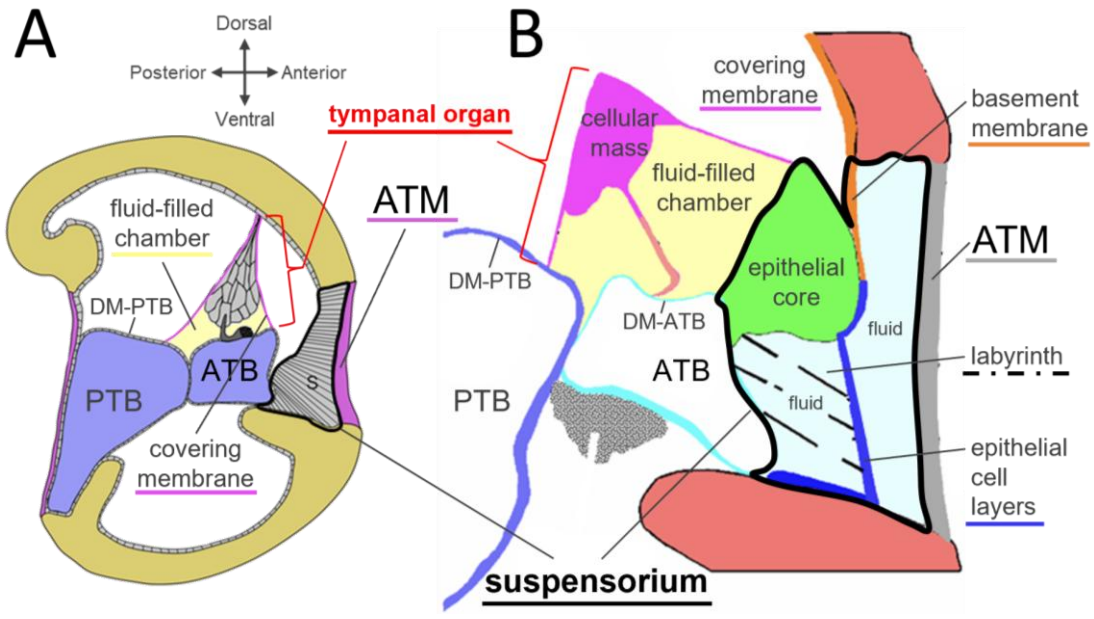

Figure 1.13 | The suspensorium is more complex than previously understood. The tissue between the Gryllinae anterior tympanal membrane (ATM) and anterior tracheal branch (ATB) has traditionally been termed the 'suspensorium' [31] and considered relatively homogeneous and simple in structure and function [28]. **(A)** A 2017 schematic of the field cricket ear adapted from [27]. **(B)** A 2019 schematic adapted from [15] illustrating a complexity of diverse structures between the ATM and ATB as highlighted by confocal laser scanning microscopy.

The tympanal organ contains two groups of sensory neurons that differ in how their dendrites connect to the cellular mass. Most belong to the distal group, with cell bodies arranged along the dorsal membrane of the anterior tracheal branch (DM-ATB) and dendrites immersed in the lipidic fluid of the fluid-filled chamber. A smaller number form the proximal group, with dendrites that attach directly to the cellular mass and are not immersed in fluid [15].

Beyond the peripheral auditory pathway, auditory neuron axons – spanning a range of frequency tunings – are bundled into the tympanal nerve, which projects proximally up the leg into the thorax and terminates in the prothoracic ganglion. Here, afferent signals are parsed into distinct interneuronal pathways. Specifically, information centred on the 5 kHz calling

song is conveyed to the brain by ascending neuron 1 (AN1), whereas higher-frequency inputs associated with the courtship cue are transmitted via ascending neuron 2 (AN2) [24].

1.12 **Gryllinae Research Gaps**

The Gryllinae ear exhibits tonotopy [20]. In the tympanal organ, the scolopidia [23] are individually tuned and organised into frequency-specific clusters corresponding to the carrier frequencies of both the calling and courtship songs [108]. These songs are produced by the male rubbing a scraper-like plectrum on one forewing against a file of teeth on the other, causing the forewings, especially the harp and mirror regions, to vibrate and radiate sound [22]. Some of the neurons of the tympanal organ are tuned to the CF of the courtship song (ranging from 11 to 16 kHz in *Gryllus bimaculatus* [16]), but most of the sensilla are sharply tuned to the dominant 4–5 kHz frequency of the calling song [3, 108]. The pure-toned calling song is what makes these ground-dwelling Gryllinae crickets immediately recognisable and acoustically distinctive [21, 25], especially when contrasted with the typically spectrally complex calls of other Gryllid (but not Gryllinae) crickets [109] and bushcrickets [110], which, unlike Gryllinae, tend to be arboreal.

The 4–5 kHz male calling song represents the frequency range where species-specific calling songs most commonly occur across field cricket species worldwide. Each Gryllinae species exhibits a much narrower, highly consistent calling frequency within this 4–5 kHz range. For example, in the Mediterranean field cricket *Gryllus bimaculatus*, also known as the two-spotted cricket, the male calling song carries at 4.7 kHz (±0.21 kHz SD), while in the Australian species *Teleogryllus commodus*, the calling song carries at 4.0 kHz (±0.15 kHz SD) [3].

1.12.1 Neurophysiological Tuning

Frequency tuning of insect auditory neurons can be determined by recording their electrical activity while presenting sounds of different frequencies and and quantifying the neuronal responses at each frequency. Such recordings have

demonstrated sharp 4–5 kHz tuning from the cricket auditory organ (Figure 1.14) [20, 24, 56].

Individual receptors in *G. bimaculatus* are tuned to characteristic frequencies between 3–11 kHz, with many most sensitive near 5 kHz, matching the carrier frequency of the male calling song (Figure 1.14A) [20]. Recordings of auditory receptor fibres (ARFs) in the tympanal nerve of *T. oceanicus* revealed three clusters of characteristic frequencies: ≤5.5 kHz, 10–12 kHz, and ≥18 kHz, corresponding respectively to the male calling song, courtship song, and ultrasonic bat echolocation cues [57] known to elicit negative phonotaxis [89].

Approximately 75% of ARFs are tuned between 3–5.5 kHz [57], close to the 5.0 kHz dominant frequency of the species' call [111], with this group also showing the sharpest tuning [57]. Recordings of summed tympanal nerve activity in *G. campestris* revealed two frequency optima near 4 kHz and around 15 kHz, corresponding respectively to the calling song CF and the main spectral peak of the courtship song [56] (Figure 1.14B). Further along the auditory pathway, interneurons AN1 and AN2 in the *G. bimaculatus* prothoracic ganglion showed distinct frequency selectivity: AN1 responded strongly near 5 kHz (the calling song CF), whereas AN2 responded more broadly to higher frequencies including the 14 kHz courtship song and ultrasonic signals [24] (Figure 1.14C). Together, these neurophysiological findings demonstrate strong selectivity to the 4–5 kHz male calling song CF at multiple central pathway levels, from sensory neurons [20] to the tympanal nerve [56] and interneurons [24].

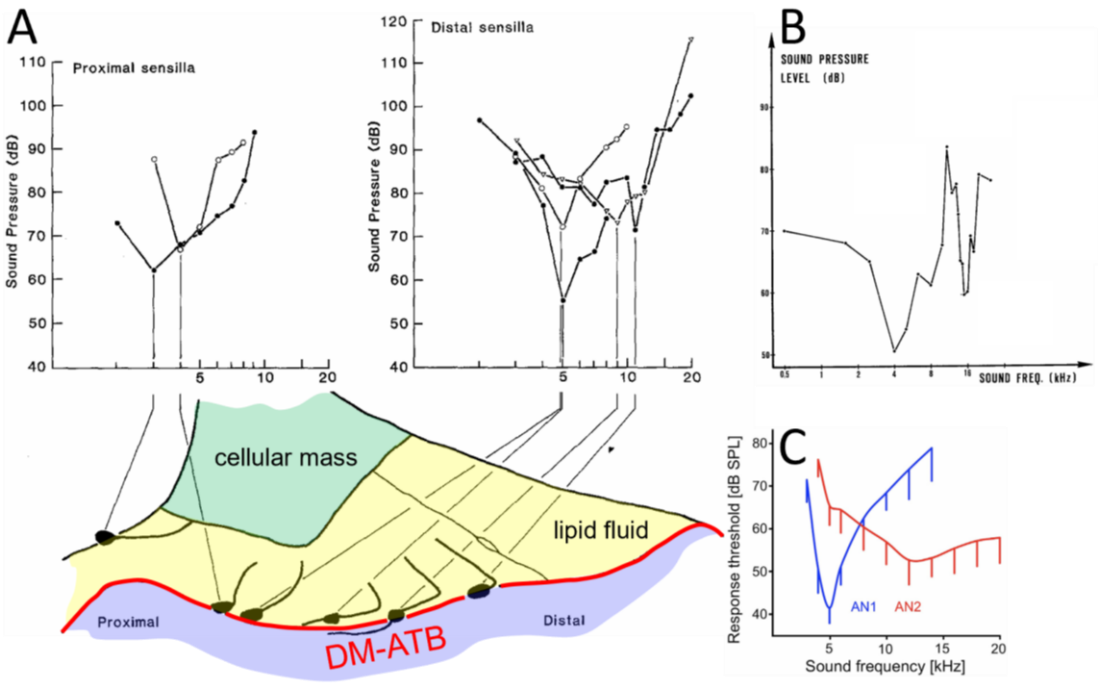

Figure 1.14 | The neurophysiological stage of the Gryllinae auditory pathway is sharply tuned to the calling song carrier frequency. Extensive literature supports the presence of sharp tuning at neurophysiological stage two of the Gryllinae auditory pathway, particularly to the conspecific carrier frequency (CF) of the male calling song. **(A)** Oldfield et al. (1986) [20] recorded frequency response thresholds from individual auditory receptors among the approximately 70 sensilla in the *Gryllus bimaculatus* tympanal organ (TO). Each receptor exhibited a characteristic frequency between 3–11 kHz, with many showing peak sensitivity near 5 kHz, closely corresponding to the CF of the species' calling song. Notably, the study confirmed a tonotopic organisation of the receptors, with low- to high-frequency tuned neurons arranged proximal-distal in the TO. This figure has been adapted to highlight the cellular mass (green), the fluid-filled chamber containing lipidic fluid (yellow), and the anterior tracheal branch (ATB, blue). As highlighted in red, most of the tonotopically arranged neuron cell bodies are positioned along the dorsal membrane of the ATB (DM-ATB). **(B)** Further along the auditory pathway, Nocke (1972) [56] recorded the summed activity of these sensilla via whole-nerve recordings of the *G. campestris* tympanal nerve, revealing two distinct peaks at 4 and 15 kHz, corresponding to the CFs of the conspecific calling and courtship songs, respectively. **(C)** Progressing further, to the prothoracic ganglion of *G. bimaculatus*, Ter Hofstede et al. (2015) [24] demonstrated that the AN1 and AN2 interneurons selectively encode these two frequency ranges. AN1 (blue)

1.12.2 Behavioural Tuning

Across different species of Gryllinae, pure-toned conspecific calling song carrier frequencies fall within a narrow range of 3–6 kHz [21], especially between 4 and 5 kHz [111]. In field crickets, conspecific carrier frequency is essential for successful reproduction, as females must localise calling males and this phonotactic behaviour is highly dependent on the species-specific frequency of the male's call (Figure 1.15) [5, 6].

Experiments using synthetic songs with identical temporal structures but varying carrier frequencies demonstrated that females respond most strongly to frequencies that match the conspecific male song. In trials with *T. commodus*, females were placed between loudspeakers, and their response was recorded when they approached and climbed onto the sound source. Responses were highest at 4.0 kHz, matching the species' natural song frequency (Figure 1.15A) [5]. Similar results were observed in *G. bimaculatus* using trackball phonotaxis experiments in which females were exposed to synthetic songs ranging from 2–13 kHz at constant intensity. The strongest steering responses occurred at 5.0 kHz, closely corresponding to the species' CF of about 4.7 kHz (Figure 1.15B) [11]. Additional behavioural experiments using trackball systems further showed that females steer reliably towards calls at the natural CF and can detect extremely small directional deviations, indicating hyperacute directional sensitivity [6] rivalled among insects only by the Ormiini fly [112]. Together, these studies demonstrate that field crickets are behaviourally tuned with high specificity not only to the temporal pattern of male calling songs but also to the conspecific dominant carrier frequency.

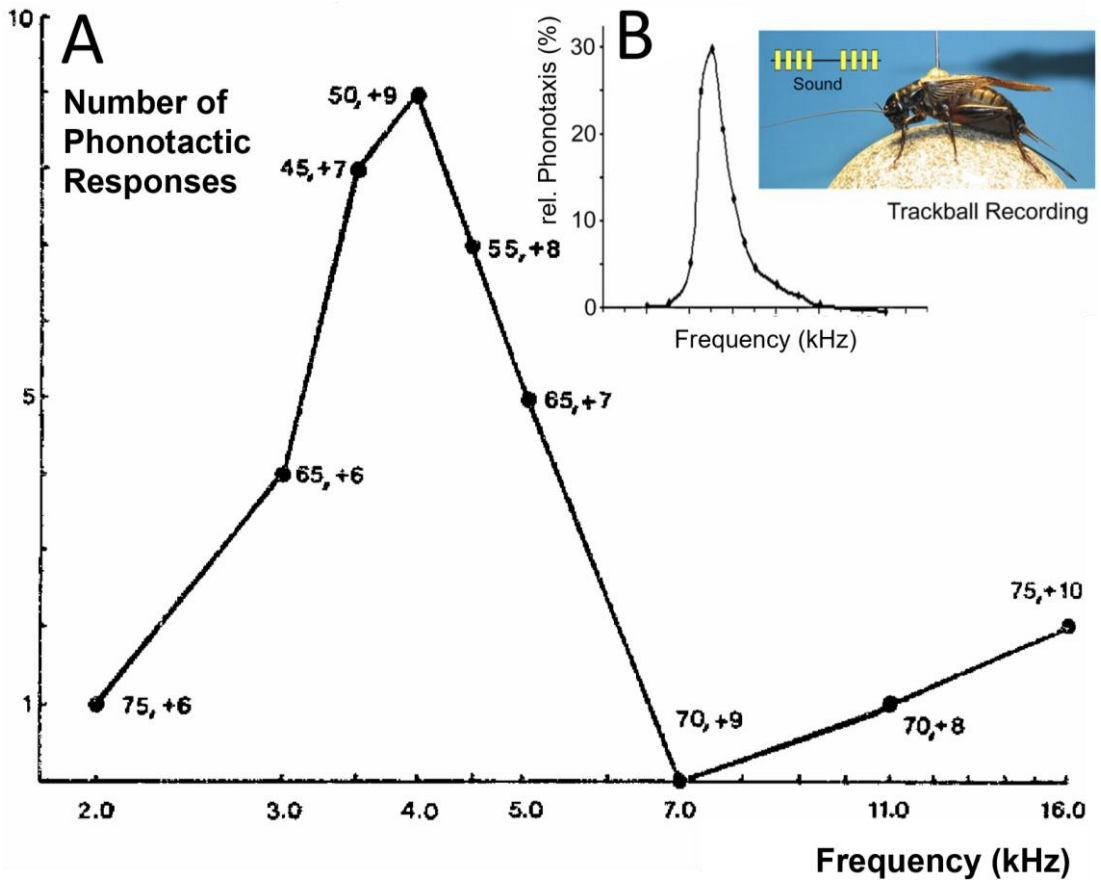

Figure 1.15 | The behavioural stage of the Gryllinae auditory pathway is sharply tuned to the calling song carrier frequency. Decades of literature support the sharp tuning of the Gryllinae auditory pathway at the behavioural level to the 4–5 kHz carrier frequency (CF) of the conspecific male calling song. **(A)** For example, Hill (1974) [5] recorded the phonotactic responses of female *Teleogryllus commodus* field crickets placed between two loudspeakers to synthetic calling songs of varying CFs between 2–16 kHz and found peak response occurred at 4.0 kHz, exactly matching the conspecific *T. commodus* calling song CF. See body text for further explanation of this figure. The numbers beside each data point on the graph provide two values. The first is the sound intensity in decibels (dB SPL). The second value shows how many decibels above the average hearing threshold that intensity was. Panel A is reproduced from [5]. **(B)** Some 20 years later, Hedwig and Poulet (2005) [113] used a trackball system to quantify phonotactic steering responses of female *Gryllus bimaculatus* to synthetic calling songs between 2–13 kHz. The strongest phonotactic response occurred at 5.0 kHz, closely matching the species' natural calling song frequency of 4.7 kHz. This further supports a sharply tuned behavioural preference for conspecific CFs. The figure here is from the Hedwig (2016) review [11] which is itself adapted from [113] data.

1.12.3 Unresolved Biomechanics and the Posterior Tympanum

Although the neurophysiological (Figure 1.14) and behavioural (Figure 1.15) stages of the field cricket auditory pathway exhibit sharp 4–5 kHz tuning, the peripheral biomechanics (stage one) underlying the response remain poorly understood [7-10, 12, 13, 15, 26].

The first component of the peripheral biomechanics is the PTM, which has been widely regarded as the primary and essential sound input of the system [5, 7, 10, 14, 26]. The ATM auditory role, in contrast, has been considered negligible [5, 7, 8, 15].

While earlier studies had shown that disrupting the PTM reduced auditory sensitivity, it remained unclear whether this reflected reduced soundcapturing or whether tympanal vibration itself was essential for activating the auditory receptors. Earlier work had clearly demonstrated the PTM's importance: a 30 dB reduction in tympanal nerve sensitivity (i.e. sound stimuli had to be 30 dB more intense to elicit neural activity) followed detaching the PTM [56], while similar drops in neural sensitivity followed immobilising the PTM with petroleum jelly or perforating it [5, 7]. Although these studies showed that the PTM acted at least as a sound window, they did not rule out the possibility that pressure changes inside the underlying tracheal branches, independent of tympanal motion, might stimulate the auditory sensilla. To test this, tympanal movement was suppressed by either submerging the leg in water or equalising internal and external pressures [14]. In both cases, neural responses were eliminated, even though sound pressure within the tracheal branches was maintained or increased. This confirmed that the PTM is not simply an acoustic entry point, but is the essential component for activating auditory neurons in the cricket ear [14].

1.12.4 Gap 1: Role of the Anterior Tympanal Membrane

The anterior tympanal membrane (ATM) (Figure 1.11C), in contrast, has long been considered as having little or no functional role in field cricket audition [5, 7, 8, 15]. Evidence supporting this interpretation has come from ATM vibrational measurements, neural recordings, and ATM ablations.

In a *T. commodus* study [5], to assess the function of the tympana, a two-stage experimental approach was used. First, phonotactic responses of female crickets to synthetic calling songs were observed in a controlled arena. In the second stage, auditory sensitivity was measured via extracellular recordings from the cervical connectives (nerve cords in the neck connecting the prothoracic ganglion to the brain) while petroleum jelly was used to block either the PTM or ATM. Each membrane was occluded separately, and neural sensitivity was retested after removal of the jelly. Blocking the PTM reduced the sensitivity of auditory interneurons by 15–25 dB, while blocking the ATM had no measurable effect [5].

Similarly, phonotaxis experiments using two loudspeakers selectively blocked either the PTM or ATM with petroleum jelly or fast-drying paint [114]. Blocking the ATM had no effect on phonotactic orientation [114].

Tympanal function was also investigated in three Gryllinae species (*Acheta domesticus*, *Gryllus pennsylvanicus*, and *T. oceanicus*) using laser heterodyne interferometry (similar to LDV), together with intracellular recordings from auditory interneurons [7]. The ATM vibrated no more than the surrounding exocuticle and showed no frequency tuning. Blocking the ATM had no effect on the PTM or on interneuron activity across the tested frequency range. These results led to the conclusion that the ATM appears *"relatively unimportant"* in stimulating the sensilla [7].

Vibrations of both the ATM and adjacent leg cuticle have also been measured using LDV, revealing no significant difference between the two [8]. These findings led to the explicit conclusion that the ATM is *"non-functional in hearing"* [8].

However, the ATM has been proposed to contribute to extending the ear's dynamic range, potentially allowing detection of both very quiet and very loud sounds without overloading the sensory system [115]. A Mössbauer effect displacement measurement technique was used to investigate tympanal vibrations in *G. campestris* [115]. This technique tracks displacements using a gamma ray source bonded to the vibrating surface, in this case the tympanal

membranes. The results showed that the ATM vibrated in phase with the PTM but with much smaller displacement.

Further ATM functionality was indicated from experiments involving whole nerve recordings in *G. campestris* conducted before and after ATM ablation [56]. After removing the ATM, responses to tones above 12 kHz were abolished, whereas responses to 5 kHz tones were retained. These results were interpreted as evidence that the ATM must be functionally coupled to high-frequency-sensitive auditory neurons [56]. However, the mechanism underlying this effect was not established, and the findings did not demonstrate how the ATM might contribute to neural activation.

Following a decade or so of the ATM largely being perceived as irrelevant [116], its role was more thoroughly reassessed. Using LDV, the vibrational response of the ATM was re-examined, measuring from both tympana and from the adjacent leg cuticle [117]. Although the PTM produced larger vibrational amplitudes, the ATM nonetheless vibrated above cuticular background levels, especially at higher frequencies. The ATM vibrated with different amplitudes depending on the direction of incoming sound. When the PTM was blocked, the ATM still exhibited a double-peaked frequency response, including a peak at high frequencies. It was concluded that the ATM could contribute sound input under conditions where the PTM is occluded, though in intact animals its role does appear minor [117]. Evidence for ATM auditory function also emerged from further behavioural studies. Individuals of *G. campestris* and *G. bimaculatus* that were either developmentally one-eared (missing a foreleg) or had one ear ablated were tested [116]. Tympana on the remaining leg were blocked with wax individually and in combination. When only the PTM was blocked, phonotaxis remained possible though less precise. When both the PTM and ATM were blocked, phonotactic behaviour was eliminated. These results led to the conclusion that the ATM does contribute a degree of sensory activation [116].

A confocal microscopy anatomical investigation re-evaluated the ATM, which at least at the time continued to be functionally enigmatic [15]. This work focused on a structure situated behind the ATM, termed the *epithelial core*,

previously referred to as the *tracheal body* [30]. This core structure lies within a complex that includes the ‘basement membrane’ and is mechanically coupled between the anterior tracheal branch and the fluid-filled sensory chamber. The study proposes that the epithelial core acts as a mechanical lever, analogous in principle to the mammalian middle ear ossicles, converting tracheal displacement into fluid motion. This model offers a possible explanation for the observation in which ATM ablation eliminated auditory responses to frequencies above 12 kHz [56]. The fluid-driven model was suggested to be particularly relevant to the high-frequency tuned *distal group* of sensory neurons. It is therefore plausible that ATM ablation inadvertently disrupted the epithelial core and its associated structures, thereby impairing the activation of these high-frequency sensitive receptors. However, the model implicates movement of the tracheal branch rather than the ATM directly, as the primary mechanical driver. Moreover, the anatomical findings highlight that the structure traditionally termed the *suspensorium* [28, 31], which lies behind and connects to the ATM, forms a more sophisticated complex of distinct structures than previously recognised, suggesting that the role of the ATM may be linked to this broader biomechanical assemblage.

1.12.5 Gap 2: Role of the Suspensorium

Unlike other ensiferans, the Gryllinae anterior tracheal branch is not coupled to its corresponding anterior tympanum (Figure 1.12). Instead, the ATB and ATM are separated by the suspensorium (Figures 1.9B and 1.12–13) [31].

Early electron microscopy investigations proposed that the suspensorium is innervated, leading to the suggestion that it functions as a structure capable of converting mechanical vibrations into electrical signals [23, 30]. However, another investigation described the suspensorium as non-sensory, consisting of a persistent layer of narrow supporting cells [28]. This anatomical characterisation implies a purely structural role. Specifically, maintaining spatial separation between the ATM and the ATB. That work likewise rejected any direct auditory function for the suspensorium [23].

Over four decades later, the suspensorium was revisited with considerably greater anatomical resolution, focusing particularly on the *epithelial core* structure embedded within (Figure 1.13B) [15]. Modern confocal laser scanning microscopy was used, incorporating a method to reconstruct confocal slices into a three-dimensional model of the Gryllinae ear. The suspensorium has traditionally been regarded as a mechanical damper that absorbs vibrations [8]. However, rather than a largely homogeneous structural tissue, this investigation highlighted several distinct anatomical components immediately behind the ATM, including the *basement membrane*, the *epithelial core*, *epithelial cell layers*, and *labyrinth*, all occupying the region previously recognised as the suspensorium and mechanically coupled to other features, such as the covering membrane and its associated fluid-filled chamber of the tympanal organ. Components of the suspensorium can be seen highlighted in Figure 1.13.

Moreover, a direct auditory role for the suspensorium has been proposed, suggesting that the epithelial core functions as a lever-like mechanism converting tracheal movement of the ATB into fluid motion inside the tympanal organ (Figure 1.6B) [15]. This proposed model awaits direct experimental testing, such as the systematic ablation of the epithelial core [15].

1.12.6 Gap 3: Vibrational Profile of the Posterior Tympanal Membrane

Unlike the cavity-like ATB, the larger PTB in Gryllinae exhibits the typical ensiferan condition, receiving direct acoustic input both via its apposition to the posterior tympanum and through its continuity with the leg trachea, and thereby with the wider acoustic trachea (Figure 1.9B).

Each acoustic spiracle has a cuticular flap that can block sound transmission through the acoustic trachea to the posterior tympanum. Because internal transmission influences tympanal motion, experiments often remove these flaps to keep the spiracles fully open and ensure consistent acoustic access to all three inputs to the posterior tympanum (Figure 2.3) [12].

For each ear, one signal arrives from the acoustic spiracle on the contralateral side of the body, travelling through the medial septum and

undergoing a phase shift [118, 119]. This contralateral signal then meets and superimposes with the signal from the spiracle on the ipsilateral side of the ear, forming a combined input at the internal surface of the large tympanum from within the PTB [12]. The level of phase shift acting upon each ear is not equal and is dependent on the direction of the sound signal. Thus, there is an interaural difference in the phase of the transmission received by each tympanum; an interaural phase difference (IPD). Accordingly, the posterior tympanum vibrates in response to stimulation not only externally but also from a phase-shifted signal acting on its internal surface [12, 73] (Figure 1.9A). However, reports disagree on how these PTM vibrations correspond to the established sharp tuning of the auditory neurons to the calling song CF [7, 12, 27, 72, 73].

Several studies have reported a sharp vibrational response of the posterior tympanum that is close to the CF of the calling song [9, 72, 115]. For instance, a distinct PTM velocity peak at 5.5 kHz was recorded [9]. A review noted a close correspondence of this finding with the tuning curve of the tympanal nerve, and the PTM was therefore implicated as a sufficient biophysical tuner to determine the CF-sensitivity of the auditory pathway at the neural and behavioural levels [11]. Similarly, a single displacement optimum at 4.0 kHz was observed, indicating the PTM *"is mechanically tuned to a relatively narrow spectrum of frequencies"* [115].

The PTM also shows strong direction-dependent tuning to the calling song CF. By isolating each of the sound inputs, a significant phase shift was calculated when the calling song frequency was approached [71]. This supported an earlier 'phase-shift hypothesis' [13, 119], whereby the internal–external phase difference exaggerates motion of the ipsilateral PTM, thus enhancing directional cues at that frequency. Experimental evidence was provided of a pronounced PTM peak close to the calling song CF when the sound source was presented ipsilaterally [72]. Together, these findings suggest the PTM is indeed sharply tuned to the CF of the calling song, either from mechanical resonance and/or directional tuning.

However, not all studies support the view that the PTM is sharply tuned to the 4–5 kHz calling song CF. Early investigations, for instance, report vibrational responses of the PTM that, while peaking near the CF, were notably broader than the acutely defined tuning curves established from the auditory sensilla [7, 8]. More recently, two studies described PTM vibrational profiles that were not only broad but also tuned substantially above the calling song CF [12, 27]. Broad PTM tuning has been reported with a vibrational optimum between 11 and 17 kHz, well above the 4–5 kHz CF of the male calling song [27]. Moreover, although earlier work reported sharp directional tuning of the PTM to the CF, more recent evaluations of the phase-shift hypothesis, while reaffirming the role of internal–external phase differences in enhancing directional sensitivity, have nonetheless observed considerably broader tuning profiles [12, 73], with optima documented above the CF.

Compounding this variability are inconsistencies regarding the number and location of PTM resonance peaks. Some studies have suggested a single, prominent resonance close to the calling song CF [7, 115], others a single peak above the CF [12, 27], and still others the presence of two distinct vibrational peaks [8, 9, 26].

Given that the posterior tympanum in field crickets forms the crucial initial link in the transmission pathway to the auditory sensilla, and clearly contributes to frequency tuning, any comprehensive account of acoustic filtering and signal transmission in this system must consider oscillations of the PTM. Yet the reported filtering characteristics of the PTM are inconsistent, with contradictory interpretations, highlighting the need for a thorough reassessment of the PTM vibrational profile.

1.12.7 Gap 4: Frequency Filtering

Studies in which PTM vibration measurements revealed tuning profiles too broad to account for the known sharp frequency selectivity of the auditory sensilla [7, 8] prompted early speculation that a second frequency filter must exist beyond the tympanal membrane [8, 10, 26]. This additional filter was even suggested to be potentially analogous to the mammalian cochlea in its

frequency-selective function [8]. More recent reports documenting broad PTM tuning [12, 27] have renewed interest in the long-standing 'second filter hypothesis', proposing that the mismatch between PTM and sensilla tuning suggests further filtering *"may arise beyond the level of tympanal membrane oscillations"*.

However, the anatomy beyond the PTM is complex [15, 23], and as noted in an anatomical study [15], the mechanism by which PTM oscillations are transmitted to the sensors has long remained *"enigmatic"*. Taken together, these findings indicate that although there is strong evidence for an additional filtering stage beyond the PTM, its anatomical basis and mechanism remain unclear.

1.12.8 Gap 5: Transmission Pathway

Tympanal vibrations are likely mechanically coupled to the tracheal branches, with a proposed mechanism being the known contact between the posterior PTB wall and the large tympanum [10, 14, 15, 27]. Moreover, the close arrangement of the two tracheal branches is likely to facilitate the transmission of vibrations from the PTM to the anterior branch that supports the auditory neurons [27]. Furthermore, the dorsal membrane of the larger branch connects directly to the PTM [15].

Based on this morphology, two possible transmission routes have been proposed [15]: one in which PTM motion couples to the dorsal membrane of the PTB (DM-PTB), affecting the fluid surrounding the sensilla, and another transmission route in which airflow through the connecting apertures causes an inflation of the ATB. However, it is noted that whether either of these hypothesised transmission pathways is in fact functional has not been determined [15].

1.12.9 Gap 6: Limitations in 3D Anatomical Characterisation

A major unresolved limitation in Gryllinae auditory biomechanics is the lack of accurate three-dimensional anatomical characterisation of the internal ear structures. Many of the key research gaps outlined above – such as the identity

of a second frequency filter or the nature of the internal transmission pathway – are contingent upon a detailed spatial and morphometric 3D understanding of internal ear anatomy. However, much of the existing anatomical knowledge of this region has, for several decades, been derived from traditional two-dimensional sectioning techniques [15, 23, 28, 31], which may limit our ability to resolve the 3D organisation of structures critical for interpreting their function.

Partly in response to this limitation, confocal laser scanning microscopy was employed in 2019 to revisit the Gryllinae peripheral auditory anatomy. Part of this confocal study included a pioneering 3D reconstruction derived from 2D confocal image stacks [15].

Nevertheless, this confocal reconstruction was not based on direct volumetric imaging, and no 3D morphometric measurements were reported [15]. Furthermore, given the anisotropic voxel resolution inherent to confocal imaging, quantitative 3D analyses – such as of thickness or volume – cannot be considered fully reliable from such a technique.

Despite these limitations, this confocal study represents a significant step forward in revisiting this system's anatomy using a modern imaging modality and provides a pioneering 3D reconstruction of the Gryllinae tympana, tracheal branches, and tympanal organ. In parallel, it underscored the need for a future direct 3D imaging approach capable of enabling accurate 3D morphometrics [15]. Consequently, the 3D spatial relationships and morphometrics of the Gryllinae peripheral auditory system remain insufficiently characterised, limiting current understanding of how biomechanical filtering and vibration transmission occur within the ear.

1.12.10 Gaps Addressed by This Research

The auditory system of Gryllinae crickets is well characterised at the neurophysiological and behavioural levels, with sharp frequency tuning to the 4–5 kHz carrier frequency of the male calling song evident in both phonotactic behaviour [5, 6, 11, 113] and neural activity [20, 56, 57]. However, how such precise tuning arises biomechanically at the periphery of the auditory pathway

remains unclear. Although the PTM is firmly established as the principal sound input [5, 7, 10, 14, 26], its vibrational responses are broad [7, 8, 12, 26, 27, 73] or tuned substantially above the calling song frequency [12, 27], raising the question of whether PTM motion alone can explain the neural selectivity (**Gap 3**). This discrepancy has revived interest in the long-standing second filter hypothesis [8, 10, 12, 26], which proposes that further frequency filtering must occur downstream of the tympanum. However, the anatomical basis and functional mechanism of this putative filter remain unknown (**Gap 4**).

Equally unclear is how vibrations from the PTM are transmitted to the tonotopically organised auditory sensilla. Two potential pathways have been proposed: mechanical coupling via the dorsal membrane of the posterior tracheal branch, or air-driven inflation of the anterior branch (ATB) via tracheal apertures [15]. However, neither of these pathways has been directly tested (**Gap 5**). Clarifying these transmission mechanisms is therefore essential.

Further compounding these gaps is the historic reliance on traditional two-dimensional anatomical methods [23, 28, 31], which limit insight into the full three-dimensional organisation of internal auditory structures. Although recent advances using confocal microscopy and 3D reconstruction represent important progress [15], they do not provide true direct volumetric three-dimensional imaging or enable robust 3D morphometric analysis, leaving the spatial mechanics of the system under-characterised (**Gap 6**).

Of these six research gaps identified, four are the specific focus of the present study: **Gap 3** (*PTM vibrational tuning*), **Gap 4** (*second filter hypothesis*), **Gap 5** (*transmission pathway*), and **Gap 6** (*3D limitations*). These four gaps are directly aligned with the following research aims:

Aim 1: To resolve the *vibrational profile* of the field cricket's posterior tympanal membrane (Chapter 3).

Aim 2: To uncover the hypothesised mechanism of *secondary frequency filtering* within the peripheral auditory system of the field cricket, including any filtering occurring beyond the posterior tympanum (Chapter 4).

Aim 3: To identify the mechanical *transmission pathway* between the posterior tympanal membrane and the auditory neurons (Chapter 4).

Aim 4: To employ micro-CT imaging for *direct 3D volumetric reconstruction* and to perform *3D morphometric analysis* of the field cricket's internal ear structures (Chapter 4).

1.13 Ormiini Research Gaps

Insect parasitoids are insects with larvae that develop in or on a host and eventually kill it. In insect parasitoids, resource competition can drive changes in traits such as egg production, foraging behaviour, body size, oviposition strategies, and mating behaviour [120]. Although adult parasitoids are free-living, their larvae rely entirely on the nutritional resources within their host for development [121]. As a result, resource availability, together with extrinsic competition (among adults for hosts) and intrinsic competition (among immatures within the host), can strongly influence developmental trajectories and fitness outcomes [120, 122]. For instance, some parasitoids prefer larger hosts and may allocate more offspring to them, since such hosts can support greater larval development [123]. Moreover, parasitoid body size at emergence is often positively correlated with the size of the host [124, 125]. Thus, host size and competition levels can significantly affect resource acquisition and developmental success in parasitoids.

Ormia ochracea (family Tachinidae, subfamily Tachininae, tribe Ormiini) is a parasitoid fly that gives birth to live larvae, uses sound to locate its hosts, and relies on field crickets (Gryllinae) for larval development [18, 121]. Gravid (pregnant) females home in on the calling songs of male crickets to find suitable hosts [18, 112]. The fly's auditory system is tuned to the carrier frequency of these calling songs [1, 126-128]. While song recognition depends on processing the temporal pattern of sound pulses [129-132].

Once *O. ochracea* detects suitable host songs [17, 133], the fly engages in aerial phonotaxis, lands, and then continues with walking phonotaxis

towards the sound source [134], where it deposits planidia (first-instar larvae) near or directly on host crickets. The planidia wave their anterior ends in the air, attach to the host, and then burrow into the cricket to begin development [135].

1.13.1 Gap 1: Cross-Populational Role of Song Learning

In North America, *O. ochracea* parasitises various field cricket species with diverse songs across geographically separated fly populations. Certain populations are known to target the predominant host species in their locality, thus exhibiting 'host specialisation' [133]. This specialisation reflects a behavioural preference, with flies choosing the song of their population's predominant host cricket [17].

The behavioural differences of some *O. ochracea* populations choosing one host cricket species, and another population preferring a different Gryllinae host, may arise from the different fly populations functioning as genetically distinct 'cryptic species' [136]. However, all fly populations in fact belong to a single genetically homogenous species, therefore suggesting that adaptive preference to a new host species is shared by all *O. ochracea*. The cross-populational differences in host preference may therefore result instead from an innate behavioural flexibility in *O. ochracea* flies, coupled with the capacity of the fly to *learn* the song of the predominant local host species [133].

Song learning has been demonstrated in a single population to be the main, if not exclusive, factor determining host preferences [137], potentially accounting for all in-field host preferences observed across populations [17]. However, this conclusion is based on data from only one population [137], and whether this pattern holds more broadly remains to be determined.

As such, understanding whether song learning consistently shapes host preference across *O. ochracea* populations represents an important direction for future research. For instance, comparative studies using laboratory-reared flies exposed to controlled song stimuli could help clarify the generality of learning mechanisms in this system.

1.13.2 Gap 2: Learning-Independent Temporal Preferences

If song learning in *O. ochracea* operates within a shared behavioural potential, this would imply the existence of a common, flexible ‘acoustical template’. However, the degree to which host preference in *O. ochracea* depends on prior exposure versus innate biases remains unclear. In particular, the contribution of learning-independent factors, such as temporal sensitivity to pulse rate, has not been systematically evaluated across fly populations.

There is evidence of population-specific tuning to temporal song parameters. For example, Florida flies strongly prefer *Gryllus rubens*, whose pulse rate differs markedly from that of the fly’s secondary host *G. firmus* [133]. Modulating the pulse rate of *G. rubens* significantly reduces phonotactic success [129]. In contrast, *Teleogryllus oceanicus*, which shares a similar pulse rate to *G. rubens*, is strongly preferred in Hawaii, despite *G. rubens* being largely rejected in that region [17, 133]. Such contrasts raise the possibility of population-specific tuning and *multiple* underlying acoustical templates.

The extent to which host preference reflects innate temporal biases rather than learned associations remains an open question. Behavioural testing of naïve flies under uniform conditions could help disentangle the relative influence of innate versus learned song features across populations.

1.13.3 Gap 3: Acoustic Parameters That Trigger Song Learning

Most previous host-preference behavioural response data to acoustic stimuli have been gathered in field settings, where individual song exposure histories are unknown [17]. Consequently, little can be known about the specific acoustic features required to trigger learning in *O. ochracea*. Defining the minimum stimulus complexity necessary to induce learning is essential for understanding the boundaries of the fly’s acoustical template.

For example, phonotactic responses to modified pulse rates, particularly when tested under consistent laboratory conditions, could offer insights into the stimulus thresholds that support learning [129]. Techniques such as trackball-based measurement of steering behaviour [131, 138] prove particularly effective for these assessments.

At present, the acoustic cues most critical for learning induction remain poorly understood. Investigating these cues could clarify how flexible or constrained the song-learning system is across populations and ecological contexts.

1.13.4 Gap 4: Differences in Larval and Adult Activity

Beyond variation in song preference, broader behavioural differences among *O. ochracea* populations may exist. Anecdotal observations have noted differences in larval and adult activity rates across populations, including in the absence of host song stimuli (Andrew Mason, personal communication). Such variation could reflect underlying physiological or behavioural divergence independent of acoustic processing or learning.

Although this aspect has not yet been formally examined, it could be explored through kinematic analysis of larval movement. For example, from video recordings of gravid female dissections. Or through adult movement tracking using a trackball to measure forward velocity and distance travelled [131].

Whether consistent differences in baseline or stimulus-driven activity exist among populations remains to be clarified. Exploring these differences could yield new insights into the broader behavioural ecology of *O. ochracea* beyond host song recognition alone.

1.13.5 Gap 5: Role of Larval Gut Excretions in Host Mortality

Once a host song has been identified and a field cricket located and parasitised, larval development within the host proceeds over 6 to 10 days [135]. During the initial three days, the planidia appear to feed primarily on haemolymph, leaving muscle tissue largely undisturbed. By the fourth day, they migrate to the abdomen, moult, attach to the abdominal wall, and form a respiratory funnel, providing protection from the host immune system and facilitating gas exchange. From this stage onwards, the larvae continue moulting and begin consuming surrounding tissues.

In the final two days of parasitisation, larvae feed on fat body and abdominal and thoracic muscles but notably spare the digestive system and central nervous system. Immediately prior to emergence, larvae purge their gut contents into the host body cavity, a process that coincides with rapid host death. The larvae then exit the host and pupate shortly thereafter [135]. Adamo et al. [135] proposed that this sudden host mortality may result from the toxic effects of the larvae's voided gut contents, yet this hypothesis remains untested.

The biochemical properties and physiological impacts of these larval gut excretions are still unknown. Elucidating their role in host Gryllinae mortality could provide novel insights into non-mechanical methods of parasitism and contribute to a deeper understanding of host-parasitoid dynamics in Ormiini flies.

1.13.6 Gap 6: Resource Competition and Developmental Success

In natural infestations, *Ormia ochracea* frequently deposits multiple larvae onto a single host cricket [139]. Although both male and female crickets can be parasitised [140], infestation rates are higher in males due to their calling behaviour, which attracts gravid females [139, 141]. Field surveys typically report one to two larvae per host [139, 142], though higher larval loads have also been documented [143].

These observations suggest that multiple larvae commonly co-occur within a single host, creating the potential for intraspecific resource competition, as all larvae depend on a finite source of host-derived resources to complete development. However, the consequences of this co-infestation for larval survival and fitness remain poorly resolved. It is not known whether all larvae in multi-larval infestations successfully reach pupation, or whether increasing larval density leads to reduced survival, slower development, or diminished adult size.

Empirical data linking larval load to developmental outcomes are limited, particularly under controlled conditions where confounding variables such as host size, sex, and condition can be isolated. While host defences

such as grooming may influence initial infestation success [144], these do not address how larvae interact after entering the host.

Consequently, a key unresolved question is how variation in larval density influences developmental success through resource limitation within the host. Addressing this gap requires controlled experimental approaches that isolate the effects of larval load and host characteristics on survival, development, and fitness outcomes.

1.13.7 Gap 7: Larval Development in Acheta domesticus Hosts

Most developmental research on *O. ochracea* has focused on natural host species [18, 135, 139] or on alternative field crickets with ecological relevance [145, 146]. These include species such as *Gryllodes sigillatus*, *Gryllus bimaculatus*, and *Modicogryllus pacificus* in Hawaii [146], and *Gryllus assimilis* in Texas [145]. While these studies have confirmed that *O. ochracea* can develop in several cricket species, comparatively little research has examined *Acheta domesticus* (the house cricket) as a host.

Due to its wide availability in the USA through commercial suppliers, *A. domesticus* presents a practical candidate for laboratory-based studies and colony establishment. However, the suitability of this species as a developmental host remains poorly characterised. Key questions remain regarding larval survival, development rate, and offspring quality when parasitising *A. domesticus*. Expanding developmental assessments to include *A. domesticus* could provide a consistent and scalable model for future experimental work and facilitate the maintenance of long-term laboratory colonies of *O. ochracea*.

1.13.8 Gaps Addressed by This Research

Current research on *Ormia ochracea* highlight several outstanding questions spanning behavioural, sensory, and developmental biology. These include the extent to which host song preferences are shaped by learning versus innate biases, as well as the acoustic cues required to initiate learning across populations. There is also scope for resolving population-level differences in

activity patterns unrelated to song exposure, and in the potential role of larval gut excretions in triggering rapid host mortality. Developmental outcomes in *natural* infestations remain incompletely characterised, particularly regarding larval competition within hosts and overall survival to emergence. Furthermore, while *O. ochracea* parasitises several field cricket species, relatively little is known about its ability to develop within *Acheta domesticus*, a species widely available for laboratory use.

This thesis specifically addresses two of these areas: the effect of resource competition on developmental success (**Gap 6**), and the suitability of *Acheta domesticus* as a host (**Gap 7**). By experimentally parasitising *A. domesticus* and manipulating host cricket size, sex, and applied larval load, this work evaluates how these variables influence pupation and eclosion success, pupal size, and the size of first-generation (F1) adult flies. The results, presented in Chapter 5 and published in Dominguez, Latham et al. [2], provide new insights into how host-related factors and resource limitation shape survival, development, and fitness outcomes in *O. ochracea*, while also assessing the feasibility of *A. domesticus* as a scalable model system for future experimental research.

Chapter 2

Methods

In this methods chapter, three principal techniques are described: scanning Laser Doppler Vibrometry (LDV) including multi-point scans to measure tympanal membrane vibrations with spatial precision; X-ray micro-computed tomography (micro-CT) to obtain 3D anatomical reconstructions of internal ear structures; and micro-CT-informed finite element analysis (FEA) modelling to simulate the mechanical behaviour of these structures in response to simulated acoustic stimuli.

For each technique, the chapter first explains how the equipment functions, followed by a description of the specific setup employed in this research. Much of this chapter, Sections 2.1–2.6, covers the methods related to the primary thesis project on Gryllinae biomechanics. The final section, Section 2.7, outlines the methodology used in the Ormiini larval development project. In both cases, more specific and detailed methods are presented in their corresponding research chapters: Chapters 3 and 4 for Gryllinae, and Chapter 5 for Ormiini.

2.1 **Animals**

The Mediterranean field cricket, *Gryllus bimaculatus*, first described by De Geer [147], is the primary model organism used in this study. Specimens for X-ray micro-CT imaging and FEA modelling were commercially sourced from Blades Biological Ltd (Cowden, UK). Those used as the principal subjects for

LDV experimentation were obtained from a local commercial supplier, Pets at Home (Pets at Home Group PLC; Cheshire, UK), in Glasgow.

In addition, the Australian species *Teleogryllus commodus*, first described by Walker [148] under the genus *Gryllus*, was included in control LDV experiments. Although now recognised in a different genus, *T. commodus* belongs to the same Gryllinae subfamily as *G. bimaculatus*. Its inclusion served as a comparative control: being a geographically and taxonomically distinct species, similar findings in both *G. bimaculatus* and *T. commodus* would suggest that the observed phenomena are not species-specific but potentially generalisable within the field cricket subfamily. Specimens were provided from a laboratory colony courtesy of Prof. Nathan Bailey, University of St Andrews, that was established from individuals originally wild-caught near Moss Vale in New South Wales, Australia.

2.1.1 Housing

All crickets were sourced as adults and housed under controlled conditions prior to experimentation. Upon arrival, *G. bimaculatus* were placed in an OVA-Easy 190 Advance Series II incubator (Brinsea Products Ltd., Weston-super-Mare, Somerset, UK) set to 26 °C. They were kept in 15-litre plastic containers inside the incubator on a 12:12 hour light:dark cycle, provided with egg-carton cardboard shelters, and fed *ad libitum* with fish-food flakes, organic wheatgerm, and gel-based water.

Individuals of *T. commodus* had been bred under laboratory conditions at the University of St Andrews, where they were maintained at 25 °C in 16-litre plastic boxes with rabbit food and water-soaked cotton pads. After transfer to the University of Strathclyde, they were briefly housed under the same incubator conditions as *G. bimaculatus* prior to experimentation.

2.2 **Specimen Preparation for X-ray Imaging**

Insect specimens are prepared prior to X-ray micro-CT imaging to enhance contrast and improve the visibility of internal structures. Such preparation is performed due to soft biological tissues exhibiting inherently low X-ray

attenuation because of their high water-content and low density. To improve contrast in reconstructed scans, preparation protocols typically incorporate a combination of fixation, dehydration, and staining steps. Fixation preserves morphology and prevents deformation or collapse of delicate structures during subsequent processing. Dehydration removes water from within tissues, thereby increasing differential X-ray attenuation between tissue types. Staining introduces heavy-metal ions that bind to biological molecules, enhancing X-ray absorption and improving the visibility of soft tissues in the final micro-CT reconstructions.

2.2.1 X-ray micro-CT Specimen Preparation Protocol

Insects were killed by exposure to ethyl acetate vapour [149] in a sealed 2-litre square clip top jar (Kilner®, Liverpool, UK). The jar was prepared with a plaster of Paris layer at the base and loosely crumpled paper placed on top to allow vapour release without damaging specimens. Individuals were left in the jar for an indefinite but conservatively long period until complete and lasting cessation of movement was observed.

Subsequent fixation and staining procedures were based on established methodological approaches for optimising contrast in X-ray micro-CT imaging across multiple animal case studies, including insect specimens [150]. The inclusion of a chemical dehydration step using hexamethyldisilazane (HMDS), a volatile silicon-based organic compound used as a chemical drying agent in biological sample preparation, was likewise adapted from previously reported micro-CT investigations of insect specimens [151].

In a comparative micro-CT study [150], iodine staining was more effective for whole-body imaging due to its ability to penetrate the cuticle and diffuse rapidly through tissues. In contrast, phosphotungstic acid (PTA) provided greater contrast for fine soft-tissue structures in smaller samples, but required specimens to be cut into millimetre-scale lengths to allow effective stain penetration [150].

Accordingly, in this study, once crickets had been killed, a portion of either the left or right prothoracic tibia was excised using microscissors. The tibia was cut just below the femur–tibia joint (i.e., the 'knee') (Figure 1.9B) and again distal to the auditory region, below the posterior tympanum. For the final X-ray micro-CT datasets selected for analysis, an equal number of male and female specimens were included. In addition, left and right prothoracic tibiae were balanced across the datasets, ensuring equal representation of left and right ears from both sexes.

The dissected tibial segment was placed in an Eppendorf tube containing a 1:1 alcoholic Bouin's solution, prepared from one part Bouin's fluid and one part 100% ethanol, and kept at room temperature (approximately 23 °C) overnight for fixation [150]. Bouin's solution is a histological fixative composed of picric acid, formaldehyde, and glacial acetic acid. The fixative was then removed, and the specimen was washed three times in 70% ethanol for 10 minutes each. This was followed by an ethanol dehydration series consisting of 10 minutes in solution and 10 minutes of air drying at room temperature at each of the following concentrations: 50%, 70%, 80%, 90%, 95%, and three cycles of 100%. The tibial sections were then stained in 0.3% PTA solution [150] and kept at room temperature for three nights. After staining, the PTA solution was removed, and specimens were rinsed in 100% ethanol (10 minutes, three cycles). Chemical drying was performed by immersion in 100% HMDS for 2 hours, followed by air drying at 35 °C overnight in a second OVA-Easy incubator [151]. Specimens were stored in sealed Eppendorf tubes containing 70% ethanol and kept at room temperature in the dark prior to X-ray imaging.

2.2.2 Two Sources of X-ray Data

It should be noted that two distinct types of X-ray micro-CT datasets were used in this study. Thickness measurements were obtained from a cohort of 12 specimens prepared using the standardised fixation, staining, and drying protocol described above, and scanned under consistent acquisition conditions (48 kV, 0.55 µm voxel size).

The 3D visualisations and finite element geometries, however, were derived from a single representative specimen scanned under different conditions (30 kV, 0.88 µm voxel size). Qualitatively, this dataset appeared to provide comparatively high image quality, although the reasons for this are not fully clear. It is possible that the lower tube voltage contributed to increased soft-tissue contrast; however, if the specimen was indeed unstained and not dehydrated, as is likely, it is somewhat unexpected that such strong contrast was achieved. In the absence of heavy-metal staining and dehydration, soft tissues would be expected to exhibit lower overall X-ray attenuation, which may also explain the use of a lower tube voltage in this case.

This represents a limitation in terms of methodological consistency, as the preparation history of this specimen is not fully documented. Future work should aim to ensure that all specimens are prepared and imaged using fully standardised and well-documented protocols.

However, the use of a single specimen was considered sufficient for capturing overall morphology and spatial geometry, rather than for performing quantitative comparisons or resolving fine structural differences. At this level of analysis, gross anatomical geometry is expected to be broadly consistent between individuals, and therefore a single high-quality dataset is considered adequate for generating representative 3D reconstructions and finite element geometries.

By contrast, the thickness analysis required precise and reproducible measurements across multiple individuals and therefore relied on a fully standardised preparation and imaging protocol.

2.3 **Scanning Laser Doppler Vibrometry (LDV)**

Laser Doppler vibrometry (LDV) is a non-contact technique used to measure the vibrational velocity or displacement of a surface. LDV has become the standard tool for experimentally measuring the motion of auditory structures in insects and has been applied across a wide range of taxa. In addition to extensive use in orthopteran acoustics (notably locusts [152], bushcrickets

[153] and crickets [27]), LDV has also been applied to butterflies [154] and moths [155], beetles [156], cicadas [157], and the praying mantis [158].

In this study, LDV was used to pursue Aim 1 of the thesis: to resolve the vibrational profile of the field cricket's posterior tympanum. Although not the first application of LDV to measure the vibrational response of the Gryllinae PTM, this present study represents a pioneering application of *scanning* LDV (acquiring automated mesh points across the tympanum) to this system and a pioneering use of LDV to directly measure the tympanum's *phase response*.

2.3.1 How Does LDV Work?

Laser Doppler vibrometry (LDV) measures the motion of a vibrating surface by detecting changes in the frequency of reflected laser light. These changes are caused by the Doppler effect, a physical phenomenon in which the frequency of a wave increases when the source moves towards the observer and decreases when it moves away. In LDV, when a surface moves towards or away from the laser beam, the reflected light shifts slightly in frequency. This means the frequency change in the reflected light shows how fast the surface is moving towards or away from the laser.

Figure 2.1 provides a diagram illustrating the key components that make up a laser Doppler vibrometer. At the core of an LDV system is a *laser*, which produces light through a process called stimulated emission. In this process, atoms are excited to a higher energy state. When they return to a lower energy state, they emit light. If this emission is triggered by an incoming photon of the same energy, the emitted photons are identical in phase, frequency, and direction. Mirrors at either end of the laser cavity amplify this effect, producing a narrow, coherent beam. Most LDV systems use a helium-neon (HeNe) gas laser that emits red light at a wavelength of 632.8 nanometres. The red light from a HeNe source is highly stable over time, and its waves remain well aligned, making it particularly suited for precision LDV measurements.

However, some LDV systems, including the Polytec MSA-100-3D used in this study, generate green light instead of red. In this system, the red light

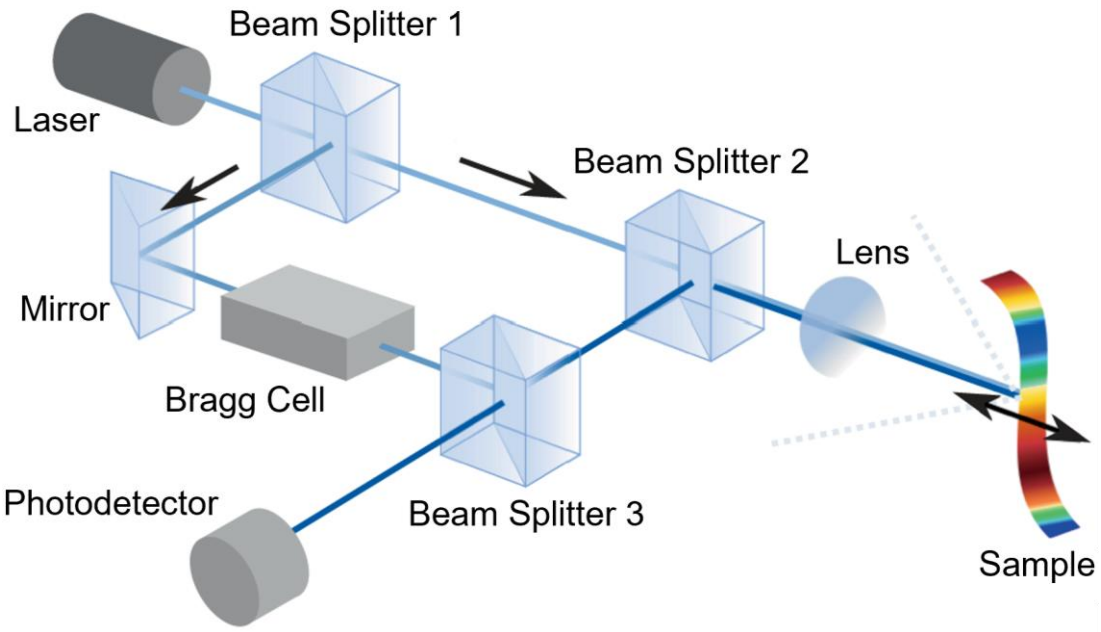

Figure 2.1 | How a laser Doppler vibrometer (LDV) works. A laser beam is split into a reference path and a measurement path by Beam Splitter 1 (BS1). The measurement beam is directed onto the sample via Beam Splitter 2 (BS2) and a focusing lens, while the reference beam passes through a Bragg cell to introduce a known frequency shift. Reflected light from the vibrating sample recombines with the reference beam at Beam Splitter 3 (BS3), and the interference pattern is detected and analysed to measure surface vibration using the Doppler effect. Figure adapted from [159].

from the helium-neon laser is passed through a special crystal that increases its frequency, reducing its wavelength to 532 nanometres and thus converting it into green light. Focusing of the laser beam is performed by the lens (Figure 2.1), not by the crystal. However, because green light has a shorter wavelength, the lens can produce a smaller minimum spot size on the sample, thereby improving spatial precision. The smaller spot size achieved by the green laser is due to the shorter wavelength, as the minimum size to which a beam can be focused is limited by diffraction and scales with wavelength. Even under ideal focusing conditions, the spot diameter remains several times larger than the wavelength itself. Overall, due to its shorter wavelength, the green light used by the MSA-100-3D produces a slightly larger Doppler frequency

shift for a given vibration velocity and can be focused to a smaller spot size, thereby improving measurement sensitivity and spatial resolution.

In an LDV, the laser beam is first split into two paths by *beam splitter 1* (BS1) (Figure 2.1). One path becomes the reference beam, which travels through a fixed internal route. The other becomes the measurement beam, which continues towards the object being studied. This beam passes through *beam splitter 2* (BS2) and is directed onto the sample by a *lens*. The lens can be manually adjusted to focus the beam onto the object's surface. The beam then reflects off the sample and returns along the same path, passing through BS2 once more.

The reflected measurement beam is then combined with the reference beam at *beam splitter 3* (BS3). Both beams continue to the *photodetector*. The photodetector receives the combined light and converts it into an electrical signal. When the two beams interfere, their wave patterns overlap. If the vibrating surface has caused the measurement beam to shift in frequency, this interference changes over time. The photodetector senses these changes and generates a signal that tells the system how fast the surface was moving. This method of comparing the two beams to detect motion is known as laser interferometry.

Prior to the reference beam combining with the measurement beam at beam splitter 3, the reference beam has followed its own path (Figure 2.1). After splitting from the measurement beam at BS1, the reference beam must pass through a *Bragg cell* (via a *mirror*).

Without the Bragg cell, the detector would only measure the magnitude of the Doppler shift and would not be able to determine whether the surface is moving *towards* or *away* from the laser, since motion in opposite directions produces frequency shifts of equal magnitude, with one increasing the frequency and the other decreasing it. The Bragg cell overcomes this limitation by introducing a fixed, known frequency shift to the reference beam, thereby creating a constant beat frequency between the reference and measurement beams even when the surface is stationary. When the surface vibrates, the Doppler shift causes this beat frequency to increase if the surface moves away

from the laser and decrease if it moves towards it. By measuring these changes relative to the known frequency offset introduced by the Bragg cell, the LDV system can determine not only the magnitude of the surface velocity, but also its direction.

Scanning LDV, which automates this measurement process across many points on a sample, remains relatively uncommon in insect acoustic research. Most LDV studies, including the majority of those focused on field crickets, have exclusively employed single-point measurements. These typically involve a reading taken from the centre of the tympanum, or a small number of recordings obtained by manually repositioning the LDV between measurements. In contrast, scanning LDV captures data from many (potentially hundreds) of points automatically, enabling full spatial mapping of tympanal motion. This provides much higher resolution and completeness, which may reveal patterns otherwise missed in limited-point studies. In the present work, for example, scanning LDV enabled mapping of the global modal response of the tympanum, demonstrating that the membrane oscillated in a uniform drum mode across its surface at both vibrational peaks – an observation that would not have been confirmable from a single centre point measurement, as has typically been employed in LDV studies of the Gryllinae ear (e.g. [8, 12]).

2.3.2 Specific LDV Setup

Given the longstanding disagreement in the LDV literature regarding the vibrational profile of the Gryllinae posterior tympanal membrane, this study aimed to provide a robust reassessment by designing multiple LDV experiments that varied key parameters, ensuring accurate and reliable characterisation of the PTM.

Three key variables were systematically varied. First, two fundamentally different loudspeaker technologies were used: a conventional cone diaphragm loudspeaker, which produces sound via piston-like motion of a solid cone, and an air motion transformer (AMT) ribbon loudspeaker, which generates sound through the movement of a folded diaphragm that squeezes air. These

technologies differ in their mode of air displacement and frequency response behaviour and were included to control for possible stimulus artefacts arising from loudspeaker performance. Second, two classes of acoustic stimuli were employed: manually controlled pure tones and automated frequency sweeps. Pure tones allowed a high-intensity, precisely defined, and consistent sound pressure level at each individual frequency tested, increasing sensitivity to subtle vibrational features, but were limited to single-point, low-throughput measurements with relatively coarse frequency sampling. In contrast, frequency sweeps enabled automated, high-resolution, multipoint scanning across the entire tympanum using the scanning capability of the Polytec MSA-100-3D system, greatly increasing spatial coverage, frequency resolution, and sample size, albeit at lower and less uniform sound intensity across frequencies. Third, the role of internal acoustic transmission pathways was assessed by manipulating spiracular state, with spiracles either surgically opened or experimentally sealed.

Together, these methodological variations defined three principal experimental conditions. (1) The first employed high-intensity pure tones with spiracles open using a cone loudspeaker, providing a consistent sound pressure level at each frequency for sensitive detection of subtle vibrations and direct comparison of resonance peaks without normalisation. (2) The second used frequency sweeps with spiracles open and a cone loudspeaker, enabling automated, high-resolution mapping of tympanal responses. (3) The third employed frequency sweeps delivered via a ribbon loudspeaker, with spiracles either open or sealed, allowing both comparison of loudspeaker technology and direct assessment of the contribution of internal acoustic pathways to the PTM vibrational profile.

Figure 2.2 shows the specific LDV setup employed by this study. In this research, a Polytec MSA-100-3D Micro System Analyser was used (Panel A). This instrument combines scanning LDV with the potential for real-time three-dimensional vibration analysis. The MSA-100-3D features a tightly focused green laser, sub-picometre sensitivity, and a precision XY scanning stage for automated surface measurements. Although capable of recording motion

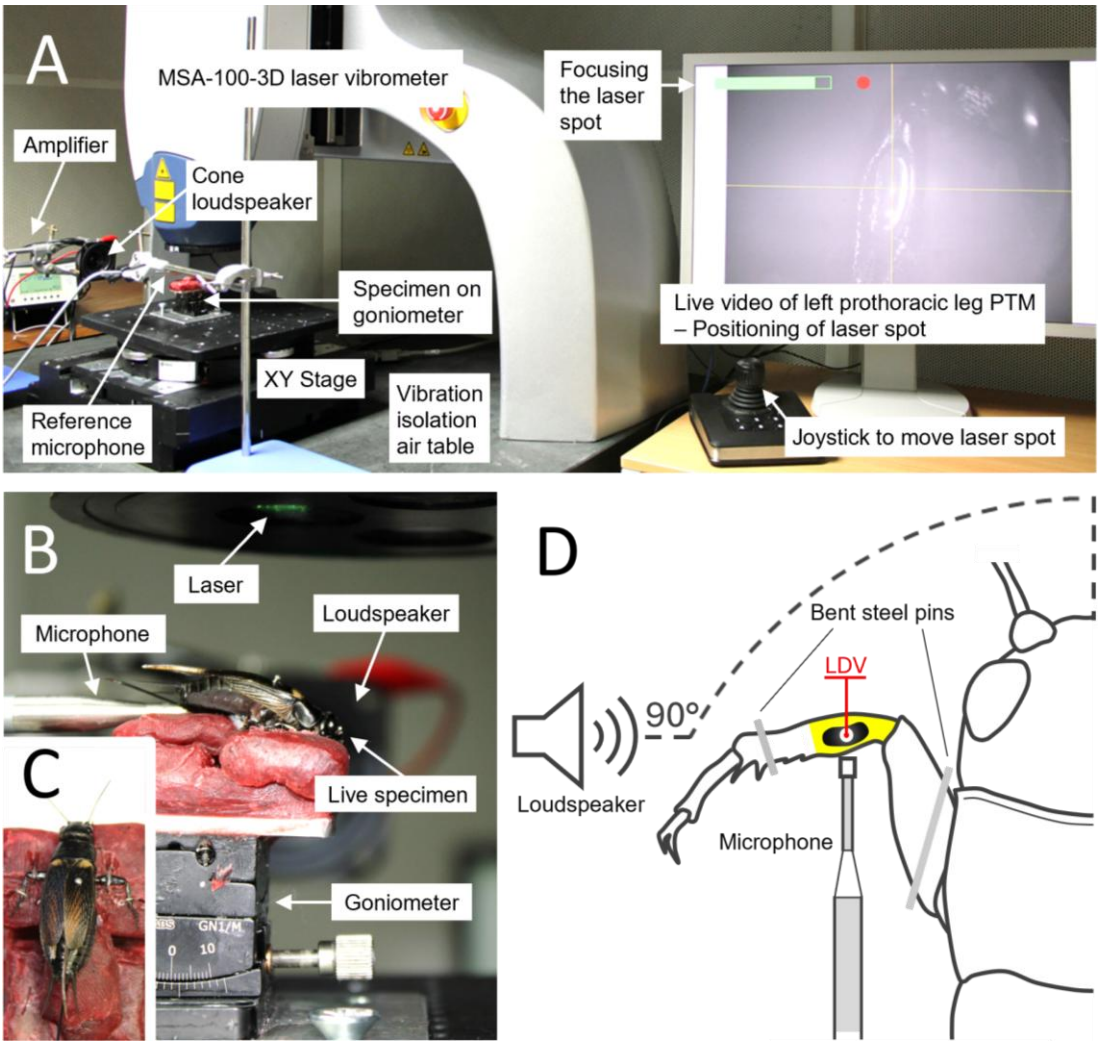

Figure 2.2 | The laser Doppler vibrometry (LDV) setup used in this study. To measure the vibrational response of the Gryllinae posterior tympanal membrane (PTM), I used **(A)** an MSA-100-3D (Polytec) scanning LDV positioned on a vibration isolation table inside a sound-insulated test room (IAC Acoustics). **(A, B)** The 5.8 cm diameter cone diaphragm loudspeaker (VISATON FR58, 8 Ω, 120–20000 Hz) as used in acoustic conditions 1–2. Acoustic condition 3 used a Heil air motion transformer (AMT) ribbon diaphragm loudspeaker (ESS, 800–20000 Hz). Across experiments, the loudspeaker was positioned 20 cm from the cricket, at 90° azimuth relative to the cricket's forward-facing orientation. The cricket, mounted on a wax bed, was secured to a goniometer via a custom aluminium plate. The goniometer itself was attached to the LDV positioning stage using a second custom plate. This setup allowed for precise alignment of the PTM relative to the laser. A 1/8″ precision pressure microphone (Type 4138 A-015; Brüel & Kjær, Naerum, Denmark) was positioned perpendicular to the direction of sound. **(C)** Downward-facing view of the cricket, secured with a pin through the abdomen and with bent pins for the prothoracic legs. **(D)** Schematic representation.

along all three spatial axes (X, Y, and Z), the system was used here in single-axis mode to record only out-of-plane vibrations, corresponding to motion along the up-down Z-axis. To ensure that the LDV measurement axis (Z) was oriented normal to the tympanal surface, the specimen was mounted on a precision goniometer to allow fine adjustment of its tilt angle (Figure 2.2B).

Vibrational responses of the posterior tympanum were recorded from a total of 41 *G. bimaculatus* and six *T. commodus* individuals. Prior to LDV measurements, crickets were cold anaesthetised by placement in a freezer at −18 °C for five minutes.

In most experiments, the two spiracular openings to the internal acoustic trachea were kept open by surgically removing the spiracle flaps using microscissors following anaesthetisation. Each acoustic spiracle is associated with a hinged cuticular structure, the flap. A spiracle opening with and without its flap can be seen in the Figure 2.3 photographs. Left unaltered, the flap can be opened or closed by the animal to regulate access to the internal tracheal pathway. Removal of the flaps from both spiracles ensured that internal acoustic transmission via the acoustic trachea to the inner surface of the PTM remained unobstructed. As a result, the measured PTM response reflected its state as a functional three-input receiver.

In the third set of experiments utilising two spiracular treatments – open vs. closed – including the closed state controlled for the possibility that the measured PTM vibrations resulted from phase-shift tuning due to internal transmissions. To close each spiracle, the flap was maintained and the entirety of the flap and the opening were covered with petroleum jelly (Vaseline®, Unilever UK Ltd., Surrey, UK).

In all LDV experiments, measurements were performed *in vivo*, that is, in living animals. Specimens were maintained alive to preserve natural physiological conditions and to prevent desiccation of the tympanal cuticle, which could alter its mechanical properties. Keeping the animals alive also allowed control of any potential contributions of active auditory processes (energy-dependent amplification and tuning of sound by the auditory system, rather than an entirely passive mechanical response).

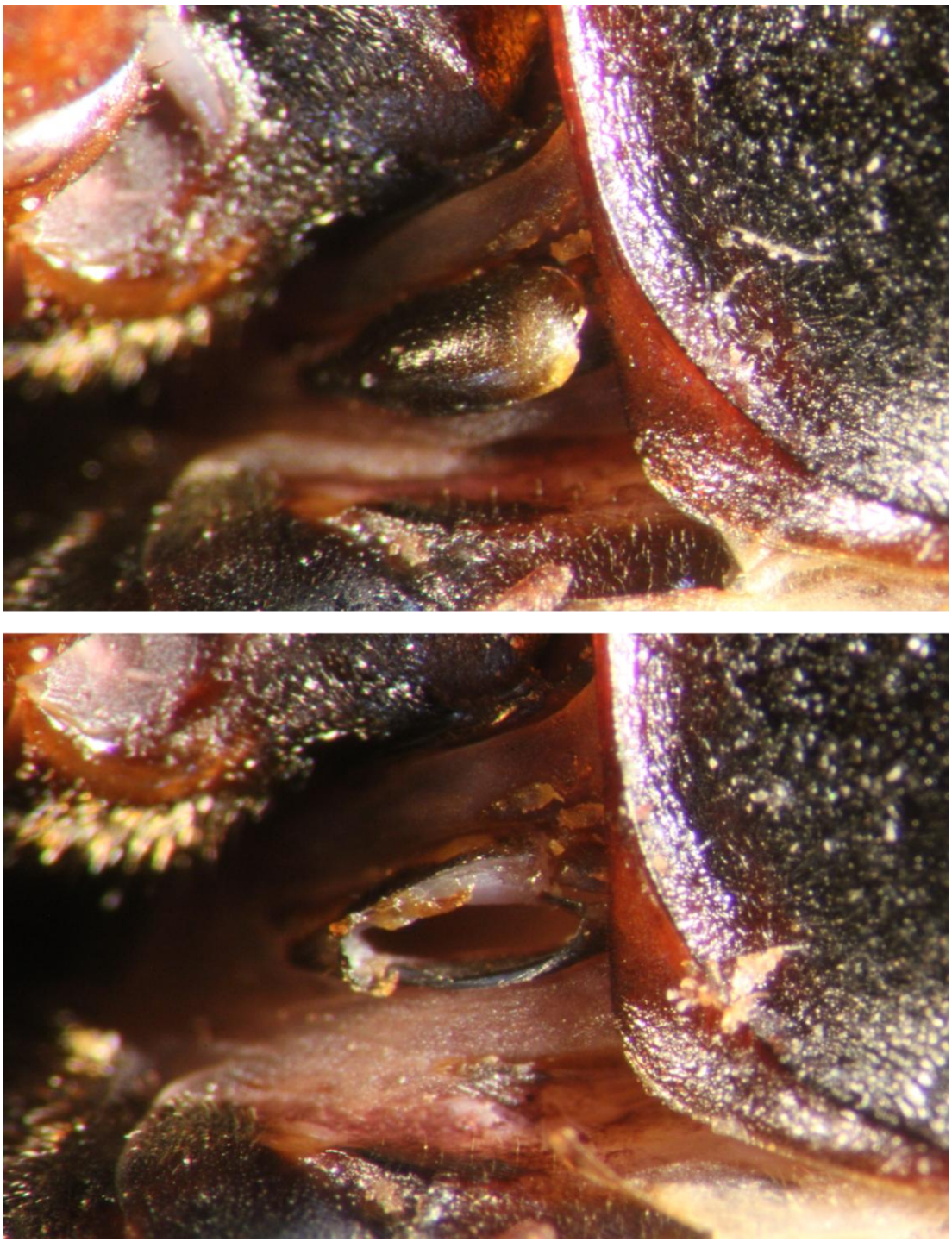

Figure 2.3 | Removal of acoustic spiracle flaps ensures internal sound transmission to the posterior tympanum. Light microscopy images of a *Gryllus bimaculatus* acoustic spiracle before (**top**) and after (**bottom**) flap removal using microscissors. Flaps were removed prior to all cone loudspeaker experiments (pure tone and sweep stimuli) and for one of two treatments using the ribbon diaphragm (sweep stimulus). This ensured that sound reached the internal surface of the posterior tympanum via the acoustic trachea.

To minimise movement during recordings, the mid and hind legs were removed in all specimens, irrespective of whether the acoustic spiracles were opened or blocked. Each cricket was positioned ventral side down with the dorsal surface, including the wings, facing upwards (Figure 2.2B,C). The body was placed on a bed of wax and secured using stainless steel entomological pins (Figure 2.2C). Pins were inserted only through the abdomen to avoid damaging the thorax, where the acoustic trachea is located. In males, to prevent any possibility of sound production from the forewings during recording, the wings were either trimmed with microscissors or held in place by inserting a pin through them.

The two prothoracic legs were carefully splayed laterally such that the posterior tympana were oriented dorsally (Figure 2.2C,D), while the anterior tympana faced downward towards the wax. Each leg was secured using several bent pins, arranged to hook around the limb and gently press it against the wax surface. This preparation resulted in a consistent overall body orientation across experiments, with animals positioned at 0° azimuth relative to the sound source (presented at 90°), and with the posterior tympanum reliably exposed to the incident sound field. While this approach provided robust and repeatable positioning of the tympana, further refinement could be achieved by incorporating more precise control of leg orientation, for example by standardising the limb position at a fixed right angle to the body axis.

The posterior tympanum had to face upward because the MSA-100-3D measures vibration along a fixed vertical (Z) axis and the laser head cannot be re-oriented. Unlike the movable single-point 1D LDV systems typically used in previous studies, the laser orientation in this system could not be adjusted. As the PTM must be positioned normal to the laser beam, this alignment had to be achieved by adjusting the specimen rather than the instrument. This constraint resulted in the anterior tympanum facing downward towards the wax.

The anterior tympanal membrane has often been considered to play a negligible role in sound reception and frequency tuning (Section 1.12.4; [5, 7, 8, 15]). In [7], it is explicitly concluded that *“covering the small membrane had*

no effect either on the large membrane vibration or on the sensitivity of the interneurons." Nevertheless, in the present study, in case the ATM were to affect the PTM response, care was taken to ensure that it did not contact the substrate. A tunnel was dug in the wax beneath each ATM so that the anterior tympanum was suspended over air.

It is conceivable that the preparation could instead have been oriented more like that of [8], in which the prothoracic leg was secured with pins on a wax and cork substrate such that neither tympanum faced the substrate. Replicating such an arrangement here would have required rotating the preparation by 180° (head directed downward, abdomen upward towards the laser) so that the PTM remained normal to the fixed laser axis. This may have better maintained equivalent acoustic exposure of both tympana. In any future experiments using an MSA-100-3D with a fixed laser axis, such an orientation would be recommended to further control for potential sound-field asymmetries.

The wax bed upon which the animal was pinned was itself rested on a custom-cut aluminium sheet attached to a goniometer (Figure 2.2B). The goniometer was secured to a second larger aluminium sheet that could be screwed into the LDV XY position stage (Figure 2.2A). Using a goniometer allowed precise adjustment of the tilt angle of the specimen. This was used to position the subject tympanum, the PTM, as level as possible beneath the vibrometer laser. Maintaining the tympanal surface level ensured that the LDV measurement axis remained normal to the membrane, thereby allowing accurate and repeatable measurement of membrane motion.

The MSA-100-3D vibrometer was mounted on a vibration isolation air table inside a walk-in, sound-absorbing, double-walled, sound-insulated test room (IAC Acoustics, High Wycombe, UK) (Figure 2.2A). The loudspeaker was positioned at the same height as the cricket, 22 cm from the longitudinal midline of the animal's body, at 90° azimuth (i.e., 90° from straight ahead), on the same side (ipsilateral) as the target PTM (Figure 2.2D). Here, 0° azimuth is defined as the longitudinal midline of the animal with the head facing straight

ahead, and all incident sound angles are defined relative to this reference (Figure 2.2D).

As this study did not aim to characterise directional tuning, a single fixed loudspeaker position was used. A lateral position of 90° azimuth was selected, consistent with previous work [27], and because it could be set reliably and reproducibly within the experimental setup. In the Gryllinae auditory system, 90° provides a strong and robust tympanal vibration response [71]. A different incidence angle (e.g. 60°) may result in a slightly greater vibration amplitude but would not be expected to alter the frequency positions of any tympanal vibrations.

Two different loudspeakers were used across three acoustic conditions. For two of the three sets of LDV experiments, a 5.8 cm diameter cone loudspeaker (VISATON FR58, 8 Ω, 120–20,000 Hz) was employed. In the third experimental setup, this was replaced with a Heil air motion transformer (AMT) ribbon diaphragm loudspeaker (ESS, 800–20000 Hz).

To measure PTM movement relative to the acoustic stimulus, a reference recording was required. This was obtained using a 1/8″ precision pressure microphone (Type 4138 A-015; Brüel & Kjær, Naerum, Denmark), connected to a conditioning amplifier (Type 2690 A-0F2 NEXUS; Brüel & Kjær) (Figure 2.2A). The microphone signal provided a direct measurement of the local sound pressure at the tympanum for each stimulus. For pure-tone experiments, this signal was used to confirm that the manually calibrated loudspeaker output was maintained at 78 dB SPL at the tympanum. For sweep stimuli, where the loudspeaker output could not be manually calibrated and exhibited frequency-dependent variation, the measured sound pressure at the tympanum was used to normalise the vibrational response at each frequency bin (i.e. as a frequency response function). This normalisation allowed tympanal responses to be compared across the full frequency range despite non-uniform stimulus amplitude. The microphone signal also served as the reference for phase measurements, with phase calculated by the LDV system as the relative timing between the recorded tympanal velocity and the local sound pressure measured at the tympanum.

The conditioning amplifier boosts the very small voltage signal generated by the microphone in response to sound pressure and scales it to a calibrated output such as a known voltage per pascal, allowing accurate measurement of the acoustic pressure at the ear. For example, it might produce exactly 1 volt for every pascal of sound pressure. This fixed relationship, called a transfer function, allows the signal to be accurately recorded, interpreted, and compared.

To accurately capture the local sound pressure at the ear, the reference microphone was positioned within 1 cm of the subject tympanum, with the length of the microphone probe aligned at a right angle (90°) to the direction of sound from the loudspeaker (Figure 2.2). This orientation ensured that the probe did not obstruct or distort the incoming sound wave and allowed measurement of local sound pressure at the probe tip rather than along the length of the probe. The alignment was set visually, but the simple 90° geometry allowed consistent and reproducible positioning across preparations. Because the microphone was placed in very close proximity to the tympanum, both experienced effectively the same local sound field. While small deviations in angle may influence absolute sound pressure amplitude, they are not expected to affect the frequency positions of tympanal resonances, which were the primary outcome measure in this study.

Three LDV experimental conditions were used to characterise the PTM vibrational profile: pure tones (cone loudspeaker; VISATON FR58, 8 Ω, 120–20000 Hz) with spiracles open; frequency sweeps (cone loudspeaker) with spiracles open; and frequency sweeps (ribbon loudspeaker; Heil air motion transformer (AMT), ESS, 800–20000 Hz) with spiracles open and closed. Vibrational velocity was recorded in all conditions, with phase obtained from sweep conditions.

Pure tones provided higher intensity, manually calibrated outputs but limited spatial and spectral coverage. Stimuli were presented at 78 dB SPL, with single-point measurements from the tympanum centre in 10 *G. bimaculatus* (5 males, 5 females). Frequencies were sampled at 200 Hz increments in the 3–6 kHz and 11–16 kHz ranges, and 1000 Hz elsewhere.

Magnitude averaging (5) was applied. Results are reported as velocity (μm/s, SD).

Frequency sweeps enabled automated multipoint scanning across the tympanum. For each specimen, the kidney-bean-shaped perimeter of the tympanal membrane was traced by hand, after which the software automatically filled the enclosed area with a single mesh of linked scan points with an average spacing of approximately 72 μm. Because tympanum area and shape varied slightly between individuals, mesh outlines differed accordingly, while average point spacing remained consistent across meshes.

Sweeps from the cone loudspeaker were applied to 20 *G. bimaculatus* and 6 *T. commodus*. In the ribbon loudspeaker experiments, sweeps were delivered to 20 *G. bimaculatus* (10 spiracles open, 10 blocked). Although the cone loudspeaker output was substantially less variable than that of the ribbon loudspeaker, it was nonetheless non-linear. Therefore, tympanal vibrations recorded under cone loudspeaker sweeps were normalised to the local sound pressure at each frequency. This produced frequency response functions (μm/s/Pa, SEM), expressing membrane velocity (μm/s) per unit sound pressure (Pa) and allowing direct comparison of response magnitude across frequencies. During data acquisition, responses were smoothed using a 5-bin moving average, and complex averaging (5) was applied.

For all sweep-based experiments, the laser was initially focused on the middle region of the tympanum, after which the membrane outline was traced, populated with measurement points, and scanning initiated. The resulting mesh of scan points was used to assess the modal behaviour of the entire tympanum and to confirm that the central region provided a representative location for reporting. Accordingly, for all sweep-derived outputs, a central scan point was manually selected from the mesh. This approach is consistent with established practice, whereby measurement locations on the tympanum are either not specified and assumed to be central or are reported as central without detailing how this position was defined [12, 27, 115]. For this representative point, approximately 1,778 frequency bins were obtained (2–20 kHz, 11.25 Hz resolution). Signal quality varied across both spatial locations

and frequency bins, with some measurements yielding lower coherence values due to suboptimal laser focus on the membrane or increased noise. After selecting the representative central point, the data were manually filtered to exclude frequency bins with a coherence value below 85%, ensuring that only high-quality, reliable data were retained for analysis.

In all experiments, across all three acoustic conditions, vibrational responses were analysed using 1600 fast Fourier transform (FFT) lines. In the sweep-based experiments, this provided a frequency resolution of 11.25 Hz over the analysed range (2–20 kHz).

In these sweep-based experiments, the stimulus frequency was continuously swept across the 2–20 kHz range, allowing vibration amplitude to be measured at fine frequency intervals across the entire range.

In the pure-tone experiments, frequencies were presented discretely (at 200 Hz or 1000 Hz increments). Although the same 1600 FFT setting was used, only the bin corresponding to the stimulus frequency contained meaningful signal, while the remaining bins reflected background signal and noise. Thus, in this case, frequency resolution was determined by the spacing of the stimulus pure-tone frequencies rather than the FFT settings. Using the same FFT configuration across all conditions ensured consistent analysis parameters and allowed for more reliable comparisons.

2.3.3 Driving-Force vs. Natural Resonance: Mathematical Theory

The LDV measurements obtained in the present study included the phase response of the posterior tympanal membrane, which is presented in Chapter 3 in terms of real and imaginary components. Analysis of these data revealed both a *natural resonance* and a *driving resonance*, identifiable from the phase behaviour. The following section outlines the mathematical framework underlying these physical phenomena of natural and driving resonances.

To describe how the PTM behaves in this context, physicists use a standard equation taken from a field known as modal analysis. This method is used to understand how physical systems respond to vibration. The equation

expresses the movement of the membrane when it is acted upon by a repeating or sinusoidal sound wave. It is written as:

$$-m\omega^2 + cj\omega + k\omega = f(\omega) \tag{2.1}$$

Each part of this equation represents a physical property of the membrane or the sound. The letter m is the mass of the membrane, which refers to how much it weighs. The letter c represents damping, which means the resistance or friction that slows down the movement. The letter k is the stiffness, which describes how firm or spring-like the membrane is. The symbol j stands for the imaginary unit, which is used in mathematics to describe timing differences in wave motion. The symbol ω, called omega, is the frequency of the sound wave, or how many times it vibrates per second. The right-hand side of the equation, $f(\omega)$, is the force applied at that frequency.

This equation shows how the movement of the membrane is influenced by a combination of its mass, stiffness, and damping. At low frequencies, the stiffness is the most important factor. At high frequencies, the mass plays a more dominant role. When the frequency reaches a particular point, known as the resonance frequency, the effects of stiffness and mass balance in such a way that the membrane moves with the greatest ease. This point is known as the natural resonance of the membrane.

To investigate this further, the equation can be rearranged into a form that shows how much the membrane moves in response to force. This involves taking either the displacement or the velocity and dividing it by the applied force. When using velocity, this creates what is known as a mobility function. Velocity is related to displacement by $v(\omega) = j\omega x(\omega)$, and substituting this into Equation (2.1) and rearranging (by factoring out ω) gives:

$$\frac{v(\omega)}{f(\omega)} = \frac{j}{-m\omega + cj + \frac{k}{\omega}} \tag{2.2}$$

This version of the equation describes how the velocity of the membrane at a given frequency, written as $v(\omega)$, relates to the force applied at that frequency, written as $f(\omega)$. The expression on the right-hand side includes the same three terms from earlier, but now they appear in a form that directly determines the response of the system. At low frequencies, the term k/ω is large, so the stiffness of the membrane dominates. At high frequencies, the term $-m\omega$ becomes dominant, meaning the mass of the membrane controls its motion. Because the dominant terms at low and high frequencies act in opposite ways, they produce opposite timing responses (lead and lag), explaining the change in phase behaviour across frequency.

Again, researchers look at this timing by separating the vibration into two parts called the real and imaginary components. The real component describes motion that is exactly in time with the sound wave. The imaginary component describes motion that is slightly ahead of or behind the sound wave. These two components together allow us to see both the amplitude of the vibration and when it happens in relation to the incoming sound.

When a membrane is vibrating because it is being *pushed* from outside, we may see a strong vibration, but the phase does not shift in any meaningful way. The motion stays more or less in time with the sound wave. In contrast, when a membrane reaches its natural resonance, a particular pattern is seen. The *real* part of the vibration drops to zero, and the imaginary part reaches either a peak or a dip, because at resonance the stiffness and mass contributions balance, leaving the response dominated by the damping (imaginary) term. This moment is called a zero crossing. It signals that the timing of the membrane's movement has changed in a way that reflects the membrane's own properties, not just the behaviour of the incoming sound wave.

In summary, by studying both the amplitude and the timing of the membrane's vibration, we can determine whether the PTM is being moved by an external resonator or is resonating due to its own physical characteristics. A strong vibration without a shift in timing points to a driving force, the 6 kHz

peak. While a shift in timing, especially one marked by a zero crossing, points to the membrane's natural resonance, the 14 kHz peak.

2.4 **X-ray micro-Computed Tomography (micro-CT)**

X-ray micro-computed tomography (micro-CT or μ-CT) is a three-dimensional imaging technique that uses X-rays to visualise the internal structures of an object in 3D without physically altering or destroying it. It uses the same underlying method as conventional medical CT, also known as a CAT scan or computed axial tomography. However, micro-CT is optimised for imaging much smaller samples at significantly higher resolution. X-ray micro-CT can resolve features as small as 1 μm (0.001 mm). The maximum sample size that can be accommodated typically does not exceed 200 mm in diameter. High X-ray micro-CT resolution is achieved through several design optimisations. These include detectors with smaller pixels that capture finer structural details, an X-ray source with a smaller focal spot that produces a narrower and sharper beam, and a system layout that positions the object closer to the detector.

In this study, X-ray micro-CT was used to address Aims 2, 3, and 4, each of which focuses on the internal structures located downstream of the posterior tympanum (Chapter 4). To investigate potential biomechanical filtering between the posterior tympanal membrane and the auditory neurons (Aim 2), the three-dimensional anatomy of the PTM–sensilla region was examined. The same anatomical information was also required to investigate the mechanical transmission pathway from the PTM to the sensory neurons (Aim 3). Historically, this PTM–sensilla region of the Gryllinae ear has been studied using physical sectioning of the prothoracic tibia and interpretation of two-dimensional histological slices [23, 28, 31]. However, such methods are limited in their ability to preserve and quantify the 3D spatial relationships between structures. The X-ray micro-CT technique employed in the present work enabled full volumetric reconstruction of the ear within intact tibiae, supporting both qualitative evaluation of 3D models and quantitative analysis including 3D thickness measurements of specific internal structures of interest (Aim 4). Mapping these thicknesses is particularly relevant to identifying

anatomical features with potential auditory function, such as filtering or transmission capability. A thin cuticle over an air-filled cavity, for instance, would be of special interest [82], because thinner structures have lower mass and stiffness, allowing greater vibrational displacement and thus increased sensitivity to acoustic waves [160].

2.4.1 How Does X-ray Micro-CT Work?

The X-ray micro-CT imaging process involves five main steps, as illustrated in Figure 2.4. These are: (1) *X-ray generation and detection*, (2) *acquisition of 2D projection images*, (3) *tomographic reconstruction*, (4) *3D volumetric visualisation*, and (5) *segmentation and quantitative analysis*. Unlike a conventional 2D medical chest X-ray, which captures a single two-dimensional image from one fixed angle and presents overlapping anatomical structures in a single plane, micro-CT collects many projection images from multiple angles as the sample rotates through either 180° or 360°. Each projection captures the internal features of the sample from a slightly different view (step 2). These projection images are then processed using tomographic reconstruction algorithms to generate a stack of cross-sectional slices (step 3). Together, the slices form a volumetric dataset composed of voxels (three-dimensional pixels), which can be visualised in 3D (step 4). The reconstructed slices can also be further processed to isolate key structures within the dataset and to apply quantitative analyses to these segmentations (step 5). Each of these five steps is described further below, with most emphasis given to step one.

1. X-ray generation and detection

X-rays are generated inside a vacuum-sealed X-ray tube, which contains two components called the cathode and the anode. The cathode is a negatively charged filament that emits electrons when heated. In many micro-CT systems, the cathode requires a short pre-heating phase when the scanner is first powered on. During a scan, the emitted electrons are accelerated towards the anode, which is a positively charged metal target, typically made of tungsten. When the electrons strike the target, they release energy in the form

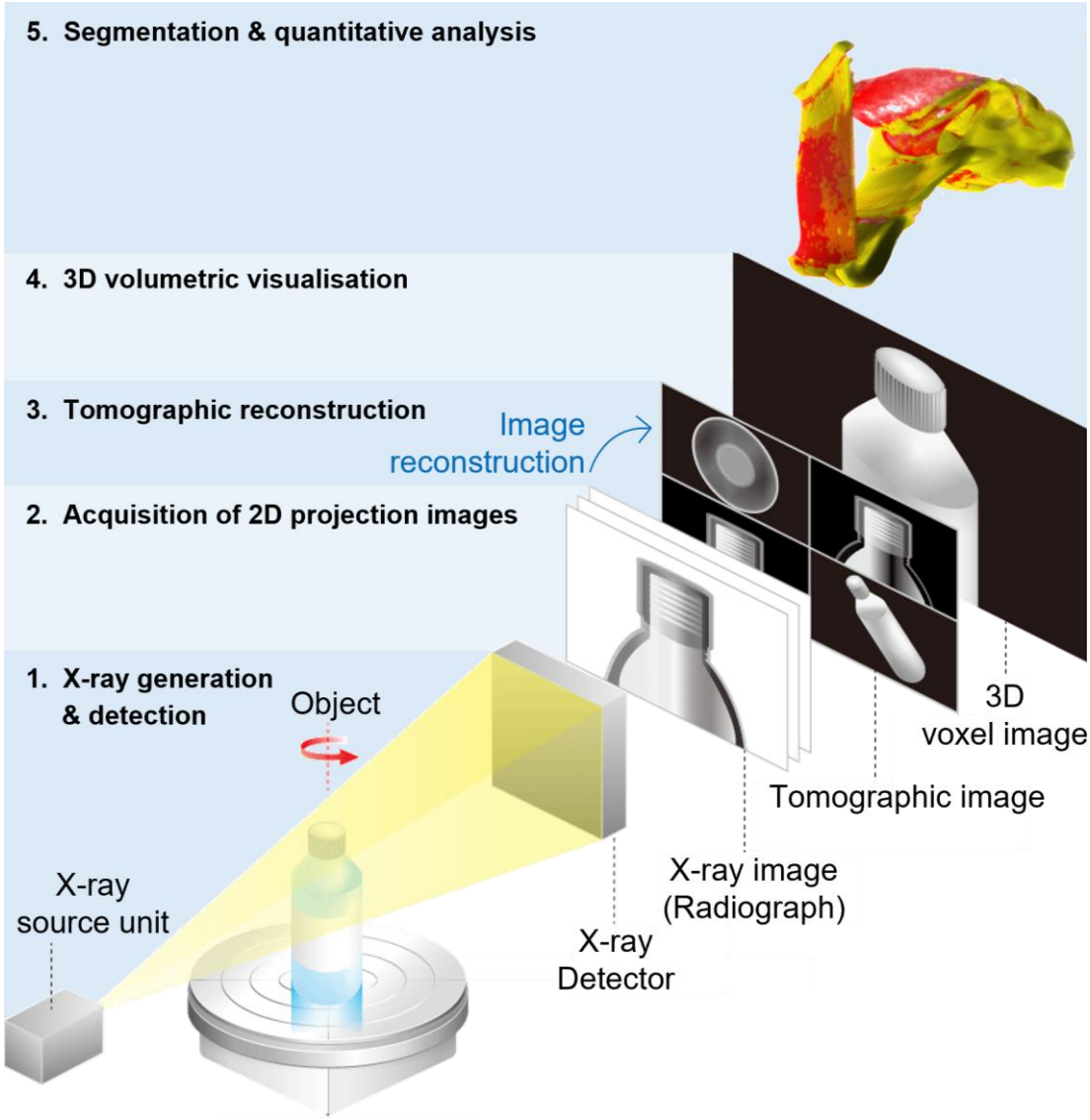

Figure 2.4 | Workflow of X-ray micro-computed tomography (micro-CT). First, **(1)** *X-ray generation and detection:* A cone-shaped X-ray beam is emitted from the source and passes through the rotating object, with transmitted photons captured by a detector. **(2)** *Acquisition of 2D projection images:* As the sample rotates, multiple radiographic projections are recorded from different angles, showing cumulative X-ray attenuation (dataset 1). **(3)** *Tomographic reconstruction:* Projection data are processed using algorithms to create a stack of voxel-based cross-sectional slices (dataset 2). **(4)** *3D volumetric visualisation:* The reconstructed images are rendered in 3D, allowing detailed inspection of internal structures from any angle. **(5)** *Segmentation and quantitative analysis:* Specific regions of interest are digitally isolated and visualised in 3D, with properties like volume measured, and segmentations differentiated by colour or locally colour-coded to represent analytical metrics such as thickness. (dataset 3). Figure adapted from [161].

of X-rays. The point where the beam is produced is called the focal spot. A smaller focal spot results in sharper images. The X-rays then diverge from the source in a cone-shaped beam, which passes through the sample. This cone beam geometry differs from the fan-shaped beam used in medical CT, as it spreads out in all directions and is more suited for imaging smaller samples.

To optimally image a sample, several acquisition settings must be adjusted. Two key parameters are the X-ray tube voltage (measured in kilovolts, kV) and current (measured in microamperes, μA). Voltage controls the energy of individual X-ray photons and determines how well they can penetrate the sample. Higher voltages allow deeper penetration and are suitable for dense or thick material but may reduce contrast in soft tissues. Lower voltages increase contrast in low-density regions but may not fully penetrate denser materials. Current affects the number of photons produced, with a higher current increasing the number of X-rays in the beam, raising image brightness. However, high current also increases exposure, the total amount of X-ray energy the sample receives.

A metal filter (e.g. aluminium or copper) is often used to remove low-energy X-rays from the beam when imaging dense samples, such as metal objects in engineering applications, thereby reducing beam hardening artefacts. However, no filter was used in this study, as retaining lower-energy X-rays improves contrast in low-density biological tissues.

In addition to voltage and current, the rotation step, exposure time, and frame averaging can all be optimised. The rotation step sets the angle between each projection image. Smaller rotation steps result in the acquisition of a greater number of projection images. This increases the number of X-ray paths intersecting each point inside the sample, thereby enhancing the resolution of the final reconstruction. Increasing the number of rotation steps, however, also increases scan duration, as more projections need to be acquired. Exposure time is the length of time the detector collects data for each projection. Longer exposures also increase scan time. Frame averaging refers to the process of acquiring multiple projection images at the same angle and then combining them into a single image by averaging the pixel values. For example, a frame

averaging setting of ‘2’ means that two separate projection images are captured in succession at each angle, and the final stored image is the result of averaging the pixel intensities across both images. This reduces random noise in the final projection by reinforcing consistent signal features while cancelling out variations caused by stochastic fluctuations in the detector or X-ray source. To achieve optimal clarity and accuracy, all these parameters must be manually adjusted by the researcher based on the specific properties of the sample, such as its size, density, and the internal features that need to be visualised.

In practice, parameter selection follows a structured but iterative optimisation procedure. The X-ray tube voltage is first selected to provide sufficient penetration through the specimen while preserving contrast between features of interest; for low-density biological samples, this typically involves using the lowest voltage that still allows complete transmission through the thickest regions. The tube current is then set to provide an adequate photon flux, improving signal-to-noise ratio without unnecessarily increasing exposure. Exposure time is subsequently adjusted to optimise detector response: increasing exposure increases the number of detected photons and reduces noise but also increases scan duration. A common approach is to inspect the detector intensity in an empty-field (no sample) image and adjust exposure such that the mean signal lies within the mid-range of the detector’s dynamic range, thereby avoiding both underexposure (poor signal-to-noise) and saturation (loss of contrast).

For each combination of voltage, current, and detector settings, a flat-field correction is performed prior to acquisition. This involves acquiring reference images with no sample present to characterise spatial variations in the X-ray beam and detector response. These reference images are used to normalise subsequent projections, correcting for spatial variations in beam intensity and detector response, and ensuring a uniform background signal. Following correction, the empty-field image should display a stable and near-uniform intensity distribution, indicating that the detector response has been appropriately calibrated. Together, these steps ensure that projection images

make effective use of the available dynamic range while minimising noise and systematic artefacts, thereby improving the quality and quantitative reliability of the reconstructed dataset.

As the X-rays pass through the specimen, different internal structures within the sample absorb or scatter them to varying degrees depending on the material's density, composition, and the energy of the X-ray photons. Attenuation refers to the reduction in the number of X-ray photons as they pass through the material. This is caused by absorption and scattering within the sample. The attenuation of X-rays depends on both material properties and photon energy and can vary significantly at different X-ray energies. The attenuation of X-rays can be described by the following relationship:

$$I_1 = I_0 \times e^{-\mu x} \tag{2.3}$$

where I_1 is the transmitted intensity, or how much of that energy remains after the beam has passed through the object. This is the level of energy that reaches the detector. I_0 is the initial intensity of the X-ray beam before it enters the material. This depends on both the number of X-ray photons and how much energy each photon carries. Here, e is a constant, a number approximately equal to 2.718, that appears in equations describing how quantities gradually decrease, such as the attenuation of X-rays. μ is the linear attenuation coefficient, which indicates how strongly a material absorbs or scatters X-rays at a given photon energy. The value of μ is not fixed for a material but varies depending on the energy of the incident X-rays. Nonetheless, materials with higher density or atomic number, such as metals, usually have higher μ values. x is the thickness of the material along the path of the beam. This is the distance the X-rays travel within the material between entering and exiting it.

Because the X-ray beam is produced from a very small focal spot, it spreads out as it travels, forming a cone-shaped beam. This cone-beam geometry is inherent to micro-CT systems that use a point X-ray source. It allows the sample to be placed very close to the source, which increases

magnification and enables very small voxel sizes and high spatial resolution. However, because the beam diverges, only a limited field of view is available at high magnification, meaning that only relatively small samples – typically on the order of millimetres to a few centimetres in maximum size – can be imaged in a single scan. This cone-beam geometry means that the recorded projection images must be processed using reconstruction algorithms to accurately recover the internal 3D structure.

In addition to geometric effects, variation in the distance travelled by X-rays through the sample contributes to a phenomenon known as beam hardening. X-ray beams used in micro-CT contain a range of photon energies. As the beam passes through the specimen, lower-energy photons are absorbed more readily than higher-energy photons, so the beam becomes progressively ‘harder’ (higher in average energy). This causes non-linear attenuation, particularly in thicker regions of the sample, and leads to image artefacts. Two common examples of beam hardening artefacts are ‘cupping’ and ‘streaking’. Cupping occurs when the centre of a relatively uniform object appears artificially less dense (brighter) than the edges, giving a slightly hollowed appearance. Streaking appears as dark or bright lines across the image, often between dense regions, which can obscure internal features.

To reduce beam hardening effects, several approaches can be used. These include selecting an appropriate X-ray voltage to ensure sufficient penetration, using filters to remove low-energy photons, and applying correction algorithms during image reconstruction. These steps help improve image quality and ensure that the reconstructed data more accurately represent the internal structure of the sample.

Another common artefact in X-ray micro-CT imaging is the ring artefact, which appears as concentric circular patterns centred on the rotation axis. These arise from small variations in detector pixel response and are typically reduced through flat-field correction and reconstruction-based correction algorithms.

Before a sample can be scanned, the sample must be appropriately mounted. The medium in which the specimen is suspended influences how X-

rays are attenuated, and which internal features are best visualised. Biological samples are commonly imaged in ethanol or in air. Imaging in air maximises contrast between soft tissues and the surrounding space, particularly for visualising air-filled cavities. Imaging in ethanol helps preserve hydration and structural integrity, reducing the risk of tissue shrinkage or deformation. Regardless of the medium used, the specimen must be securely fixed, as even slight movement during scanning can compromise the dataset. This is especially important for high-resolution scans, which can take several hours. The orientation of the mounted sample also affects how close the X-ray source can be positioned, which in turn can influence the resolution of the scan.

2. Acquisition of 2D projection images

During scanning, the sample is incrementally rotated through either 180° or 360°, and a sequence of 2D X-ray projection images, also referred to as radiographs, is acquired from multiple angular positions. In most X-ray micro-CT systems, a rotation of 180° is sufficient to reconstruct the internal structure because projection data from opposite directions contain redundant information. This allows faster scans and reduces X-ray exposure to the sample. However, a full 360° rotation can be used to improve image quality in some cases, particularly for larger or more complex samples, as it provides additional data that can reduce noise and certain reconstruction artefacts. The choice between 180° and 360° therefore represents a trade-off between scan time and image quality.

Each projection image records the cumulative attenuation of X-rays through the sample from a specific direction, producing a shadow-like representation of the internal structure. Although these radiographs resemble conventional X-ray images in appearance, such as those used in chest radiography, their purpose in micro-CT is different. Rather than serving as final diagnostic images, they are collected from many angles and function solely as raw input for image reconstruction. The complete stack of projection radiographs constitutes the raw dataset exported from the scanner. This is the first dataset associated with this workflow.

3. Tomographic reconstruction

Projection images acquired from the scanner system are subsequently processed using reconstruction software. This reconstruction stage requires input from the researcher. Before initiating reconstruction, the user must adjust the grey value range, which is the range of pixel brightness values that represent X-ray attenuation within the sample. Setting this range is necessary for optimising image contrast and minimising artefacts, as it determines which intensity values are included in the final reconstruction.

Once configured, the reconstruction software applies a tomographic reconstruction algorithm, which combines attenuation data from all angular projections to generate a series of two-dimensional tomographic slices. Each slice corresponds to a true cross-sectional plane within the object and reveals internal features with high spatial fidelity. This process is referred to as computed (or computerised) tomography because the cross-sectional images are not directly measured but are mathematically reconstructed from multiple 2D projections using computer algorithms. The reconstructed tomographic cross-sectional images form the second dataset of this workflow.

Following reconstruction, an additional post-processing stage is often performed in which image filtering is applied to the reconstructed dataset, although no such filtering was applied in this study. These filters, such as Gaussian or median filters, are typically used to reduce noise, smooth artefacts (e.g., cupping, streaking, or ring artefacts), and enhance overall image quality, thereby improving segmentation of structures of interest.

4. 3D volumetric visualisation

Following reconstruction, the full stack of tomographic slices is compiled into a three-dimensional digital volume composed of voxels, which are small cubic elements that represent local X-ray attenuation values. This volume can be visualised and manipulated using software, such as Bruker's *CTVox*, that allows the user to rotate the dataset, inspect it from different angles, and generate virtual slices in any orientation. In contrast to conventional two-dimensional radiographs, which compress internal structures into a single

overlapping view, this three-dimensional dataset enables detailed and non-destructive examination of internal architecture with high resolution and contrast.

5. Segmentation and quantitative analysis

The final step in the workflow involves segmentation and quantitative analysis of specific structures within the reconstructed volume. Segmentation refers to the digital isolation of regions of interest (ROIs) based on differences in greyscale intensity or spatial boundaries. In this study, segmentation was conducted using Bruker *CTAn* as well as the open-source platform *3D Slicer*. Other commonly used software for segmentation and analysis includes *Amira* and *Avizo*, developed by Thermo Fisher Scientific, and *Dragonfly*, developed by Object Research Systems.

Once segmented, individual structures can be quantitatively analysed using three-dimensional quantitative analysis tools. Segmentation can be visualised in 3D, as for the original volumetric dataset, but with a key difference: whereas volumetric visualisation shows the full greyscale reconstruction, segmented datasets display only the isolated regions of interest. Moreover, these visualised segmentations are often colour-coded to distinguish between separate structures or to overlay analytical information, such as local thickness. A common approach during the segmentation process involves applying a greyscale threshold window to define a target range of attenuation values, followed by binarisation. This converts the selected voxels into a binary mask (included vs. excluded), resulting in a simplified 3D object. Unlike the original volume, which consists of millions of voxels with varying intensity values, segmented datasets are typically composed of solid, discrete blocks that are less memory-intensive and more suitable for targeted analysis.

This segmentation output constitutes the third and final dataset in the micro-CT workflow.

2.4.2 Specific X-ray Micro-CT Setup

The scans in this study were performed using a Bruker SkyScan 1172 X-ray micro-computed tomography scanner (Bruker, Kontich, Belgium), as shown in Figure 2.5A. The Bruker SkyScan 1172 is a desktop cone-beam micro-CT system comprising a sealed microfocus X-ray source, a digital detector, and a rotating specimen stage. Although the Bruker SkyScan 1172 is capable of higher operating currents, the specific system used in this study was limited to a tube voltage of 100 kV and a current of 100 µA, with a microfocus spot size of 5–8 µm. Projection images are acquired using this detector, whereby X-rays are converted into visible light via a scintillator and recorded as digital images (up to 4000 × 2300 pixels at the highest acquisition setting). This enables isotropic voxel sizes down to the submicron scale (typically 0.5–1 µm under high magnification conditions). The scanner accommodates samples up to 70 mm in height, with a field of view of 27–35 mm in standard mode and up to 68 mm using camera offset. The system is housed within a shielded cabinet measuring 130 cm × 69 cm × 39 cm and operates using a cone-beam geometry with a motorised stage for 180° or 360° rotation. Integrated software is provided for image acquisition (SkyScan 1172 control software), reconstruction (NRecon), segmentation and quantitative analysis (CTAn), and visualisation of 3D reconstructions (CTVox) (Bruker, SkyScan 1172 User Manual).

For clarity, the detector resolution (e.g. 4000 × 2300 pixels) refers to the number of pixels in each 2D projection image, whereas the voxel size (e.g. 0.55 µm) represents the physical dimensions of each element in the reconstructed 3D volume. While detector resolution defines the sampling of the projection data, the true spatial resolution of the system is influenced by additional factors such as the X-ray focal spot size and system geometry and is typically larger than the voxel size.

In this study, specimens were imaged in air. Prepared tibial samples (Section 2.2) were mounted vertically on a brass sample rod (Figure 2.5B). A small portion of the exocuticle immediately distal to the tibial section was embedded in a base of dental wax. In some cases, the wax base was

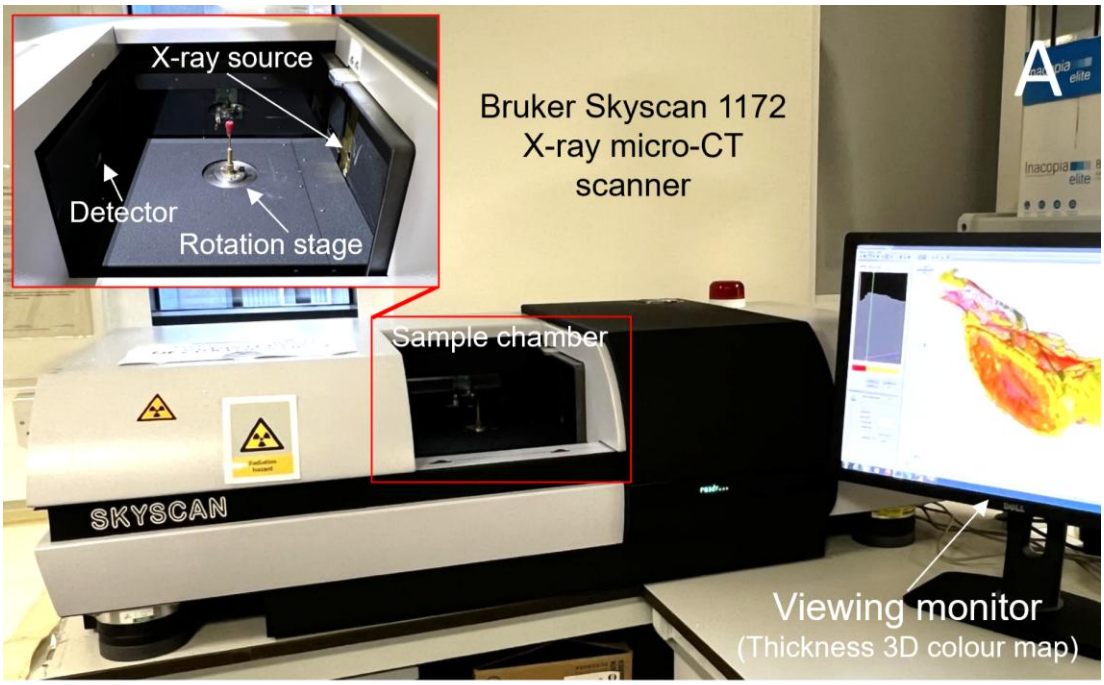

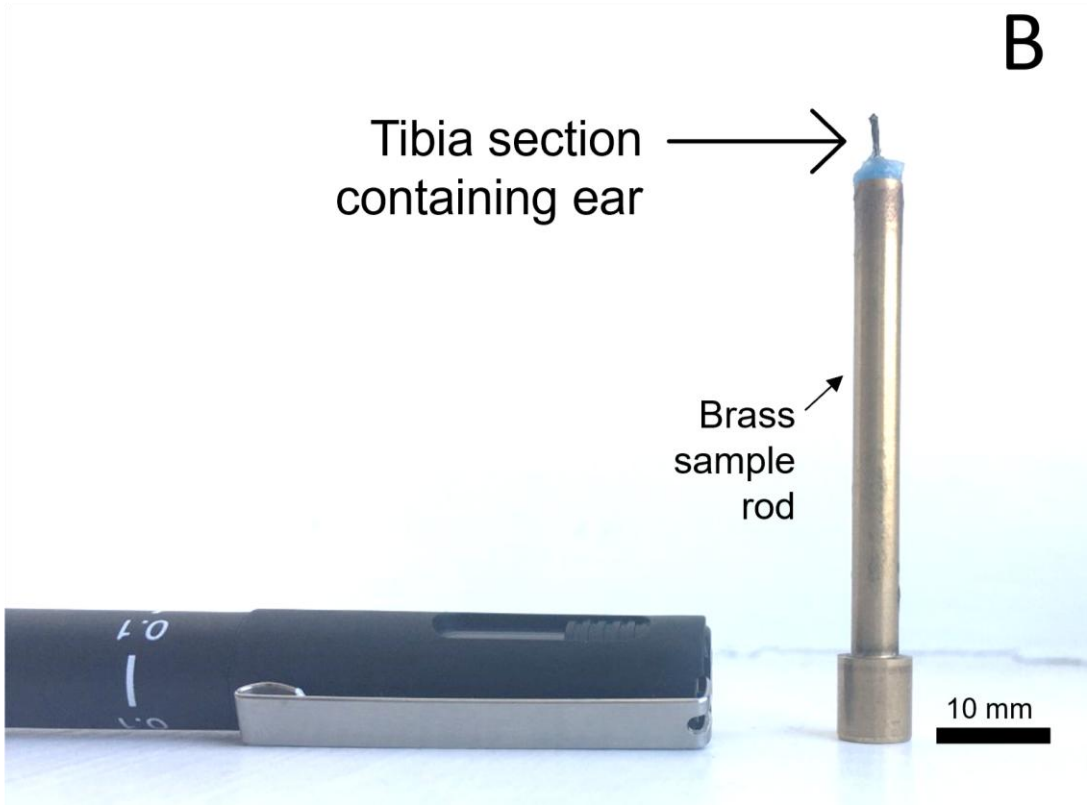

Figure 2.5 | X-ray micro-computed tomography (micro-CT) setup used in this study. To image Gryllinae 3D peripheral auditory anatomy, **(A)** the Bruker Skyscan 1172 scanner shown here was used. **(B)** Excised proximal section of a prothoracic *Gryllus bimaculatus* tibia following preparation. Sample is mounted with distal end up and secured below ear region with dental wax and adhesive. Pen for scale. *Scale bar:* 10 mm.

reinforced with a minimal application of cyanoacrylate adhesive (‘super glue’; LOCTITE®, Henkel Ltd., Hemel Hempstead, UK), with care taken to ensure that all auditory structures, especially the large tympanum, remained free from wax or glue.

All scans were performed with an exposure time of 1325 ms, 0.2° rotation steps over 180°, a frame averaging of 2, a current of 100 µA, and without a metal filter. Thickness measurements were obtained from 12 individuals (six female, six male) scanned with an X-ray tube voltage of 48 kV and an isotropic voxel size of 0.55 µm. Membrane and air column finite element models were derived from a single representative specimen (female), scanned at 30 kV and 0.88 µm voxel resolution. Projection images were reconstructed using Bruker NRecon version 1.6.9.18.

2.5 **Finite Element Analysis (FEA)**

Finite element analysis (FEA) is a computer-based process used to predict how a system behaves under conditions such as stress, heat, or vibration. It uses the finite element method, which is a mathematical approach that discretises a continuous system into smaller parts called elements to make the problem easier to solve. Finite element modelling is used to create a model that represents the real system – defining geometry, material properties, and boundary conditions – and FEA is then performed on this model to obtain results. In summary, *finite element analysis* refers to the overall computational process used to obtain solutions, the *finite element method* is the underlying mathematical technique that enables the analysis, and *finite element modelling* defines the system for analysis. In practice, however, FEA is commonly used as an umbrella term for the entire workflow, encompassing model definition, solution, and post-processing.

2.5.1 How does FEA work?

The FEA process consists of six key stages.

The first stage is (1) *discretisation*, in which the object under analysis is divided into many small, manageable sub-regions called elements. These

elements are connected at specific points known as nodes, forming a network referred to as a mesh. The mesh allows the complex geometry of the object to be represented as a collection of simpler parts.

The second stage is (2) *mathematical modelling*, where each element in the mesh is assigned physical properties that reflect the material and context. These might include properties such as stiffness, strength, or how well it conducts heat. The behaviour of each element is then described using mathematical relationships that represent how it responds to forces or other physical influences.

The third stage is (3) *assembly*, during which all the individual mathematical descriptions are combined to form a complete model of the entire structure. This step ensures that the interactions between elements are properly represented and that the model behaves as a single, continuous system. It also involves defining how different parts of the model connect or interact. Mating surfaces or contact conditions are introduced to describe these interactions – for example, whether parts are bonded, can slide, or may separate under load. Boundary conditions are also introduced at this stage in a general sense, to indicate how the model will be constrained and loaded.

The fourth stage is (4) *physics definition*, in which the governing physical laws and equations are specified for the problem. This includes selecting the appropriate physics (e.g., structural, thermal, or fluid behaviour) and fully defining the boundary conditions, such as supports, loads, or prescribed displacements. This step determines how the system behaves under given conditions and must be completed before the model can be solved.

In the fifth stage, (5) *solving*, the computer calculates the results based on the assembled model. It determines important quantities, such as how much the object bends, where stress is concentrated, or how heat flows through the material. These calculations provide a detailed picture of how the structure responds under specific conditions.

Finally, (6) *post-processing* involves visualising and interpreting the results. This usually includes graphical outputs such as colour-coded images

showing areas of high stress, deformation, temperature, or indeed acoustic vibration. These visualisations allow engineers to assess design performance and identify potential weaknesses or failure points. In biological contexts, they can help researchers better understand the biomechanics of the system under study.

2.5.2 Specific FEA Setup

In this study, FEA data were extracted from three distinct models: (1) a simplified simulation that was designed to test the influence of coupling on PTM vibrations (Figure 4.9); (2) the principal FEA model of this research, of the PTM and tracheal branches, constructed from simplified X-ray micro-CT tracings, which produced the majority of the FEA results presented in this work (Figures 4.7–12); and (3) a segmented mesh of the internal airspace, derived directly from X-ray micro-CT data, used to investigate the resonance properties of the air cavity inside the tracheal branches (Figure 4.13).

All three of these FEA models were simulated using the software COMSOL Multiphysics® (version 6.1). This COMSOL platform is particularly effective for modelling systems where multiple physical effects influence one another. This makes the FEA software used in this study especially suitable for the simulation of complex biological systems.

2.6 **Data Analysis**

For Gryllinae biomechanics, most statistical analyses were performed using the software *R*. See Section 4.2.3 for an exact description of the statistical methods used for the X-ray micro-CT 3D thickness comparisons (corresponding to Figure 4.8). For vibrometry recordings (Chapter 3), specifically those from automated multipoint data points under frequency sweeps, only those data values with above 85% coherence were subsequently kept for analysis. Frequency response functions (FRFs) were smoothed by a moving average filter of five frequency bins.

2.6.1 Standard Deviation vs. Standard Error of the Mean

Standard deviation (SD) describes how spread-out individual measurements are around the mean. It reflects the variability between data points or individuals. In contrast, the standard error of the mean (SEM) describes how precisely the mean has been estimated. It decreases as more measurements are included and reflects confidence in the mean, rather than the spread of the data. SEM is calculated from the SD and the number of observations (n), such that it becomes smaller as sample size increases (i.e. by dividing the SD by the square root of n), whereas SD itself reflects only the spread of the data and does not decrease simply with increasing sample number.

Both SD and SEM are used in this research project. SD is appropriate for datasets where the aim is to represent biological or experimental variability between measurements, while SEM is appropriate for datasets where the aim is to represent the precision of an averaged response.

Where data points were manually collected and relatively sparse, the primary question is how much variability exists between individuals. SD was used for two figures in this project: one pertaining to LDV (Figure 3.2) and one pertaining to X-ray micro-CT (Figure 4.8). In Figure 3.2, pure-tone LDV measurements were *manually* recorded at relatively coarse frequency intervals (200–1000 Hz) and from a relatively small number of individuals (n=10), meaning the variation primarily reflects between-individual differences; SD is therefore an appropriate measure. Similarly, the X-ray micro-CT thickness data underlying Figure 4.8 consist of only one measurement per structure per individual (and only n=12); the spread largely reflects biological differences between specimens and therefore SD is also appropriate here.

SEM was used in this project only for the automatically collected frequency sweep LDV data (Figures 3.3–3.5), which were acquired across dense frequency bins (11.25 Hz resolution) and many spatial points across each tympanum. These datasets comprise many measurements per individual, with signal averaging applied per measurement point during the data acquisition. As a result, the mean response from these datasets

represents a *well-sampled* reflection of the system's behaviour, and SEM is therefore an appropriate measure to indicate the *precision* of this mean.

2.7 **Ormiini Methods**

The following section outlines the methodology used to investigate larval development of *Ormia ochracea* in the *Acheta domesticus* (Gryllinae) host.

2.7.1 Animals, Morphometrics, Infestation, and Data Analysis

Recently moulted adult *Acheta domesticus* (4–6 days post final moult) were acquired from a supplier (Bug Co., Ham Lake, Minnesota). A total of 600 crickets (300 males and 300 females) were used as host crickets for this study. Ten gravid female *Ormia ochracea* from a laboratory colony that originated from Gainesville, Florida, USA were used as larval donors.

Along with host cricket sex and larval load (competition level), we recorded morphometric traits across life stages: pronotum width, pronotum length, and hind femur length for crickets; width and length for pupae; and mesothorax length for eclosed (hatched) first-generation F1 flies. Host cricket body mass was also recorded.

O. ochracea can be propagated in the laboratory using a manual infestation procedure described by Vincent and Bertram [162]. Manual parasitisations are performed by extracting larvae from freshly dispatched donor flies. This involves dissecting the fly's abdomen and spreading the larvae from its reproductive tract onto a petri dish lined with filter paper. Freshly extracted larvae move actively, often standing on their posterior ends and waving their anterior ends. On damp filter paper, larvae remain highly active for the first two hours after removal but can survive for up to 7–8 hours [163]. In this state, larvae readily attach to a wooden probe. Once attached, they are placed on the cricket's articular sclerites, an area of soft tissue between the pronotum and thorax. For further information, including the exact numbers of crickets and flies used per treatment, see Section 5.2.3.

Statistical analyses were performed in *R* to examine factors influencing pupation and eclosion success in flies. Generalised linear mixed-effects

models (GLMMs) assessed the impact of host traits (sex, structural size, mass) and larval number, with donor ID as a random effect. Pupation and eclosion success were defined using absolute and proportional measures. Correlations among host morphological traits were analysed using Spearman's rank correlation, a statistical measure that assesses how strongly and consistently two variables are related based on the order (rank) of their values rather than their exact numerical differences, indicating whether higher values of one variable tend to correspond to higher (or lower) values of the other, due to non-normality, revealing strong associations among size metrics and prompting the use of pronotum length to avoid multicollinearity. Linear and logistic regressions explored how host traits and resource competition influenced pupal and adult fly size, and their relationship to eclosion success. For a more detailed description, refer to Section 5.2.4.

Chapter 3

The Frequency Filtering Profile of the Posterior Tympanum

The Gryllinae auditory pathway is sharply tuned to the male calling song carrier frequency at both the neural and behavioural levels, but the biomechanical basis of this filtering remains unclear. At the start of this auditory pathway is the posterior tympanum (PTM), which functions as the first link in the path of transmission to the sensilla [5, 7, 14, 26] and contributes, at least in part, to frequency filtering [7-9, 12, 26, 72, 73, 115]. Any attempt to understand filtering and transmission in the Gryllinae acoustical system must therefore understand the vibrational profile of the PTM. Yet the exact vibrational profile of the PTM is in dispute.

Accordingly, this chapter addresses Aim 1 of the present study: to resolve the vibrational tuning profile of the field cricket posterior tympanum. To investigate this, a pioneering laser Doppler vibrometry (LDV) protocol was developed, comprising three sets of experiments conducted under different acoustic stimuli.

The LDV findings presented here are shared in the 2024 peer-reviewed publication by Latham et al. [1] in the *Journal of the Royal Society Interface* (Appendix C).

3.1 **The Unresolved Filtering Profile**

Frequency selectivity of the Gryllinae auditory pathway is established at the neurophysiological and behavioural levels (Sections 1.12.1–2), showing sharp tuning to the conspecific carrier frequency (CF) (4.7 kHz in *Gryllus bimaculatus* and 4.0 kHz in *Teleogryllus commodus* [111]).

As the first mechanical interface between airborne sound and the auditory system, the PTM is expected to influence both the transmission and spectral filtering of acoustic signals before they reach the sensory neurons. Its vibrational tuning profile is therefore likely to play a central role in determining the frequency selectivity observed in the downstream stages of processing. For the PTM to fully account for the observed neurophysiology and behaviour, it would be expected to respond with a sharp vibrational peak at the calling song CF, while also effectively discriminating spectra associated with the courtship song [16] and ultrasonic predatory calls [89].

Such a role has been claimed for the PTM, suggesting that its vibrational response sufficiently matches the downstream filtering [11, 71, 72, 115]. In contrast, other studies have argued that the PTM alone cannot fully account for mechanical frequency filtering in the Gryllinae ear [7, 8, 10, 12, 26, 27].

Studies conducted over several decades measuring the vibrational response of the field cricket posterior tympanum have produced seemingly conflicting reports. Some indicate a sharply tuned PTM vibrational profile that matches the calling song CF and that may be sufficient to explain the selectivity in receptor neurons [11, 71, 72, 115]. Others describe a 4–5 kHz PTM tuning that is nonetheless too broad to match the neural tuning data [7, 26, 73]. While the most recent studies report broad tuning with vibrational optima shifted to higher frequencies, above the calling song CF altogether [12, 27]. In some cases, a single principal vibrational peak is reported [7, 12, 27, 115]; in others, two distinct vibrational optima are presented [9, 26, 71]. Furthermore, in studies that do report a mismatch between PTM tuning and the known neural and behavioural data, many have hypothesised the existence of a 'second

filter' located downstream of the tympanum [8, 10, 12, 26], a mechanical filter that has nonetheless remained unidentified.

3.2 **Results: PTM Vibrational Profile Revealed by LDV**

Frequency sweeps from the cone loudspeaker (Figure 3.1A) produced a relatively stable but non-linear output across the 2–20 kHz range. Sound pressure oscillated within a band of approximately 50–60 dB across the spectrum, indicating frequency-dependent variation but overall robust performance. In contrast, the ribbon loudspeaker (Figure 3.1B) exhibited substantially greater variability and a clear decline in output with increasing frequency. Sound pressure decreased from approximately 55 dB at low frequencies to around 35 dB beyond 14 kHz, representing an approximate 20 dB drop. This corresponds to a much larger reduction in sound intensity, approximately 100-fold, compared to the roughly 10-fold variation observed across the 10 dB range for the cone loudspeaker (Figure 3.1A). Thus, the ribbon loudspeaker was more variable and substantially less performant.

3.2.1 Vibrational Velocities: Pure-Tone Stimulation via Cone Loudspeaker (Spiracles Open)

Under the first set of LDV experiments, where 78 dB SPL pure-tone stimuli were presented to *Gryllus bimaculatus* (n=10), vibrational velocity measurements taken from the centre of the posterior tympanal membrane revealed a consistent pattern with two prominent peaks in the frequency response, as demonstrated in Figure 3.2.

The first peak occurred at a mean frequency position of 5.6 kHz, where the average vibrational velocity reached 112 μm/s. This peak was highly consistent across individuals, with frequencies ranging from 5.4–6.0 kHz. The standard deviation bars around this point were relatively small, indicating low variability in both the frequency position and amplitude of the response.

The second peak occurred at a mean frequency of 13.8 kHz, where the PTM reached a higher average velocity of 186 μm/s. This peak was more variable across individuals, with frequency positions ranging from 12.2 to 16.0

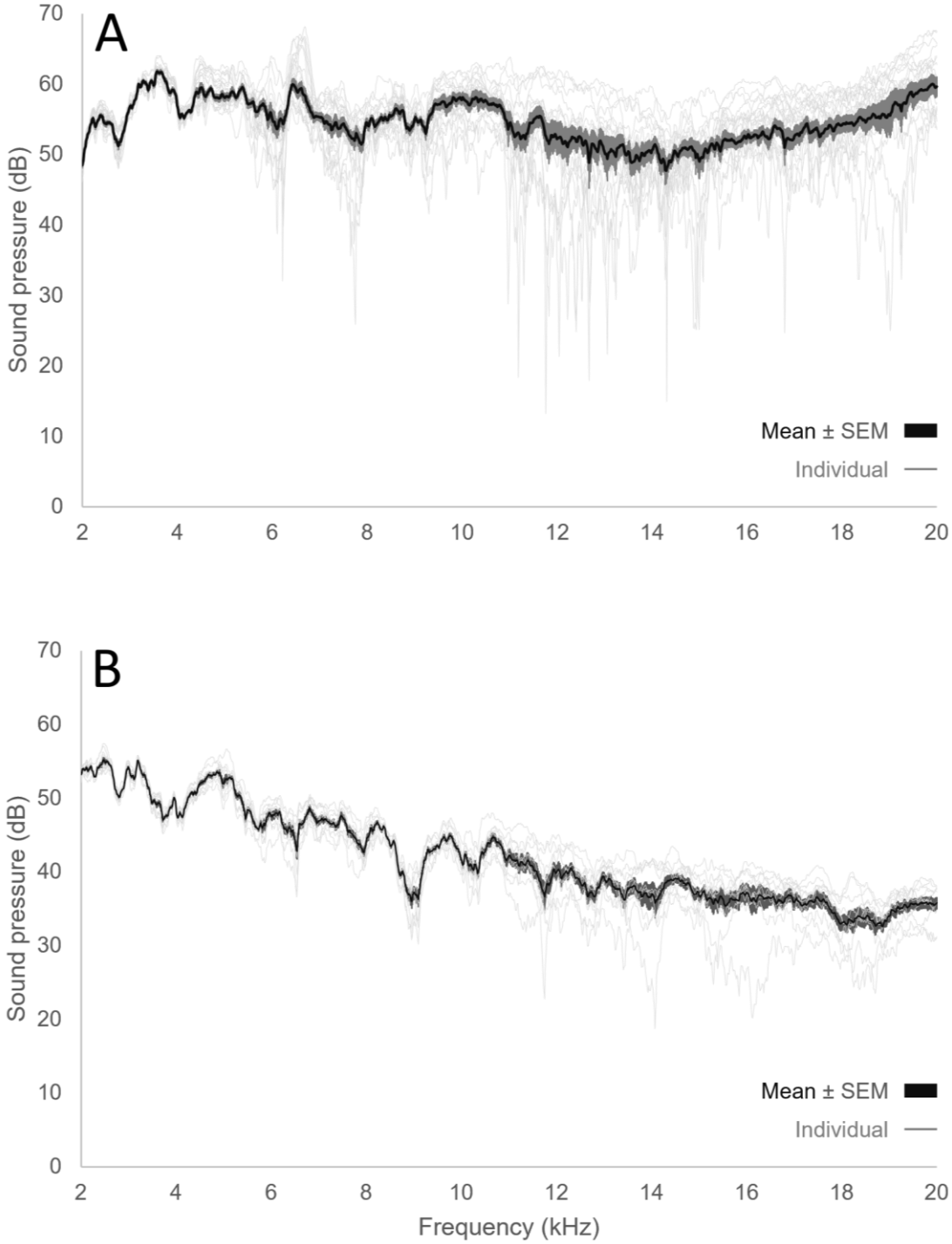

Figure 3.1 | Divergent frequency responses of cone and ribbon loudspeakers. Sound pressure levels (SPLs) across 2–20 kHz for **(A)** frequency sweeps delivered via a 5.8 cm diameter cone diaphragm loudspeaker (spiracles open; n=20) and **(B)** frequency sweeps delivered via a ribbon diaphragm air motion transformer (AMT) loudspeaker (spiracles open, n=10; closed, n=10). In both panels, thin light-grey lines show individual measurements, and the bold black line indicates the mean ± standard error.

kHz. The standard deviation in this range was larger than that around the first peak, indicating greater spread in both frequency and amplitude between individuals.

A third peak near 18 kHz can be seen in the mean velocity trace; however, this feature is not considered a true vibrational optimum. The associated standard deviation is more than twice that of the preceding peaks (Figure 3.2), and inspection of individual traces reveals that this feature is driven by an extreme response in a single individual, with most individuals showing no discernible peak in this region. This outlier disproportionately elevates both the mean and variability and is not representative of the overall response. The feature at 18 kHz is therefore unlikely to reflect a consistent response of the PTM and likely arises from experimental artefact.

Between the first and second peaks, there was a reduction in vibrational velocity between approximately 6.5 and 10 kHz. This region appears as a trough in the mean trace. However, care is needed when interpreting the shape and detail of this part of the spectrum. Unlike the peak regions, which were sampled in finer frequency steps of 200 Hz, this middle-frequency range was measured in 1000 Hz increments.

In summary, vibrational velocity responses of the PTM under 78 dB pure-tone stimulation showed two clear and repeatable peaks (Figure 3.2). The first peak, a lower-frequency peak at 5.6 kHz with a mean velocity of 112 μm/s, was consistent across individuals. The second peak, at 13.8 kHz with a higher mean velocity of 186 μm/s, was more variable (Figure 3.2).

The yellow and green shaded regions in Figure 3.2 indicate the inter-individual frequency ranges of the first (driving-force) and second (natural resonance) vibrational peaks, respectively, derived from phase-response measurements under sweep (cone loudspeaker) stimulation (Figure 3.3B,C; n=20). The second peak exhibited greater variability in frequency position across individuals. Although derived from a separate experimental condition, these ranges are shown here to facilitate comparison across LDV datasets. Equivalent ranges for *T. commodus* are shown in Figure 3.4.

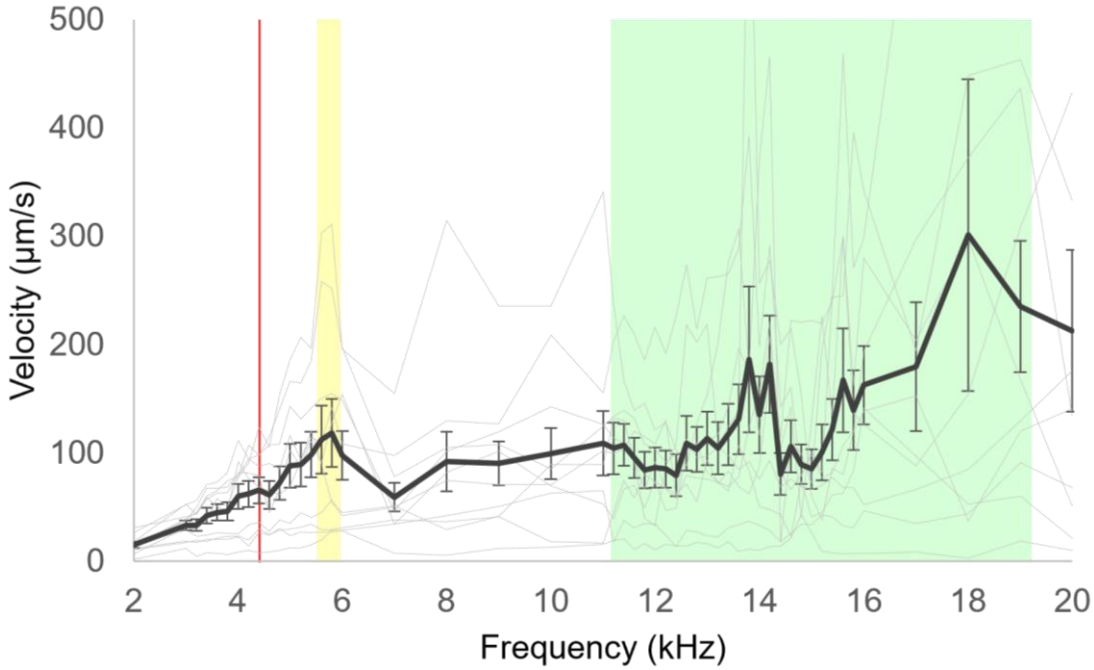

Figure 3.2 | Posterior tympanal membrane exhibits two distinct vibrational peaks under pure-tone stimulation. Vibrational velocity of the *Gryllus bimaculatus* posterior tympanal membrane (PTM), measured at the centre of the membrane, in response to 78 dB SPL pure-tone stimuli delivered via a 5.8 cm cone diaphragm loudspeaker (spiracles open; n=10). Two vibrational peaks are observed at approximately 5.8 kHz and 13.8 kHz. Thin grey traces represent individual measurements, while the thick black line denotes the mean ± standard deviation. Yellow and green shaded regions indicate the frequency ranges of the first and second peaks, respectively, derived from tympanal phase responses measured under cone loudspeaker sweep conditions (n=20); each shaded region spans the range of peak frequencies observed across individuals. Between 3–6 kHz and 11–16 kHz, the PTM was sampled at 200 Hz intervals, corresponding to the carrier frequency ranges of calling and courtship songs, respectively; all other regions were sampled at 1000 Hz intervals to optimise experimental duration. The red vertical line marks the conspecific carrier frequency at 4.7 kHz.

3.2.2 Vibrational Velocities: Frequency Sweeps via Cone Loudspeaker (Spiracles Open)

The same cone-diaphragm loudspeaker used for pure-tones was used to provide frequency sweeps with automated multipoint recordings across the tympanum. The vibrational amplitude of the PTM was measured in 20 *G. bimaculatus* individuals (Figure 3.3A).

The vibrational velocities normalised to sound pressure (Frequency Response Function, FRF) traces for *G. bimaculatus* reveal a consistent response profile with two distinct peaks in the averaged curve (Figure 3.3A). The first peak occurs at a mean frequency of 6.0 kHz, with a mean-average velocity of 963 μm/s Pa. This peak is associated with a pronounced elevation in FRF amplitude and is relatively narrow and consistent across individuals, as indicated by the narrow band showing the standard error of the mean (SEM) around the mean (thick black line) trace.

The second peak is observed at a mean frequency of 14.3 kHz, where the mean-average FRF velocity reaches 1631 μm/s/Pa. The SEM band in this region is somewhat wider than at the first peak, suggesting greater spread in both frequency position and amplitude among the 20 specimens.

FRF amplitude is highest at 18 kHz. However, this feature is broad and inconsistent across individuals. The SEM in this region is among the widest in the dataset, and the shape of the elevation lacks the sharpness or repeatability seen at the principal two peaks. For these reasons, this feature is not identified as a third distinct peak.

In addition to the two peaks at 6.0 and 14.3 kHz, several other potential subpeaks appear throughout the frequency response. One such elevation is seen near 4.2 kHz, which presents as a small but relatively consistent rise preceding the 6.0 kHz maximum. Further possible subpeaks are evident near 7.9 kHz and 11.2 kHz.

Frequency sweep stimuli from the same cone-diaphragm loudspeaker were also applied to the control species *Teleogryllus commodus*. The mean (n=6) vibrational response for this species is presented in Figure 3.4A.

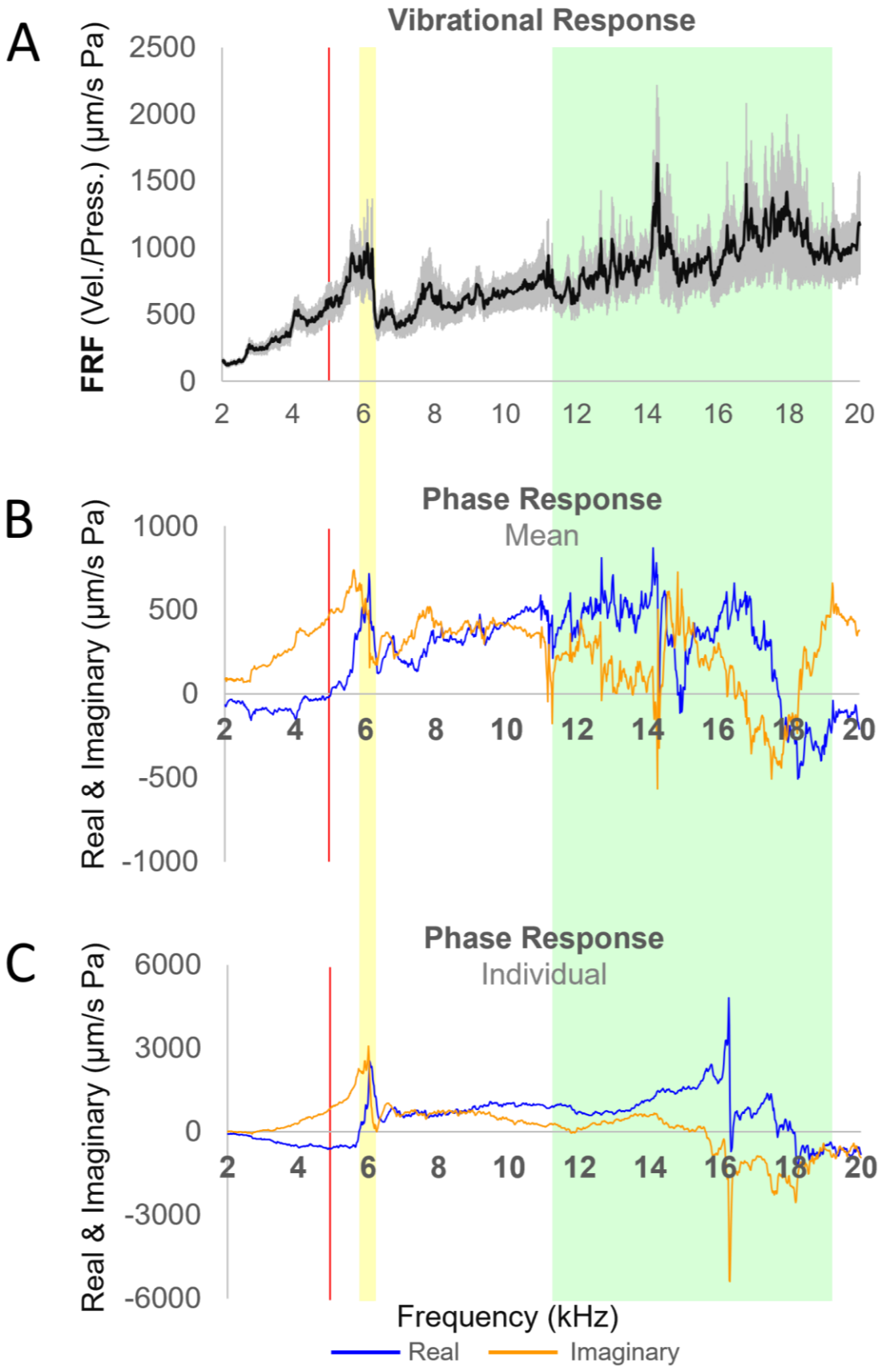
A
Vibrational Response
FRF (Vel./Press.) (µm/s Pa)
2500
2000
1500
1000
500
0
2
4
6
8
10
12
14
16
18
20
B
Phase Response
Mean
Real & Imaginary (µm/s Pa)
1000
500
0
-500
-1000
C
Phase Response
Individual
Real & Imaginary (µm/s Pa)
6000
3000
0
-3000
-6000
Frequency (kHz)
Real
Imaginary

Figure 3.3 | Posterior tympanum exhibits a low-frequency driven peak and a high-frequency natural resonance. In **(A)**, frequency response function (FRF) shows vibrational velocity of the posterior tympanal membrane in *Gryllus bimaculatus*, normalised to sound pressure, in response to sweep stimuli delivered via a 5.8 cm cone diaphragm loudspeaker. Two velocity peaks are observed around 6.0 kHz and 14.3 kHz. The thick black line shows the mean response (n=20), and the shaded area indicates ± standard error. **(B)** Mean real and imaginary components (representing phase information) from the same 20 individuals, revealing a driven peak near 6.0 kHz and a natural resonance near 14.3 kHz. **(C)** Real and imaginary components of the response from a representative individual, demonstrating a clear driven peak at 6.0 kHz and a natural resonance at 16.2 kHz. **(A–C)** All responses are recorded at a representative point near the centre of the tympanum, chosen from a spatial mesh. Yellow and green shaded bands indicate the frequency ranges of observed driven and natural resonance peaks, respectively. The red vertical line marks the conspecific calling frequency at 4.7 kHz.

The FRF traces from *T. commodus* also show two clear peaks (Figure 3.4A). The first at 6.4 kHz, and the second at 12.2 kHz. One of the possible subpeaks in the *T. commodus* mean-average trace at 4.0 kHz exactly matches the conspecific calling song frequency (vertical red line).

In contrast to *G. bimaculatus*, a third distinct peak is also observed in *T. commodus* at 18.7 kHz (Figure 3.4A). This feature is considered a distinct peak, because it does appear as a sharp and repeatable elevation in the mean FRF trace, accompanied by a relatively narrow SEM range.

3.2.3 Phase Responses: Frequency Sweeps via Cone Loudspeaker (Spiracles Open)

In this study, phase is not expressed directly in degrees or radians. Instead, the LDV responses are presented as two components, referred to as the real and imaginary. Together, these describe both how much the membrane moves and how its motion is timed relative to the acoustic stimulus. The real component corresponds to membrane motion that is in phase with the reference signal, while the imaginary component represents motion that is

shifted by a quarter of a cycle (90°) with respect to that reference. As outlined in Section 2.3.3, the way these components change with frequency allows a clear distinction between responses driven directly by the stimulus and motion arising from the membrane's natural resonance.

PTM phase responses revealed that, at the 6 kHz vibrational peak (Figures 3.2–3.3A), the tympanum was oscillating in-phase relative to the wavefront of the stimulus. This can be seen in Figure 3.3B (mean, n=20) as the real and imaginary plots (blue and orange, respectively) trending together at the 6 kHz position.

An in-phase response is characteristic of a resonant system which remains dominated by its mass momentum below its natural resonance peak. This means that whatever was generating the PTM peak at 6 kHz was a *driving-force* external to the tympanum itself.

The position of this driving-force matches well with the PTM vibrations from both pure tone and sweep cone-diaphragm stimuli, as highlighted by the yellow band (Figures 3.2–3). The width of the yellow highlight corresponds to the 5.9–6.2 kHz range in identified driving-force position across the 20 individuals, with the mean-average trace displayed in Figure 3.3B.

In contrast, at the second vibration peak near 14 kHz (Figures 3.2–3.3A), the phase of the membrane sharply diverges. This is seen in Figure 3.3B (mean, n=20) as the blue and orange plots trending *away* from each other at the 14 kHz position. This out-of-phase response is characteristic of the *natural resonance* of a membrane, wherein the motion of the membrane is governed by its own mass–stiffness properties and therefore lags relative to the stimulus phase.

The position of the PTM natural resonance is highlighted by the green band. The considerable width of the green-shaded band corresponds to the 11.2–19.3 kHz variability between individuals (n=20), with the mean-average shown in Figure 3.3B.

As an example from a single representative specimen, the results shown in Panel C of Figure 3.3 exhibit a PTM driving resonance at

approximately the 5.9 kHz position. The natural resonance of the posterior tympanum for this individual was at approximately 16.2 kHz (Figure 3.3C).

Figure 3.4B reveals the phase response of the *T. commodus* posterior tympanum (mean, n=6). The results here likewise indicate that peak–1 at 6.4 kHz, in the amplitude traces (Panel A of Figure 3.4), is a *driving-force* peak. While peak–2 at 12.2 kHz is the *natural resonance* of the *T. commodus* PTM.

The presence of an 18.7 kHz peak in the *T. commodus* vibrational data (Figure 3.4A) is further supported by the phase response (Figure 3.4B), which shows a discrete transition in phase lag at this third frequency position, consistent with a distinct resonance. This 18.7 kHz frequency position corresponds to a possible second-order rolling mode of the *T. commodus* tympanal membrane, as seen in online supplementary material in [1]. At lower frequencies, the tympanum oscillates in a uniform drum-like mode, with the membrane moving largely in phase across its surface. As frequency increases, it becomes energetically favourable for the membrane to deform rather than move as a single unit, giving rise to higher-order vibrational modes in which different regions move out of phase with one another, producing more complex spatial patterns of motion. This behaviour was observed only in the control species; however, given that the vibrational optima in *T. commodus* are consistently shifted relative to those of *G. bimaculatus*, it is conceivable that a comparable higher-order mode may occur in *G. bimaculatus* at frequencies beyond the 20 kHz range examined here.

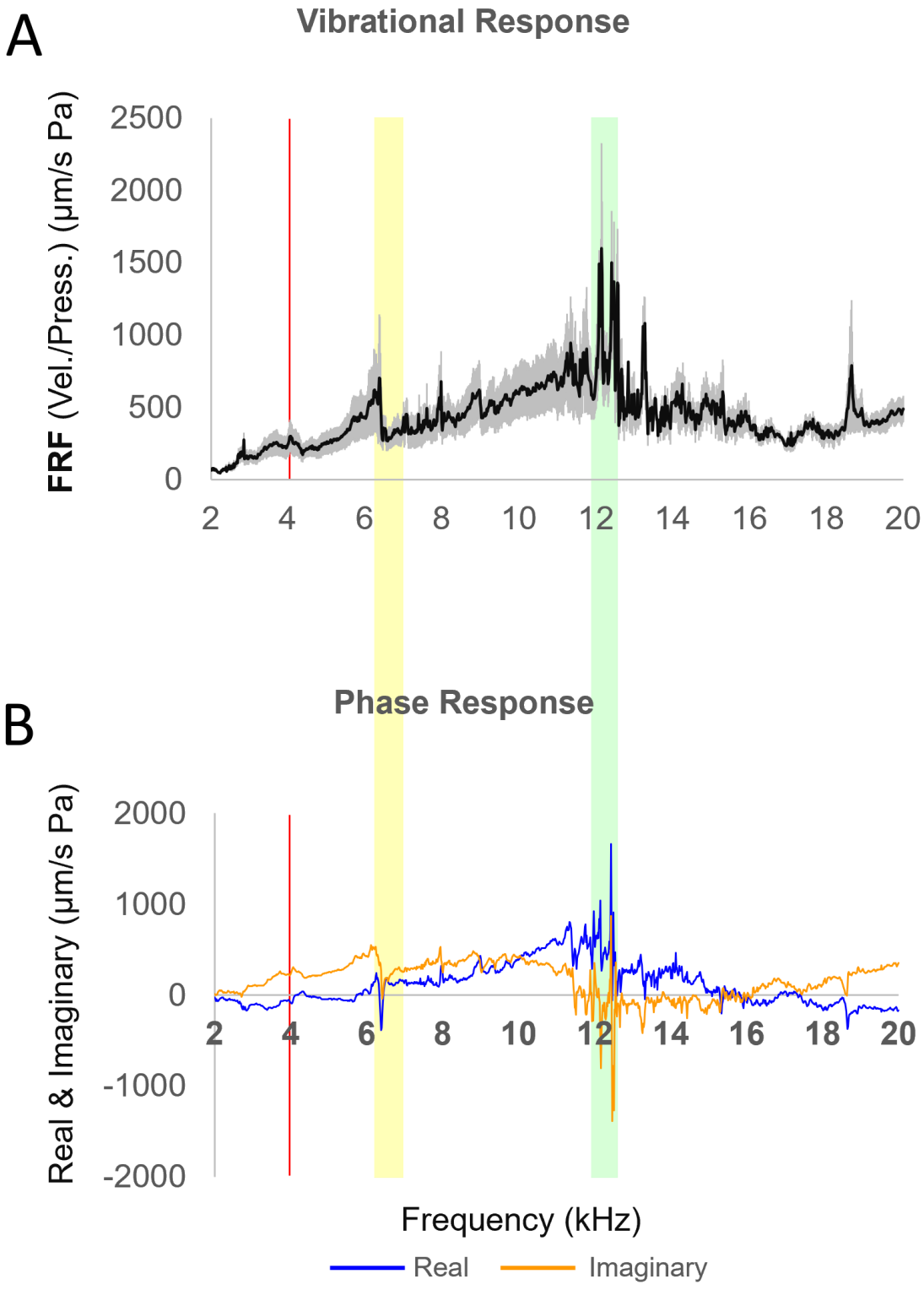
A
Vibrational Response
FRF (Vel./Press.) (µm/s Pa)
2500
2000
1500
1000
500
0
2
4
6
8
10
12
14
16
18
20
B
Phase Response
Real & Imaginary (µm/s Pa)
2000
1000
0
-1000
-2000
2
4
6
8
10
12
14
16
18
20
Frequency (kHz)
Real
Imaginary

Figure 3.4 | Control species shows driven and natural resonance peaks in posterior tympanal response. In **(A)**, frequency response function (FRF) shows vibrational velocity of the posterior tympanal membrane in *Teleogryllus commodus*, normalised to sound pressure, in response to sweep stimuli delivered via a 5.8 cm cone diaphragm loudspeaker. Two principal velocity peaks are observed around 6.4 kHz and 12.3 kHz, with an additional peak at 18.7 kHz. The thick black line shows the mean response (n=6), and the shaded area indicates ± standard error. **(B)** Mean real and imaginary components (representing phase information) from the same 6 individuals, revealing a driving-force peak near 6.4 kHz and a natural resonances near 12.3 kHz. **(A,B)** All responses are recorded at a representative point near the centre of the tympanal membrane, chosen from a spatial mesh. Yellow and green shaded bands indicate the frequency ranges of observed driving and primary natural resonance peaks, respectively. The red vertical line marks the conspecific calling frequency at 4.0 kHz.

3.2.4 Effect of Spiracle Closure and Ribbon Loudspeaker

To investigate whether internal acoustic transmission via the auditory spiracles could be causing the 6 kHz driving force peak, rather than any second resonator, responses were recorded under frequency sweeps from a ribbon-diaphragm loudspeaker with spiracles either open or sealed, the results from which are presented in Figure 3.5. The resulting tympanal velocity responses are shown in Panel A of Figure 3.5, while the corresponding phase response from a single individual with sealed spiracles is shown in Figure 3.5B.

In Figure 3.5A, both the black and orange traces show the mean average velocity of the posterior tympanum across individuals (n=10 per treatment). SEM shading is included only for the black trace, representing the open spiracle group. For the orange trace (spiracles sealed), SEM has been omitted to aid visual readability.

The teal-coloured AMT loudspeaker output in Figure 3.5A aids in interpreting the tympanal response and confirms the loudspeaker output was not spectrally flat. This variability in the loudspeaker output may have influenced the recorded tympanal response.

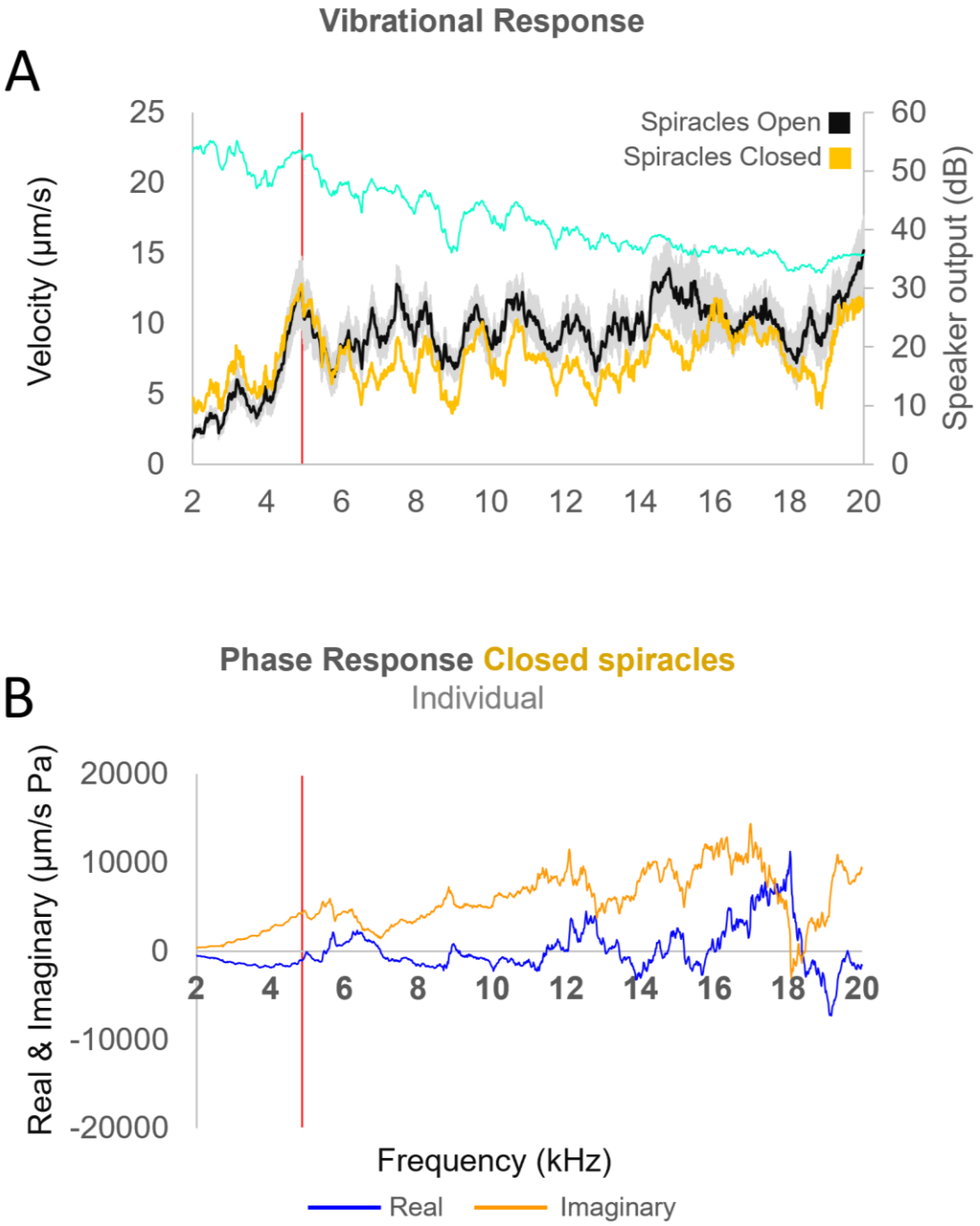
A
Vibrational Response
Spiracles Open
Spiracles Closed
Velocity (µm/s)
Speaker output (dB)
25
20
15
10
5
0
60
50
40
30
20
10
0
2
4
6
8
10
12
14
16
18
20
B
Phase Response Closed spiracles
Individual
Real & Imaginary (µm/s Pa)
20000
10000
0
-10000
-20000
Frequency (kHz)
Real
Imaginary

Figure 3.5 | Spiracle closure experiments yield inconclusive posterior tympanal responses due to variability in stimulus output. (A) Vibrational velocity of the posterior tympanal membrane (PTM) in *Gryllus bimaculatus* in response to frequency sweep stimuli delivered via an air motion transformer (AMT) ribbon diaphragm loudspeaker. Responses are shown for crickets with spiracles open (black trace, n=10) and spiracles sealed (orange trace, n=10). Traces represent mean responses; shaded area denotes ± standard error of the mean (SEM) for the open-spiracle condition. Loudspeaker output is shown in teal, showing substantial variability across frequency that is reflected in the tympanal responses and limits interpretation. **(B)** Real and imaginary components of the phase response from a representative individual with spiracles sealed. Despite noise in the velocity data, the phase response shows a pattern near 6.0 kHz consistent with a driven response. The red vertical line marks the conspecific calling frequency at 4.7 kHz.

From these third set of experiments, it appears that the posterior tympanum vibrated with a distinct peak at 4.8 kHz, which matches exactly the carrier frequency of the male calling song (vertical red line) (Figure 3.5A). This peak was consistent across both experimental groups, appearing whether the auditory spiracles were open (black) or sealed closed (orange). However, the 4.8 kHz feature also coincides with a corresponding peak in the AMT loudspeaker output (see teal trace, Figure 3.5A), indicating it likely reflects a feature of the stimulus spectrum rather than a valid vibrational response of the tympanum.

Yet, despite the noise, the corresponding phase data from a single individual (Figure 3.5B) suggests a maintained 6 kHz driving force after the spiracles had been blocked. The real and imaginary components in this individual's response show a broadly in-sync phase response around 6 kHz, suggesting that blocking the spiracles does not shift the position of this feature. However, given the overall noise in the dataset, this observation is retained only as an indication, with the primary identification of the 6 kHz driving response based on the more reliable cone loudspeaker data, where this feature is more clearly defined.

Both traces (closed and open) appear much aligned (Figure 3.5A), and so a conclusion might be that the closing of the spiracles had no effect on the tympanal response.

However, the overall velocity data in Figure 3.5A were considered too noisy to support any confident interpretation. The noise observed in the data is likely due to the fluctuating loudspeaker output (teal). Indeed, the vibrational responses of the tympana (Figure 3.5A) follow the pattern output of the AMT loudspeaker (teal). For example, the peak at around the 5 kHz position directly corresponds with a peak in the loudspeaker output (teal) and is therefore likely an artefact.

As such, the effect of closing the spiracles on the maintenance or otherwise of the 6 kHz driving resonance was largely determined from literature data, as discussed in Section 3.3.

3.2.5 3D Spatial Distribution of Tympanal Movement

Rather than being a product of either an external resonator or internal spiracular transmission, conceivably the driving-force peak at 6 kHz (Figures 3.2–3.3A) may have arisen from the modal shape of the tympanum itself. That is, from the three-dimensional spatial pattern of its surface-motion at different frequencies. Were the tympanum to vibrate with a simple up-down drum mode at all frequencies, including at both the 6 kHz and 14 kHz positions shown in Figures 3.2–3.3A, then it would be physically impossible for both peaks to be associated with the natural resonance of the membrane [160]. In other words, under a consistent up-down drum mode, the identified 6 kHz peak could not be explained as a consequence of modal effects in the way the tympanum moved at that stimulus frequency.

The PTM oscillated with a fundamental drum mode across the 2–20 kHz frequency spectrum (Figure 3.6). This was revealed by mapping the maximal vibrational velocity of each of the approximately 100 scan points obtained from across the tympanal surface in the 20 specimens recorded under from second set of experiments (sweeps, open spiracles, cone loudspeaker). The spatial velocity maps corresponding to the frequency positions of the two identified

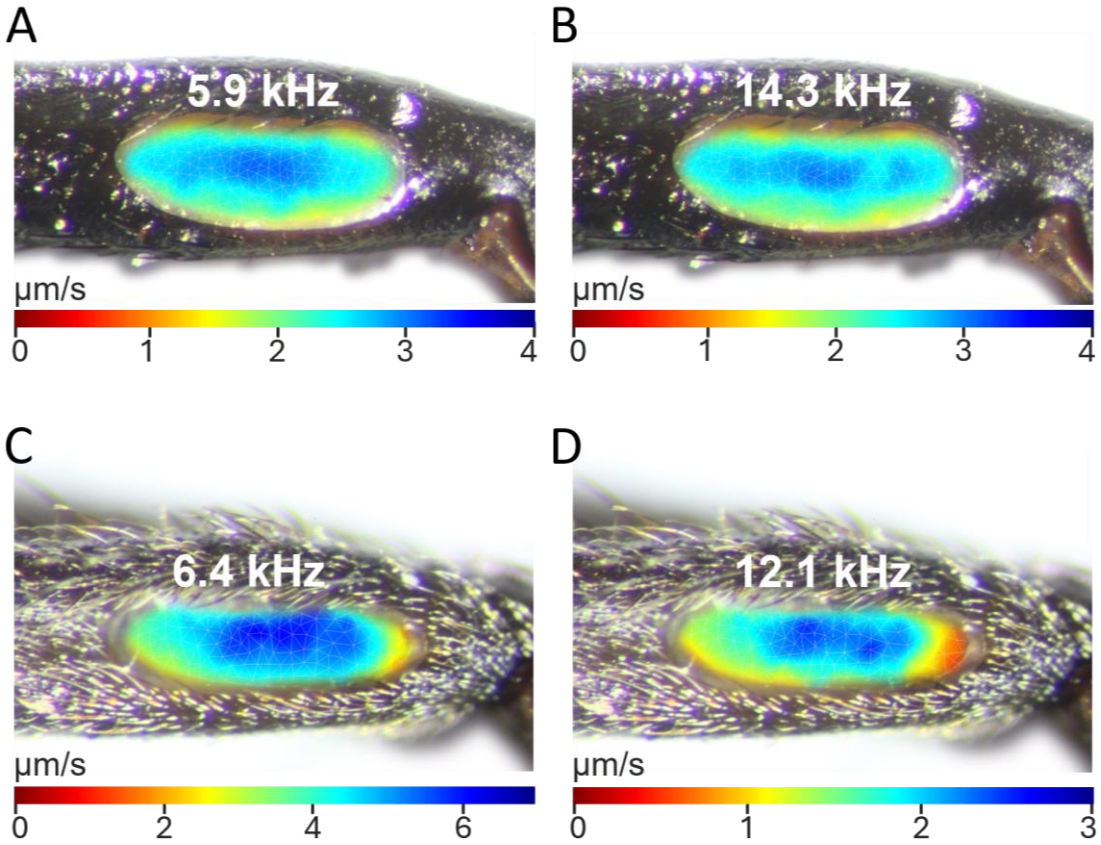

Figure 3.6 | Posterior tympanum exhibits a consistent drum mode across frequencies. Maximum velocity recorded at each point of a mesh grid of laser Doppler vibrometry scan points covering the entire posterior tympanal membrane (PTM) is shown for **(A, B)** *Gryllus bimaculatus* and **(C, D)** *Teleogryllus commodus* during frequency sweep stimulation (cone loudspeaker, spiracles open). Panels correspond to the frequency positions of peak 1 and peak 2 for each species. The spatial distribution of these maxima reveals a consistent up–down drum mode at both peak frequencies in both species. This mode is reflected in the uniform distribution of high-velocity regions across the central membrane area, indicating that these regions moved together in phase.

peaks from both species are presented in Figure 3.6. Panels A and B show membrane movement of a representative *G. bimaculatus* posterior tympanum, while Panels C and D present corresponding examples from a *T. commodus*. Again, the selected frequencies presented here correspond to peak 1 and

peak 2 of each species, as identified in their respective velocity amplitude spectra (Figures 3.2–3.3A and 3.4A).

LDV animations of tympanal movement across the frequency range are available online as supplementary material to [1]. These animations show that both species exhibit a consistent and spatially uniform drum mode at the two principal peak frequencies. However, in *T. commodus*, a possible higher-order rolling mode may be observed at a frequency beyond the second peak, as highlighted in the *T. commodus* animation. These animations were obtained from individuals with opened spiracles under sweep stimuli and correspond to Figure 3.6 and relate to Figures 3.3 and 3.4. These spatial data shown in Figure 3.6 and in the animations confirm that no change in modal shape occurred at either peak 1 or peak 2 for either species.

Given the membrane resonated with the same drum mode at both peaks, only one of them can be the natural resonance derived from the membrane. The other must necessarily arise from out with the tympanum itself.

3.3 **Discussion: A Revised Model of PTM Frequency Filtering**

The LDV results presented here support a revised model of Gryllinae posterior tympanal membrane (PTM) frequency filtering, defined by four principal findings. First, contrary to previous conclusions, the PTM exhibits two distinct vibrational optima rather than a single peak, with a consistent low-frequency response near 6 kHz and a second peak around 14 kHz (Figures 3.2–3.3A). Second, mapping the membrane using scanning LDV demonstrates that both peaks arise from the same drum mode of motion (Figure 3.6), indicating that only one can represent the membrane's intrinsic resonance. Third, phase-response measurements identify this natural resonance (Figure 3.3B,C), showing that the higher-frequency optimum corresponds to the membrane's intrinsic resonance. Fourth, the lower-frequency peak near 6 kHz instead reflects a driven response rather than an intrinsic tympanal property (Figure 3.3B,C). These findings are consistent with those observed in the control species (Figure 3.4). Collectively, these findings provide empirical support for the long-hypothesised second mechanical filter, demonstrate that the

frequency filtering profile of the posterior tympanum is being shaped by feedback from this external filter, and consequently reframe the PTM not as an isolated membrane but as part of a coupled system.

These findings help reconcile a literature that has remained notably inconsistent. Studies have claimed *sharp* tuning aligned with the calling song carrier frequency [9, 11, 71, 72, 115], whereas others describe *broader* CF-centred tuning [7, 26, 73]. A third group identifies broad tuning *above* the calling song frequency altogether [8, 12, 27]. Finally, studies have differed in whether the PTM exhibits *one* [7, 12, 27, 115] or *two* [8, 9, 26, 71] resonance peaks. Despite these divergent interpretations, multiple authors have independently proposed that an additional mechanical filter must exist downstream of the posterior tympanum [8, 10, 12, 26].

Closer examination shows that the claims of a single sharply tuned peak around the calling song CF are not supported even within the data presented in those studies themselves. An early report of sharp tuning aligned with the calling frequency show that the peak position is shifted above the stated value and occurs alongside secondary, higher-frequency responses that are compressed on a logarithmic scale [115]. Similarly, a study describing a PTM profile defined by a single frequency nevertheless present data showing a distinct second higher-frequency resonance [9]. A subsequent review of this same study has incorrectly interpreted it as supporting a PTM profile that matches the tuning of the rest of the auditory pathway at the calling frequency [11], despite the original data in fact showing a shift of approximately 1800 Hz above that frequency [9].

A comparable pattern emerges in studies of directional tuning, where early work reports a sharply defined response centred on the CF of the calling song [71, 72]. However, these conclusions are based on largely theory-driven [71] or sample-limited [72] methodologies and are not supported by later work demonstrating less acute directional tuning [73].

More recent studies have concluded that the PTM exhibits a single broad resonance shifted above the calling song frequency [12, 27]. However, this interpretation is best explained by methodological limitations. Data

normalisation likely obscures distinct spectral peaks by averaging them into a single broad response [12], while insufficient frequency resolution prevents any detection of lower-frequency optima whatsoever [27]. Although these studies therefore fail to resolve the dual-peak structure identified here, they importantly revive earlier suggestions [7, 8] that tympanal mechanics alone cannot account for auditory tuning, reinforcing the need for an additional filtering mechanism.

Overall, the findings of the present study align more closely with earlier work that reported two resonance peaks, typically near 5–7 kHz and between approximately 14–20 kHz [8, 9, 26, 71]. However, the study here advances these data by distinguishing between intrinsic and driven responses. It is now shown, here, that the higher-frequency peak represents the natural resonance of the PTM, whereas the lower-frequency peak reflects input from an external resonator (Figures 3.3–3.4). By revealing the distinct mechanical sources of the two resonances, the findings here not only help resolve longstanding ambiguity over the number and positions of the tympanal optima but also suggest that their differing origins may help account for some of the discrepancies observed across the earlier literature. Notably, blocking the spiracles did not shift peak frequencies, which align with those observed here under open-spiracle conditions, but the relative amplitudes of the two peaks were reversed, with the lower-frequency peak (near 6 kHz) much larger in amplitude [9]. This may reflect the system having functioned as a single-input system without spiracular input, together with the significantly greater stimulus intensity used (94 dB vs 78 dB here); conceivably, the louder stimulus enhanced the contribution of an internally driven resonance relative to the intrinsic tympanal response [9].

Curiously, in the present data, the position of the higher-frequency peak shows appreciable variation between individuals, spanning 12.2–16.0 kHz in pure tone experiments and 11.2–19.3 kHz in sweep-based phase data. This variability is substantially greater than that observed for the lower-frequency response near 6 kHz, which remains comparatively stable across individuals. Such inter-individual variation in the higher-frequency optimum broadly

parallels reported variation in courtship song carrier frequencies in *G. bimaculatus*, which range from 11 to 16 kHz across males [16], but contrasts with the much narrower variation in male calling song dominant frequency, which varies by less than 1 kHz across individuals [111]. A similarly broad range is observed here in female tympanal tuning at the higher-frequency peak, with responses spanning frequencies comparable to the range of courtship song carrier frequencies. While the present study does not directly test this relationship, the correspondence raises the possibility that the intrinsic resonance of the posterior tympanum may be aligned with courtship song frequencies, whereas the lower-frequency driven response may contribute to sensitivity to calling song frequencies.

The results here also provide direct support for the long-held second filter hypothesis proposed in multiple studies [8, 10, 12, 26]. However, here, rather than invoking an abstract downstream mechanism, the present findings identify and describe a specific mechanical source for this additional filtering: an external resonator that drives the tympanum at approximately 6 kHz. This reframes secondary filtering as an integral component coupled to the PTM rather than a speculative addition to it.

Since earlier LDV studies of PTM vibrational behaviour, more recent higher-resolution confocal microscopy has provided clearer insight into the structures associated with the posterior tympanum [15]. This confocal work identified a membrane clearly coupled to the inner surface of the PTM, positioned approximately perpendicular to it and located around one quarter of the distance from its dorsal edge [15], termed here the dorsal membrane of the posterior tracheal branch (DM-PTB).

In light of the findings presented in this study, the dorsal membrane of the posterior tracheal branch emerges as the most plausible candidate for the inferred second resonator responsible for the observed 6 kHz driven response. Given its direct mechanical coupling, orientation, and membrane-like properties, this structure is well positioned to influence posterior tympanal motion and may function as an independent resonator vibrating at around 6 kHz, thereby imposing this frequency on the filtering profile of its coupled PTM.

Within this framework, the PTM should be understood not as an isolated membrane governed solely by its intrinsic properties, but as part of a mechanically coupled chain of independently tuned resonators that includes the DM-PTB. However, as both confocal and earlier imaging approaches largely provide only two-dimensional data, further three-dimensional imaging is required to confirm the DM-PTB behind the PTM as the proposed downstream second filter.

Chapter 4

Filtering and Transmission Behind the Posterior Tympanum

X-ray micro-computed tomography (micro-CT) imaging was used to investigate structures associated with the posterior tympanum (PTM) that may enable secondary frequency filtering (Aim 2). Using X-ray micro-CT enabled 3D visualisation of the spatial relationships of diverse structures inside the ear. The technique produces a volumetric dataset composed of isotropic voxels (equal-sized in all directions) reconstructed from X-rays passing through the specimen from multiple angles, thereby capturing the true 3D geometry directly. It also enabled the isolation of segmented structures of interest, which could then be quantified for 3D morphometrics such as thickness. As such, X-ray micro-CT was critical in clarifying the path of mechanical transmission from the posterior tympanum to the sensilla (Aim 3).

The direct 3D visualisation and morphometric 3D measurements of the Gryllinae ear presented here constitute a previously unreported application to this system. Here, direct 3D refers to a non-invasive volumetric dataset composed of isotropic voxels, where spatial resolution is uniform in all directions. Few if any such volumetric 3D visualisations of the field cricket acoustical system have previously been performed.

A recent landmark anatomical study [15] employed confocal microscopy to achieve a degree of 3D visualisation; however, this approach reconstructs 3D from optical slices acquired with light, where the Z-axis (depth into the sample) is less precise due to light-scattering and attenuation. In that method, the outer cuticle was partly removed, many thin images were taken at successive depths, structures were manually traced in each slice, and the slices were then subsequently stacked to form a 3D model. This results in anisotropic resolution (unequal in different directions, particularly poorer in depth) and a reconstruction that depends on both optical limits and user interpretation, rather than a truly direct volumetric dataset. In addition, that study did not provide quantitative 3D morphometric analysis.

The use of X-ray micro-CT described here therefore breaks new ground, moving beyond traditional 2D sectioning techniques (Aim 4).

In addition to 3D visualisation and morphometric analysis, X-ray imaging was used to inform the geometry of finite element analysis (FEA) meshes of ear structures, enabling simulation of their responses to acoustical stimuli. This FEA work is also reported here.

The X-ray micro-CT and FEA findings presented here are published in a 2024 peer-reviewed article in the *Journal of the Royal Society Interface* (see Appendix C) [1]. One figure from this chapter, Figure 4.7, was selected by the journal as the cover image for the June 2024 issue.

4.1 **Established Functional Anatomy of the Gryllinae Ear**

Field cricket auditory neurons are not directly coupled to the tympanum, unlike in many other insects (e.g. moths) [83]. Instead, the posterior tympanum is separated from the approximately 70 auditory sensilla [23] by two air-filled tracheal branches, each exhibiting a membranous dorsal wall [15]. The neurons themselves are arranged in a tonotopic fashion along the dorsal membrane of the smaller anterior branch (DM-ATB) [15, 20]. Most of these sensilla are immersed in a lipid-rich fluid within a tentlike complex commonly referred to as the tympanal organ (TO) [15].

Here, a direct 3D X-ray micro-CT volumetric visualisation revealed the tympanal organ (Figure 4.5B). In the illustration added to Figure 4.1B, the lipidic fluid-filled chamber is highlighted in yellow. Immersed in this lipid fluid are the auditory neurons, represented in Figure 4.1B by a single sensor in green. The cell bodies of these sensory neurons are positioned proximo-distally. The anterior tracheal branch is cavity-like, unlike in other ensiferans. The dendritic tips of the sensilla project upward and attach to the cellular mass (Figure 4.1B, light blue) via attachment (cap) cells. The cellular mass is suspended from the exocuticular ceiling of the tibia by ligaments. Surrounding the tympanal organ is the covering membrane (Figure 4.1B, dark blue). Anteriorly, the covering membrane is connected to the epithelial core. The epithelial core, not represented in these figures, is a structure located in the region historically termed the supsensorium, which separates the ATB from the anterior tympanum (Figure 1.13). Posteriorly, part of the covering membrane attaches to the dorsal membrane of the posterior tracheal branch (Figure 1.13), which is the candidate driver identified in Chapter 3 that is coupled at approximately 90° to the inside surface of the PTM sound window [15].

Within the internal anatomy between the posterior tympanum and the tympanal organ there has remained uncertainty as to how movement of the PTM is communicated to the sensilla. However, it is well known that the posterior wall of the large PTB lies flush against the posterior tympanum, and it has therefore been conjectured that this PTM–tracheal physical coupling may provide a means of transferring acoustical energy from the PTM to further inside the ear [10, 14, 15, 27]. Moreover, the arrangement of the two tracheal branches beside each other has been thought to enable a further connection from the PTM eventually to the ATB that supports the sensilla [27]. In addition, while the posterior wall of the PTB lies apposed to the PTM, its dorsal membranous wall (DM-PTB) is also coupled to the PTM but more perpendicularly [15].

Based on these established anatomical arrangements, Nishino et al. [15] proposed in their 2019 study two potential routes for auditory transmission in inside the field cricket ear. One involves the solid-to-solid coupling of the

PTM to the PTB's dorsal membrane (DM-PTB) pulling on the covering membrane of the tympanal organ and thereby disturbing the fluid surrounding the sensilla. The other posits a fundamentally different mechanism whereby airflow in the air column of the tracheal branches passes through the two connecting apertures causing an inflation of the ATB cavity and thus stimulating the tympanal organ attached. However, the authors explicitly acknowledge that it is unknown whether either of these proposed transmission pathways is in effect [15].

4.2 **Using X-ray Micro-CT to Explore Filtering and Transmission**

In using X-ray micro-CT to explore anatomical structures associated with auditory function – specifically filtering (Aim 2) and transmission (Aim 3) – particular attention was given to regions where a thin cuticle overlies an air-filled cavity. Such configurations are mechanically favourable for sound-induced vibration, as reduced mass and stiffness permit greater displacement and thus increased sensitivity to acoustic waves [82, 160]. Accordingly, the X-ray micro-CT data were further analysed to identify and quantify 3D cuticular thickness, enabling the detection of candidate thin membrane-like structures that may contribute to these auditory processes.

4.2.1 Preparing and Mounting X-ray Micro-CT Tibial Specimens

Adult *G. bimaculatus* were killed using ethyl acetate [149]; tibial sections were excised, fixed in alcoholic Bouin's solution [150], ethanol-dehydrated, stained in 0.3% PTA [148], and chemically dried in HMDS [151]. For X-ray imaging, specimens were mounted vertically on a brass rod and scanned in air using a Bruker SkyScan 1172 micro-CT system. Scans were acquired with a 1325 ms exposure, 0.2° rotation steps over 180°, frame averaging of 2, and a current of 100 µA, without a metal filter (see Section 2.2, Chapter 2 for details).

4.2.2 3D Thickness Analysis of Tracheal Boundaries

Thickness measurements (Figures 4.1 and 4.8) were obtained from 12 individuals (six female, six male) scanned with an X-ray tube voltage of 48 kV and an isotropic voxel resolution of 0.55 µm. (Whereas for the FEA models, Figures 4.2–4.4, geometries were derived from a single representative female specimen scanned at 30 kV and 0.88 µm voxels).

Figure 4.1 illustrates the methodology this study employed to analyse the thickness relationships of the dividing membrane (DivM) with surrounding structures. Segmentations were performed on each X-ray micro-CT dataset (n=12) using the CT Analyser (version 1.14.10.0) software, 'CTAn' for short, that accompanies the Bruker Skyscan 1172. Thicknesses were sampled at the midpoint of the PTM (Figure 4.1A) using cylindrical volumes of interest (VOIs) (diameter 20 µm, height 55 µm) from each target structure (Figure 4.1B).

The thicknesses of five structures were analysed across the 12 specimens (Figure 4.1B): (i) the posterior tympanum (PTM), (ii) the dorsal membrane of the posterior tracheal branch (DM-PTB), (iii) the dividing membrane (DivM), (iv) the ventral wall of the anterior tracheal branch (VW-ATB), (v) and the VW-PTB. The dorsal membrane of the ATB was not segmented as this structure could not be differentiated in the X-ray data from adhered non-DM-ATB material.

The five samples were binarised by global threshold (21–255 greyscale intensity units) and denoised (removal of all except largest object, in 3D). Thickness was then determined in CTAn using the maximal diameter sphere-fitting technique [164].

4.2.3 Statistical Analysis of X-ray Micro-CT Thickness Data

Figure 4.8 presents the mean (n=12) X-ray micro-CT thickness measurements of the PTM and four internal tracheal boundaries, reported as mean ± standard deviation. Thickness is a key predictor of auditory functionality [82, 160]. Given that the PTM is a known auditory structure and is relatively thin, internal

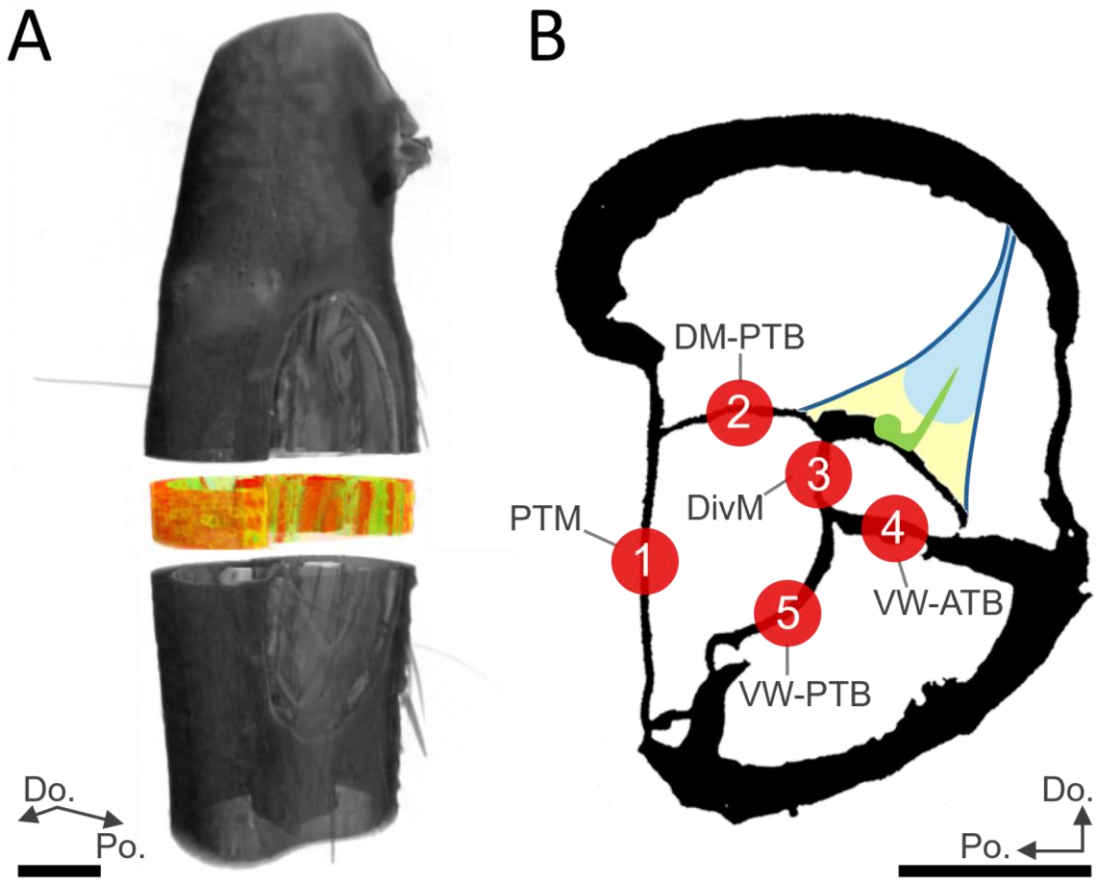

Figure 4.1 | X-ray micro-CT approach for 3D thickness analysis of tympanal and tracheal structures. Overview of the thickness analysis (n=12). **(A)** Volumetric rendering indicating the position of the sampled region at the midpoint of the posterior tympanal membrane (PTM), from which five cylindrical volumes of interest (20 µm × 55 µm) were extracted. **(B)** Single binarised axial X-ray micro-CT slice showing the five sampled structures and the central locations within each used for cylindrical segmentations: (1) PTM; (2) dorsal membrane of the posterior tracheal branch (DM-PTB); (3) dividing membrane (DivM); (4) ventral wall of the anterior tracheal branch (VW-ATB); (5) ventral wall of the posterior tracheal branch (VW-PTB). This binarised axial slice is representative of the stack used to define the geometry of FEA Model 2. The overlaid illustration of the tympanal organ is adapted from previous literature (e.g., [15, 27]): dark blue = covering membrane; light blue = cellular mass; green = auditory neuron; yellow = lipidic fluid. *Scale bars:* 200 µm.

structures exhibiting comparable thickness may also have a potential auditory role.

To formally compare thickness across structures, statistical analysis was conducted. Prior to selecting an appropriate test, the underlying assumptions of parametric analysis were assessed. Normality was evaluated using the Shapiro–Wilk test applied to residuals, where residuals represent the differences between individual measurements and their group means; this assesses whether the variation in the data follows an approximately normal (bell-shaped) distribution, an assumption required for many statistical tests. Homogeneity of variances was then assessed using Levene's test, which determines whether the spread (variability) of measurements is similar across all groups, ensuring that comparisons between groups are not biased by unequal variability.

As these assumptions were satisfied, a one-way analysis of variance (ANOVA) was employed to test for overall differences in mean thickness between the structures. ANOVA evaluates whether the variation between group means is greater than would be expected from random variation within groups. Where a significant effect was detected, Tukey's honestly significant difference (HSD) post-hoc test was applied to identify which specific pairs of structures differed from one another, while controlling for the increased risk of error associated with multiple comparisons. Statistical significance was defined as $p < 0.05$, and all analyses were performed in *R* (version 3.6.1) using base statistical functions (*stats* package), with Levene's test implemented via the *car* package and visualisation conducted using *ggplot2*.

4.2.4 The Air Column as an Alternative Filter and Transmitter

Rather than solid–solid tracheal coupling, transmission [15, 119] and filtering [7] have also been hypothesised to involve the air-filled space, the air column, contained inside the tracheal branches. This air column comprises the continuous air-filled lumen of the anterior and posterior tracheal branches, including the connecting apertures. Conceivably, acoustic energy may be transmitted not via mechanical coupling of cuticular structures, but via pressure fluctuations within this enclosed air volume.

Inspection here of the three-dimensional X-ray micro-CT reconstructions suggests a possible geometry consistent with an acoustic resonator. In particular, the anterior tracheal branch presents as a relatively cavity-like volume that is connected via a narrow aperture to a larger air space continuous with the spiracular input and leg trachea. This arrangement resembles a Helmholtz resonator, in consisting of a cavity connected to the outside or to another volume through a narrow opening. A familiar example of a Helmholtz resonator is a bottle, where blowing across the opening causes the air within the cavity to oscillate and produce a tone at a specific frequency. In such systems, air oscillates between regions when driven by sound, producing a frequency selective filtered response. As such, the air column may act to filter incoming sound by preferentially transmitting certain frequencies over others before the signal reaches the sensory neurons.

As such, the air column too was segmented from the X-ray data. This mesh was not created using the morphologies of the two tracheal branches as a guide but rather was segmented *directly* from the X-ray data such that the mesh geometries exactly match that of the biology. Figure 4.4 presents the mesh of the segmentation used to simulate the tracheal air column. The segmentation of the air column was performed in 3D Slicer (version 4.11.20210226) using the threshold paint tool. The mesh was cleaned in MeshLab (version 2021.07) before exporting as an STL file for subsequent finite element (FEA) modelling.

4.3 **Using FEA to Explore Filtering and Transmission**

Key structures inside the Gryllinae ear were identified via X-ray micro-CT that present relevance to potential frequency filtering and–or transmission functionality. These structures, being hidden inside the prothoracic tibia, could be imaged and measured via X-ray micro-CT but could not be easily experimentally tested for their responses to acoustic stimuli without compromising the integrity of the whole ear. Therefore, to assess their functionality beyond visual or morphometric description, the identified structures were modelled and simulated using finite element modelling. The

geometries of all FEA models were based, either indirectly or directly, on X-ray source data.

A total of three FEA meshes were constructed corresponding to three identified research interests. (1) Model 1: whether the DM-PTB (the candidate driver identified in Chapter 3) could be driving the lower-frequency peak of the PTM profile (Figure 4.2). (2) Model 2: simulating the vibrational responses of the entire intact system including the PTM and the internal membranes, as well as whether the PTM motion could be altering tracheal air pressure significantly (Figure 4.3). (3) Model 3: whether air column resonance inside the air-filled branches could present an alternative frequency filtering mechanism (Figure 4.4). These FEA numerical calculations were performed in COMSOL Multiphysics® (version 6.1).

4.3.1 FEA Model 1: Demonstrating Coupled Resonators

LDV revealed the 6 kHz peak to be a driving-force rather than the natural resonance of the tympanum, which was identified at around 14 kHz (Figures 3.2–3). To demonstrate that this experimental finding can be reproduced by the action of a mechanically coupled resonator, the PTM was simulated with and without its DM-PTB coupling, as shown in Figure 4.2. In other words, the phase response of the PTM vibrations (experimentally recorded in Chapter 3) was *simulated* with and without the PTM joined to the DM-PTB membrane. Recall from the experimental recordings of the PTM phase response (Chapter 3), that the lower-frequency 6 kHz peak was revealed to be characteristic of a driving-resonance, evidencing an external resonator.

The PTM in Model 1 was implemented in COMSOL as a thin elliptical shell geometry (1083 × 397 μm) with an assigned thickness of 8 μm. When coupled, a second shell element (240 × 1100 μm) representing the DM-PTB was attached 50 μm above the tympanum's major axis and assigned a thickness of 4 μm. In COMSOL, shell elements are defined as two-dimensional geometries with an explicitly assigned thickness parameter, allowing both structures to be modelled consistently within a thin-shell formulation. The

difference between the two components therefore reflects geometry and thickness only, not element type.

It should be noted that, unlike Model 2, Model 1 was not intended to replicate the full anatomical or material complexity of the system and was therefore not directly parameterised from X-ray micro-CT thickness measurements. Instead, Model 1 was designed as a simplified, controlled representation to isolate the mechanical effect of coupling between two structures. Accordingly, while the overall proportions and dimensions of the tympanum (and, by extension, the coupled element) were informed by X-ray micro-CT observations, the assigned thickness values were approximate and selected within a realistic physiological range. This simplification is justified by the specific aim of the model, which was to determine whether coupling alone could reproduce the observed driving-resonance behaviour and whether this response is retained or altered upon decoupling. The positioning and orientation of the coupled membrane – mounted approximately one-fifth along the tympanum's major axis and at right angles – were likewise guided by visual inspection of the X-ray data.

The model was solved using the Solid Mechanics physics interface in the frequency domain. A harmonic load was applied as a uniform normal pressure of 1 Pa to the tympanal surface, representing an incident acoustic driving force. The tympanum was mechanically constrained at its periphery, and at the attachment point of the coupled membrane, to reflect anatomical boundary conditions. No propagating acoustic field was explicitly modelled; rather, the analysis represents a forced structural response to a prescribed harmonic excitation.

Coupled–uncoupled simulations were swept over the frequency domain from 1 to 20 kHz in 100 Hz steps. Instantaneous velocity was calculated from the tympanum in isolation and when coupled, before conversion into real and imaginary values ($\mu m\ s^{-1}\ Pa^{-1}$) for standard modal analysis.

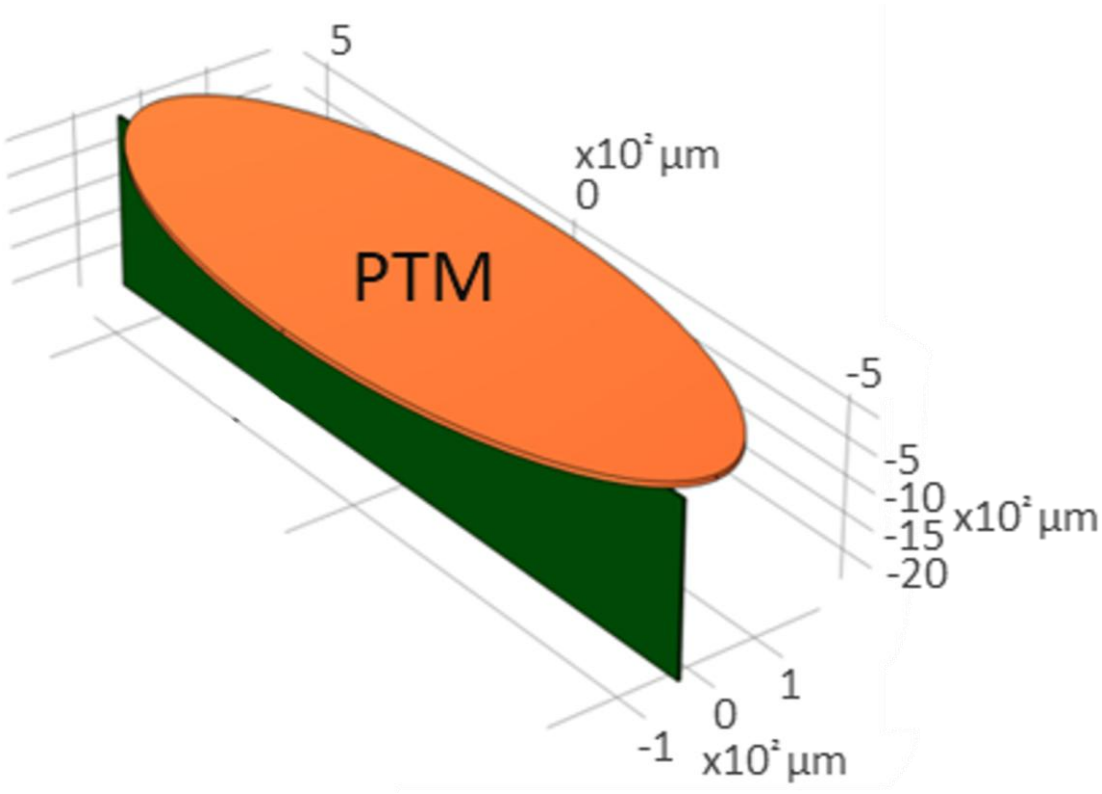

Figure 4.2 | Geometry construction of FEA Model 1. Simplified FEA model used to investigate the effect of tympanum coupling to an internal resonator, specifically comparing PTM response with and without coupling. Shown here in the coupled configuration, with the ellipsoidal posterior tympanal membrane (PTM) in orange (1083 × 397 µm), dimensions taken from segmented X-ray micro-CT data, and a second element (green; 240 × 1100 µm) representing the candidate 6 kHz resonator, the dorsal membrane of the posterior tracheal branch (DM-PTB). The coupled element is positioned approximately 50 µm from the dorsal edge of the PTM and oriented at right angles, based on visual inspection of both the literature and reconstructed X-ray data. Thickness values were not directly measured but assigned as approximate, order-of-magnitude estimates (8 µm for the PTM; 4 µm for the coupled membrane). As this model was designed as a simplified, controlled system to isolate the mechanical effects of coupling, precise anatomical parameterisation from X-ray data was not critical.

4.3.2 FEA Model 2: Simulating the Tracheal Branches

FEA Dimensions from X-ray Data

Geometry for Model 2, including structure thicknesses, was carefully taken from X-ray micro-CT scan data. This X-ray scan was obtained of a female prothoracic proximal tibia. Cross-sectional micro-CT slices were segmented by binary-threshold. An example of a binary-threshold axial slice can be seen as the basis of Figure 4.1B as well as accompanying the Model 2 meshes reproduced in Figures 4.3B–D. The full stack of binarised images were used to outline the proportions of the tracheal branches by placing vertices at the points where the tracheal boundaries intersect with each other (see coloured points illustrated on the accompanying slices of Figures 4.3B–D). Given the inherent irregularity of anatomical positions, traces were made on arbitrary slices through the stack of slices by visual inspection of significant anatomical features (points of intersection). Outlines were made on 10 irregularly spaced axial slices, such as the one shown in Figures 4.1 and 4.3, together covering the full extent of the tracheal branches. A total of 63 such vertices were obtained that were then connected by linear interpolation to form the wireframe mesh.

Following tracheal tracings, the posterior tympanum was added to the mesh (Figure 4.3A). The dimensions for this PTM were obtained from measuring X-ray micro-CT morphometrics using 3D Slicer segmentation software. Maximal length and width of the PTM were measured from the same micro-CT dataset as used for tracing the tracheal branches. The measured dimensions of the tympanum were assigned as the major and minor axes of a 1083 × 397 μm elliptical element (ellipsoid; a 3D ellipse), positioned coincident with the posterior side of the hexahedral mesh.

FEA Thicknesses from X-ray 3D Analysis

The wireframe mesh was converted to a COMSOL shell physics model and the thicknesses from micro-CT measurements – those presented in Figure 4.8 – were assigned to corresponding elements of the model: the PTM was assigned a thickness of 6.8 μm; the DM-PTB, 5.2 μm; DivM, 6.2 μm; DM-ATB,

5.2 μm; non-membrane (tracheal wall) elements, 9.1 μm. The DM-ATB, which could not be segmented and therefore was never measured for thickness, was given the same thickness value as its neighbouring dorsal membrane of the PTB. The thicknesses of all non-membranous elements were assigned as the mean average (specifically, 9.1 μm) of the two ventral wall thickness values.

FEA Material Properties from the Literature

The material properties of the Gryllinae PTM and tracheal branches are unknown, and as such were based on previous FEA modelling of the locust tympanum by Malkin et al. [165]. Model 2 was made an isotropic linear-elastic solid and assigned a Poisson's ratio of 0.3 and a density of 1300 kg m^{-3}. The PTM was given a fixed boundary condition and assigned a Young's modulus of 20 MPa. All non-PTM elements were given a lower value of 2 MPa, in line with the cuticle of the trachea inside the cricket leg known to contain the rubber-like protein resilin [166]. Model 2 was swept over the frequency domain in steps of 100 Hz from 1 to 20 kHz. Maximum velocity of each element (μm s^{-1}) and strain energy density at the element's midpoint (J $μm^{-2}$) were calculated. Volume change of the anterior branch has previously been proposed, albeit from aperture airflow [15]. Membrane-mediated volumetric increase was therefore also calculated, as the integral of the displacements of all ATB boundaries ($μm^3$).

4.3.3 FEA Models 2 and 3: The Air Column

Model 2

The role of the PTM in affecting pressure change [15, 119] inside the tracheal branches was investigated using the shell physics model (Model 2; Figure 4.3) and applying 1 Pa pressure to the tympanum. Doing so had little effect on ATB air pressure which indicated movement of the PTM exerts a negligible influence on internal air pressure.

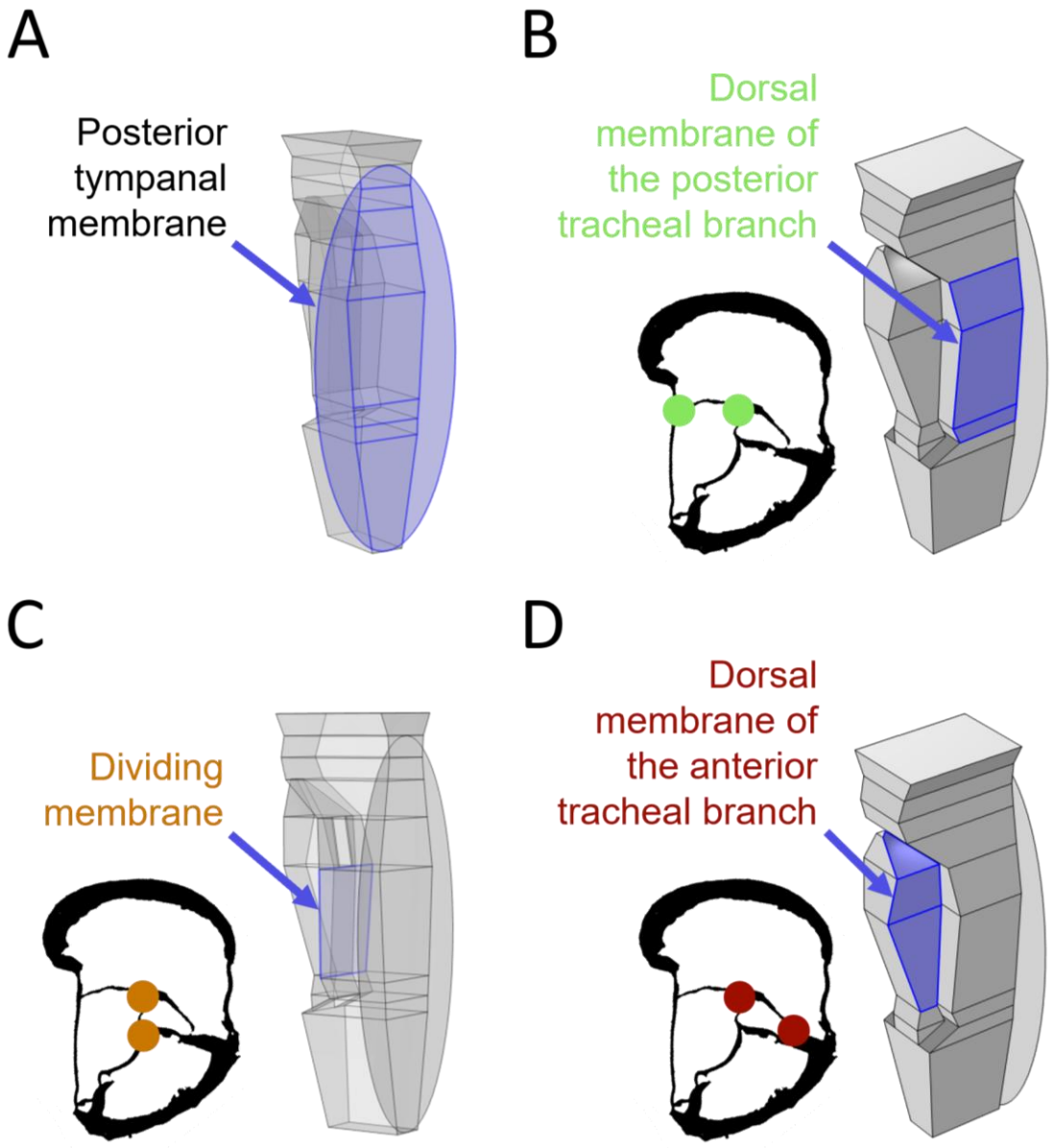

Figure 4.3 | Geometry construction of FEA Model 2 from X-ray micro-CT data. (A) Posterior tympanal membrane (PTM) represented as an idealised elliptical shell based on micro-CT morphometric measurements. **(B–D)** Internal membrane geometries of the posterior tracheal branch (PTB), dividing membrane (DivM), and anterior tracheal branch (ATB) derived from binarised axial X-ray micro-CT slices (examples shown). Tracheal boundaries were segmented by binary thresholding, and intersection points between boundaries were identified (coloured nodes) and used to define vertex positions across multiple slices. These vertices were subsequently connected by linear interpolation to generate the finite element mesh of the tracheal system. The PTM geometry was then added separately to this mesh, positioned on the posterior face.

Model 3

A cavity resonance [7] was investigated using the direct X-ray micro-CT segmentation of the air column (Figure 4.4), which was treated as a thermoviscous pressure acoustics model. The proximal opening that leads into the large posterior branch from the acoustic spiracles was the only pressure input in Model 3, given the PTM input was found to be negligible. The morphology of the tracheal branches and apertures resemble a Helmholtz resonator [167], in that X-ray micro-CT showed the ATB to be a mostly enclosed cavity connected to the outside air by a narrow opening (the proximal aperture). Therefore, any transmission loss, defined as a sudden decrease in sound pressure down the air column of the main leg trachea continuous with the PTB branch, was considered indicative of a Helmholtz resonance frequency filter. Transmission loss was calculated as the average pressure (Pa) below the apertures (that is, distal) relative to that of the proximal spiracular input above (represented by the green arrow in Figure 4.16A).

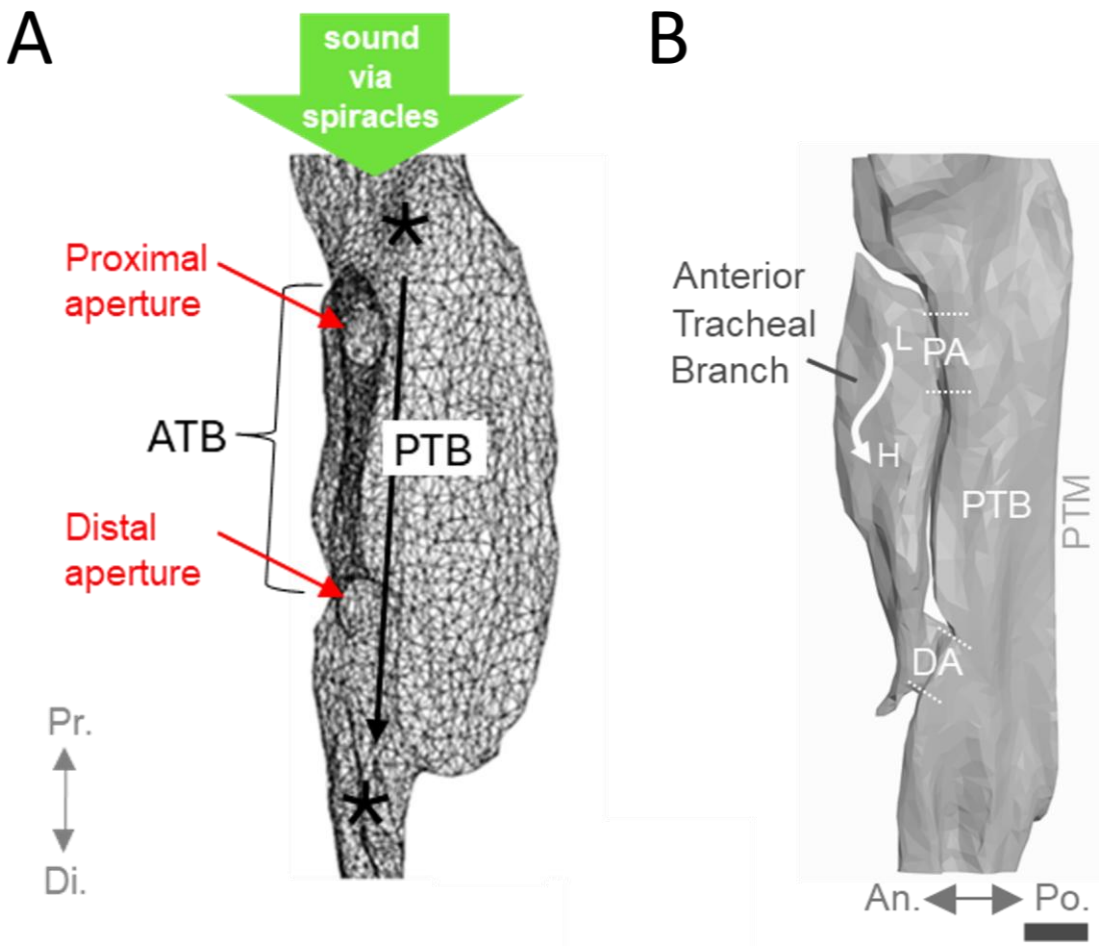

Figure 4.4 | Geometry of FEA Model 3 (air column). The enclosed air volume used to investigate potential Helmholtz-type cavity resonance within the tracheal branches. **(A)** Stereolithography (STL) mesh derived directly from segmentation of an X-ray micro-CT scan of the tracheal branches, used to define the geometry of the FEA model. The anterior tracheal branch (ATB) and posterior tracheal branch (PTB) are indicated, along with the proximal aperture (PA) and distal aperture (DA), and the direction of sound input via the spiracles. **(B)** The same STL geometry rendered as a solid surface. White arrow represents low- (L) to high-frequency (H) sensilla [15]. Anatomical orientation: Pr., proximal; Di., distal; An., anterior; Po., posterior. *Scale bar:* 100 µm.

4.4 **Results: X-ray Micro-CT and FEA Reveal Filtering and Transmission Behind the PTM**

This study used the designed X-ray micro-CT and FEA protocols (Sections 4.2–3) to investigate unresolved filtering and transmission research gaps (Aims 2 and 3 respectively).

4.4.1 Identification and Functionality of the 'Dividing Membrane'

Exploration of 3D spatial anatomy behind the posterior tympanum (PTM) began with X-ray micro-CT volumetric visualisations, such as those shown in Figure 4.5A,B. In Panels A and B of Figure 4.5, a septum dividing the two tracheal branches is labelled 'DivM', the 'dividing membrane'.

However, this structure was not initially identifiable from the volumetric reconstructions alone. Its recognition only became clear after segmentation of the cuticular structures, application of a 3D thickness analysis, and visualisation using a 3D colour map (Figures 4.6C–7). 3D thickness mapping highlights cuticle thinner than 10 μm in red and thicker cuticle in yellow. In Figures 4.6C and 4.7, the dividing membrane (DivM) is clearly revealed in <10 μm red and also is demonstrated to be physically connected to the PTM and DM-PTB membranes, which are respectively known or hypothesised [15] to play auditory roles. The combination of its colouration and its three-dimensional spatial positioning therefore indicates that this red-coloured structure (i) falls within the same thickness range and (ii) is physically continuous with both the PTM and DM-PTB, suggesting it may also be a membranous component positioned to receive acoustic energy.

Subsequent dissection and removal of the PTM allowed for further analysis under light microscopy. The DivM appeared semitranslucent, with a well-defined border (see Figure 4.6A,B).

To further evaluate its thickness similarity with the PTM and the intermediary DM-PTB (the candidate driver proposed in Chapter 3), statistical comparisons were conducted. Figure 4.8 shows the mean thickness values from five segmentations: PTM, 6.8 ± 1.2 μm; DM-PTB, 5.2 ± 2.1 μm; DivM, 6.2

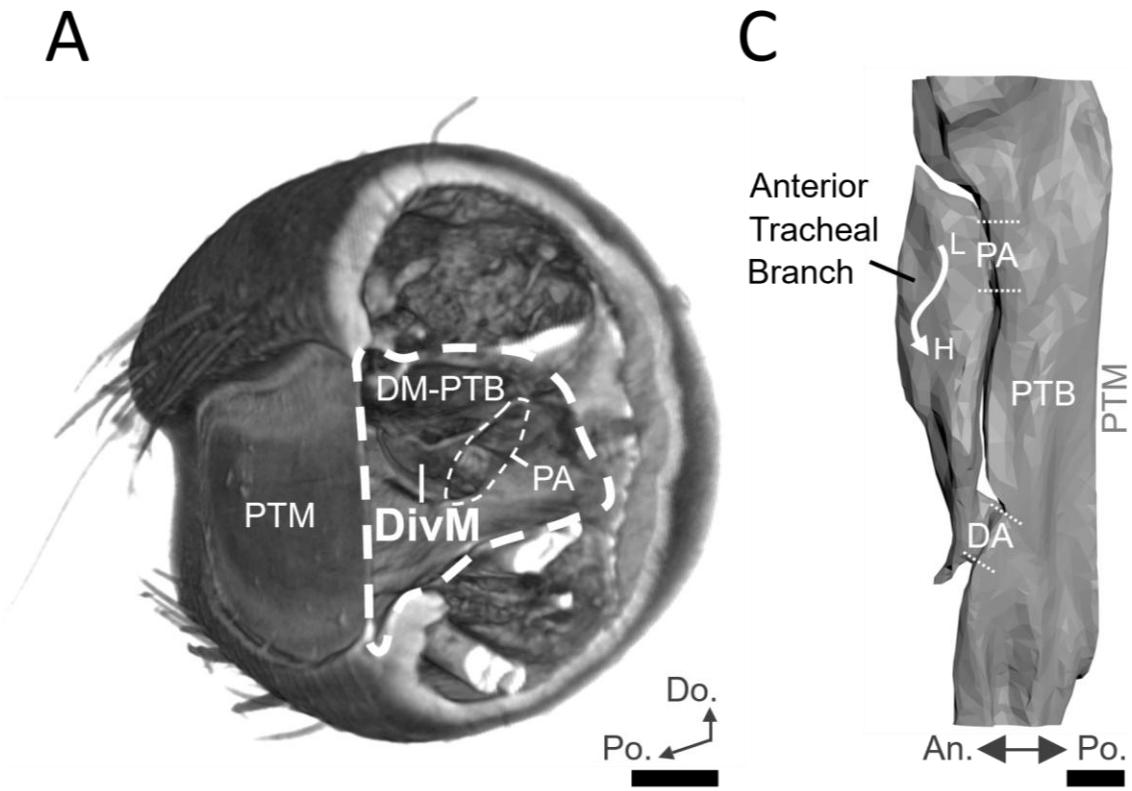
A
DM-PTB
PA
PTM
DivM
Do.
Po.
C
Anterior
Tracheal
Branch
L
PA
H
PTB
PTM
DA
An.
Po.

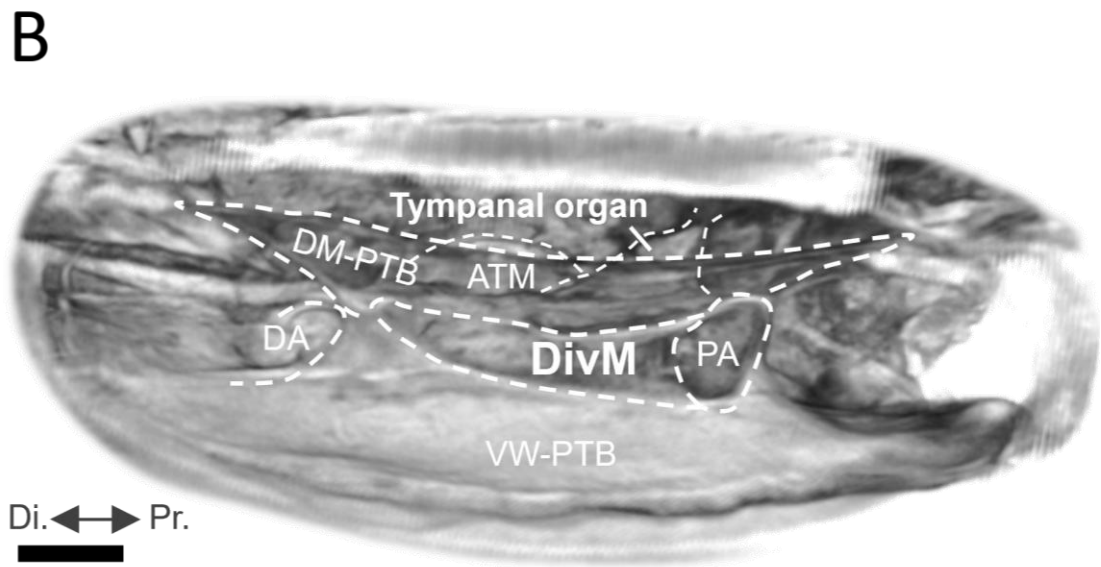
B
Tympanal organ
DM-PTB
ATM
DA
DivM
PA
VW-PTB
Di.
Pr.

Figure 4.5 | Volumetric visualisation and segmentation show the tympanal organ and asymmetric tracheal branches. (A) Transverse virtual section through the prothoracic tibia. The PTB is continuous with the leg trachea, unlike the ATB which is accessible only via the two apertures. Internal membranes visible, including the dividing membrane and the DM-PTB connected to the PTM. **(B)** Longitudinal view after virtual PTM removal, exposing internal membranes and TO. **(C)** Segmentation of air column (empty space) within tracheal branches – The white arrow represents the approximate positions of the low- (L) to high-frequency (H) tuned mechanoreceptors as based on Nishino et al. [15]. ATM, anterior tympanal membrane; TO, tympanal organ; DivM, dividing membrane; PA, proximal aperture; DA, distal aperture; DM-PTB, dorsal membrane of the posterior tracheal branch; VW-PTB, ventral wall of the posterior tracheal branch; PTM, posterior tympanal membrane. Anatomical orientation: Pr., proximal; Di., distal; An., anterior; Po., posterior; Do., dorsal. *Scale bars:* 100 µm.

± 1.2 µm; VW-ATB, 9.3 ± 1.6 µm; VW-PTB, 8.8 ± 2.5 µm (n=12, mean ± SD). The DivM was significantly thinner than the VW-ATB (***$p < 0.001$) and the VW-PTB (**$p < 0.01$). In other words, while the DivM differs significantly from the two thicker wall structures, its thickness correspondingly aligns with that of the PTM and DM-PTB membranes.

Taken together, the 3D thickness maps (Figures 4.6C–7), light microscopy (Figure 4.6A,B), and quantitative analysis (Figure 4.8) consistently suggest a thin membranous structure positioned to receive acoustical energy. These observations support a potential auditory functionality. As such, a structure initially overlooked in this study and largely unrecognised in the literature is here termed the ‘Dividing Membrane’.

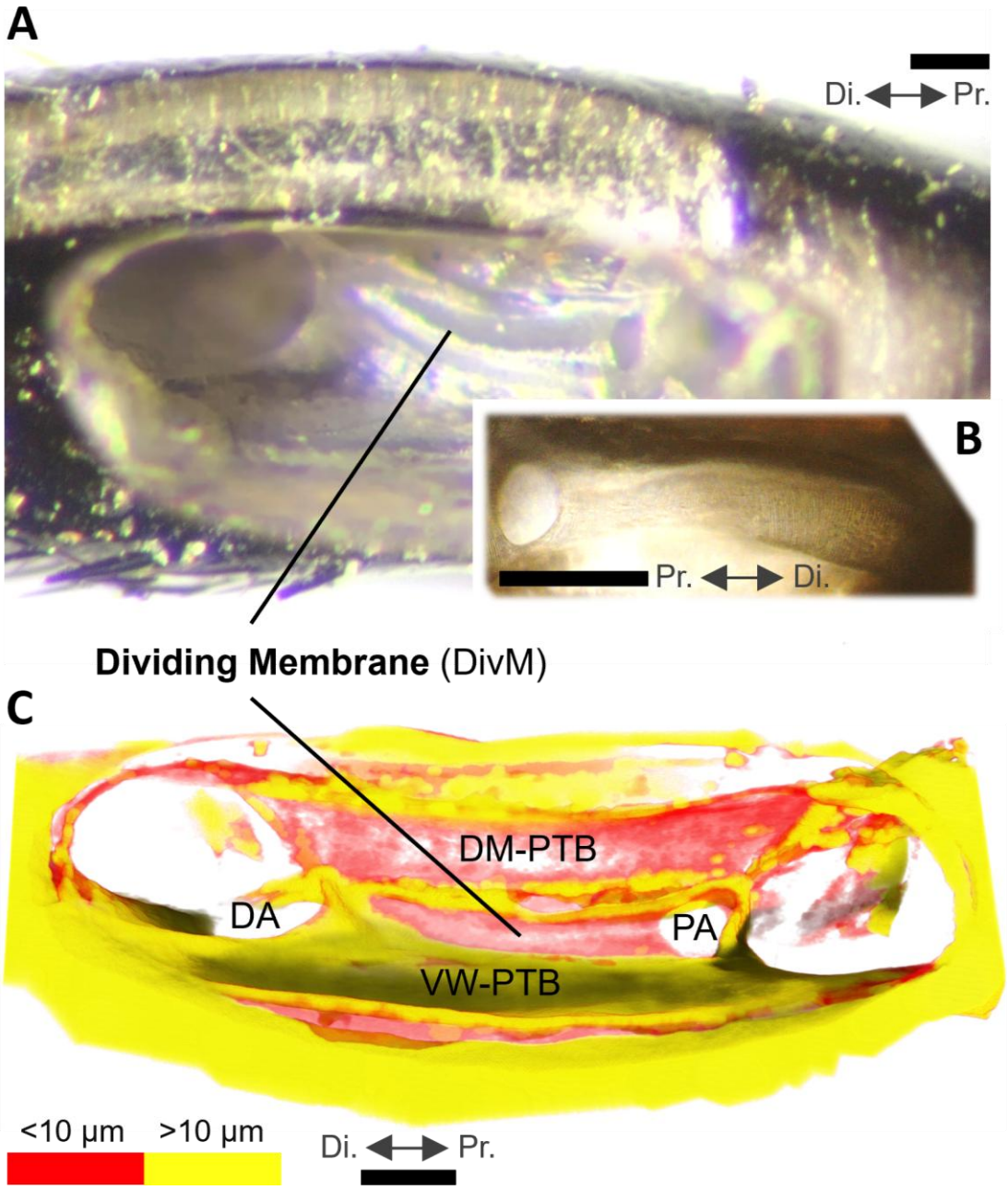

Figure 4.6 | 3D thickness mapping and light microscopy reveal the dividing membrane. (A, B) Light microscopy images of the dividing membrane (DivM) from the left **(A)** and right **(B)** prothoracic tibia, showing its position at the interface with the small anterior tracheal branch cavity. **(C)** Three-dimensional cuticle thickness map generated from micro-CT data. Colour coding indicates cuticle thickness: red marks regions thinner than 10 µm, while yellow marks regions thicker than 10 µm. Abbreviations: DivM, dividing membrane; PA, proximal aperture; DA, distal aperture; DM-PTB, dorsal membrane of the posterior tracheal branch; VW-PTB, ventral wall of the posterior tracheal branch. *Scale bars:* 100 µm.

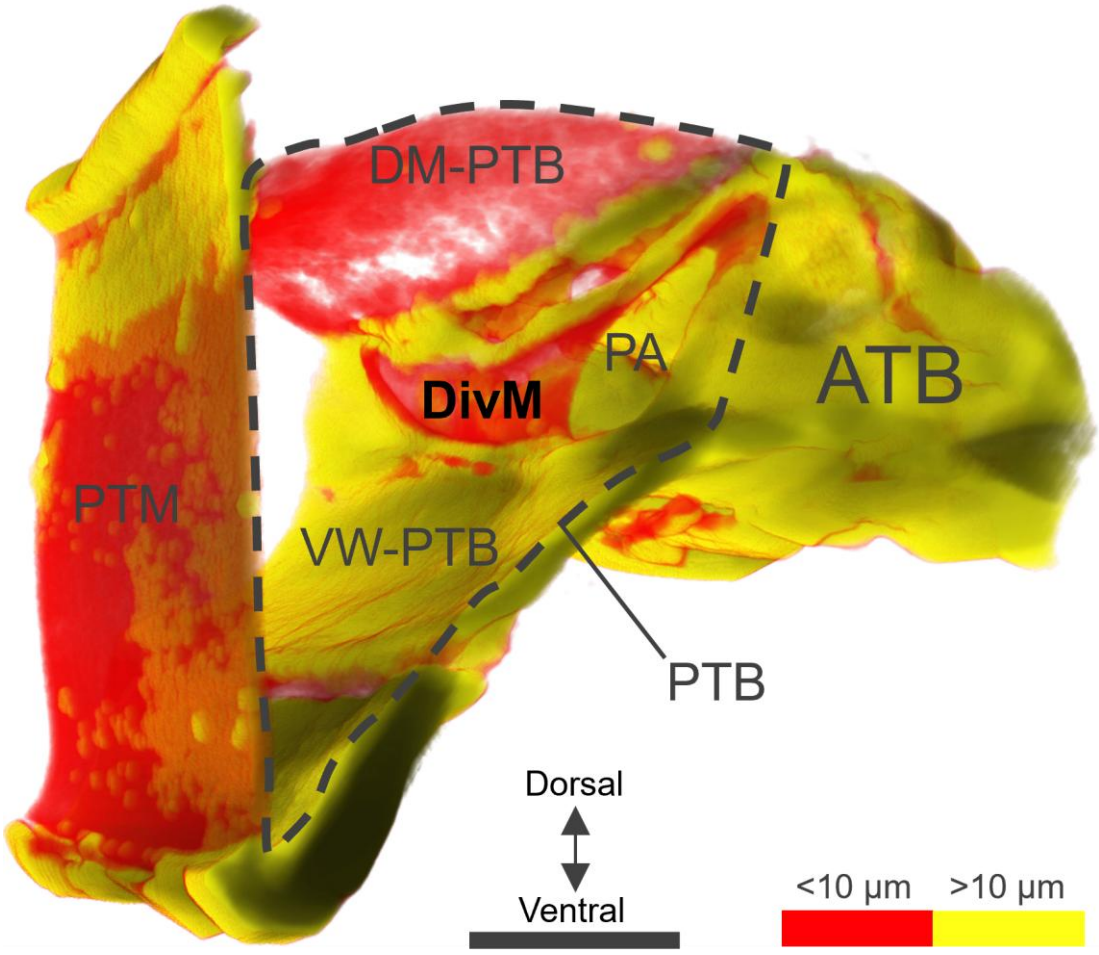

Figure 4.7 | 3D thickness mapping reveals three interconnected membranes. Three-dimensional cuticle thickness map generated from micro-CT data. Colour coding denotes cuticle thickness: red indicates regions thinner than 10 µm, while yellow indicates regions thicker than 10 µm. The data reveal three apparently coupled membranes: the posterior tympanal membrane, the dorsal membrane of the posterior tracheal branch, and the dividing membrane at the interface with the anterior tracheal branch, where the sensilla are positioned on its dorsal membrane. Abbreviations: PTB, posterior tracheal branch; ATB, anterior tracheal branch; PTM, posterior tympanal membrane; DM-PTB, dorsal membrane of the PTB; VW-PTB, ventral wall of the PTB; DivM, dividing membrane; PA, proximal aperture. *Scale bar:* 100 µm.

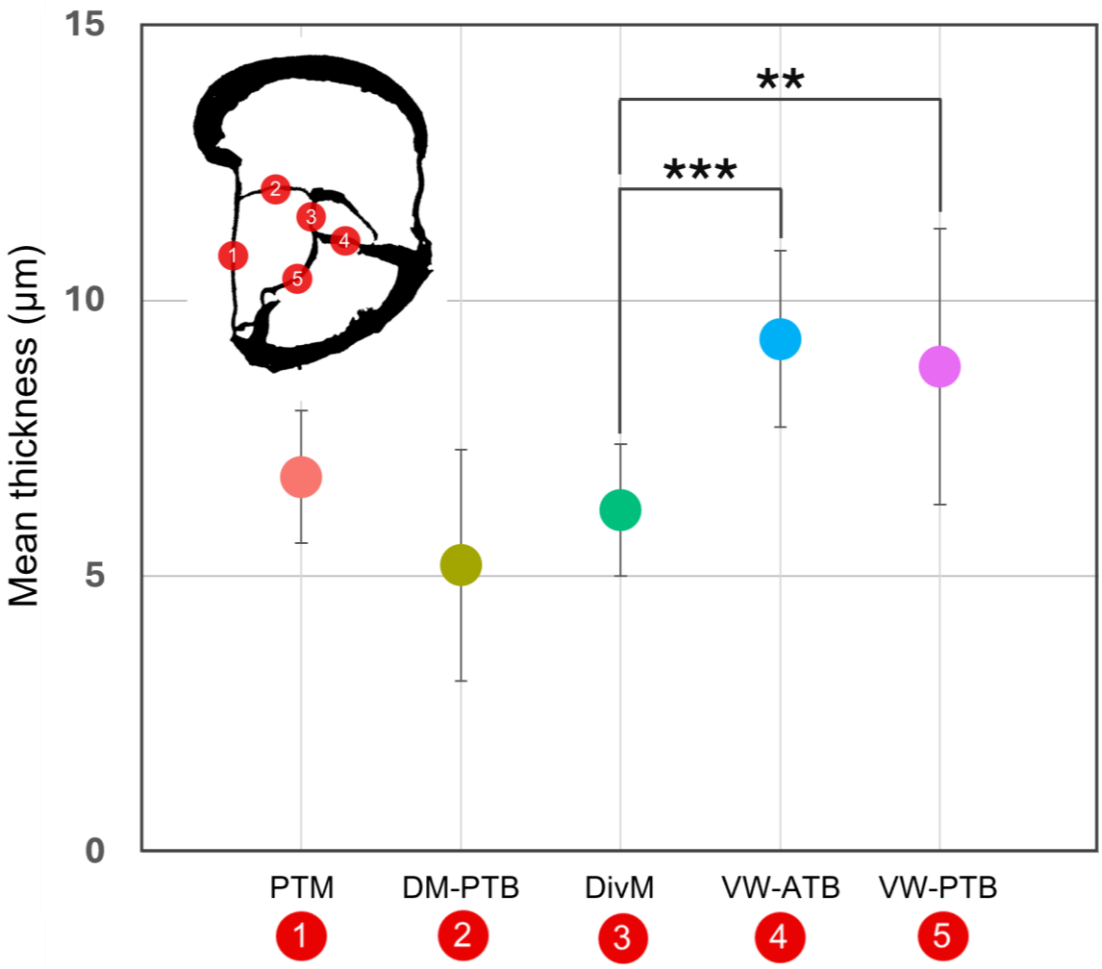

Figure 4.8 | Dividing membrane thickness is comparable to that of established membranes. Mean thickness of the posterior tympanal membrane (PTM) and four tracheal structures from 12 individuals (n=12; error bars represent standard deviation). One-way ANOVA with Tukey's HSD post hoc test revealed that the dividing membrane (DivM) is significantly thinner than the VW-ATB (***$p < 0.001$) and VW-PTB (**$p < 0.01$). (Only significant differences involving the DivM are shown). The DivM's comparable thinness to the PTM and the dorsal membrane of the PTB, structures with established and hypothesised auditory roles, suggests that the DivM may likewise serve an auditory function. PTM, posterior tympanal membrane; DM-PTB, dorsal membrane of the posterior tracheal branch; DivM, dividing membrane; VW-ATB, ventral wall of the anterior tracheal branch; VW-PTB, ventral wall of the PTB.

4.4.2 Driving Resonator Coupling Demonstrated by FEA

The capacity for an external resonator coupled to the tympanum to generate a driving-force peak on the PTM was demonstrated using numerical FEA modelling (Model 1; Figure 4.9). The phase response of PTM vibrations was simulated with (Figure 4.9A) and without (Figure 4.9B) coupling to the DM-PTB membrane. The lower-frequency driving-force peak (PTM peak–1) was present only in the coupled condition, indicating that it arises from interaction with the DM-PTB. This driving resonance role of the DM-PTB membrane is highlighted in Figure 4.9 by coloured shaded regions: the green band marks the natural resonance of the PTM, conserved in both simulations (Panels A and B), while the yellow band (Panel A) identifies a driving-force peak present only when the system was coupled. Panel C shows the FEA Model 1 geometry in its coupled configuration.

4.4.3 A Chain of Coupled Membranes according to FEA

In addition to the DM-PTB candidate resonator (Chapter 3), X-ray micro-CT identified the dividing membrane (DivM) to be a further candidate resonator that was also coupled (indirectly) to the PTM (Figures 4.6–8). Thus, three membranes, connected in sequence to each other, are noted in this present study: (1) the PTM itself, (2) the directly coupled DM-PTB, and (3) the indirectly coupled DivM. Evidence of this third membrane, the DivM, inflating the ATB (Figure 4.14) suggests this chain of membranes is concluded by a fourth membrane, the (4) dorsal membrane of the ATB (DM-ATB) upon which the sensilla are tonotopically positioned.

How these four membranes influence the complete peripheral auditory functional anatomy of the Gryllinae, from the PTM to the ATB that supports the tympanal organ, was numerically FEA-modelled (Figures 4.10–14) using the principal (Model 2) FEA-mesh of this study (Figure 4.3). The results of these Model 2 simulations are here presented.

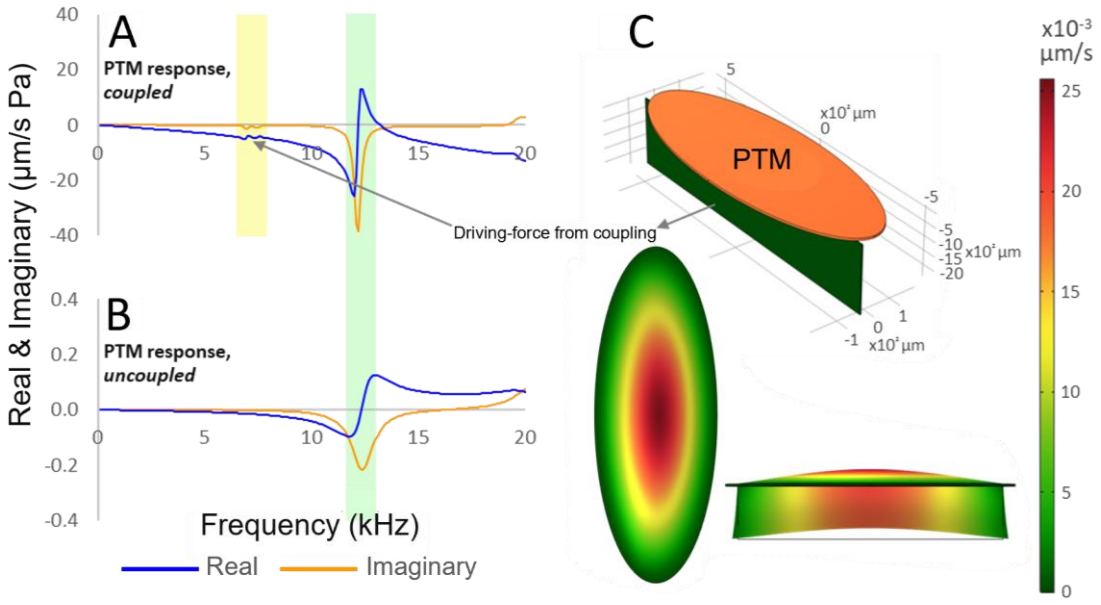

Figure 4.9 | Low-frequency PTM peak occurs only when internally coupled. Finite element analysis (FEA) was used to simulate the phase response of the posterior tympanal membrane (PTM) with **(A)** and without **(B)** coupling to an external resonator. **(A, B)** A driving-force resonance peak–1 appears in the PTM response only when the PTM is coupled to a resonator. The driving-force and natural resonance PTM responses are indicated by the yellow and green shaded regions, respectively. **(C)** FEA model (model 1 of thesis) showing the PTM (orange) in the coupled configuration with the external resonator (dark green).

Vibrational Tuning of Four Membranes

In Figure 4.10, each membrane exhibits a distinct principal resonance that shifts progressively to lower frequencies along the chain of coupled membranes. The PTM (Panel A, black) exhibits its main resonance at 10.7 kHz, while the DM-PTB (Panel B, green) peaks at 7.2 kHz, the DivM (Panel C, orange) at 7.0 kHz, and the DM-ATB (Panel D, red) at 5.1 kHz. Panel A shows all vibrational responses together, with the PTM displayed as a bold black profile. In contrast, Panels B–D each show two responses: the membrane of interest as a bold coloured trace, with the PTM included as a thinner black reference. The principal resonance of each membrane is indicated by a semi-transparent vertical band in the corresponding colour, and the thin red vertical

line marks the calling song frequency of *G. bimaculatus*. Each panel also includes the FEA model (Model 2), with the relevant structure highlighted in blue.

The FEA-calculated vibrational profile of the PTM, shown as Panel A of Figure 4.10, indicated strong qualitative agreement with the experimental LDV data presented in Chapter 3 (Figures 3.2–3A). In finite element modelling, validation is typically based on agreement in the overall response characteristics – such as the number, relative positioning, and amplitude distribution of resonance peaks – rather than exact numerical correspondence of individual frequency values, which are sensitive to uncertainties in geometry, boundary conditions, and material properties.

In this study, Model 2 was constructed from manual segmentation of micro-CT data rather than direct geometric extraction, introducing an additional level of approximation in the reconstructed morphology. Furthermore, material properties were assigned based on values reported in the literature, as no Gryllinae-specific experimental data were available for tympanal and cuticular material properties. These necessary assumptions further limit the expectation of exact frequency matching.

Despite these constraints, Model 2 (Figure 4.10) reproduces the key features of the experimental response, namely a lower-amplitude peak at 7.2 kHz followed by a broader, dominant resonance at 10.7 kHz. Notwithstanding the expected discrepancies, these frequencies remain in close agreement with the experimental observations, where the primary resonance occurs at the 11–19 kHz range (Figure 3.3, green bar), and the lower-frequency peak occupies a similar relative position. The preservation of the overall vibrational profile and peak structure therefore provides confidence that the model captures the essential mechanics of the system. Satisfactory validation of FEA Model 2 was thus concluded.

In line with the DM-PTB candidate resonator (Chapter 3) functioning as the resonant driver of peak 1, the 7.2 kHz simulated PTM peak (Figure 4.10A, black trace) exactly correlated with the principal sharp resonance of the DM-PTB membrane (Figure 4.10B, green trace). In agreement with the X-ray

micro-CT investigation pointing to a DivM function, the simulated dividing membrane vibrated with its dominant resonance at 7.0 kHz (Figure 4.10C, orange trace). Moreover, the DivM showed significant displacement at this resonant frequency (Figure 4.11C) and exhibited a torque multiplication of the vibrational energy it received from the PTM (Figure 4.12). At the tympanum's dominant frequency position of 10.7 kHz, the DivM amplified its received force by approximately 34-fold. Finally – closer to the conspecific calling song carrier frequency of 4.7 kHz (Figure 4.10, vertical red lines) – the dorsal membrane of the ATB that supports the sensilla vibrated with a distinct first resonance of 5.1 kHz (Figure 4.10D, red trace).

Together, these data (Figures 4.11–4.12) suggest a chain of sequentially tuned resonators: the dominant second peak of the PTM (10.7 kHz in Model 2; Figure 4.10A) gives rise to the 7.2 kHz principal peak of the internally coupled DM-PTB (Figure 4.10B), and, enhanced by the interfacing DivM resonating at 7.0 kHz (Figures 4.10C and 4.12), ultimately leads to the 5.1 kHz resonance of the DM-ATB (Figure 4.10D).

All internal membranes (Figure 4.10, Panels B–D) also exhibit a second major peak at around 10.7 kHz, likely driven by the dominant resonance of the PTM (Panel A).

Figure 4.13 presents zoomed views of both the simulated and experimental responses to aid visual inspection: Panel A shows the simulated vibrational response of the ATB dorsal membrane beneath the sensilla (corresponding to Figure 4.10D), while Panel B shows the experimentally measured PTM response (corresponding to Figure 3.3A, Chapter 3). In Panel A, the distinct DM–ATB resonance at 5.1 kHz corresponds to a very subtle yet discernible perturbation in the simulated PTM profile, marked by the left-hand star. A potentially corresponding feature in the experimental PTM profile is observed in Panel B as a minor subpeak at approximately 4.2 kHz, also indicated by a left-hand star. In both panels, the right-hand star highlights the resonance associated with the first of the two principal PTM peaks, visible in the simulated response (black trace in Panel A) and in the experimental data (Panel B).

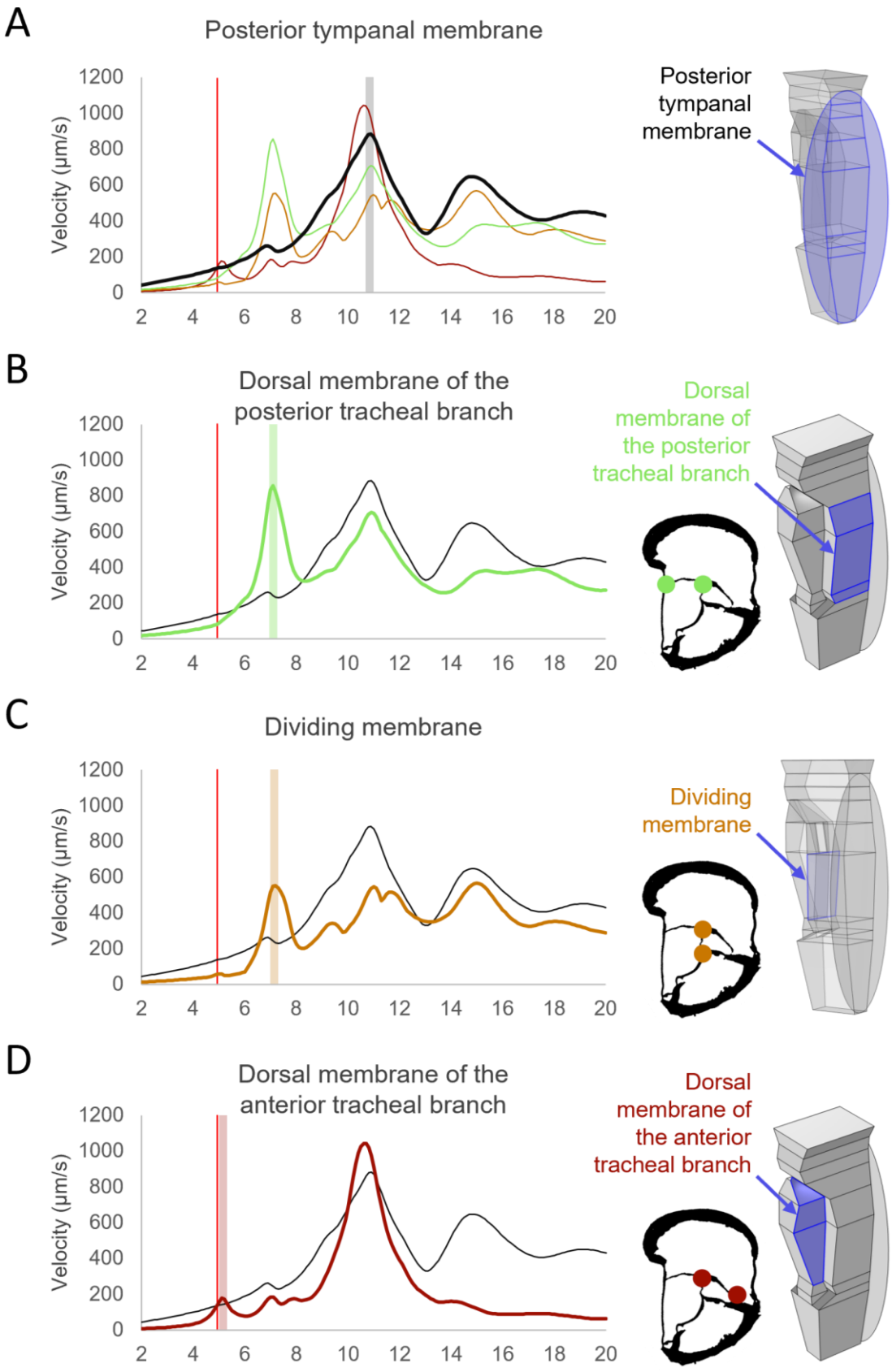
A
Posterior tympanal membrane
Velocity (μm/s)
1200
1000
800
600
400
200
0
2 4 6 8 10 12 14 16 18 20
Posterior tympanal membrane
B
Dorsal membrane of the posterior tracheal branch
Velocity (μm/s)
Dorsal membrane of the posterior tracheal branch
C
Dividing membrane
Velocity (μm/s)
Dividing membrane
D
Dorsal membrane of the anterior tracheal branch
Velocity (μm/s)
Dorsal membrane of the anterior tracheal branch

Figure 4.10 | Internal membranes exhibit sequentially tuned resonances, with DM-PTB matching the first PTM peak. (A) The velocity profile of the PTM exhibited a robust match with experimental results in showing a main resonance at 10.7 kHz with a lower-frequency peak at 7.2 kHz that **(B)** exactly matched the dominant resonance of the internally connected DM-PTB. **(C)** The DivM resonated with a peak velocity of 7.0 kHz. **(D)** The dorsal membrane of the ATB, which supports the sensory neurons, responded with a distinct resonance of 5.1 kHz, closer to the carrier frequency of the conspecific calling song. **(B–D)** Internal membrane geometries were derived from binarised (black-and-white) axial X-ray micro-CT slices (shown), where boundary intersections were identified and used to define vertex positions (illustrated by coloured nodes). These vertices were subsequently connected to generate the finite element mesh, with the PTM geometry added separately as an idealised ellipsoid. Abbreviations: PTM, posterior tympanal membrane; DM-PTB, dorsal membrane of the posterior tracheal branch; DivM, dividing membrane; DM-ATB, dorsal membrane of the anterior tracheal branch.

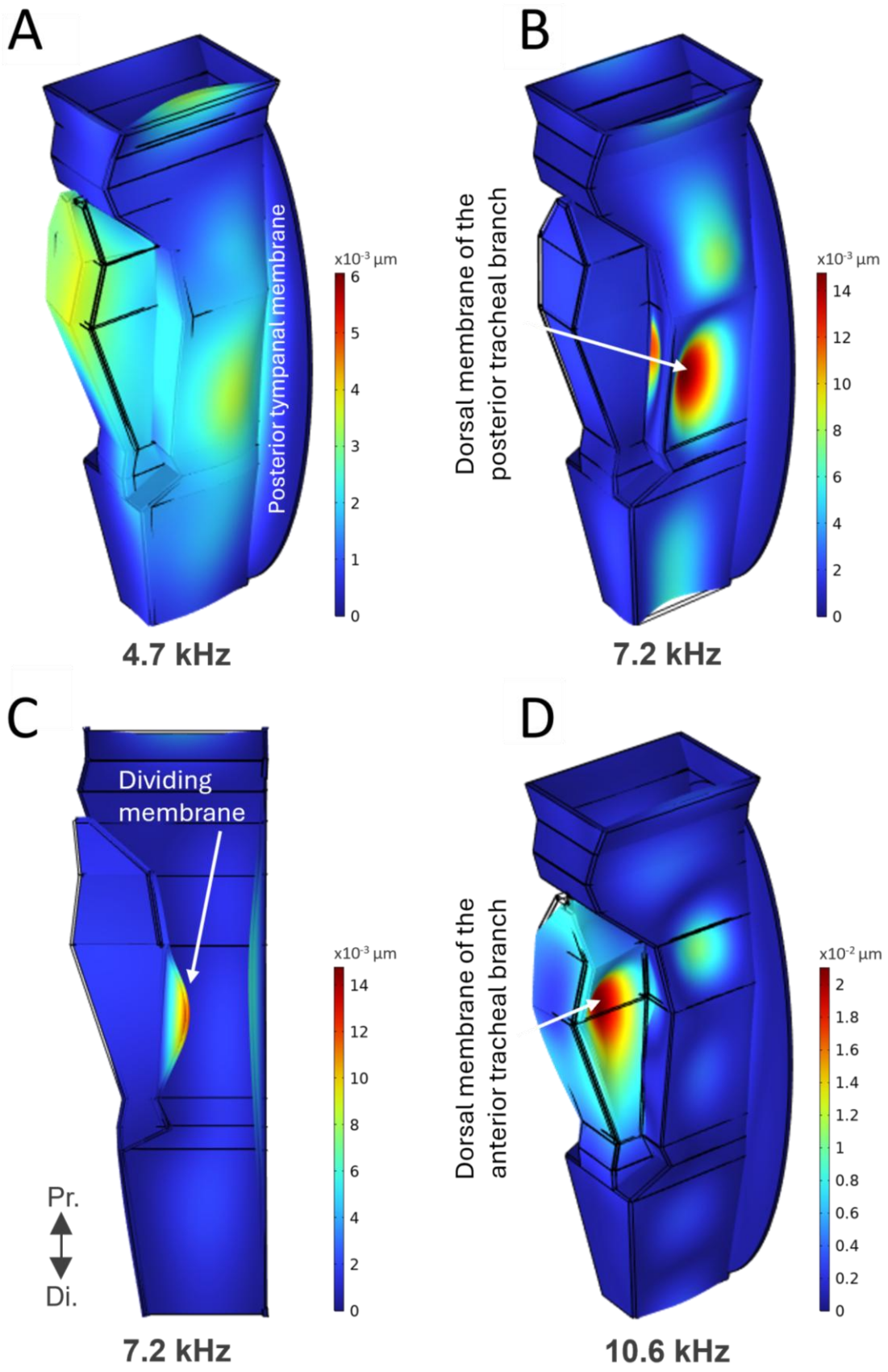
A
Posterior tympanal membrane
x10⁻³ µm
6
5
4
3
2
1
0
4.7 kHz
B
Dorsal membrane of the posterior tracheal branch
x10⁻³ µm
14
12
10
8
6
4
2
0
7.2 kHz
C
Dividing membrane
Pr.
Di.
x10⁻³ µm
14
12
10
8
6
4
2
0
7.2 kHz
D
Dorsal membrane of the anterior tracheal branch
x10⁻² µm
2
1.8
1.6
1.4
1.2
1
0.8
0.6
0.4
0.2
0
10.6 kHz

Figure 4.11 | Further Model 2 geometry and frequency-specific displacement of four membranes. Finite element analysis (FEA) model showing the mesh colour-coded according to vibrational displacement amplitude (μm) across model surfaces at selected frequencies (blue = low displacement, red = high displacement). The model is based on X-ray micro-CT–derived geometry with PTM dimensions taken from direct measurements. **(A)** Response at 4.7 kHz, the conspecific calling song frequency, showing lateral expansion of the anterior tracheal branch (ATB) cavity. **(B, C)** Displacement at 7.2 kHz, corresponding to peak resonance of the dorsal membrane of the posterior tracheal branch (DM-PTB) and the dividing membrane (DivM), respectively. **(D)** Response at 10.6 kHz, corresponding to the principal second resonance peak in the PTM response identified from the full-model simulation.

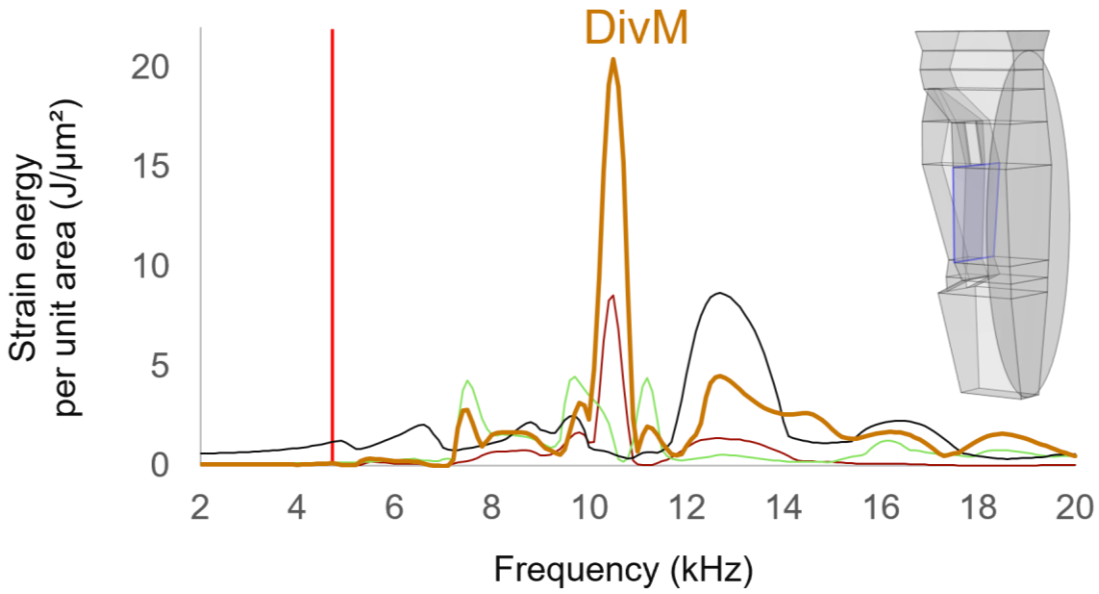

Figure 4.12 | Dividing membrane amplifies PTM vibrations up to 34-fold. Strain energy per unit area of the ear's primary sound input, the posterior tympanal membrane (PTM; black trace), the two dorsal tracheal membranes (green and red traces), and the dividing membrane (DivM; gold trace), as a function of frequency. Results are from Model 2, see inset with the DivM boundary highlighted. At a frequency of 10.7 kHz, which matches the dominant PTM resonance observed in the velocity simulations, the DivM shows a 34-fold increase in strain energy. This suggests a possible mechanical force amplification. The vertical red line marks the 4.7 kHz carrier frequency of the *Gryllus bimaculatus* calling song.

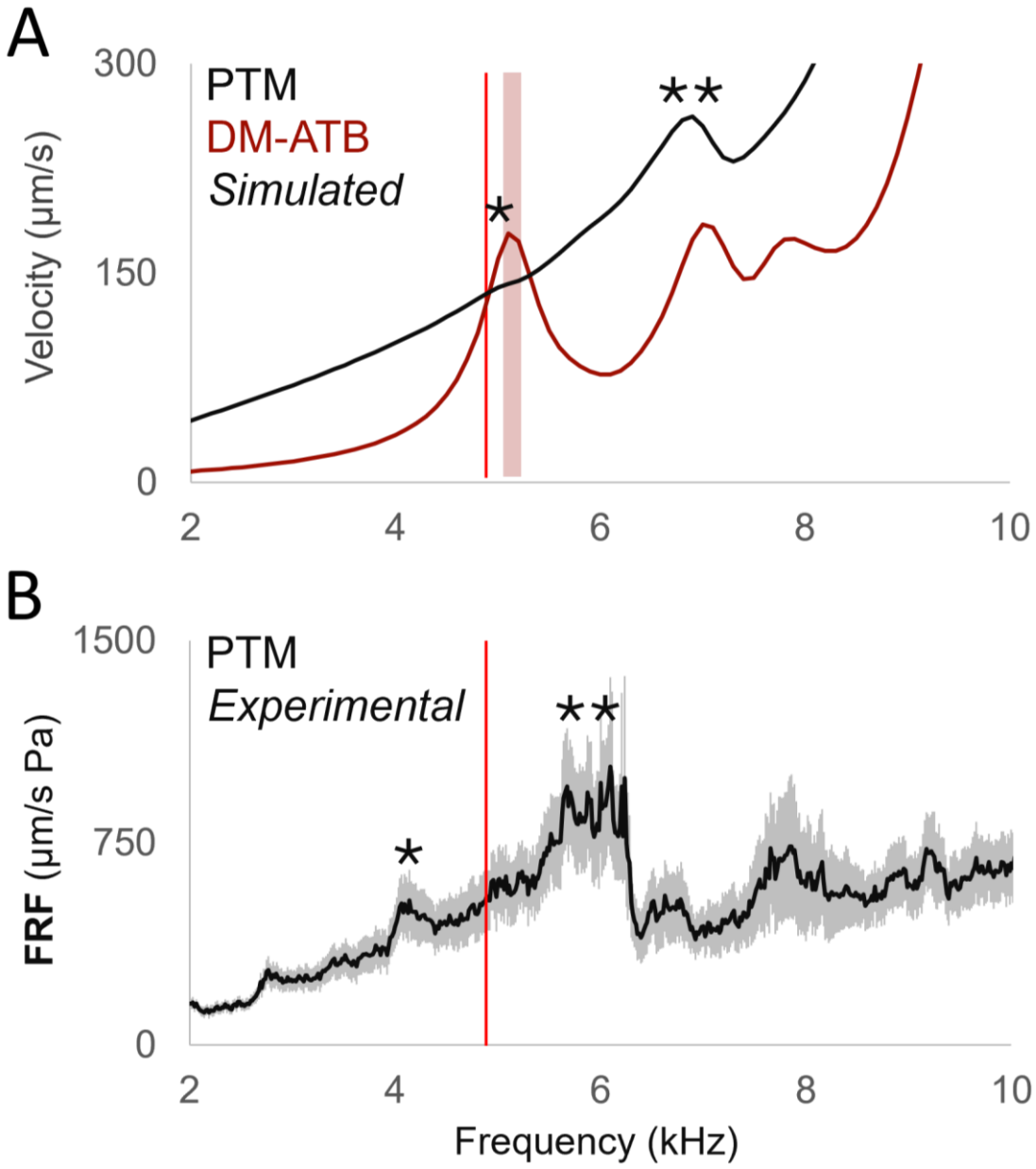

Figure 4.13 | Simulated and experimental PTM subpeak aligns with DM-ATB resonance. Vibrational responses of the posterior tympanal membrane (PTM) were assessed through both finite element modelling and laser Doppler vibrometry (LDV) (Chapter 3), while the dorsal membrane of the anterior tracheal branch (DM-ATB) could be analysed only via simulation. **(A)** Simulated PTM vibration velocity (black trace) shows a very subtle rise in vibrational amplitude near 5.1 kHz (*), which aligns with the principal resonance of the DM-ATB membrane supporting the sensilla (red trace). The first of the PTM's two principal peaks is also marked (**). **(B)** Experimental LDV recordings show a minor PTM deviation in amplitude near 4.2 kHz (*), which, given the simulation results in (A), might reflect a DM-ATB resonance. PTM peak–1 is also indicated in the experimental data (**).

Membrane-Mediated ATB Volume Change

The cavity-like anterior tracheal branch (ATB), which supports the auditory neurons and interfaces with the dividing membrane, exhibits frequency-dependent volume changes during PTM oscillation (Figure 4.14). The calculated ATB volume (Figure 4.14A) shows cyclic inflation and deflation over the range 4.8–10.4 kHz. Local maxima in volume are interspersed with distinct nulls (highlighted) at 5.1 kHz and 7.1 kHz, corresponding to the resonances of coupled membranes: the DM–ATB, and the DivM and DM–PTB, respectively (Figure 4.10B–D). The largest increase in ATB volume occurs at 10.4 kHz (Figure 4.14A), aligning with the dominant resonance of the tympanum (Figure 4.10A).

If functioning as a resonant membrane, the DivM appears to be well-positioned at the interface of the ATB to possibly contribute to an ATB volume change (e.g., see visualised in Figure 4.10). As such, ATB volume was calculated with (teal) and without (black) the DivM in place (Figure 4.14A). Without the DivM, there was a 24.5% loss in ATB volume at the maximal peak and all peaks shifted down by approximately 600 Hz.

Indicating how these volume changes arise from structural deformation, Panel B of Figure 4.14 visualises the frequency-dependent motion of the anterior branch, with ATB colours indicating displacement magnitude across the ATB surfaces as the branch inflates and deflates. (Note that the rest of the Model 2 mesh is not shown here but that the full model, including the DivM, was included in these computations).

Reading the sequence from low to high frequency, the ATB is in a state of relative deflation at 2 kHz, then increases in volume towards 4.7 kHz, followed by a slight decrease, before expanding to maximal volume around 10 kHz, and then again deflating towards 18 kHz (Figure 4.14B). The curved white arrows in Figure 4.14B indicate the approximate positions of the low- (L) to higher-frequency (H) tuned auditory sensilla, as based on [15].

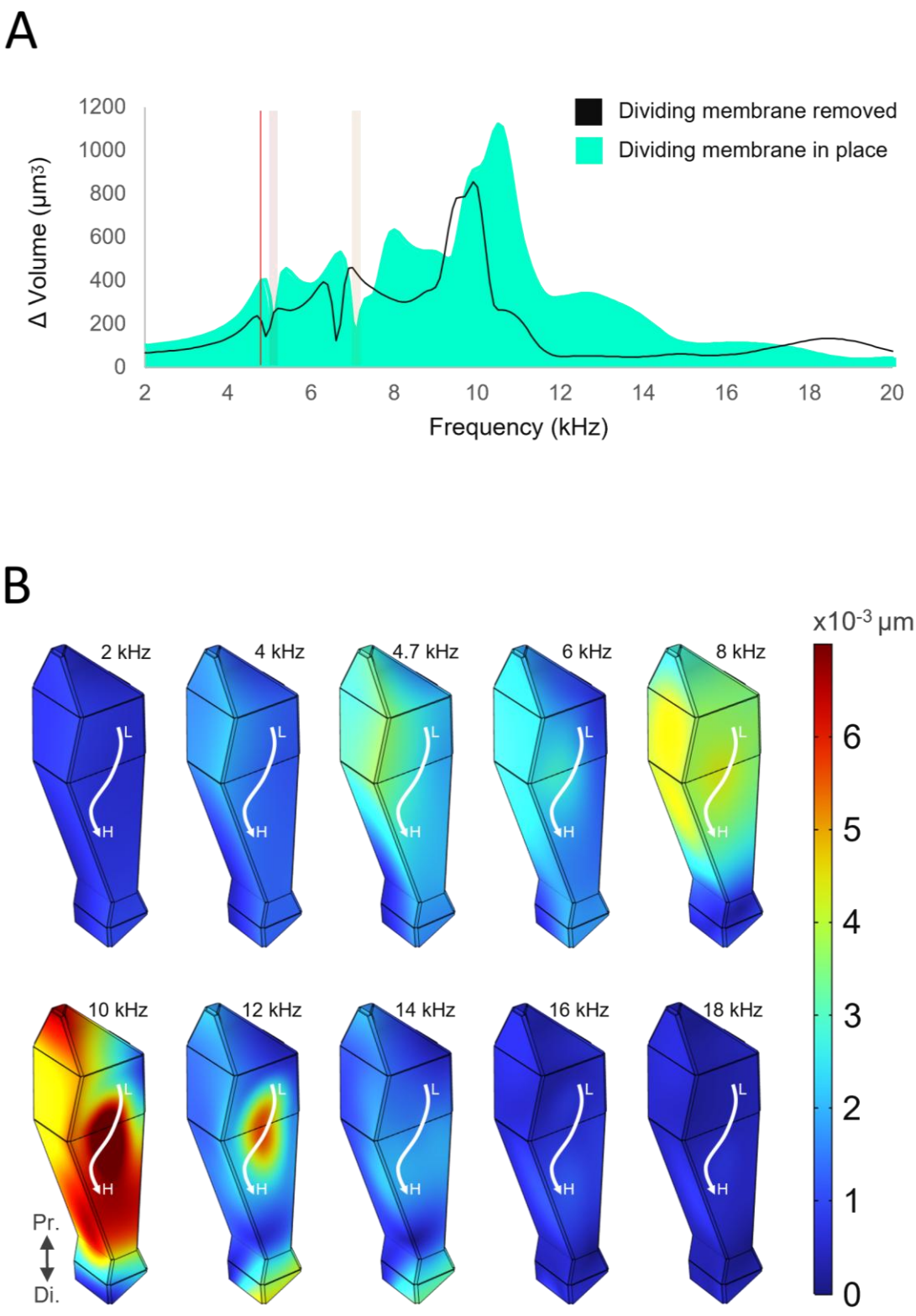
A
Dividing membrane removed
Dividing membrane in place
Δ Volume (μm³)
1200
1000
800
600
400
200
0
2
4
6
8
10
12
14
16
18
20
Frequency (kHz)
B
x10⁻³ μm
2 kHz
4 kHz
4.7 kHz
6 kHz
8 kHz
10 kHz
12 kHz
14 kHz
16 kHz
18 kHz
L
H
Pr.
Di.
6
5
4
3
2
1
0

Figure 4.14 | ATB cavity beneath the sensilla exhibits frequency-specific volume fluctuations. Inflation of the cavity-like anterior tracheal branch (ATB) has been proposed via an airflow mechanism through the apertures [15]. In contrast, here, finite element analysis (FEA) evidence suggests a possible *membrane*-mediated fluctuation in ATB volume. **(A)** The ATB inflated and deflated within a biologically relevant frequency range, between 4.8 and 10.4 kHz. The intermediate nulls were correlated with the membrane resonances. Removing the DivM (dividing membrane) from the system (black) reduced ATB volume by 24.5% at maximal peak and lowered all spectra by around 600 Hz. **(B)** Mosaic showing ATB boundary displacements at different frequencies. The rest of the system, including the PTM, was present in simulation (with the DivM in place) but only the ATB is here shown. The ATB exhibited relative deflation at 2 kHz with increasing volume towards 4.7 kHz, then a slight decrease, before expanding to maximal volume around 10 kHz and then deflating towards 18 kHz. The white arrow represents the approximate positions of the low- (L) to high-frequency (H) tuned mechanoreceptors as based on Nishino et al. [15].

4.4.4 Air Column Pressure and Resonance according to FEA

Oscillating the PTM of Model 2 (Figure 4.15A) with 1 Pa pressure resulted in a less than 10% pressure change inside the ATB relative to that applied (Figure 4.15B), indicating PTM movement has a negligible influence on tracheal air pressure.

Using a segmentation of the air column (Figure 4.16A) and the spiracular input as the sole pressure source (green arrow), a cavity resonance (calculated as transmission loss) was not reached until 70.3 kHz (Figure 4.16B), which is considerably higher than the spectral compositions of the relevant calling, rivalry and courtship songs [3, 16, 56]. Cavity resonance in the air column of the tracheal branches can therefore be concluded to be an improbable mechanism for frequency filtering in the Gryllinae ear.

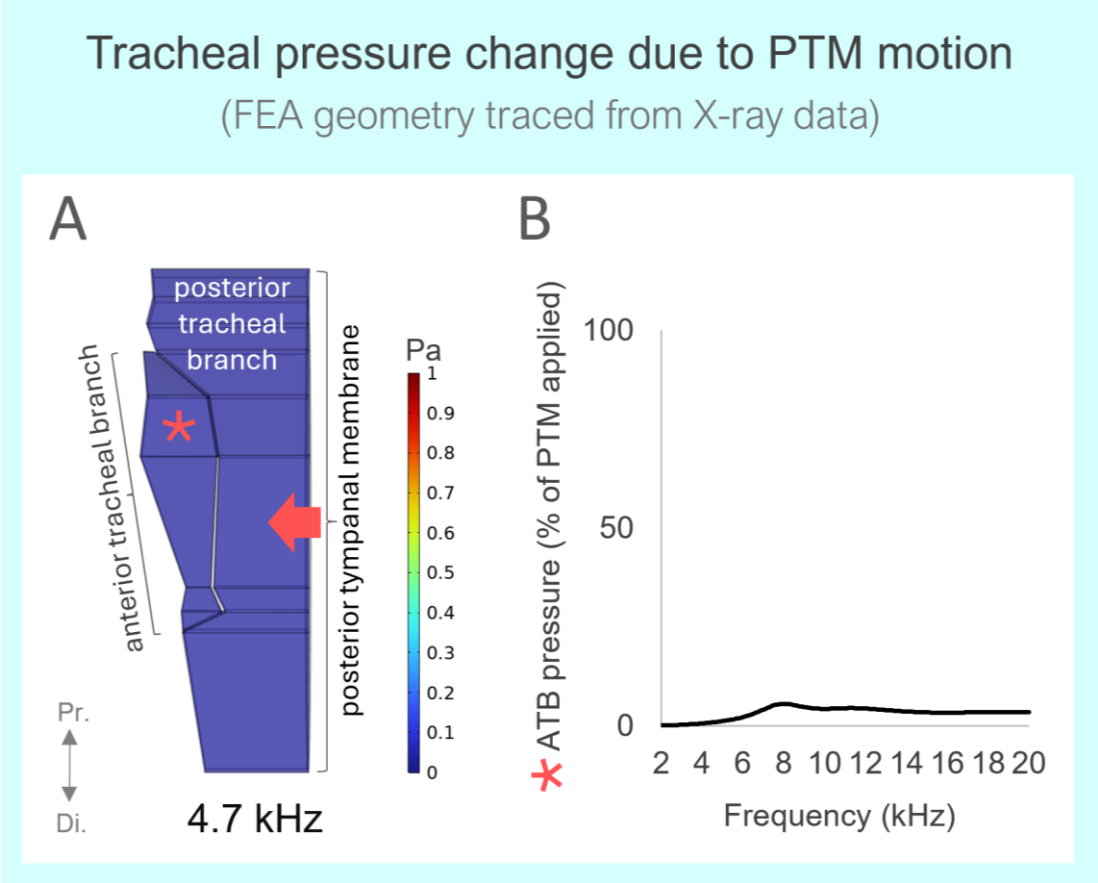

Figure 4.15 | PTM motion produces negligible changes in internal tracheal air pressure. Simulated air pressure change (Pa) within the tracheal branches resulting from driving the posterior tympanal membrane (PTM) with a 1 Pa input. **(A)** Air pressure distribution within both tracheal branches at 4.7 kHz. Pressure remained <0.1 Pa throughout. (FEA Model 2). **(B)** Air pressure measured within the anterior tracheal branch (ATB), expressed as a percentage of PTM input, across frequencies (2–20 kHz). Air pressure within the ATB remained <10% of the applied PTM pressure, indicating that PTM motion has a negligible effect on internal tracheal air pressure.

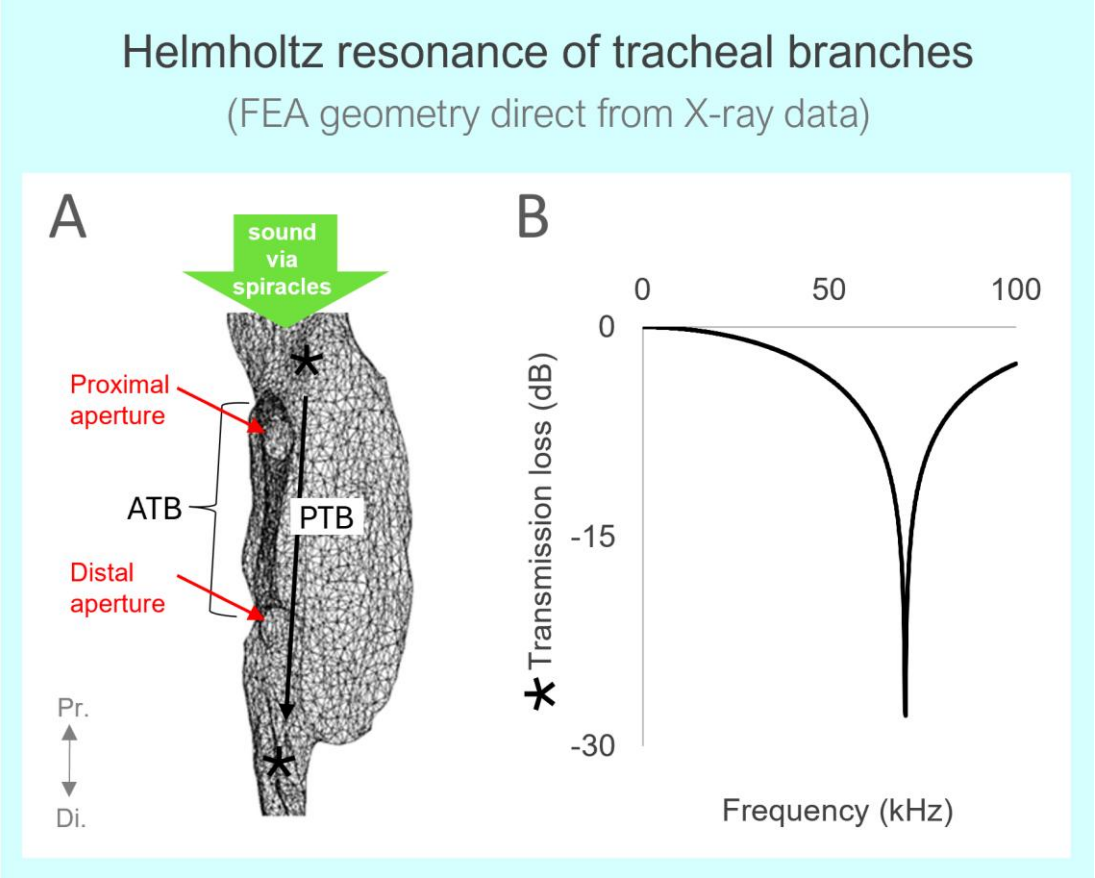

Figure 4.16 | Tracheal Helmholtz resonance does not align with communication frequencies. The anterior tracheal branch (ATB) forms a small air-filled cavity connected via a narrow neck (proximal aperture) to the larger air-filled posterior tracheal branch (PTB), together comprising a complex resembling a Helmholtz resonator in which resonance of the enclosed air may selectively filter specific input frequencies. **(A)** Mesh from segmentation of an X-ray micro-CT scan of the tracheal branches, used directly to define the geometry of the FEA model. **(B)** Resonance was assessed as transmission loss at the distal end of the tracheal branches relative to the proximal (spiracular) input. No resonance-related frequency filtering was observed below 70.3 kHz; the tracheal air column resonated only at 70.3 kHz, well above the frequency range of Gryllinae communication signals.

4.5 **Discussion: A Chain of Coupled Resonators Behind the Posterior Tympanum**

Previous studies have proposed the existence of an additional frequency filter [7-12, 15] and an unidentified transmission pathway [7, 10, 13-15] located behind the posterior tympanum of the field cricket (Gryllinae) ear. LDV recordings of PTM vibrations have further suggested the presence of an internally coupled secondary resonator (Chapter 3), likely responsible for the lower of the two principal resonances long observed in the PTM profile [8, 9, 26, 71]. In addition, the dorsal membrane of the posterior tracheal branch (DM-PTB) has been proposed as the candidate driver of the 6 kHz PTM response, supporting a framework in which the PTM operates as part of a coupled filtering–transmission sequence (Chapter 3).

However, the extent to which the DM-PTB fulfils this proposed driver role, and how the multiple downstream internal structures collectively contribute to signal filtering and transmission, could not be confirmed on the basis of existing anatomical understanding, which has largely been derived from 2D imaging approaches [15, 23, 28, 31]. In this study, X-ray micro-CT 3D imaging with FEA modelling have now been successfully employed to characterise the mechanical behaviour of three identified internal membranes downstream of the PTM, thereby clarifying the filtering–transmission pathway from the PTM to the dorsal membrane of the anterior tracheal branch (DM-ATB) serving as the sensilla attachment site.

Previously, the auditory biomechanics behind the PTM was not well understood; however, this can now be more fully characterised.

(1) In support of the DM-PTB functioning as the candidate 6 kHz driver, the PTM profile exhibits a first driving-resonance peak only when coupled to the DM-PTB (Figure 4.9) (if the tympanum is not internally coupled, then its profile does not present a first peak), and the DM-PTB itself exhibits a principal resonance that directly aligns with this first peak in the PTM profile (Figure 4.10B).

(2) Another internal membrane is identified: a previously largely overlooked structure, termed here the *dividing membrane*, which is

significantly thin (Figure 4.8), mechanically coupled to the DM-PTB (Figure 4.7), exhibits its own resonance (Figure 4.10C), and efficiently amplifies received energy more than any other structure (Figure 4.12). It also enhances frequency-specific inflation–deflation fluctuations of the ATB cavity (Figure 4.14A).

(3) The ATB itself inflates and deflates beneath the sensilla in a frequency-dependent manner (Figure 4.14).

(4) Finally, the last membrane behind the PTM, immediately preceding the sensilla – the dorsal membrane of the ATB – is tuned to a distinct resonance at a lower frequency than any upstream membranes (Figure 4.10D), and may even be faintly discernible as a feedback effect (similar to the DM-PTB driver, but more subdued) in both the simulated (Figure 4.13A) and experimental (Figure 4.13B) PTM profiles.

(5) In contrast, the competing air-based transmission–filtering hypothesis was shown to be ineffective (Figures 4.15–16).

Taken together, these X-ray micro-CT and FEA findings strongly support the DM-PTB as the candidate 6 kHz resonator acting on the posterior tympanum, providing empirical evidence for the long-speculated second filter mechanism and clarifying the filtering and transmission processes occurring behind the PTM. The results indicate not just a single additional filter (DM-PTB), but a chain of multiple internal, successively tuned, mechanically coupled membranes operating behind the posterior tympanum, extending from the PTM to the DM-ATB beneath the sensilla.

Chapter 5

Within-Host Competition and Parasitoid Development

There are several species of field cricket (Gryllinae) in North America, many of which are hosts to the acoustic parasitoid fly *Ormia ochracea* (Tachinidae).

This chapter examines how specific traits of Gryllinae hosts, specifically the cricket traits of size and sex, as well as the level of resource competition between larvae inside the cricket, affect the developmental outcomes of *O. ochracea*.

Resource competition is defined as the presence of either one or two larvae within a single cricket host. The developmental outcomes considered in this thesis are pupation success, eclosion (hatching of pupae into adults) success, pupal size, and the size of the next generation (F1) adult flies. These developmental outcomes fall into two categories, those that reflect fly offspring *quantity* (pupation and eclosion success), and those that reflect the *quality* of those offspring flies (the size of the pupae and eclosed adults).

Pupation success is the extent to which larvae successfully develop into pupae, while eclosion success refers to the extent to which those pupae emerge as adult flies. Both measures are recorded in absolute terms (the total number of pupae and adults reproduced) and proportional terms (the number of pupae and adults *relative* to the input larval load of either one or two larvae).

To investigate these outcomes, male and female *Acheta domesticus* crickets of varying sizes were manually parasitised. The number of larvae deposited per host was controlled experimentally, with either one or two larvae introduced, to vary the level of competition for resources within the host.

This chapter has two main aims. The first is to examine the effect of resource competition on the development of *O. ochracea*. The second is to assess the suitability of *A. domesticus*, a commercially available Gryllinae species in N. America, as a viable host for sustaining laboratory colonies of *O. ochracea*. These two aims correspond to Gap 6 and Gap 7 reviewed in Section 1.13.

5.1 **Ecological and Developmental Host–Parasitoid Context**

Ormia ochracea is an insect parasitoid, and as such its development is constrained by limited host resources, with host size and intra-host competition shaping life-history outcomes [120-122]. Among insect parasitoids, larger hosts typically support higher larval loads and produce larger emerging parasitoids [123-125], highlighting the role of resource availability in determining developmental success.

A larviparous, internally developing dipteran parasitoid, *O. ochracea* acoustically locates Gryllinae hosts and deposits planidia on or near them for development within the host [18, 121]. Gravid females eavesdrop on male calling songs, to which their hearing is tuned (4–5 kHz), using both spectral and temporal cues to identify suitable hosts [1, 18, 112, 126-132]. Following aerial and terrestrial phonotaxis, larvae are deposited and subsequently penetrate the host to initiate internal development [134, 135].

Development inside the cricket proceeds over a period of 6 to 10 days [135]. During the initial three days, the larvae appear to subsist on the host's haemolymph, avoiding muscle tissues. On day four, they relocate to the host's abdomen, moult, affix themselves to the abdominal wall, and form a respiratory funnel. This funnel serves to shield the larvae from the host's immune system while maintaining an air connection to the outside. The larvae continue to moult and consume adjacent tissues. In the final two days of parasitism, they target

fat bodies and abdominal and thoracic muscles, sparing both the digestive and central nervous systems. Just before exiting the host, larvae void their gut contents internally, leading to the death of the cricket. They then leave the host's body and enter pupation within a few hours of emergence [135].

In natural settings, a single cricket host may receive one or multiple larvae from a female fly [139]. Although both male and female crickets are susceptible to parasitism by *O. ochracea* [140], males face higher parasitism rates due to the fact it is the male emitting the acoustic signal that attracts the fly [139, 141]. Field surveys indicate that most parasitised hosts harbour between one and two larvae [139, 142], though occasionally more than two larvae have been recorded inside cricket hosts [143]. However, these studies do not report whether all deposited larvae successfully complete development to the adult emergence (eclosion) stage. In controlled lab settings, hosts were never observed to carry more than two larvae post-larviposition, possibly due to host grooming behaviour, which can successfully remove larvae before they burrow in [144].

Past research has primarily explored parasitism outcomes in host Gryllinae species that naturally coexist in the same environments as *O. ochracea* populations [18, 135, 139, 145, 146]. These investigations have shown that *O. ochracea* can successfully develop in alternative field crickets to their ancestral or most utilised host species. Successfully parasitised alternative cricket species include *Gryllodes sigillatus*, *Gryllus bimaculatus*, and *Modicogryllus pacificus* in Hawaii [146], as well as *Gryllus assimilis* in Texas [145]. Few studies, however, have assessed developmental success in the house cricket, *Acheta domesticus*, a Gryllinae species that nowhere coinhabits with naturally occurring *O. ochracea*. This species is nevertheless readily available to research laboratories in the USA via commercial suppliers. Although *A. domesticus* does not inhabit any of the geographic regions of N. America supporting *O. ochracea* populations, the commercial availability of large numbers of *A. domesticus* would make this Gryllinae species, if a viable host, a practical candidate for establishing robust laboratory colonies of *O. ochracea*.

In this research, how host characteristics (cricket sex and body size) and levels of larval competition (single vs. dual infestations) influence *Ormia ochracea*'s developmental success are examined. This thesis specifically investigates how these factors impact pupation and adult emergence rates, both in absolute numbers and proportional terms, as well as the sizes of pupae and F1 adult flies. To evaluate these effects, this thesis experimentally parasitised male and female *Acheta domesticus* of varying sizes and manipulated the number of larvae per host to adjust competitive pressure. A key goal of this collaborative project was to assess the suitability of *A. domesticus* as a developmental host and determine the optimal conditions for maximising larval survival and growth, balancing offspring *quantity* (reproductive success) against offspring *quality* (fitness, inferred from size).

5.2 **Protocol for Morphometrics, Infestations, and Statistical Analysis**

Recently moulted adult *Acheta domesticus* (4–6 days after final moult) were acquired from a supplier (Bug Co., Ham Lake, Minnesota, USA). A total of 600 crickets (300 males and 300 females) were used as host crickets for this thesis. Ten gravid female *Ormia ochracea* from a laboratory colony of the Lee Lab originating from Gainesville, Florida were used as larval donors.

5.2.1 Rearing of Crickets and Flies

Prior to being utilised as hosts, crickets were kept in large population containers in the Lee Lab (Minnesota) where they were allowed to mate. After parasitisation, *A. domesticus* were housed individually in 3.25 oz sauce cups with perforated lids to allow for respiration and kept at approximately 21°C in a laboratory room with natural lighting. Crickets were provided with water and food (Purina Complete alfalfa rabbit feed pellets) *ad libitum* (i.e., they had unlimited access). Individual housing containers were checked daily for fly larval emergence, pupation, and animal deaths.

Donor *O. ochracea* were reared in temperature-, humidity-, and light-controlled environmental chambers (Powers Scientific Inc, model DROS52503, Pipersville, Pennsylvania, USA) set to a 12-hr light / 12-hr dark

cycle at 75% humidity, 25°C, and provided with butterfly nectar (The Birding Company, Massachusetts, USA) *ad libitum*. Eclosed F1 flies were kept in the same sauce cup as the cricket they parasitised. Flies were fed butterfly nectar via a cotton stick that was changed daily.

5.2.2 Measuring Cricket Size and Fly Pupal and Adult Size

Along with host cricket sex and larval load (competition level), this thesis recorded morphometric traits across life stages: pronotum width, pronotum length, and hind femur length for crickets; width and length for fly pupae; and mesothorax length for eclosed (hatched) F1 flies. Host cricket body mass was also recorded.

Mass vs. Dimensions as a Measure of Size

Both body mass [168] and structural body dimensions, measured as pronotum length [169], can serve as proxies for field cricket (Gryllinae) size.

In host–parasitoid interactions, body mass is widely regarded as a direct measure of the nutritional resources available for the parasitoid larvae [168, 170, 171]. This is reflected in the parasitoid-to-host weight ratio, with Ormiini pupae typically weighing 3–10% of their host's pre-infestation mass, and heavier species of host yielding heavier pupae [168].

Despite this, changes in hydration and gut contents can cause cricket body mass to fluctuate [172], making body *dimensions* a more consistent metric for host size. Moreover, structural size, measured as fly tibia length, has been shown in other tachinid studies to directly correlate with fecundity, with structurally larger flies exhibiting higher egg counts [171, 173].

This is relevant for *O. ochracea*, where the number of planidia per gravid female can range from 65 to over 500 larvae inside one pregnant fly [140]. To sustain colonies of *O. ochracea* in the laboratory, as is the case in the Lee Lab of St. Olaf College, approximately 4,000 larvae must be obtained each month through the manual selection and then dissection of gravid female flies. Since the structural size of those selected flies is the more immediately observable

variable compared to their body mass, structural size provides a more practical measure for efficiently choosing suitable flies for infesting crickets.

Additionally, in host crickets, this thesis found a modest but significant correlation between structural size and mass (R^2 = 0.46, p < 0.0001). This correlation between cricket size and mass therefore introduces the risk of multicollinearity if both metrics were to have been included throughout the analyses employed in this chapter.

Given these considerations, initially only one of these variables, pronotum length, was selected. Pronotum length was selected as the predictor variable for subsequent developmental morphometric outcomes for the fly pupae and fly F1 adults. In line with choosing cricket structural size (pronotum length) as the predictor variable, for the fly pupae and F1 adults only width and length *structural* measurements, and not mass, were obtained.

Imaging and Measurement

Crickets were cold-anaesthetised in a –20°C freezer for 10 minutes to facilitate imaging. They were then positioned with the dorsal aspect upwards for pronotum imaging (Panel A of Figure 5.1) and the ventral aspect upward for hind femur imaging (Figure 5.1B). After imaging, crickets were weighed using a digital scale (Sartorius Entris, 1241-IS Balance 120g x 0.1mg), assigned a unique ID, and recorded in the data collection log. Imaging was completed prior to the manual parasitisation procedure. Pupal images were taken before eclosion, with pupae positioned to display their maximal length (from between the spiracles to the opposite end) and width (widest perpendicular distance) (Figure 5.1C). Eclosed F1 flies were cold-anaesthetised in a –20°C freezer for 10 minutes, then pinned dorsal side up on a petri dish with agar using Minutien pins for mesothorax length imaging (Figure 5.1D).

Images of crickets, pupae, and flies were captured using CellSens Dimension (version 3.24) with an Olympus SZX16 stereomicroscope, an SDFPLAP0 0.8x objective, and a DP80 camera. This setup produced images with a calibrated scale for measuring morphological features (Panels A–D of Figure 5.1). Captured images were imported into ImageJ (version 1.53) for

morphometric analysis. The 2 mm scale bar was used to convert pixel values to real-world measurements. The line tool was then used to measure pronotum length, pronotum width, and hind femur length in crickets (Figure 5.1A,B); length and width in pupae (Figure 5.1C); and mesothorax length in eclosed flies (Figure 5.1D).

5.2.3 Protocol for Manually Infesting Gryllinae Hosts

O. ochracea can be propagated in the laboratory using a manual infestation procedure described by Vincent and Bertram [162]. Manual parasitisations are performed by extracting larvae from freshly dispatched donor flies. This involves dissecting the fly's abdomen and spreading the larvae from its reproductive tract onto a petri dish lined with filter paper. Freshly extracted larvae move actively, often standing on their posterior ends and waving their anterior ends. On damp filter paper, larvae remain highly active for the first two hours after removal but can survive for up to 7–8 hours [163]. In this state, larvae readily attach to a wooden probe. Once attached, they are placed on the cricket's articular sclerites, which is an area of soft tissue between the pronotum and thorax.

In this thesis, larvae from 10 gravid female flies were used to infest 600 *A. domesticus* crickets, evenly split between males and females. Half of the crickets in each sex group were infested with one larva, while the other half received two larvae to test for resource competition. Per donor fly, 60 crickets were infested, with 15 females and 15 males receiving one larva, and another 15 females and 15 males each receiving two larvae. In total, 150 females and 150 males were infested with one larva, and another 150 females and 150 males with two larvae, totalling 900 larvae across 600 crickets.

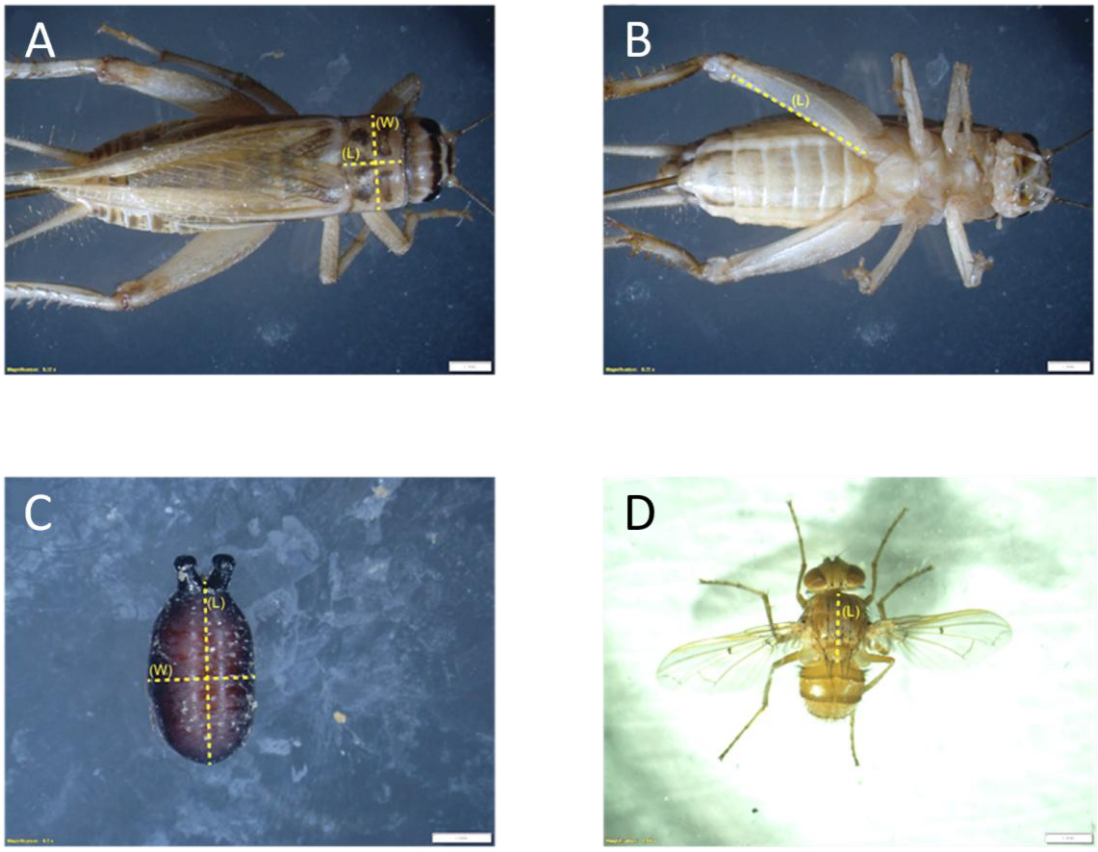

Figure 5.1 | Imaging and measurement of crickets, pupae, and eclosed flies. (A) Dorsal view of an *Acheta domesticus* cricket host showing pronotum length (L) and pronotum width (W). **(B)** Ventral view of a cricket with hind femur length (L) indicated. **(C)** Emerged *Ormia ochracea* pupa positioned to display maximal length between spiracles (L) and width (W). **(D)** Dorsal view of an eclosed F1 (first generation) fly showing mesothorax length (L). Crickets, pupae, and flies were imaged using an Olympus SZX16 stereomicroscope and measured using ImageJ. Dashed yellow lines indicate measured morphological features. Scale bars represent 2 mm.

5.2.4 Statistical Analysis

Statistical analyses were conducted in *R* software (version 4.4.2) using RStudio.

Pupation and Eclosion Success

This thesis used generalised linear mixed-effects models (GLMMs) to assess the effects of host cricket sex, pronotum length, body mass, and larval number on pupation and eclosion success (Figure 5.3), implemented in *glmer* (*lme4* R package, version 1.1-36). These variables were included as fixed effects, with donor fly ID as a random effect.

Generalised linear mixed-effects models (GLMMs) are statistical models that allow the effects of key variables of interest to be tested while accounting for additional sources of variation in the data. In this study, the variables of interest, known as fixed effects, included larval load, host sex, and host size, while differences between individual donor flies were treated as a random effect. GLMMs were used because the response variables, pupation success and eclosion success, are proportions representing success or failure and therefore require modelling with a binomial distribution. Using GLMMs allowed for the effects of resource competition and host traits on development to be assessed while accounting for natural variation between individual flies.

Pupation success was analysed using two GLMMs based on different definitions. The first defined pupation success as whether a host *cricket* yielded any pupation (Figure 5.3A). The second defined pupation success as the proportion of *larvae* that successfully pupated (Figure 5.3B). A third GLMM assessed eclosion success, defined as the proportion of *pupae* that eclosed into adult flies (Figure 5.3C).

Additionally, Figure 5.3D visualises the absolute numbers of pupae and eclosed flies for each larval treatment.

Assessing Correlations among Host Cricket Traits

Q-Q plots and the Shapiro-Wilk Test assessed normality, revealing that male cricket pronotum width, hind femur length, and mass, as well as female

pronotum width and hind femur length, violated normality assumptions. Consequently, Spearman's Rank Correlation was used to examine relationships among host cricket morphological traits.

The correlation matrix showed strong positive associations among cricket pronotum length, width, and mass (r = 0.673–0.685), suggesting proportional body size scaling. In contrast, cricket hind femur length exhibited weaker correlations (r = 0.287–0.421), suggesting greater independence from overall body size.

High intercorrelations among cricket pronotum length, width, and mass raised multicollinearity concerns. Linear regression confirmed significant correlations between pronotum length and pronotum width (Adjusted R^2 = 0.41, $p < 0.0001$) and mass (Adjusted R^2 = 0.46, $p < 0.0001$). To mitigate multicollinearity, this thesis at first prioritised cricket pronotum length as the sole predictor, taking only width and length measurements from fly pupae and F1 adults accordingly.

Host, Pupal, and Fly Size

Nevertheless, because host body mass is an important predictor of resource availability for larval development [168], and the length-mass relationship left over 50% of the variance unexplained, this thesis separately analysed the effects of host pronotum length, body mass, and their interaction on pupal structural size (pupal width) using three linear regression models.

The effects of resource competition on pupal width (Figure 5.4A), host sex on pupal width (Figure 5.4B), and resource competition on adult fly size (mesothorax length) (Figure 5.5C) were analysed in this thesis using box plots for visualisation and Wilcoxon rank sum tests for statistical comparison. A binomial logistic regression model assessed the relationship between pupal width and eclosion success for pupae from the two-larvae treatment, with eclosion success as a binary response variable (0 = failure, 1 = success) (Figure 5.5A). A linear regression model examined the influence of pupal width on mesothorax length (Figure 5.5B).

Symbols Used

The symbols used in this chapter are standard statistical notation for describing model results and testing hypotheses. **β** (beta) represents the estimated effect size of a predictor variable, indicating both the direction and magnitude of its influence on a response variable; for example, a negative β value for larval number indicates that increasing competition reduces pupation success. **χ^2** (chi-squared) is a test statistic used to compare observed and expected frequencies; here, it is used to show that the total number of pupae and eclosed flies differs significantly between single- and double-larva treatments. **σ^2** (sigma squared) denotes variance, reflecting unexplained variability in the data, such as small differences between donor flies included as a random effect in mixed models. The **z** statistic expresses how far an estimated effect deviates from zero relative to its standard error; for instance, z-values are reported when testing whether factors like host sex or larval competition significantly affect pupation outcomes. **R^2** (and **adjusted R^2**) quantify how much of the variation in a response variable is explained by a model; in this study, adjusted R^2 values were used to compare different linear models predicting pupal width and assess their overall fit. The **F** statistic is used to evaluate whether a model or its predictors significantly improve explanation of the data; for example, F-statistics are reported in model comparisons to determine whether variables such as larval number treatment and cricket sex contribute meaningfully to explaining variation in pupal width.

5.3 Results: Cricket Traits and In-Host Resource Competition

Within 30 minutes of infesting a Gryllinae cricket host, the *O. ochracea* larvae pierced the membrane of the articular sclerites and burrowed into the cricket. Larvae emerged from host crickets 6–10 days later (Figure 5.2A,B) and pupated within several hours of emergence. Emergence and pupation began on day 6 post-parasitisation, with one larva (0.02% of total successful pupations) successfully emerging and pupating on this day (Figure 5.2B). Most larvae, across treatments, emerged and pupated on day 8 post-infestation (72.33%, 366 of 506 pupae), while the remaining larvae did so by day 10 (day

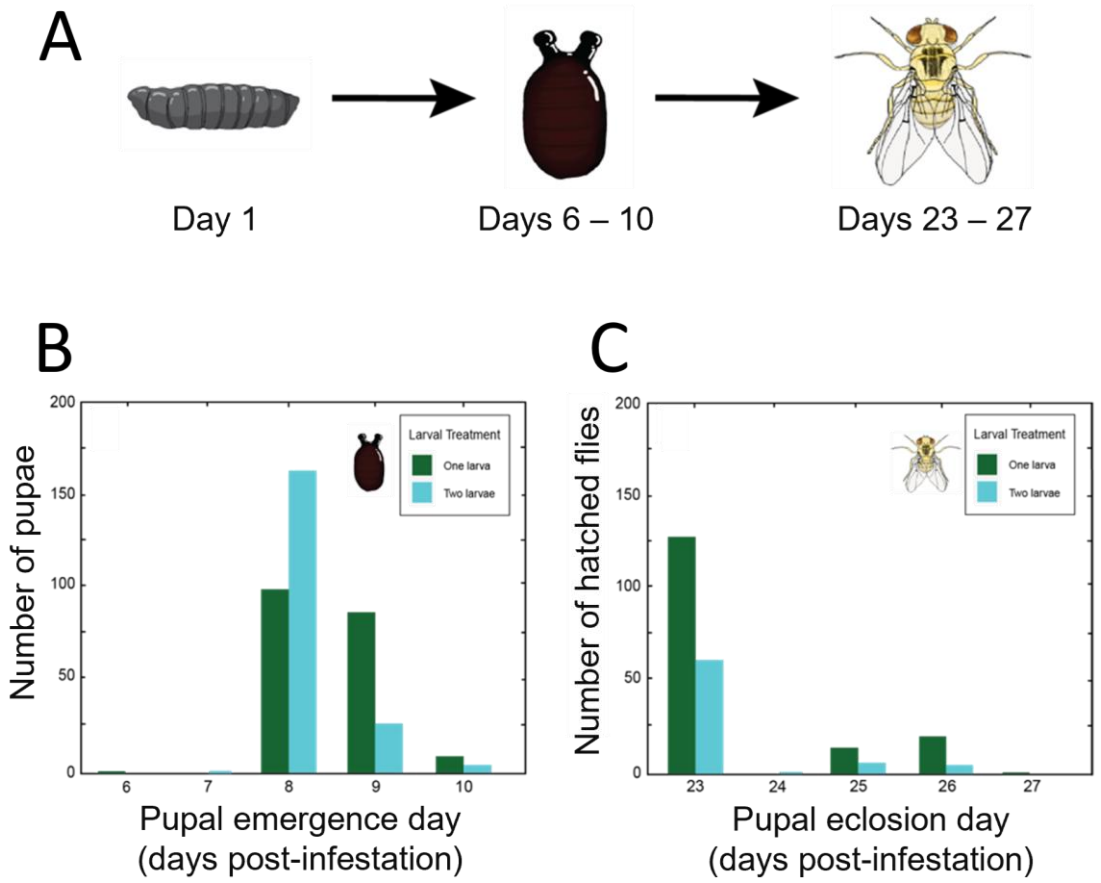

Figure 5.2 | Timeline of larval development, pupation, and eclosion. (A) Schematic of the *O. ochracea* life cycle with observed timings of larval parasitisation (Day 1), pupation following development inside host *A. domesticus* (Days 6–10), and adult fly eclosion (Days 23–27). **(B)** Number of pupae recorded per day of emergence post-infestation, separated by larval parasitisation treatment (one larva vs. two larvae). Across treatments, most larvae emerged and pupated on Day 8 (72.33%, 366 of 506 pupae). **(C)** Number of flies that successfully eclosed per day post-parasitisation, with peak eclosion occurring on Day 23. Bars represent counts of individuals from the one-larva (dark green) and two-larvae (cyan) treatments.

9: 23.52%, 119/506; day 10: 2.57%, 13/506) (Figure 5.2B). Flies eclosed approximately 23–27 days post-infestation (Figure 5.2C).

5.3.1 Effect of In-Cricket Resource Competition on Fly Quantity

Pupation success, when defined as the proportion of *crickets* (300 per group) yielding some level of pupation, was unaffected by resource competition (**β** = -0.034, SE = 0.17, *z* = -0.199, p = 0.841), cricket sex (**β** = -0.078, SE = 0.24, *z* = -0.325, *p* = 0.745), pronotum length (**β** = -0.280, SE = 0.50, *z* = -0.560, *p* = 0.575), or cricket mass (**β** = 1.989, SE = 1.68, *z* = 1.181, *p* = 0.238). Among crickets infested with a single larva, 63.33% of those crickets yielded pupation, compared to 62.33% of those infested with two larvae (Figure 5.3A), with no significant difference between treatments ($\chi^2(1) = 0.03$, p = 0.87).

When pupation success was defined as the proportion of *larvae* (n=300 or n=600) that successfully pupated, neither cricket sex (**β** = -0.252, SE = 0.25, *z* = -1.006, *p* = 0.314), pronotum length (**β** = -0.031, SE = 0.47, *z* = -0.067, *p* = 0.947), nor cricket mass (**β** = -0.745, SE = 1.27, *z* = -0.586, *p* = 0.558) had a significant effect. However, resource competition significantly reduced pupation success (**β** = -0.428, SE = 0.18, *z* = -2.397, *p* = 0.017). In the absence of competition, 63.33% of larvae successfully pupated, whereas under competitive conditions, 52.67% reached pupation (Figure 5.3B), a significant difference ($\chi^2(1) = 8.82$, *p* = 0.003).

Resource competition also affected the proportion of *pupae* that successfully eclosed into adult flies (**β** = -0.697, SE = 0.24, *z* = -2.875, *p* = 0.004). However, eclosion success was not influenced by cricket sex (**β** = -0.438, SE = 0.31, *z* = -1.422, *p* = 0.155), pronotum length (β = -0.006, SE = 0.76, *z* = -0.008, *p* = 0.994), or cricket mass (**β** = -1.530, SE = 2.17, *z* = -0.703, *p* = 0.482). Among pupae that emerged in the absence of competition, 84.74% successfully eclosed, whereas only 74.05% of pupae from larvae that had competed for resources developed into adults (Figure 5.3C), indicating a significant effect of resource competition ($\chi^2(1) = 7.30$, *p* = 0.007).

In terms of absolute counts (Figure 5.3D), rather than proportions (Figures 5.3A–C), parasitising each cricket with two larvae resulted in a higher number of pupae and successfully eclosed F1 flies compared to single-larva infestations. Among the 300 doubly infested crickets, a total of 316 pupae emerged, significantly more than the 190 pupae produced from 300 singly

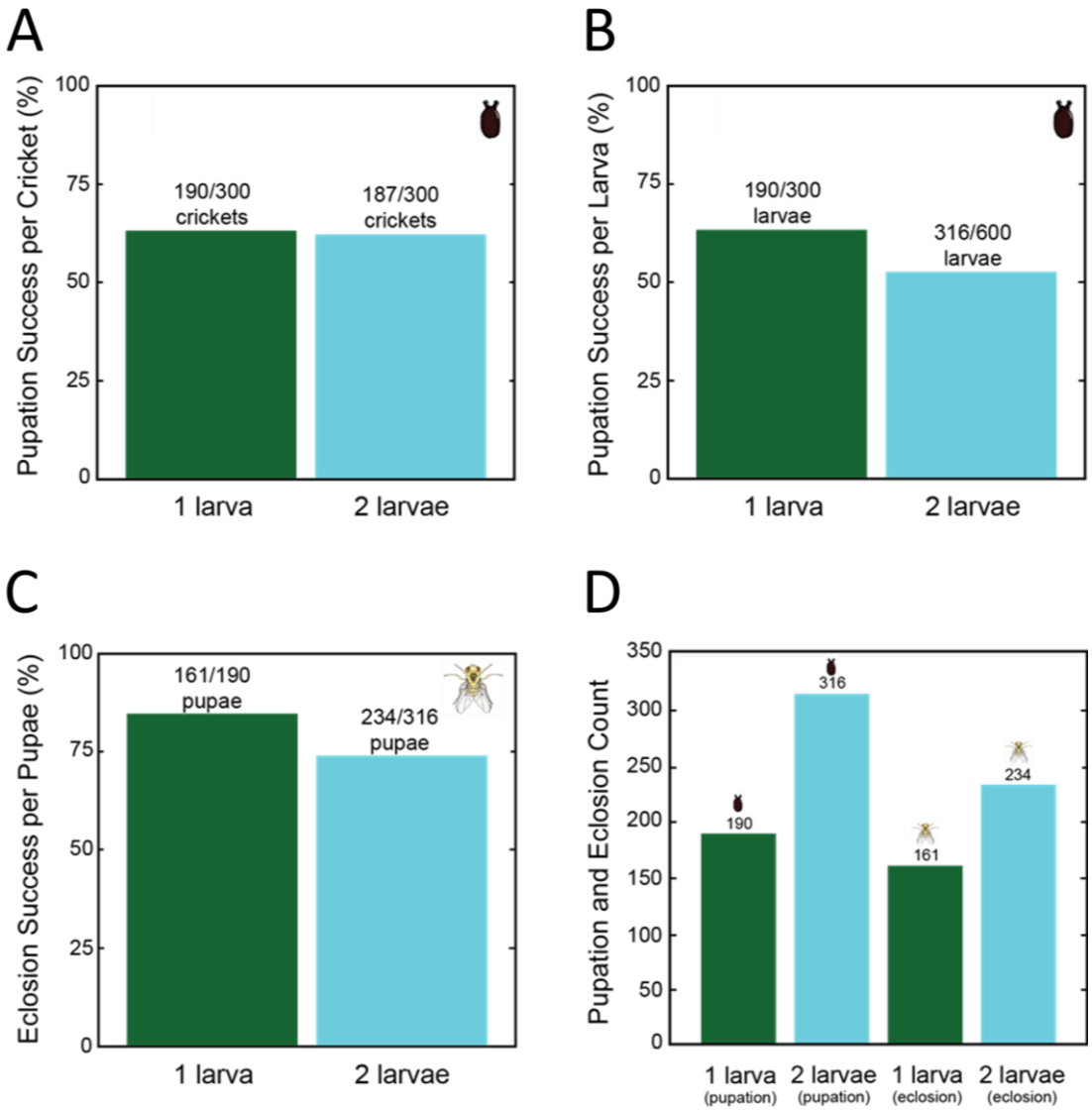

Figure 5.3 | Effect of resource competition on pupation and eclosion success. (A) Pupation success per *cricket*, the proportion of crickets yielding at least one pupa, did not differ between treatments. **(B)** Pupation success per *larva*, the proportion of individual larvae that successfully pupated, was significantly lower under competition. **(C)** Eclosion success per *pupa*, the proportion of pupae that successfully hatched into adult flies, was also reduced under competition. **(D)** Absolute counts of pupae and eclosed flies per treatment. Despite lower per-larva pupation and per-pupa eclosion success (B, C), total pupae and adult flies were higher in the two-larvae treatment due to the greater initial number of larvae per host. This resulted in an average reproductive output of 0.78 flies per cricket under double infestation versus 0.54 in the one-larva treatment. Dark green bars represent the one-larva treatment, and cyan bars represent the two-larvae competitive treatment.

infested hosts ($\chi^2(1) = 31.38$, $p < 0.001$). Likewise, double infestation led to 234 eclosed F1 flies, significantly exceeding the 161 adults obtained from the single-larva treatment ($\chi^2(1) = 13.49$, $p < 0.001$). This translates to an average reproductive output of 0.78 flies per cricket under double infestation, compared to 0.54 flies per cricket with a single larva.

5.3.2 Effect of Cricket Size on Fly Pupal Size

Among the crickets that yielded pupation (377/600, 62.83%), host size ranged from 2.55 to 3.30 mm in pronotum length and from 0.34 to 0.64 g in body mass. Of these, 241 were males and 265 were females. On average, males measured 2.62 ± 0.14 mm in pronotum length and weighed 0.32 ± 0.04 g, while females measured 4.75 ± 0.24 mm and weighed 0.43 ± 0.07 g.

Pronotum length of Gryllinae hosts was independently a significant predictor of fly pupal width ($\boldsymbol{\beta} = 0.264$, SE = 0.090, $t = 2.931$, $p = 0.004$). For every millimetre increase in host pronotum length, pupal width is expected to increase by approximately 0.26 mm. The overall model was statistically significant ($F(1,229) = 8.59$, $p = 0.004$). However, pronotum length explained only 3.20% of the variance in pupal width (Adjusted $R^2 = 0.032$).

Similarly, host mass was also independently a significant predictor of pupal width ($\boldsymbol{\beta} = 0.564$, SE = 0.237, $t = 2.382$, $p = 0.018$). For every gram increase in host body mass, pupal width is expected to increase by approximately 0.56 mm. The overall model was statistically significant ($F(1,229) = 5.68$, $p = 0.018$), though host mass explained only 1.99% of the variance in pupal width (Adjusted $R^2 = 0.020$).

A linear regression model was used in this thesis to examine the interactive effects of cricket mass and pronotum length on pupal width. The overall model was statistically significant ($F(3,227) = 3.57$, $p = 0.015$) but explained only 3.24% of the variance in pupal width (Adjusted $R^2 = 0.032$). Neither mass ($\boldsymbol{\beta} = 4.515$, SE = 3.247, $t = 1.390$, $p = 0.166$) nor pronotum length ($\boldsymbol{\beta} = 0.827$, SE = 0.470, $t = 1.760$, $p = 0.080$) were significant predictors. Additionally, the interaction between mass and pronotum length was non-significant ($\boldsymbol{\beta} = -1.575$, SE = 1.173, $t = -1.343$, $p = 0.181$).

5.3.3 Resource Competition on Fly Pupal and Adult Size

Resource competition significantly affected pupal width (Figure 5.4A). Pupae from crickets parasitised by a single larva were larger than those from crickets infested with two larvae ($W = 7810$, $p < 0.001$). Pupae that developed without competition were not only significantly larger than both pupae that emerged under the two-larvae treatment ($W = 3858.5$, $p < 0.001$), but also significantly larger than those that developed when only one of two larvae successfully pupated ($W = 3951.5$, $p = 0.022$). These latter pupae accounted for a subgroup of 18.35% (58/316) of all pupae in the two-larvae treatment and remained considerably larger than those from hosts where both larvae pupated, though this difference was not statistically significant ($W = 770$, $p = 0.083$).

Pupal width was a significant positive predictor of eclosion ($\boldsymbol{\beta} = 1.445$, SE = 0.454, $z = 3.180$, $p = 0.001$) (Figure 5.5A), based on pupae that emerged from double infestations, indicating that larger pupae had a higher probability of successfully eclosing into adult flies. At a pupal width of approximately 2.63 mm, 50% of the pupae can be expected to successfully eclose.

Larger pupae resulted in larger adult flies, as pupal width was a strong positive predictor of F1 mesothorax length ($\boldsymbol{\beta} = 0.616$, SE = 0.05, $t = 12.245$, $p < 0.001$) (Figure 5.5B). For every millimetre increase in pupal width, mesothorax length increased by approximately 0.62 mm. This relationship was highly significant ($F(1,158) = 149.9$, $p < 0.001$), with pupal width explaining nearly half of the variation in mesothorax length (Adjusted $R^2 = 0.48$).

Resource competition also significantly influenced adult fly size, as measured by F1 mesothorax length (Figure 5.5C). Flies that developed from larvae growing alone in their host (1-larva treatment) were significantly larger than those from hosts where two larvae co-developed and both successfully pupated ($W = 3773$, $p < 0.001$). However, they were not significantly larger than flies from a two-larvae infestation where only one larva successfully pupated ($W = 3818.5$, $p = 0.059$) – a group that accounted for 17.52% (41/234) of flies with a history of resource competition and produced significantly larger flies than those from double pupations ($W = 828$, $p = 0.016$). Nonetheless, flies

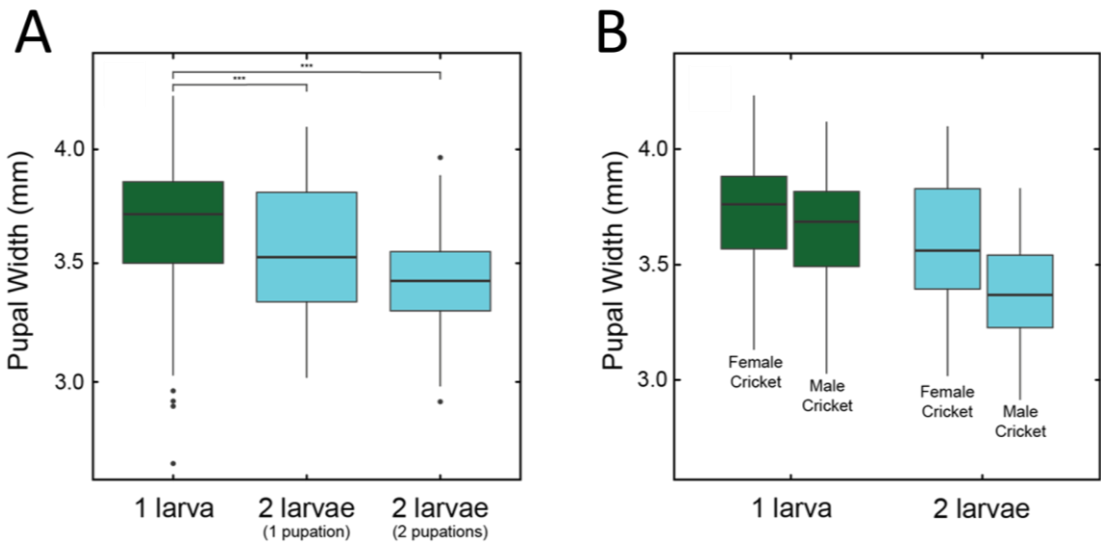

Figure 5.4 | Effects of resource competition and host sex on pupal size. **(A)** The size (width) of pupae was significantly reduced under resource competition. Pupae from singly parasitized crickets were larger than those from double infestations, whether both larvae pupated or only one did. Pupae from single-pupation double infestations (18.35% of pupae from the competitive treatment) remained larger than those from double pupations, though this difference was not significant. **(B)** Pupae from male crickets were typically smaller than from female crickets, regardless of larval treatment. Dark green represents the one-larva treatment, and cyan represents the two-larvae competitive treatment. Box plots depict the first and third quartiles, median values, with the length of the whiskers showing no less (lower) or more (upper) than 1.5 times the interquartile range.

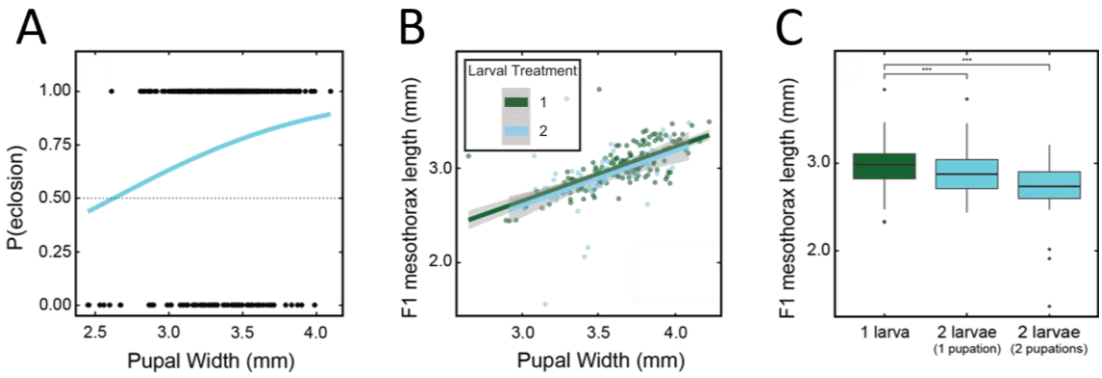

Figure 5.5 | Effect of pupal size and resource competition on adult fly size. (A) Larger pupae had a significantly higher probability of successful eclosion. Fitted line (cyan) from a generalized linear model with a binomial logit link predicts eclosion success. Dotted line depicts chance level (50%) success. Black data points indicate individual successful eclosion events (top), and unsuccessful eclosion events (bottom). **(B)** Pupal width strongly predicted eclosed fly size (mesothorax length) but did not depend on the level of competition. Lines of best fit and data points for 1 larva versus 2 larvae per host are indicated in green and cyan, respectively. **(C)** Adult fly size was significantly affected by resource competition. Flies that had developed in the absence of competition were significantly larger than those from a competitive treatment regardless of whether one or both larvae pupated. Among flies with a history of resource competition, those from a larva where the other larva failed to pupate were larger, but not significantly so. Dark green represents the one-larva treatment, and cyan represents the two-larvae competitive treatment. Box plots depict the first and third quartiles, median values, with the length of the whiskers showing no less (lower) or more (upper) than 1.5 times the interquartile range.

that developed without competition remained substantially larger than those from single pupations following a competitive treatment (p = 0.059).

5.4 Discussion: Quantity–Quality Trade-Offs and Larval Load

This thesis investigated the developmental outcomes of *Ormia ochracea* larvae in the presence and absence of resource competition while developing within *Acheta domesticus* as the host cricket. Although the likelihood of at least 1 larva pupating did not differ between hosts with 1 or 2 larvae (Figure 5.3A),

individual larvae in co-infested hosts exhibited reduced pupation (Figure 5.3B) and eclosion success (Figure 5.3C), indicating strong within-host competition. Competition also led to smaller pupal size (Figure 5.4A), which was associated with lower eclosion probability (Figure 5.5A). Additionally, pupae tended to be smaller when developing in male versus female crickets (Figure 5.4B). Finally, pupal size positively correlated with adult body size (Figure 5.5B), and the largest flies developed from larvae that did not experience competition (Figure 5.5C). These findings highlight the roles of host Gryllinae traits and larval competition in shaping parasitoid fly developmental outcomes.

Despite the negative effects of resource competition, this thesis found that 2-larva infestations resulted in significantly higher overall yield (Figure 5.3D). From the same number of hosts (300 crickets), double infestations produced 234 adult flies compared to 161 under single infestation, averaging 0.78 vs. 0.54 flies per host. Thus, infesting with 2 larvae per host led to a greater absolute number of offspring. In fact, across studies, the mean number of larvae that tachinid flies deposit per host is nearer to 2 than to 1: 1.7 ± 1.0 in Adamo et al. [139], 1.8 ± 1.2 in Kolluru and Zuk [142], 2.13 ± 0.18 and 1.92 ± 0.09 in Lehmann [168], and 2.28 ± 0.22 and 2.90 ± 0.19 in Reitz and Adler [171]. Interestingly, this is despite maximum reproductive yield being achieved with an even larger clutch size of 4 to 5 larvae [139, 168, 174], prompting the conclusion that there *"must be some ecological advantage"* to infesting with approximately 2 larvae rather than 4 or 5 [174].

Previous studies have shown that as clutch size increases from 1 to 4 larvae, the reproductive yield rises steadily while fitness (pupal size) consistently declines [139, 168, 170]. Lehmann [168] determined that as clutch size increased, pupal weight and the proportion of pupae hatching into adult flies decreased, and that over time smaller adult Ormiini flies may impact life-history traits or potentially the ability of parasitoid flies to locate hosts. Although this thesis tested only up to a 2-larvae regime, the results of this three-lab collaboration followed the same trend, with yield (quantity) increasing (Figure 5.3D) and fitness – pupal and adult size (quality) – declining with competition (Figures 5.4A and 5.5C). However, among the flies that developed under 2-

larvae conditions, this present study identified a subset (17.52%) that emerged from hosts in which the other larva failed to pupate. These flies were larger than those from hosts in which both larvae pupated. These findings not only raise the possibility of competitive exclusion [175] but also suggest that this subset may help offset the average fitness costs of 2-larvae infestations, offering a conceivable explanation for why natural clutch sizes tend towards two. However, the subset of 2 larvae (1 pupation) flies was not *significantly* larger.

This research demonstrates clear advantages to avoiding resource competition through single parasitisation. Larvae developing alone exhibited significantly higher pupation success per larva (Figure 5.3B) and eclosion success per pupa (Figure 5.3C). Consistent with previous findings [139, 168], singly infested larvae also produced significantly larger pupae (Figure 5.4A), which were more likely to eclose (Figure 5.5A) into larger adult flies (Figure 5.5B,C). In tachinids, such increases in size are closely linked to higher fecundity [170, 171, 173, 176]. These results therefore suggest that a single-larva parasitisation strategy may offer the most effective balance between reproductive yield (offspring quantity) and fitness (offspring quality).

Indeed, 1-larva parasitisation appears to be the most common (although not the mean-average) strategy employed by Ormiini flies. Adamo et al. [139] dissected *Gryllus* hosts, *G. texensis* (formerly *G. integer*), and *G. rubens*, naturally parasitised by *O. ochracea* and found that single-larva infestations predominated, occurring twice as often as the next most frequent clutch size of 2. A similar pattern was reported by Kolluru and Zuk [142], nearly twice as many single-larva infestations as double infestations in field-collected *Teleogryllus oceanicus* in Hawaii, also parasitised by *O. ochracea*. In another field study, Lehmann [168] compared 2 European species of bushcricket (katydids), *Poecilimon mariannae* and *Poecilimon thessalicus*, which are parasitised by the Ormiini fly *Therobia leonidei*, and found that *T. leonidei* mostly parasitised with a single larva, with over 50% of *P. mariannae* and 38% of *P. thessalicus* harbouring just 1 larva. Most frequently infesting a host with a single larva therefore appears to be a conserved strategy across diverse

host taxa and body sizes, in both natural and non-native hosts, suggesting it may be an inherent or adaptive trade-off for balancing yield and fitness.

If other variables such as host size also influence offspring quantity or quality, then Ormiini flies might be expected to modulate their clutch size accordingly. This strategy is known as clutch size adjustment [177] has been demonstrated in parasitoid wasps, where females lay more eggs in larger hosts to maximise reproductive return [178] whilst presumably maintaining offspring fitness. These findings align with evidence that parasitoid fitness scales with host size: Cohen et al. [125] reported larger hosts yielding correspondingly larger wasp parasitoids, while Lehmann [168] that the larger bushcricket species *P. mariannae* resulted in heavier pupae and positively influenced adult fly eclosion. In this thesis, larvae developing in female crickets tended to form larger pupae than those from males (Figure 5.4B), likely reflecting size differences between host sexes.

However, despite the significant between-species effect observed by Lehmann [168], the study found no significant within-species effect of host size on pupal size. Consistent with this finding, none of the models in this thesis showed that host size, whether measured as pronotum length or mass, significantly influenced pupal width. In the final published version of this chapter, Prof. Lee's table indicates that host sex was only borderline significant across the best models. In contrast, larval number consistently emerged as a strong predictor of pupal size [2]. Moreover, multiple studies on tachinid flies have shown that variations in host size do not influence the number of larvae deposited. *O. ochracea* did not increase larval number with larger *Gryllus* or *Teleogryllus* hosts [139, 142], *T. leonidei* showed no significant difference in brood size between large and small *Poecilimon* species [168], and *Ormia lineifrons* exhibited no difference in parasitoid load across 4 *Neoconocephalus* bushcricket species of varying sizes [179]. Together, these findings suggest that, for tachinid flies, the optimal number of larvae per host is constrained to a narrow range, rather than being contextually modulated via clutch size adjustment to exploit variation in the quality of Gryllinae hosts.

Given the limited influence of host cricket size on developmental outcomes, this may afford *O. ochracea*, which is known to parasitise a range of Gryllinae species [17, 129, 140, 180], increased plasticity in host switching. *O. ochracea* is native to the continental US, where geographically separated populations parasitise at least 17 species of field cricket, with certain fly populations exhibiting host specialisation by preferentially targeting the locally predominant cricket species [17, 133]. In Hawaii, *O. ochracea* was introduced without its ancestral hosts, and its behavioural plasticity in host choice has been evident from its successful exploitation of the Pacific field cricket, *Teleogryllus oceanicus*, a non-native cricket that has become its preferred host [146, 181]. More recently, rapid ongoing changes in host acoustic traits of crickets in Hawaii, including the emergence of multiple morphs of *T. oceanicus* that produce more cryptic songs, have dramatically altered the host Gryllinae signal landscape [182-186], potentially selecting for Hawaiian *O. ochracea* with more sensitive hearing [181, 187], and prompting host switching to the alternative cricket species in Hawaii [146].

Here, this thesis demonstrates that another non ancestral host *A. domesticus* is viable for propagating *O. ochracea* in the laboratory. Although few studies have examined its suitability, *A. domesticus* has previously been successfully used to rear laboratory populations [137]. Wineriter and Walker [140] described *A. domesticus* as *"less satisfactory"*, but their findings were influenced by cricket mortality unrelated to larval development, possibly due to housing conditions. To assess host viability, Thomson et al. [145] manually infested three species of Gryllus with 2 *O. ochracea* larvae per cricket and observed the highest larval emergence (pupation) success of 54% to 61% in the natural host cricket species *G. texensis*. Using the same methodology with two larvae, this thesis recorded a comparable success rate of 62.33% in *A. domesticus* (Figure 5.3A).

Chapter 6

Discussion

6.1 **Key Findings and the Revised Filtering–Transmission Model**

The key findings of this study culminate in a revised biomechanical model of frequency filtering and sound transmission in the field cricket (Gryllinae) ear. Collectively, these findings successfully fulfil the primary research aims of this research: (1) resolving the vibrational profile of the field cricket's posterior tympanal membrane; (2) uncovering the hypothesised mechanism of secondary frequency filtering within the peripheral auditory system, including processes occurring downstream of the posterior tympanum; (3) identifying the mechanical transmission pathway between the posterior tympanal membrane and the auditory neurons; and (4) employing X-ray micro-CT imaging to enable direct three-dimensional volumetric reconstruction and 3D morphometric analysis of the internal ear structures.

6.1.1 The Proposed Model

The model proposed here conceptualises frequency filtering and sound transmission in the field cricket peripheral auditory pathway as a sequential, mechanically coupled process. It begins with the ear's primary input, the posterior tympanum (PTM), characterised by a vibrational profile with two distinct optima at 6 kHz and 14 kHz (Aim 1). The 6 kHz peak arises from internal coupling with the dorsal membrane of the posterior tracheal branch,

which is posited to function as the first internal membrane downstream of the PTM in a series of independently tuned resonators operating in sequence. This series extends through the dividing membrane, which is inferred to amplify incoming energy from the PTM via combined mechanical leverage and surface-area reduction and then transmit this energy to the anterior tracheal branch (ATB) chamber, contributing to a frequency-specific deformation of the ATB beneath the supported sensilla. The final membrane, the ATB dorsal membrane, directly stimulates the sensilla and is proposed to resonate at an even lower frequency optimum, more closely matching the conspecific calling frequency. Collectively, these mechanically coupled membranes mediate both frequency filtering (Aim 2) and sound transmission (Aim 3), an integrated interpretation enabled by X-ray micro-CT imaging and 3D morphometric analysis (Aim 4).

6.1.2 Host–Parasitoid Interactions and Recommended Protocol

The secondary investigation of host–parasitoid interactions between *Acheta domesticus* and *Ormia ochracea* identifies resource competition as the key factor influencing parasitoid larval development, revealing a trade-off between offspring quantity and individual fitness (addressing Gap 6, Section 1.13). These findings establish *A. domesticus*, a readily commercially available species, as a viable laboratory model host for propagating *O. ochracea* colonies, despite not being a natural host (Gap 7). Given the labour-intensive difficulty of maintaining *O. ochracea* in laboratory settings, this represents a practical advance for laboratory-based research on *O. ochracea*. On this basis, a rearing protocol is recommended: utilising *A. domesticus* as a model host; parasitising each host with a single larva to maximise individual offspring fitness; and preferentially selecting female hosts.

6.1.3 Contributions to Knowledge

This research has contributed the following to knowledge, as published in Latham et al. (2024) [1] (Appendix C):

1. Using scanning laser Doppler vibrometry (LDV), this research has advanced understanding of the vibrational profile of the primary sound input of the field cricket (Gryllinae) acoustical system, the posterior tympanal membrane (PTM), revealing, contrary to recent literature [12, 27], that the large tympanum resonates with two distinct frequency optima, at approximately 6 kHz and 14 kHz.
2. Phase response data obtained through LDV presented here show that the first PTM vibrational peak (6 kHz) exhibits characteristics of a *driving resonance* likely driven by the internally coupled dorsal membrane of the posterior tracheal branch, rather than from the tympanum itself. In contrast, this thesis has also identified the second peak (14 kHz) as the natural resonance of the membrane. These findings provide new evidence in support of a longstanding secondary filtering hypothesis [8, 10, 12, 26] and help to elucidate the first stages of the *"enigmatic"* [15] transmission pathway between the PTM and the sensory neurons.
3. Evidence from both X-ray micro-computed tomography (micro-CT) and micro-CT-based finite element analysis (FEA) point to the coupled resonance potential of a previously largely overlooked structure, here termed the 'dividing membrane'.
4. FEA results further suggest a train of independently tuned coupled resonators.
5. FEA results also point to a possible membrane-mediated frequency-specific volume change of the anterior tracheal branch supporting the auditory sensilla.

Via a co–lead-author three-lab, three-country collaboration, as published in Dominguez, Latham et al. (2025) [2] (Appendix B), this research has made the following further contributions to knowledge:

6. Using the field cricket *Acheta domesticus* as a host, this thesis identifies *resource competition* as a principal factor influencing the developmental outcomes of the parasitoid fly *Ormia ochracea*. Infesting *A. domesticus* with two larvae significantly increased offspring *yield* (quantity), with a

reproductive output of 0.78 flies per host compared to 0.54 via single-larva parasitisation. Nevertheless, larvae in the absence of resource competition developed into significantly larger pupae and hatched adult flies, indicating superior individual *fitness* (quality). In addition, in the absence of resource competition, a higher proportion of individuals reached pupation and successfully hatched as adults.

7. Among the pupae and flies that developed from a competitive treatment, this thesis identifies a subset of approximately 18% in which the other larva failed to pupate. Individuals from this subset were larger (though not significantly so) than those from hosts where both larvae successfully developed, suggesting the possibility of *competitive exclusion* perhaps helping to offset the fitness costs of resource competition.
8. A borderline effect of host cricket sex was also found to influence pupal size, with female crickets tending to produce slightly larger *O. ochracea* pupae.
9. Finally, this thesis validates the *A. domesticus* field cricket as a viable host for maintaining *O. ochracea* colonies in the laboratory and recommends a lab-rearing protocol of manually parasitising each preferably female *A. domesticus* host with a single larva to maximise individual offspring fecundity.

6.2 **Host–Parasitoid Interactions and Competitive Exclusion**

The additional study on host–parasitoid Gryllinae–Ormiini interactions showed that, among host crickets parasitised by two fly larvae, around 18% of the resulting adult flies developed under conditions in which only one of the two larvae successfully pupated (i.e., the second larva failed to complete development and emerge from the cricket). These sole individuals from a 2-larvae treatment were considerably larger than flies that had developed from hosts in which both larvae successfully pupated. This finding suggests a possible role for competitive exclusion.

Specifically, one larva may outcompete the other for access to limited resources within a Gryllinae host, thereby gaining a developmental advantage. This form of competitive exclusion may serve an ecological function for *Ormia ochracea* by partially offsetting the fitness costs associated with multi-larval parasitism. Accordingly, whether the pattern identified in this study does indeed reflect competitive exclusion, and, if so, what ecological role it may serve, warrants further investigation.

Nevertheless, despite the suggestion of a possible competitive exclusion role in mitigating the negative effects of a two-larva regime, a one-larva protocol is here recommended. For the maintenance and propagation of *O. ochracea* laboratory colonies, the recommended protocol is to introduce a single larva into each host, preferably a female *Acheta domesticus*, to maximise individual offspring fecundity.

These insights were derived from an experimental design that relied on manual infestations. The ability of *O. ochracea* to naturally parasitise *A. domesticus* remains unexplored and therefore also merits further investigation.

6.3 **The Dividing Membrane**

An unexpected finding from the primary biomechanics study is the identification of a structure here termed the dividing membrane (DivM), a component of the Gryllinae auditory apparatus that has hitherto been largely overlooked. Most anatomical investigations of the field cricket ear do not mention this structure [15, 23, 29].

Using X-ray micro-CT imaging and 3D thickness analysis, this study indicates that the DivM, which separates the two tracheal branches, may serve an important auditory role. This is supported by (i) its coupling to the dorsal membrane of the posterior tracheal branch, which is itself coupled to the PTM, and (ii) a thickness comparable to that of these two coupled structures.

The dividing membrane was initially overlooked in this study as well. Its coupling and resonance potential only became apparent following the application of a 3D thickness colour map. Further validation was subsequently

provided through light microscopy, statistical evaluation, and numerical modelling.

Nevertheless, this structure has received some prior consideration. The tracheal branches have been described as being separated by a cuticular wall [30]. This separating feature was also later referred to as a partition [10], and a potential auditory role was proposed, speculating it acts as a pressure-difference receiver similar to the posterior tympanum. Although this role was considered unlikely, the proposal indicates that the DivM has previously been recognised as a potentially resonant structure within the peripheral auditory pathway.

Moreover, it has long been acknowledged that solid–solid coupling between the PTM and adjacent tracheal branches may provide a pathway for transmission to the sensory neurons [10, 14, 15, 27]. Furthermore, transmission from the PTM is likely via the tracheal walls of the PTB and ATB [10], while the PTM–PTB–ATB configuration is suggestive of a coupled system [27].

Here, evidence is presented supporting PTM–tracheal coupling as a viable transmission pathway. X-ray micro-CT thickness analysis identifies the dividing membrane as a potential resonator. Furthermore, micro-CT-based FEA modelling indicates that the DivM enhances PTM transmission, contributes to ATB volume fluctuations beneath the sensilla, and resonates at a specific frequency. A defined pathway is therefore presented, involving tracheal coupling that enables both transmission and filtering – from the posterior tympanum to the dividing membrane via the intermediary dorsal membrane of the posterior tracheal branch.

6.4 **Tracheal Coupling in Other Ensiferans**

The tracheal branches of the ensiferan ear have previously been thought to function mainly to channel sound in the air column to the tympana [188], rather than providing any frequency filtering or mechanical transmission role as presented here. However, in 2021, the bushcricket (Tettigoniidae) tracheal septum, a structure that is analogous to the Gryllinae dividing membrane, was

shown through optical coherence tomography (OCT) to move in phase with the PTM, indicating a role in mechanically coupling transmission from the PTM to the sensory neurons [189]. In the same year, an OCT study on the tree cricket (Oecanthinae) acoustic trachea revealed similar results [188]. While the morphology of the Gryllinae tracheal branches differs from that of these other ensiferans, the findings presented here align with these studies and reinforce the importance of future investigations into how tracheal structures in Ensifera mechanically transmit and filter signals from the tympana to the auditory sensilla.

6.5 **Gryllinae Filtering–Transmission and the Mammalian Ear**

This study provides evidence for a *second filter* (Figure 6.1), as previously hypothesised and compared to the mammalian ear [8]. Key findings on filtering and transmission are presented here alongside those of the mammalian system.

FEA simulations from this study indicates that the ATB dorsal membrane resonates at a lower frequency than the adjacent DM–PTB, concentrated at 5.1 kHz. This is closer to the 4.7 kHz calling song carrier frequency than any other modelled membrane. The progressive shift towards lower resonant frequencies indicates, for the first time, not just a single additional filter downstream of the PTM, but a chain of multiple internal membrane filters, each tuned to different frequencies.

If correct, this multi-filter model may help explain earlier observations in which restricting PTM motion eliminated high-frequency responses while lower-frequency (around 4 kHz) auditory neuron responses persisted [56], potentially due to continued resonance within one or more of the internal membranes.

From the primary finite element model, at the PTM dominant frequency (10.7 kHz), the force transmitted through the dividing membrane was approximately 34 times greater than the PTM input. This indicates that the DivM is the most effective of the three internal membranes in amplifying force. A comparable mechanism is seen in vertebrate hearing, where mechanically

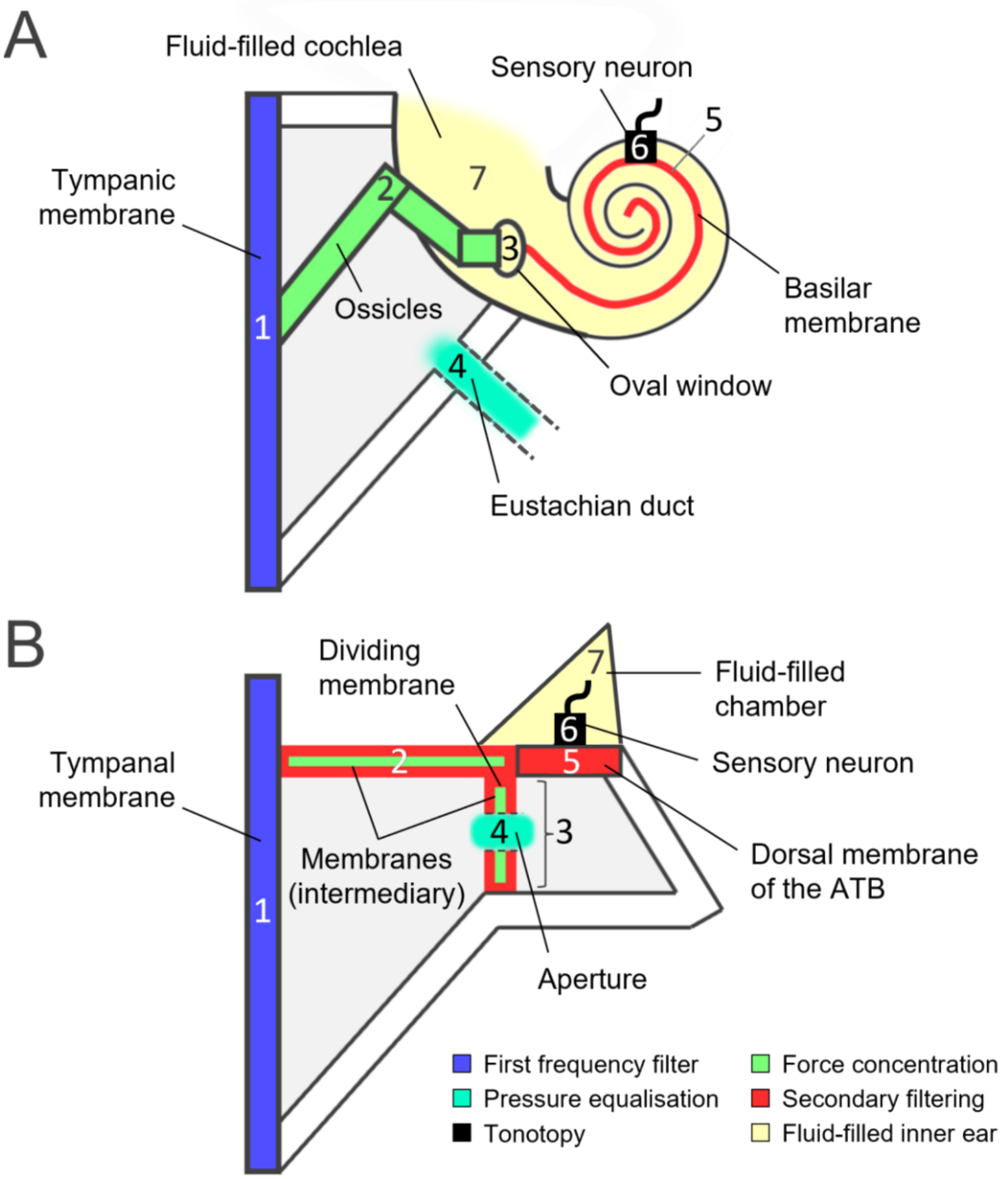

Figure 6.1 | Proposed Gryllinae analogues to well-characterised mammalian ear mechanisms. The field cricket ear may exhibit a sequence of mechanisms analogous to those of the canonical mammalian system. Both **(A)** the mammalian ear and **(B)** the Gryllinae ear can be interpreted as employing: (1) a tympanum for initial sound capture and frequency filtering; (2) coupled mechanical levers to concentrate force onto (3) a smaller surface area; (4) an aperture-based mechanism for pressure equalisation, protecting the sensory cavity from barotrauma; (5) an internal membranous mechanism for secondary frequency filtering; (6) coupling of tonotopically arranged sensilla to a secondary filtering membrane; and (7) immersion of the sensilla within a fluid-filled chamber, facilitating their stimulation.

coupled elements concentrate force onto a smaller interface, increasing acoustic energy [190] (Figure 6.1).

Force concentration transmitted through the dividing membrane may lead to volumetric expansion of the ATB cavity. The DivM, positioned at the interface with the ATB, is well placed to facilitate this effect, and indeed its presence was found to decrease the extent of ATB volumetric fluctuation and affect its frequency filtering. While previous work speculated that ATB volume changes might arise from airflow through the apertures [15], the present study found that air column pressure remains largely unchanged when driven by the PTM. Moreover, even if spiracular input could alter internal pressure, sensory neurons do not appear to respond to pressure changes alone [14]. The air column is therefore unlikely to play a significant role in frequency tuning. Although direct membrane stimulation via the spiracles cannot be fully excluded, such a mechanism would make the PTM redundant, which contradicts extensive evidence identifying it as the primary auditory input and *first frequency filter* [5, 7, 14, 26].

Instead, this study identifies membrane-driven peaks in ATB volume fluctuation beginning at 4.8 kHz, enhanced by the DivM. These results support an alternative mechanism for ATB inflation. The apertures are therefore unlikely to act as airflow pathways for volume increase, as previously suggested [15]. Rather, they may serve a protective role by *equalising pressure* within the ATB sensory cavity, analogous to the function of the Eustachian tube in the mammalian ear [191] (Figure 6.1).

6.6 **Possibility of a Travelling Wave in the Gryllinae Ear**

Unlike the bushcricket ear [92], the means of tonotopy in the field cricket remains undefined, although it has been suggested to involve a travelling wave [11]. Applying optical coherence tomography to the Gryllinae ear would provide direct measurements of the internal membranes highlighted here, as would LDV recordings if the identified membranes could be exposed without compromising the integrity of the whole system. Such direct experimental

measurements, especially of the dorsal membrane of the anterior tracheal branch supporting the sensilla, may elucidate a travelling wave if present.

While no direct evidence of a morphological gradient sufficient to support a travelling wave is here identified, several morphological observations suggest the possibility for a facilitated travelling wave. The anterior tracheal branch exhibits a morphological progression, transitioning from a relatively bulbous proximal region to a narrower distal form, and this graded morphology is also broadly aligned with the tonotopic organisation of the sensilla along its length. In addition, finite element simulations in this study of ATB inflation and deflation indicate a possibly non-uniform pattern of displacement, with larger, more proximal regions tending to exhibit greater motion, suggestive of a graded mechanical response. Finally, the identified dividing membrane displays a wedge-like morphology, reminiscent of tapering structures associated with travelling wave systems such as the bushcricket *crista acustica* – It is therefore conceivable that a travelling wave propagation along the DivM could interact with the adjacent ATB cavity, producing spatially progressive, frequency-dependent displacements that may contribute to stimulating the overlying sensilla.

6.7 **Neuroethological Insights and Potential Bioinspired Applications**

An integral part of the field cricket's value as a neuroethological model [25] lies in its frequency tuning at each stage of the auditory pathway [11]. Building on the present study, continued clarification of the biomechanical basis of this pathway may help contextualise frequency filtering at the downstream neural and behavioural levels.

Lastly, the chain of coupled membranes proposed here, capable of facilitating both filtering and transmission on the microscale, is noteworthy. Despite being unusually small [15], the Gryllinae ear is sharply tuned to low frequencies [6] and is capable of spectral decomposition [20]. The microscale membranes characterised in this study may therefore be relevant to the bioinspiration of improved microelectromechanical systems (MEMS) diaphragm microphones, such as those used in modern smartphones and

hearing aids [43]. This prospect is especially compelling given that the Orminii fly ear, tuned to precisely the same Gryllinae frequency cue, has already inspired at least 10 patented MEMS microphone designs [38]. Further experimental testing of the biomechanical filtering–transmission model presented here may therefore prove fruitful.

Bibliography

The references in this work have been formatted according to the *IEEE* (Institute of Electrical and Electronics Engineers) citation style. References are listed in the order in which they appear in the body text, with numerical in-text citations enclosed in square brackets.

[1] B. Latham, A. Reid, J. C. Jackson-Camargo, J. A. Williams, and J. F. Windmill, "Coupled membranes: a mechanism of frequency filtering and transmission in the field cricket ear evidenced by micro-computed tomography, laser Doppler vibrometry and finite element analysis," *Journal of the Royal Society Interface,* vol. 21, no. 214, p. 20230779, 2024.

[2] J. A. Dominguez, B. Latham *et al.*, "Resource competition affects developmental outcomes of the acoustic parasitoid fly Ormia ochracea," *Annals of the Entomological Society of America,* p. saaf018, 2025.

[3] K. Kostarakos, M. R. Hennig, and H. Römer, "Two matched filters and the evolution of mating signals in four species of cricket," *Frontiers in Zoology,* vol. 6, pp. 1-12, 2009.

[4] C.-C. Lin and B. Hedwig, "Wing movements underlying sound production in calling, rivalry, and courtship songs of the cricket Gryllus bimaculatus (DeGeer)," *Journal of Insect Physiology,* vol. 134, p. 104299, 2021.

[5] K. Hill, "Carrier frequency as a factor in phonotactic behaviour of female crickets (Teleogryllus commodus)," *Journal of comparative physiology,* vol. 93, pp. 7-18, 1974.

[6] S. Schöneich and B. Hedwig, "Hyperacute directional hearing and phonotactic steering in the cricket (Gryllus bimaculatus deGeer)," *PLoS One,* vol. 5, no. 12, p. e15141, 2010.

[7] J. A. Paton, R. R. Capranica, P. R. Dragsten, and W. W. Webb, "Physical basis for auditory frequency analysis in field crickets (Gryllidae)," *Journal of comparative physiology,* vol. 119, pp. 221-240, 1977.

[8] O. N. Larsen and A. Michelsen, "Biophysics of the ensiferan ear: III. The cricket ear as a four-input system," *Journal of comparative physiology,* vol. 123, pp. 217-227, 1978.

[9] O. N. Larsen, "Mechanical time resolution in some insect ears: II. Impulse sound transmission in acoustic tracheal tubes," *Journal of comparative physiology,* vol. 143, pp. 297-304, 1981.

[10] O. N. Larsen, H.-U. Kleindienst, and A. Michelsen, "Biophysical aspects of sound reception," in *Cricket behavior and neurobiology*: Cornell University Press, 1989, pp. 364-390.

[11] B. Hedwig and A. Stumpner, "Central Neural Processing of Sound Signals in Insects," in *Insect Hearing*, (Springer Handbook of Auditory Research, 2016, ch. Chapter 8, pp. 177-214.

[12] M. J. Lankheet, U. Cerkvenik, O. N. Larsen, and J. L. van Leeuwen, "Frequency tuning and directional sensitivity of tympanal vibrations in the field cricket Gryllus bimaculatus," *Journal of The Royal Society Interface,* vol. 14, no. 128, p. 20170035, 2017.

[13] K. Hill and G. Boyan, "Sensitivity to frequency and direction of sound in the auditory system of crickets (Gryllidae)," *Journal of comparative physiology,* vol. 121, no. 1, pp. 79-97, 1977.

[14] H. U. Kleindienst, D. W. Wohlers, and O. N. Larsen, "Tympanal membrane motion is necessary for hearing in crickets," *Journal of Comparative Physiology□ A,* vol. 151, no. 4, pp. 397-400, 1983.

[15] H. Nishino, M. Domae, T. Takanashi, and T. Okajima, "Cricket tympanal organ revisited: morphology, development and possible functions of the adult-specific chitin core beneath the anterior tympanal membrane," *Cell Tissue Res,* vol. 377, no. 2, pp. 193-214, Aug 2019.

[16] F. Libersat, J. Murray, and R. Hoy, "Frequency as a releaser in the courtship song of two crickets, Gryllus bimaculatus (de Geer) and Teleogryllus oceanicus: a neuroethological analysis," *Journal of Comparative Physiology A,* vol. 174, pp. 485-494, 1994.

[17] D. A. Gray, C. Banuelos, S. E. Walker, W. H. Cade, and M. Zuk, "Behavioural specialization among populations of the acoustically orienting parasitoid fly Ormia ochracea utilizing different cricket species as hosts," *Animal Behaviour,* vol. 73, no. 1, pp. 99-104, 2007/01/01/ 2007.

[18] W. Cade, "Acoustically orienting parasitoids: fly phonotaxis to cricket song," *Science,* vol. 190, no. 4221, pp. 1312-1313, 1975.

[19] H. Romer, "Directional hearing in insects: biophysical, physiological and ecological challenges," *J Exp Biol,* vol. 223, no. Pt 14, Jul 30 2020.

[20] B. Oldfield, H. U. Kleindienst, and F. Huber, "Physiology and tonotopic organization of auditory receptors in the cricket Gryllus bimaculatus DeGeer," *Journal of Comparative Physiology A,* vol. 159, pp. 457-464, 1986.

[21] A. Michelsen, "The tuned cricket," *Physiology,* vol. 13, no. 1, pp. 32-38, 1998.

[22] F. Montealegre-Z, T. Jonsson, and D. Robert, "Sound radiation and wing mechanics in stridulating field crickets (Orthoptera: Gryllidae)," *Journal of Experimental Biology,* vol. 214, no. 12, pp. 2105-2117, 2011.

[23] D. Young and E. Ball, "Structure and development of the auditory system in the prothoracic leg of the cricket Teleogryllus commodus (Walker)," *Zeitschrift für Zellforschung und mikroskopische Anatomie,* vol. 147, no. 3, pp. 293-312, 1974.

[24] H. M. Ter Hofstede, S. Schöneich, T. Robillard, and B. Hedwig, "Evolution of a communication system by sensory exploitation of startle behavior," *Current Biology,* vol. 25, no. 24, pp. 3245-3252, 2015.

[25] S. Schöneich, "Neuroethology of acoustic communication in field crickets-from signal generation to song recognition in an insect brain," *Progress in Neurobiology,* vol. 194, p. 101882, 2020.

[26] A. Popov, A. Michelsen, and B. Lewis, "Changes in the mechanics of the cricket ear during the early days of adult life," *Journal of Comparative Physiology A,* vol. 175, pp. 165-170, 1994.

[27] E. S. Schneider, H. Romer, T. Robillard, and A. K. D. Schmidt, "Hearing with exceptionally thin tympana: Ear morphology and tympanal membrane vibrations in eneopterine crickets," *Sci Rep,* vol. 7, no. 1, p. 15266, Nov 10 2017.

[28] K. Michel, "Das tympanalorgan von Gryllus bimaculatus Degeer (saltatoria, gryllidae)," *Zeitschrift für Morphologie der Tiere,* vol. 77, pp. 285-315, 1974.

[29] E. Eibl, "Morphology of the sense organs in the proximal parts of the tibiae of Gryllus campestris L. and Gryllus bimaculatus deGeer (Insecta, Ensifera)," *Zoomorphologie,* vol. 89, pp. 185-205, 1978.

[30] M. H. Friedman, "An electron microscopic study of the tympanal organ and associated structures in the foreleg tibia of the cricket, Gryllus assimilis," *J Morphol,* vol. 138, no. 3, pp. 329-47, Nov 1972.

[31] J. Schwabe, *Beiträge zur Morphologie und Histologie der tympanalen Sinnesapparate der Orthopteren*. E. Schweizerbartsche Verlagsbuchhandlung (E. Nägele), 1906.

[32] N. E. Stork, "How many species of insects and other terrestrial arthropods are there on Earth?," *Annual review of entomology,* vol. 63, no. 2018, pp. 31-45, 2018.

[33] M. D. Greenfield, "Evolution of acoustic communication in insects," in *Insect hearing*: Springer, 2016, pp. 17-47.

[34] B. Warren and M. Nowotny, "Bridging the gap between mammal and insect ears–A comparative and evolutionary view of sound-reception," *Frontiers in Ecology and Evolution,* vol. 9, p. 667218, 2021.

[35] D. D. Yager and R. R. Hoy, "The cyclopean ear: a new sense for the praying mantis," *Science,* vol. 231, no. 4739, pp. 727-729, 1986.

[36] L. A. Miller, "Structure of the green lacewing tympanal organ (Chrysopa carnea, Neuroptera)," *Journal of Morphology,* vol. 131, no. 4, pp. 359-382, 1970.

[37] R. Miles, D. Robert, and R. Hoy, "Mechanically coupled ears for directional hearing in the parasitoid fly Ormia ochracea," *The Journal of the Acoustical Society of America,* vol. 98, no. 6, pp. 3059-3070, 1995.

[38] Y. Zhang, A. Reid, and J. F. C. Windmill, "Insect-inspired acoustic micro-sensors," *Current opinion in insect science,* vol. 30, pp. 33-38, 2018.

[39] D. J. Mackie, "Biologically inspired acoustic systems, from insect ears to MEMS microphone structures," 2015.

[40] L. Díaz-García, A. Reid, J. C. Jackson-Camargo, and J. F. Windmill, "Toward a bio-inspired acoustic sensor: Achroia grisella's ear," *IEEE Sensors Journal,* vol. 22, no. 18, pp. 17746-17753, 2022.

[41] S. Martinelli, J. Windmill, and A. B. Reid, "3D printed sensor inspired by trichoid sensilla of insects, early studies of the mechanical structure," *Invertebrate Sound and Vibration 2023,* 2023.

[42] J. F. C. Windmill and J. C. Jackson, "Mechanical Specializations of Insect Ears," in *Insect Hearing*, (Springer Handbook of Auditory Research, 2016, ch. Chapter 6, pp. 125-157.

[43] M. A. Shah, I. A. Shah, D.-G. Lee, and S. Hur, "Design Approaches of MEMS Microphones for Enhanced Performance," *Journal of Sensors,* vol. 2019, pp. 1-26, 2019.

[44] T. R. Neil, Z. Shen, D. Robert, B. W. Drinkwater, and M. W. Holderied, "Moth wings are acoustic metamaterials," *Proceedings of the National Academy of Sciences,* vol. 117, no. 49, pp. 31134-31141, 2020.

[45] D. Robert, R. Miles, and R. Hoy, "Directional hearing by mechanical coupling in the parasitoid fly Ormia ochracea," *Journal of Comparative Physiology A,* vol. 179, no. 1, pp. 29-44, 1996.

[46] H. Xu, X. Xu, H. Jia, L. Guan, and M. Bao, "A biomimetic coupled circuit based microphone array for sound source localization," *The Journal of the Acoustical Society of America,* vol. 138, no. 3, pp. EL270-EL275, 2015.

[47] N. Ono, A. Saito, and S. Ando, "Design and experiments of bio-mimicry sound source localization sensor with gimbal-supported circular diaphragm," in *TRANSDUCERS '03. 12th International Conference on Solid-State Sensors, Actuators and Microsystems. Digest of Technical Papers (Cat. No.03TH8664)*, 8-12 June 2003 2003, vol. 1, pp. 935-938 vol.1.

[48] C. C. Chen and Y. T. Cheng, "Physical Analysis of a Biomimetic Microphone With a Central-Supported (C-S) Circular Diaphragm for Sound Source Localization," *IEEE Sensors Journal,* vol. 12, no. 5, pp. 1504-1512, 2012.

[49] C. Gibbons and R. Miles, "Design of a biomimetic directional microphone diaphragm," in *ASME International Mechanical Engineering Congress and Exposition*, 2000, vol. 19098: American Society of Mechanical Engineers, pp. 173-179.

[50] K. Yoo *et al.*, "Fabrication of a biomimetic corrugated polysilicon diaphragm with attached single crystal silicon proof masses," in *Transducers' 01 Eurosensors XV: The 11th International Conference on Solid-State Sensors and Actuators June 10–14, 2001 Munich, Germany*, 2001: Springer, pp. 130-133.

[51] R. N. Miles, Y. Liu, Q. Su, and E. Cui, "A silicon directional microphone with second-order directivity," in *Proc. Inter. Congress Acoust*, 2007.

[52] J. Pourghader *et al.*, "Bioinspired flow-sensing capacitive microphone," *The Journal of the Acoustical Society of America,* vol. 157, no. 5, pp. 3897-3906, 2025.

[53] R. N. Miles *et al.*, "A low-noise differential microphone inspired by the ears of the parasitoid fly Ormia ochracea," *The Journal of the Acoustical Society of America,* vol. 125, no. 4, pp. 2013-2026, 2009.

[54] A. Reid, "Directional hearing at the micro-scale: bio-inspired sound localization," 2017.

[55] Y. Zhang, R. Bauer, J. C. Jackson, W. M. Whitmer, J. F. Windmill, and D. Uttamchandani, "A low-frequency dual-band operational microphone mimicking the hearing property of Ormia ochracea," *Journal of Microelectromechanical Systems,* vol. 27, no. 4, pp. 667-676, 2018.

[56] H. Nocke, "Physiological aspects of sound communication in crickets (Gryllus campestris L.)," *Journal of comparative physiology,* vol. 80, pp. 141-162, 1972.

[57] K. Imaizumi and G. S. Pollack, "Neural coding of sound frequency by cricket auditory receptors," *Journal of Neuroscience,* vol. 19, no. 4, pp. 1508-1516, 1999.

[58] Y. Zhang, A. Reid, and J. F. C. Windmill, "Insect-inspired acoustic micro-sensors," *Curr Opin Insect Sci,* vol. 30, pp. 33-38, Dec 2018.

[59] Images-Of-Research-Competition. [Online]. Available: https://www.strath.ac.uk/workwithus/publicengagement/publicevents/imagesofresearch/2024/exploringtheunseen/eartoear/.

[60] UK-Canada-Doctoral. [Online]. Available: https://www.ukri.org/opportunity/uk-canada-globalink-doctoral-exchange-scheme-2/.

[61] 3-Minute-Thesis. [Online]. Available: https://vitae.ac.uk/support-services/vitae-three-minute-thesis-3mt-competition/.

[62] Glasgow-Science-Festival-2024. [Online]. Available: https://pureportal.strath.ac.uk/en/activities/glasgow-science-festival-2024-did-you-know-you-can-see-sound.

[63] Pint-Of-Science-2022. [Online]. Available: https://pintofscience.co.uk/event/Sine-Language.

[64] G. S. Pollack and R. R. Hoy, "Temporal pattern as a cue for species-specific calling song recognition in crickets," *Science,* vol. 204, no. 4391, pp. 429-432, 1979.

[65] C. Couchoux and T. Dabelsteen, "Acoustic cues to individual identity in the rattle calls of common blackbirds: a potential for individual recognition through multi-syllabic vocalisations emitted in both territorial and alarm contexts," *Behaviour,* vol. 152, no. 1, pp. 57-82, 2015.

[66] K. H. Kochvar, S. Peters, M. N. Zipple, and S. Nowicki, "Maturational changes in song sparrow song," *Journal of Avian Biology,* vol. 2022, no. 1, 2022.

[67] N. Stange and B. Ronacher, "Grasshopper calling songs convey information about condition and health of males," *Journal of Comparative Physiology A,* vol. 198, no. 4, pp. 309-318, 2012.

[68] Wave_Britannica. [Online]. Available: https://www.britannica.com/science/wave-physics.

[69] B. Mortimer, A. Soler, C. R. Siviour, R. Zaera, and F. Vollrath, "Tuning the instrument: sonic properties in the spider's web," *Journal of The Royal Society Interface,* vol. 13, no. 122, p. 20160341, 2016.

[70] L. Díaz-García, B. Latham, A. Reid, and J. Windmill, "Review of the applications of principles of insect hearing to microscale acoustic engineering challenges," *Bioinspiration & Biomimetics,* vol. 18, no. 5, p. 051002, 2023.

[71] A. Michelsen, A. Popov, and B. Lewis, "Physics of directional hearing in the cricket Gryllus bimaculatus," *Journal of Comparative Physiology A,* vol. 175, pp. 153-164, 1994.

[72] A. Michelsen and G. Löhe, "Tuned directionality in cricket ears," *Nature,* vol. 375, no. 6533, pp. 639-639, 1995.

[73] K. M. Seagraves and B. Hedwig, "Phase shifts in binaural stimuli provide directional cues for sound localisation in the field cricket Gryllus bimaculatus," *J Exp Biol,* vol. 217, no. Pt 13, pp. 2390-8, Jul 1 2014.

[74] G. S. Pollack, "Insect bioacoustics," *Acoustics Today,* vol. 13, no. 2, pp. 26-34, 2017.

[75] N. Skals and A. Surlykke, "Hearing and evasive behaviour in the greater wax moth, Galleria mellonella (Pyralidae)," *Physiological Entomology,* vol. 25, no. 4, pp. 354-362, 2000.

[76] M. Hutchings and B. Lewis, "Response properties of primary auditory fibers in the cricket Teleogryllus oceanieus (Le Guillou)," *Journal of comparative physiology,* vol. 143, no. 1, pp. 129-134, 1981.

[77] A. W. Orr, B. P. Helmke, B. R. Blackman, and M. A. Schwartz, "Mechanisms of mechanotransduction," *Developmental cell,* vol. 10, no. 1, pp. 11-20, 2006.

[78] B. Fritzsch and H. Straka, "Evolution of vertebrate mechanosensory hair cells and inner ears: toward identifying stimuli that select mutation driven altered morphologies," *Journal of Comparative Physiology A,* vol. 200, no. 1, pp. 5-18, 2014/01/01 2014.

[79] R. Fettiplace and P. A. Fuchs, "Mechanisms of hair cell tuning," *Annual review of physiology,* vol. 61, no. 1, pp. 809-834, 1999.

[80] R. G. Kavlie and J. T. Albert, "Chordotonal organs," *Current Biology,* vol. 23, no. 9, pp. R334-R335, 2013.

[81] L. H. Field and T. Matheson, "Chordotonal organs of insects," in *Advances in insect physiology*, vol. 27: Elsevier, 1998, pp. 1-228.

[82] J. E. Yack, "The structure and function of auditory chordotonal organs in insects," *Microscopy research and technique,* vol. 63, no. 6, pp. 315-337, 2004.

[83] D. D. Yager, "Structure, development, and evolution of insect auditory systems," *Microscopy Research and Technique,* vol. 47, no. 6, pp. 380-400, 1999.

[84] M. Roy, E. Sivan-Loukianova, and D. F. Eberl, "Cell-type–specific roles of Na+/K+ ATPase subunits in Drosophila auditory mechanosensation," *Proceedings of the National Academy of Sciences,* vol. 110, no. 1, pp. 181-186, 2013.

[85] A. Chaiyasitdhi, M. Nowotny, M. Van der Heijden, and B. Warren, "A stretching mechanism evokes mechano-electrical transduction in auditory chordotonal neurons," *bioRxiv,* p. 2025.06. 27.662008, 2025.

[86] M. J. Kernan, "Mechanotransduction and auditory transduction in Drosophila," *Pflügers Archiv-European Journal of Physiology,* vol. 454, no. 5, pp. 703-720, 2007.

[87] B. Warren and T. Matheson, "The role of the mechanotransduction ion channel candidate Nanchung-Inactive in auditory transduction in an insect ear," *Journal of Neuroscience,* vol. 38, no. 15, pp. 3741-3752, 2018.

[88] J. H. Fullard, E. Forrest, and A. Surlykke, "Intensity responses of the single auditory receptor of notodontid moths: a test of the peripheral interaction hypothesis in moth ears," *Journal of Experimental Biology,* vol. 201, no. 24, pp. 3419-3424, 1998.

[89] T. G. Nolen and R. R. Hoy, "Phonotaxis in flying crickets: I. Attraction to the calling song and avoidance of bat-like ultrasound are discrete behaviors," *Journal of Comparative Physiology A,* vol. 159, pp. 423-439, 1986.

[90] G. Von Békésy, "Experiments in hearing," 1960.

[91] G. Zweig, "Basilar membrane motion," in *Cold Spring Harbor symposia on quantitative biology*, 1976, vol. 40: Cold Spring Harbor Laboratory Press, pp. 619-633.

[92] A. Palghat Udayashankar, M. Kossl, and M. Nowotny, "Tonotopically arranged traveling waves in the miniature hearing organ of bushcrickets," *PLoS One,* vol. 7, no. 2, p. e31008, 2012.

[93] F. Montealegre-Z, T. Jonsson, K. A. Robson-Brown, M. Postles, and D. Robert, "Convergent evolution between insect and mammalian audition," *Science,* vol. 338, no. 6109, pp. 968-971, 2012.

[94] J. F. C. Windmill, M. C. Göpfert, and D. Robert, "Tympanal travelling waves in migratory locusts," *Journal of Experimental Biology,* vol. 208, no. 1, pp. 157-168, 2005.

[95] H. Stölting and A. Stumpner, "Tonotopic organization of auditory receptors of the bushcricket Pholidoptera griseoaptera (Tettigoniidae, Decticinae)," *Cell and Tissue Research,* vol. 294, no. 2, pp. 377-386, 1998/10/01 1998.

[96] J. Hummel, M. Kössl, and M. Nowotny, "Morphological basis for a tonotopic design of an insect ear," *Journal of Comparative Neurology,* vol. 525, no. 10, pp. 2443-2455, 2017.

[97] E. G. Gray, "The fine structure of the insect ear," *Philosophical Transactions of the Royal Society of London. Series B, Biological Sciences,* vol. 243, no. 700, pp. 75-94, 1960.

[98] J. r. m. Sueur, J. F. C. Windmill, and D. Robert, "Tuning the drum: the mechanical basis for frequency discrimination in a Mediterranean cicada," *Journal of Experimental Biology,* vol. 209, no. 20, pp. 4115-4128, 2006.

[99] R. Stephen and H. Bennet-Clark, "The anatomical and mechanical basis of stimulation and frequency analysis in the locust ear," *Journal of Experimental Biology,* vol. 99, no. 1, pp. 279-314, 1982.

[100] A. Michelsen, "The physiology of the locust ear: I. Frequency sensitivity of single cells in the isolated ear," *Zeitschrift für vergleichende Physiologie,* vol. 71, no. 1, pp. 49-62, 1971.

[101] G. Gibson, B. Warren, and I. J. Russell, "Humming in tune: sex and species recognition by mosquitoes on the wing," *Journal of the Association for Research in Otolaryngology,* vol. 11, no. 4, pp. 527-540, 2010.

[102] A. Kamikouchi, T. Shimada, and K. Ito, "Comprehensive classification of the auditory sensory projections in the brain of the fruit fly Drosophila melanogaster," *Journal of Comparative Neurology,* vol. 499, no. 3, pp. 317-356, 2006.

[103] J. Strauß, L. Moritz, and P. T. Rühr, "The subgenual organ complex in stick insects: Functional morphology and mechanical coupling of a complex mechanosensory organ," *Frontiers in Ecology and Evolution,* vol. 9, p. 632493, 2021.

[104] A. K. Schmidt and H. Römer, "Diversity of acoustic tracheal system and its role for directional hearing in crickets," *Frontiers in zoology,* vol. 10, no. 1, p. 61, 2013.

[105] N. Mhatre, F. Montealegre-Z, R. Balakrishnan, and D. Robert, "Mechanical response of the tympanal membranes of the tree cricket Oecanthus henryi," *Journal of comparative physiology. A, Neuroethology, sensory, neural, and behavioral physiology,* vol. 195, pp. 453-62, 03/01 2009.

[106] D. Veitch *et al.*, "A narrow ear canal reduces sound velocity to create additional acoustic inputs in a microscale insect ear," *Proceedings of the National Academy of Sciences,* vol. 118, no. 10, p. e2017281118, 2021.

[107] C. Woodrow, C. Pulver, H. Song, and F. Montealegre-Z, "Auditory mechanics in the grig (Cyphoderris monstrosa): tympanal travelling waves and frequency discrimination as a precursor to inner ear tonotopy," *Proceedings of the Royal Society B: Biological Sciences,* vol. 289, no. 1973, p. 20220398, 2022.

[108] H. Esch, F. Huber, and D. W. Wohlers, "Primary auditory neurons in crickets: Physiology and central projections," *Journal of comparative physiology,* vol. 137, no. 1, pp. 27-38, 1980/03/01 1980.

[109] T. Robillard, P. Grandcolas, and L. Desutter-Grandcolas, "A shift toward harmonics for high-frequency calling shown with phylogenetic study of frequency spectra in Eneopterinae crickets (Orthoptera, Grylloidea, Eneopteridae)," *Canadian Journal of Zoology,* vol. 85, no. 12, pp. 1264-1275, 2007.

[110] A. Keuper and R. Kühne, "The acoustic behaviour of the bushcricket Tettigonia cantans II. Transmission of airborne-sound and vibration signals in the biotope," *Behavioural Processes,* vol. 8, no. 2, pp. 125-145, 1983/05/01/ 1983.

[111] K. Kostarakos, M. R. Hennig, and H. Römer, "Two matched filters and the evolution of mating signals in four species of cricket," *Frontiers in Zoology,* vol. 6, no. 1, p. 22, 2009.

[112] A. C. Mason, M. L. Oshinsky, and R. R. Hoy, "Hyperacute directional hearing in a microscale auditory system," *Nature,* vol. 410, no. 6829, pp. 686-690, 2001/04/01 2001.

[113] B. Hedwig and J. F. A. Poulet, "Mechanisms underlying phonotactic steering in the cricket Gryllus bimaculatus revealed with a fast trackball system," *Journal of Experimental Biology,* vol. 208, no. 5, pp. 915-927, 2005.

[114] W. J. Bailey and P. Thomson, "Acoustic Orientation in the Cricket Teleogryllus Oceanicus (Le Guillou)," *Journal of Experimental Biology,* vol. 67, no. 1, pp. 61-75, 1977.

[115] B. Johnstone, J. Saunders, and J. Johnstone, "Tympanic membrane response in the cricket," *Nature,* vol. 227, no. 5258, pp. 625-626, 1970.

[116] F. Huber, H. U. Kleindienst, T. Weber, and J. Thorson, "Auditory behavior of the cricket," *Journal of Comparative Physiology A,* vol. 155, no. 6, pp. 725-738, 1984/11/01 1984.

[117] O. N. Larsen, "The cricket's anterior tympanum revisited," *The Science of Nature,* vol. 74, no. 2, pp. 92-94, 1987/02/01 1987.

[118] G. Wendler and G. Löhe, "The role of the medial septum in the acoustic trachea of the cricket Gryllus bimaculatus," *Journal of Comparative Physiology A,* vol. 173, no. 5, pp. 557-564, 1993/11/01 1993.

[119] N. H. Fletcher and S. Thwaites, "Acoustical analysis of the auditory system of the cricket Teleogryllus commodus (Walker)," *The Journal of the Acoustical Society of America,* vol. 66, no. 2, pp. 350-357, 1979.

[120] P. J. Ode, D. K. Vyas, and J. A. Harvey, "Extrinsic Inter- and Intraspecific Competition in Parasitoid Wasps," *Annual Review of Entomology,* vol. 67, no. Volume 67, 2022, pp. 305-328, 2022.

[121] H. C. J. Godfray, *Parasitoids: Behavioral and Evolutionary Ecology*. Princeton University Press, 1994.

[122] J. A. Harvey, E. H. Poelman, and T. Tanaka, "Intrinsic Inter- and Intraspecific Competition in Parasitoid Wasps," *Annual Review of Entomology,* vol. 58, no. Volume 58, 2013, pp. 333-351, 2013.

[123] J. R. Nechols and R. S. Kikuchi, "Host Selection of the Spherical Mealybug (Homoptera: Pseudococcidae) by Anagyrus indicus (Hymenoptera: Encyrtidae): Influence of Host Stage on Parasitoid

Oviposition, Development, Sex Ratio, and Survival," *Environmental Entomology,* vol. 14, no. 1, pp. 32-37, 1985.

[124] K. L. Kouamé and M. Mackauer, "Influence of aphid size, age and behaviour on host choice by the parasitoid wasp Ephedrus californicus: a test of host-size models," *Oecologia,* vol. 88, no. 2, pp. 197-203, 1991/10/01 1991.

[125] J. E. Cohen, T. Jonsson, C. B. Müller, H. C. J. Godfray, and V. M. Savage, "Body sizes of hosts and parasitoids in individual feeding relationships," *Proceedings of the National Academy of Sciences,* vol. 102, no. 3, pp. 684-689, 2005.

[126] D. Robert, J. Amoroso, and R. R. Hoy, "The Evolutionary Convergence of Hearing in a Parasitoid Fly and Its Cricket Host," *Science,* vol. 258, no. 5085, pp. 1135-1137, 1992.

[127] D. Robert, R. N. Miles, and R. R. Hoy, "Tympanal mechanics in the parasitoid fly Ormia ochracea: intertympanal coupling during mechanical vibration," *Journal of Comparative Physiology A,* vol. 183, no. 4, pp. 443-452, 1998/10/01 1998.

[128] M. L. Oshinsky and R. R. Hoy, "Physiology of the Auditory Afferents in an Acoustic Parasitoid Fly," *The Journal of Neuroscience,* vol. 22, no. 16, pp. 7254-7263, 2002.

[129] T. J. Walker, "Phonotaxis in femaleOrmia ochracea (Diptera: Tachinidae), a parasitoid of field crickets," *Journal of Insect Behavior,* vol. 6, no. 3, pp. 389-410, 1993/05/01 1993.

[130] N. Lee and A. C. Mason, "How spatial release from masking may fail to function in a highly directional auditory system," *eLife,* vol. 6, p. e20731, 2017/04/20 2017.

[131] N. Lee, A. T. Kirtley, I. S. Pressman, K. J. Jirik, D. Koucoulas, and A. C. Mason, "Developing a Phonotaxis Performance Index to Uncover Signal Selectivity in Walking Phonotaxis," (in English), *Frontiers in Ecology and Evolution,* Methods vol. Volume 7 - 2019, 2019-September-18 2019.

[132] K. J. Jirik *et al.*, "Parasitoid–host eavesdropping reveals temperature coupling of preferences to communication signals without genetic coupling," *Proceedings of the Royal Society B: Biological Sciences,* vol. 290, no. 2005, p. 20230775, 2023.

[133] D. A. Gray, H. D. Kunerth, M. Zuk, W. H. Cade, and S. L. Balenger, "Molecular biogeography and host relations of a parasitoid fly," *Ecology and Evolution,* vol. 9, no. 19, pp. 11476-11493, 2019.

[134] N. Lee, D. O. Elias, and A. C. Mason, "A precedence effect resolves phantom sound source illusions in the parasitoid fly Ormia ochracea," *Proceedings of the National Academy of Sciences,* vol. 106, no. 15, pp. 6357-6362, 2009.

[135] S. A. Adamo, D. Robert, and R. R. Hoy, "Effects of a tachinid parasitoid, Ormia ochracea, on the behaviour and reproduction of its male and female field cricket hosts (Gryllus spp)," *Journal of Insect Physiology,* vol. 41, no. 3, pp. 269-277, 1995/03/01/ 1995.

[136] M. A. Smith, D. M. Wood, D. H. Janzen, W. Hallwachs, and P. D. N. Hebert, "DNA barcodes affirm that 16 species of apparently generalist tropical parasitoid flies (Diptera, Tachinidae) are not all generalists," *Proceedings of the National Academy of Sciences,* vol. 104, no. 12, pp. 4967-4972, 2007.

[137] J. Paur and D. A. Gray, "Individual consistency, learning and memory in a parasitoid fly, Ormia ochracea," *Animal Behaviour,* vol. 82, no. 4, pp. 825-830, 2011/10/01/ 2011.

[138] G. K. Lott, M. J. Rosen, and R. R. Hoy, "An inexpensive sub-millisecond system for walking measurements of small animals based on optical computer mouse technology," *Journal of Neuroscience Methods,* vol. 161, no. 1, pp. 55-61, 2007/03/30/ 2007.

[139] S. A. Adamo, D. Robert, J. Perez, and R. R. Hoy, "The response of an insect parasitoid, Ormia ochracea (Tachinidae), to the uncertainty of larval success during infestation," *Behavioral Ecology and Sociobiology,* vol. 36, no. 2, pp. 111-118, 1995/02/01 1995.

[140] S. A. Wineriter and T. J. Walker, "Rearing phonotactic parasitoid flies [Diptera: Tachinidae, ormiini, ormia spp.]," *Entomophaga,* vol. 35, no. 4, pp. 621-632, 1990/12/01 1990.

[141] M. Zukl, L. W. Simmons, and L. Cupp, "Calling characteristics of parasitized and unparasitized populations of the field cricket Teleogryllus oceanicus," *Behavioral Ecology and Sociobiology,* vol. 33, no. 5, pp. 339-343, 1993/11/01 1993.

[142] G. R. Kolluru and M. Zuk, "Parasitism patterns and the size-fecundity relationship in the acoustically orienting dipteran parasitoid Ormia ochracea," *Canadian Journal of Zoology,* vol. 79, no. 6, pp. 973-979, 2001.

[143] J. H. Gallagher, E. D. Broder, A. W. Wikle, H. O'Toole, C. Durso, and R. M. Tinghitella, "Surviving the serenade: how conflicting selection pressures shape the early stages of sexual signal diversification," *Evolution,* vol. 78, no. 5, pp. 835-848, 2024.

[144] C. M. Vincent and S. M. Bertram, "Crickets groom to avoid lethal parasitoids," *Animal Behaviour,* vol. 79, no. 1, pp. 51-56, 2010/01/01/ 2010.

[145] I. R. Thomson, C. M. Vincent, and S. M. Bertram, "Success of the Parasitoid Fly Ormia ochracea (Diptera: Tachinidae) on Natural and Unnatural Cricket Hosts," *Florida Entomologist,* vol. 95, no. 1, pp. 43-48, 6, 2012.

[146] E. D. Broder *et al.*, "A well-studied parasitoid fly of field crickets uses multiple alternative hosts in its introduced range," *Evolutionary Ecology,* vol. 37, no. 3, pp. 477-492, 2023/06/01 2023.

[147] C. de Geer, *Mémoires pour servir à l'histoire des insectes*. De l'imprimerie de L.L. Grefing, 1771.

[148] B. M. D. o. Zoology, F. Walker, and J. E. Gray, *Catalogue of the Specimens of Dermaptera Saltatoria and Supplement of the Blattariæ in the Collection of the British Museum* (no. pts. 1-4). Trustees of the British museum, 1869.

[149] J. Alba-Tercedor, I. Alba-Alejandre, and F. E. Vega, "Revealing the respiratory system of the coffee berry borer (Hypothenemus hampei; Coleoptera: Curculionidae: Scolytinae) using micro-computed tomography," *Scientific Reports,* vol. 9, no. 1, p. 17753, 2019/11/28 2019.

[150] B. D. Metscher, "MicroCT for comparative morphology: simple staining methods allow high-contrast 3D imaging of diverse non-mineralized animal tissues," *BMC Physiology,* vol. 9, no. 1, p. 11, 2009/06/22 2009.

[151] I. Alba-Alejandre, J. Alba-Tercedor, and W. B. Hunter, "Anatomical study of the female reproductive system and bacteriome of Diaphorina citri Kuwayama, (Insecta: Hemiptera, Liviidae) using micro-computed tomography," *Scientific Reports,* vol. 10, no. 1, p. 7161, 2020/04/28 2020.

[152] T. T. Austin, C. Woodrow, J. Pinchin, F. Montealegre-Z, and B. Warren, "Effects of age and noise on tympanal displacement in the Desert Locust," *Journal of Insect Physiology,* vol. 152, p. 104595, 2024.

[153] F. A. Sarria-S, B. D. Chivers, C. D. Soulsbury, and F. Montealegre-Z, "Non-invasive biophysical measurement of travelling waves in the insect inner ear," *Royal Society Open Science,* vol. 4, no. 5, p. 170171, 2017.

[154] K. M. Lucas, J. F. Windmill, D. Robert, and J. E. Yack, "Auditory mechanics and sensitivity in the tropical butterfly Morpho peleides (Papilionoidea, Nymphalidae)," *Journal of Experimental Biology,* vol. 212, no. 21, pp. 3533-3541, 2009.

[155] J. Windmill, J. Fullard, and D. Robert, "Mechanics of asimple'ear: tympanal vibrations in noctuid moths," *Journal of Experimental Biology,* vol. 210, no. 15, pp. 2637-2648, 2007.

[156] M. Ward, "Notes from the Underground: An Exploration of Burying Beetle Thermal Ecology, Sound Production and Reception, and Brain Morphology," Ph.D., University of New Hampshire, United States -- New Hampshire, 29169280, 2022.

[157] J. F. Windmill, J. Sueur, and D. Robert, "The next step in cicada audition: measuring pico-mechanics in the cicada's ear," *Journal of Experimental Biology,* vol. 212, no. 24, pp. 4079-4083, 2009.

[158] D. Yager and A. Michelsen, "A traveling wave in the curious ear of the praying mantis," in *Sixth International Congress of Neuroethology, Bonn, Germany*, 2001.

[159] M. Franck, D. Berft, and K. Hameyer, "Robotergestützte 3D-Laser-Doppler-Vibrometrie zur experimentellen Modalanalyse von elektrischen Maschinen," *e & i Elektrotechnik und Informationstechnik,* vol. 140, no. 2, pp. 281-289, 2023/04/01 2023.

[160] S. S. Rao and F. F. Yap, *Mechanical vibrations*. Addison-Wesley New York, 1995.

[161] Matsusada-Precision. [Online]. Available: https://www.matsusada.com/product/xray/micro-ct-scanners/micro-ct-software/.

[162] C. M. Vincent and S. M. Bertram, "Collection and laboratory culture of Ormia ochracea (Diptera: Tachinidae)," *Journal of Entomological Science,* vol. 45, no. 1, pp. 1-7, 2010.

[163] O. M. Beckers, C. M. Martin, and W. E. Wagner Jr, "Survival rates of planidial larvae of the parasitoid fly Ormia ochracea (Diptera: Tachinidae)," *Journal of the Kansas Entomological Society,* vol. 84, no. 3, pp. 235-237, 2011.

[164] G. Van Dalen and M. Koster, "2D & 3D particle size analysis of micro-CT images," *Unilever Res Dev Netherlands,* 2012.

[165] R. Malkin, T. R. McDonagh, N. Mhatre, T. S. Scott, and D. Robert, "Energy localization and frequency analysis in the locust ear," *Journal of The Royal Society Interface,* vol. 11, no. 90, p. 20130857, 2014.

[166] E. Ball and A. Cowan, "Ultrastructural study of the development of the auditory tympana in the cricket Teleogryllus commodus (Walker)," *Development,* vol. 46, no. 1, pp. 75-87, 1978.

[167] S. Dogra and A. Gupta, "Low-frequency noise control in ducts," in *Recent Advances in Computational and Experimental Mechanics, Vol—I: Select Proceedings of ICRACEM 2020*: Springer, 2022, pp. 527-535.

[168] G. Lehmann, "How different host species influence parasitism patterns and larval competition of acoustically-orienting parasitoid flies (Tachinidae: Ormiini)," *Animal behavior: new research,* pp. 93-132, 2008.

[169] K. A. Judge and V. L. Bonanno, "Male weaponry in a fighting cricket," *PLoS one,* vol. 3, no. 12, p. e3980, 2008.

[170] S. Nakamura, "Optimal clutch size for maximizing reproductive success in a parasitoid fly, Exorista japonica (Diptera: Tachinidae)," *Applied Entomology and Zoology,* vol. 30, no. 3, pp. 425-431, 1995.

[171] S. R. Reitz and P. H. Adler, "Fecundity and oviposition of Eucelatoria bryani, a gregarious parasitoid of Helicoverpa zea and Heliothis virescens," *Entomologia experimentalis et applicata,* vol. 75, no. 2, pp. 175-181, 1995.

[172] H. A. MacMillan and B. J. Sinclair, "The role of the gut in insect chilling injury: cold-induced disruption of osmoregulation in the fall field cricket, Gryllus pennsylvanicus," *Journal of Experimental Biology,* vol. 214, no. 5, pp. 726-734, 2011.

[173] I. Lauziere, J. C. Legaspi, B. C. Legaspi Jr, J. W. Smith Jr, and W. A. Jones, "Life-history studies of Lydella jalisco (Diptera: Tachinidae), a parasitoid of Eoreuma loftini (Lepidoptera: Pyralidae)," *BioControl,* vol. 46, no. 1, pp. 71-90, 2001.

[174] C. Welch, "Intraspecific competition for resources by Ormia depleta (Diptera: Tachinidae) larvae," *Florida Entomologist,* pp. 497-501, 2006.

[175] D. H. Feener Jr and B. V. Brown, "Diptera as parasitoids," *Annual review of entomology,* vol. 42, no. 1, pp. 73-97, 1997.

[176] G. T. Ho, R. T. Ichiki, and S. Nakamura, "Reproductive biology of the microtype tachinid fly Zenillia dolosa (Meigen)(Diptera: Tachinidae)," *Entomological science,* vol. 14, no. 2, pp. 210-215, 2011.

[177] D. Lack, "The significance of clutch-size," *Ibis,* vol. 89, pp. 302-352, 1947.

[178] I. Hardy, N. Griffiths, and H. Godfray, "Clutch size in a parasitoid wasp: a manipulation experiment," *Journal of Animal Ecology,* pp. 121-129, 1992.

[179] K. J. Rogers and O. M. Beckers, "Multi-species host use by the parasitoid fly Ormia lineifrons," *Insects,* vol. 14, no. 9, p. 744, 2023.

[180] K. M. Sakaguchi and D. A. Gray, "Host song selection by an acoustically orienting parasitoid fly exploiting a multispecies assemblage of cricket hosts," *Animal Behaviour,* vol. 81, no. 4, pp. 851-858, 2011.

[181] A. W. Wikle *et al.*, "Neural and behavioral evolution in an eavesdropper with a rapidly evolving host," *Current Biology,* vol. 35, no. 5, pp. 1074-1084. e7, 2025.

[182] M. Zuk, J. T. Rotenberry, and R. M. Tinghitella, "Silent night: adaptive disappearance of a sexual signal in a parasitized population of field crickets," *Biology letters,* vol. 2, no. 4, pp. 521-524, 2006.

[183] R. M. Tinghitella, E. D. Broder, G. A. Gurule-Small, C. J. Hallagan, and J. D. Wilson, "Purring crickets: the evolution of a novel sexual signal," *The American Naturalist,* vol. 192, no. 6, pp. 773-782, 2018.

[184] R. M. Tinghitella, E. D. Broder, J. H. Gallagher, A. W. Wikle, and D. M. Zonana, "Responses of intended and unintended receivers to a novel sexual signal suggest clandestine communication," *Nature Communications,* vol. 12, no. 1, p. 797, 2021.

[185] J. G. Rayner, S. Aldridge, F. Montealegre-Z, and N. W. Baile, "A silent orchestra," *Ecology,* vol. 100, no. 8, pp. 1-4, 2019.

[186] E. D. Broder *et al.*, "Behavioral responses of a parasitoid fly to rapidly evolving host signals," *Ecology and evolution,* vol. 12, no. 8, p. e9193, 2022.

[187] R. R. Hoy, "Hawaiian love songs: Coevolutionary conflict between mate attraction and parasite escape," *Current Biology,* vol. 35, no. 5, pp. R189-R191, 2025.

[188] N. Mhatre, J. B. Dewey, P. M. Quiñones, A. Mason, B. E. Applegate, and J. S. Oghalai, "Reconstruction of sound driven, actively amplified and spontaneous motions within the tree cricket auditory organ," *bioRxiv,* p. 2021.11.14.468538, 2021.

[189] A. Vavakou, J. Scherberich, M. Nowotny, and M. van der Heijden, "Tuned vibration modes in a miniature hearing organ: Insights from the bushcricket," *Proceedings of the National Academy of Sciences,* vol. 118, no. 39, p. e2105234118, 2021.

[190] J. Vincze and G. Vincze-Tiszay, "The Biophysical Function of the Human Middle Ear," *Jour Med Resh and Health Sci,* vol. 4, no. 5, pp. 1245-1252, 2021.

[191] J. Casale, K. R. Shumway, and J. D. Hatcher, "Physiology, eustachian tube function," 2018.

Appendix A

UK–Canada Research Proposal

Research Proposal written by the author of this thesis and submitted to the UKRI and Mitacs in application to the *UK–Canada Globalinks Doctoral Exchange Scheme*. In response to this research proposal the position was successfully awarded. The secondment to the University of Toronto eventually resulted in Chapter 5 of this thesis.

UK Research and Innovation

Mitacs

UK-Canada doctoral exchange scheme: Placement Proposal

1. Student statement of interest

This scheme will provide me with a unique, exciting, and important opportunity to up-skill my competencies as a researcher and to establish personal international networks, all in association with a team of scientists producing world-class research within my field of 'insect acoustics'. The 12-week Canada placement amongst this group will immerse me in skills, research pursuits and colleague-relationships that are distinct but highly complimentary to my UK-based doctoral training. The UK base where I work is helping lead the way at the biomimetic interface of the field, and as such I serve as one of the few biologists in what is largely an engineering environment. Biology is the first link in the biomimicry chain and therefore it is of incalculable value that I seize opportunities to experience more of the biology side of my field and develop into the best biological researcher I can be. Nowhere could provide this biological perspective on insect acoustics better than the laboratory of Professor Andrew Mason of the University of Toronto Scarborough.

Prof. Mason's focus is on acoustic and vibrational communication in insects and spiders, with an internationally recognised expertise on the auditory processing of the fly *Ormia ochracea*, possibly the flagship organism of my field. The placement laboratory boasts a suite of expertise and equipment not available at my UK institution, including the means of precise behavioural measurements of insects using a 'trackball'. It is striking that, prior to learning of this scheme, I had anticipated the need in my doctoral research for collaboration to learn how to build and use one of these trackballs. Moreover, it is notable that the *O. ochracea* fly, the subject of the following proposal, is the natural parasitoid of my PhD subject-organism, the field cricket. As such, this placement project will enhance my UK-based research in both practice and theory.

2. Placement proposal

2.1 Background

Tachinid flies are parasitoids[1], and many tachinids 'eavesdrop' on the mating song of a male host and use the signal to phonotactically orientate towards the sound source[1,2]. In North America, *Ormia ochracea* parasitises various cricket species with diverse songs, across geographically separated fly populations. Certain populations are known to target the predominant host species in its locality, thus exhibiting 'host specialisation'[3]. Field data indicates local specialisation is a preference behaviour; flies choose the song of their population's natural host cricket[4].

Conceivably, these differences in behavioural preferences could be due to populations functioning as 'cryptic species'[5]. In fact, fly populations belong to a single genetically homogenous species, indicating adaptive preference is an inherent potential within all *O. ochracea* flies. Cross populational differences in host preference may therefore be due to an innate scope for behavioural flexibility combined with an ability to learn the song of the predominant local host species[3].

Song learning has been demonstrated in a *O. ochracea* population to be the main if not exclusive factor in determining host preference[6], and as such might account for all in-field host preferences across populations[4]. However, learning data exists only for one population[6], and therefore we do not know the cross-populational role of song learning.

Song learning operating within a common potential for behavioural adaptation would necessitate a single broad 'acoustical template'. Since the degree of song preference independent of learning opportunity has not been investigated across populations, the boundaries of such a template remain undetermined.

Moreover, evidence suggest a degree of population specific temporal tuning to certain songs. For example, Florida flies almost entirely prefer the host *Gryllus rubens*, the dominant species of the region, the song of which is highly divergent in its pulse rate to that of the secondary host *G. firmus*[3]. Modulating *G. rubens* pulse rate considerably reduces phonotactic success[7]. Yet, in contrast, *Teleogryllus oceanicus* shares a similar pulse rate to the largely rejected *G. rubens*[3], but in Hawaii receives considerable preference[4]. Such seemingly acute differences might suggest the operation of multiple acoustical templates across populations, not just one.

Previous host-preference data have been collected in the field[4], whereas this project will be the first to investigate cross-populational host preferences in laboratory reared flies. Phonotactic steering accuracy will be recorded on a trackball[8,9] in response to the songs.

Acoustical template boundaries will be explored by modulating pulse rates[7] under otherwise the same experimental conditions as above.

The relative role of song learning across populations will be ascertained by exposing each treatment of laboratory reared flies exclusively to one of the host songs within a five-day period immediately preceding phonotactic steering trials[6].

In addition: Observations of adult and even larval flies have suggested the possibility of differential rates of activity in flies across populations, including in the absence of an immediate host song stimulus (Andrew Mason, personal communication). Larval activity rates between populations will be measured by kinematic analysis of video recordings of gravid female dissections. From these larvae, adult activity rates will be established by recordings on the trackball of 'forward velocity' and 'total distance'[9] before during and after song exposure.

2.2 Objectives

Research question 1 What is the role of learning-independent temporal preferences in determining host preferences across *Ormia ochracea* populations?

- ***Objective 1*** To record phonotactic steering accuracy on a trackball in response to different song signals across population treatments of laboratory reared flies.

Research question 2 What are the minimally effective song parameters for eliciting song learning across populations of *O. ochracea*?

- **Objective 2** To record phonotactic steering accuracy on a trackball in response to different song signals, *and to altered song pulse rates*.

Research question 3 What is the role of song learning in determining host preferences across *O. ochracea* populations?

- **Objective 3** To expose each of the populations-derived treatments to five-days of exclusive exposure to one host song, immediately prior to recording phonotactic steering accuracy on a trackball in response to that same signal.

Research question 4 How do adult and larval activity rates compare across populations?

- **Objective 4** To measure larval activity rates across populations by kinematic analysis of video recordings of gravid female dissections.
    - **Sub-objective 4B** In adults from these larvae, to record trackball 'forward velocity' and 'total distance' before during and after song exposure.

2.3 Significance

The auditory apparatus of Ormia flies enables sound source localisation at a precision comparable to that of humans and unsurpassed among invertebrates[10]. This novel mechanism has been the inspiration of numerous patented engineering designs of 'MEMS' microphones[11], the type found inside iPhones. With the continued miniaturisation of technologies in this electronic age, these sensors are only going to grow in their relevance to both industry and

society. However, such microphones are of course constrained by size and therefore limited in the acoustic parameters they can receive, especially at low frequencies[12]. By investigating the extent of Ormia directionality to a diversity of acoustic stimuli, this research may help elucidate what sensory range might be possible in the micro-scale sensors of tomorrow.

2.4 Timeline

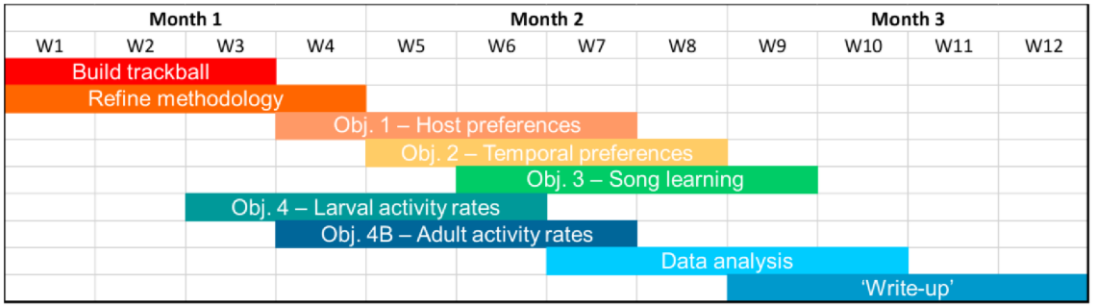

2.5 Cited literature

1. Cade, W. (1975). Acoustically orienting parasitoids: fly phonotaxis to cricket song. *Science*, *190*(4221), 1312-1313.

2. Köhler, U., & Lakes-Harlan, R. (2001). Auditory behaviour of a parasitoid fly (Emblemasoma auditrix, Sarcophagidae, Diptera). *Journal of Comparative Physiology A*, *187*(8), 581-587.

3. Gray, D. A., Kunerth, H. D., Zuk, M., Cade, W. H., & Balenger, S. L. (2019). Molecular biogeography and host relations of a parasitoid fly. *Ecology and evolution*, *9*(19), 11476-11493.

4. Gray, D. A., Banuelos, C., Walker, S. E., Cade, W. H., & Zuk, M. (2007). Behavioural specialization among populations of the acoustically orienting parasitoid fly Ormia ochracea utilizing different cricket species as hosts. *Animal Behaviour*, *73*(1), 99-104.

5. Smith, M. A., Wood, D. M., Janzen, D. H., Hallwachs, W., & Hebert, P. D. (2007). DNA barcodes affirm that 16 species of apparently generalist tropical parasitoid flies (Diptera, Tachinidae) are not all generalists. *Proceedings of the national academy of sciences*, *104*(12), 4967-4972.

6. Paur, J., & Gray, D. A. (2011). Individual consistency, learning and memory in a parasitoid fly, Ormia ochracea. *Animal behaviour*, *82*(4), 825-830.

7. Walker, T. J. (1993). Phonotaxis in female Ormia ochracea (Diptera: Tachinidae), a parasitoid of field crickets. *Journal of insect behavior*, *6*(3), 389-410.

8. Lott, G. K., Rosen, M. J., & Hoy, R. R. (2007). An inexpensive sub-millisecond system for walking measurements of small animals based on optical computer mouse technology. *Journal of neuroscience methods*, *161*(1), 55-61.

9. Lee, N., Kirtley, A. T., Pressman, I. S., Jirik, K. J., Koucoulas, D., & Mason, A. C. (2019). Developing a phonotaxis performance index to uncover signal selectivity in walking phonotaxis. *Frontiers in Ecology and Evolution*, 334.

10. Mason, A. C., Oshinsky, M. L., & Hoy, R. R. (2001). Hyperacute directional hearing in a microscale auditory system. *Nature*, *410*(6829), 686-690.

11. Zhang, Y., Reid, A., & Windmill, J. F. C. (2018). Insect-inspired acoustic micro-sensors. *Current opinion in insect science*, *30*, 33-38.

12. Shah, M. A., Shah, I. A., Lee, D. G., & Hur, S. (2019). Design approaches of MEMS microphones for enhanced performance. *Journal of sensors*, *2019*.

3. Benefits to the UK and Canada

3.1 Strengthening Canada's research and innovation capacity

My project will focus on North American *Ormia ochracea* populations, mostly in the USA. The bulk of today's impact on this research area is likely arising from US institutions; this project will help towards maintaining Canada's competitiveness in this stream of enquiry. My unique background may facilitate the transfer of new insights to the team in Canada that I will be working with. This background includes: 1) my training as both a biologist but also as a visualiser (the processing of imaging data, such as micro-CT, to develop 3D anatomical models); 2) my experience of a world leading research laboratory working on the biomimetic side of insect acoustics. Lastly, I have identified in my project, to my knowledge, ideas never explored, which should be of benefit to my hosts in Toronto, including: 1) the application of a cross-populational methodology to a laboratory setting; 2) and a song-learning protocol to more than one *O. ochracea* population; 3) as well as the use of video kinematics on larvae activity rates across populations.

3.2 Strengthening the UK's research and innovation capacity

In the UK research group led by my home supervisor Professor James Windmill, I help serve as a conduit between biology and engineering, to assist in providing the source of biological insight necessary for the development of novel insect-inspired acoustic sensors. Via the placement project in Canada, I will receive a thorough introduction to the more biological side of the field, which should bring back to our UK team an improved grounding for these sources of biological inspiration. In turn, this should sharpen the UK's cutting-edge in insect-inspired biomimetics.

Prof. Mason's laboratory in Canada is well-established on the biology side of insect acoustics. The laboratory co-founded the Integrative Behaviour & Neuroscience (IBN) Group in 2001 at what is Canada's number one research-intensive university. The IBN is a diverse community of biological scientists. By pursuing my project in the context of the IBN, insights into 'how things are done' will inevitably be obtained, and some insights might be transferred to my UK institution.

The laboratory in Canada in which I will be working boasts a suite of skills and infrastructure that may well be of inspiration to Prof. Windmill's research group at home, and these include: 1) the means to take careful measurements of insect acoustic behaviour – within these skills I intend to learn how to build a phonotaxis trackball which I will later set up in the UK laboratory; 2) the capabilities to make neurophysiological recordings in insects; 3) and lastly, a year-round in house invertebrate rearing facility with a range of organisms that could be of biomimetic interest, from *O. ochracea* flies to black widow spiders and their webs.

3.2 Collaborations between participating researchers

3.2.1 Does this project build on an existing international collaboration?

Yes ✓ No _____

3.2.2 Does this project create potential for future collaborations?

Yes ✓ No _____

3.2.3 Please describe briefly the existing, planned or future collaboration.

Professors Mason and Windmill and their respective research groups are already well acquainted in a professional capacity. However, to my knowledge biology personnel have never been exchanged. Over a 12-week period this project will strengthen the existing link which will mutually transfer skills and insights. In turn this could encourage longer periods of future collaboration.

4. Interaction

The project that I will be undertaking at the University of Toronto Scarborough (UTSC) will be one that is very much in line with Professor Mason's existing personal research. As such, Prof Mason will be extremely involved in this project and supervisor-intern interactions will be conducted on a weekly if not daily basis. These interactions will be two-fold, both mentorship – receiving feedback on how to conduct the experiments – and training. The training will be one-to-one under Prof Mason's supervision and will generate skills associated with obtaining data on sensory-guided behaviour in the *Ormia ochracea* fly, specifically: 1) video kinematics, 2) phonotaxis on a trackball (spherical treadmill), and 3) techniques in sensory neurophysiological recordings.

The 12 weeks of research will take place at the host university of UTSC for 100% of the allotted period. This research will be conducted in the laboratory of Prof Mason which is part of the Department of Biological Sciences at the UTSC. The Scarborough campus (UTSC) is one of three integrated campuses that form the University of Toronto. The buildings on this campus that I will be associated with are 'SW 566' and 'SW421-H', and the address is: *Dr. Andrew C Mason, Integrative Behaviour and Neuroscience, University of Toronto Scarborough, 1265 Military Trail, Scarborough ON, M1C 1A4 Canada*.

In addition, I may have interactions with my host supervisor's colleagues (and their respective students): Prof *Maydianne Andrade*, Associate Prof *Kenneth Welch*, Prof *Nathan Lovejoy*, Assistant Prof *Ina Anreiter*, Assistant Prof *Tod R. Theile*, and Assistant Prof *Minoru Koyama*.

Appendix B

2025 – *Annals of the Entomological Society of America*

Paper

J. A. Dominguez†, B. **Latham†**, L. C. Mongui, A. Rossinow, Y. Xiong, B. V. Schmidt, Q. Vu, B. L. Torres-Lopez, P. A. Henderson, A. C. Mason, N. Lee, "Resource competition affects developmental outcomes of the acoustic parasitoid fly *Ormia ochracea*," *Annals of the Entomological Society of America*, 2025.
doi: 10.1093/aesa/saaf018

- **† "Co-first authors contributed equally to this work"**

This paper is not Open Access and therefore has not been reproduced in full here.

This paper was selected by the journal as the cover image for its July 2025 issue (Volume 118, Issue 4).

The cover image, along with the text abstract and graphical abstract, are reproduced here.

JOURNAL ARTICLE

Resource competition affects developmental outcomes of the acoustic parasitoid fly *Ormia ochracea*

Get access >

Jimena A Dominguez, Brendan Latham, Lauren Bitner, Laura C Mongui, Addie Rossinow, Yeng Xiong, Briella V Schmidt, Quang Vu, Blanca L Torres-Lopez, Parker A Henderson ...
Show more

Annals of the Entomological Society of America, Volume 118, Issue 4, July 2025, Pages 303–314, https://doi.org/10.1093/aesa/saaf018
Published: 10 July 2025 **Article history** ▾

Abstract

In parasitoid systems, resource competition can significantly impact developmental outcomes. This study investigates how larval competition and host characteristics influence development in the acoustic parasitoid fly *Ormia ochracea*, using the house cricket *Acheta domesticus* as a host. We experimentally manipulated larval load (1 vs. 2 larvae per host) and recorded host sex and size to assess their effects on pupation and eclosion (adult hatching) success, as well as pupal and adult fly size. While double infestations increased total yield (0.78 vs. 0.54 flies per host), larvae developing without competition exhibited higher relative pupation and eclosion success and produced larger pupae and adult flies, indicating greater individual fitness. Although female host crickets yielded larger pupae, resource competition was the dominant factor shaping developmental outcomes. These results highlight the trade-offs between reproductive yield and offspring fitness driven by resource competition and validate the commercially available *A. domesticus* as a viable host.

Graphical Abstract

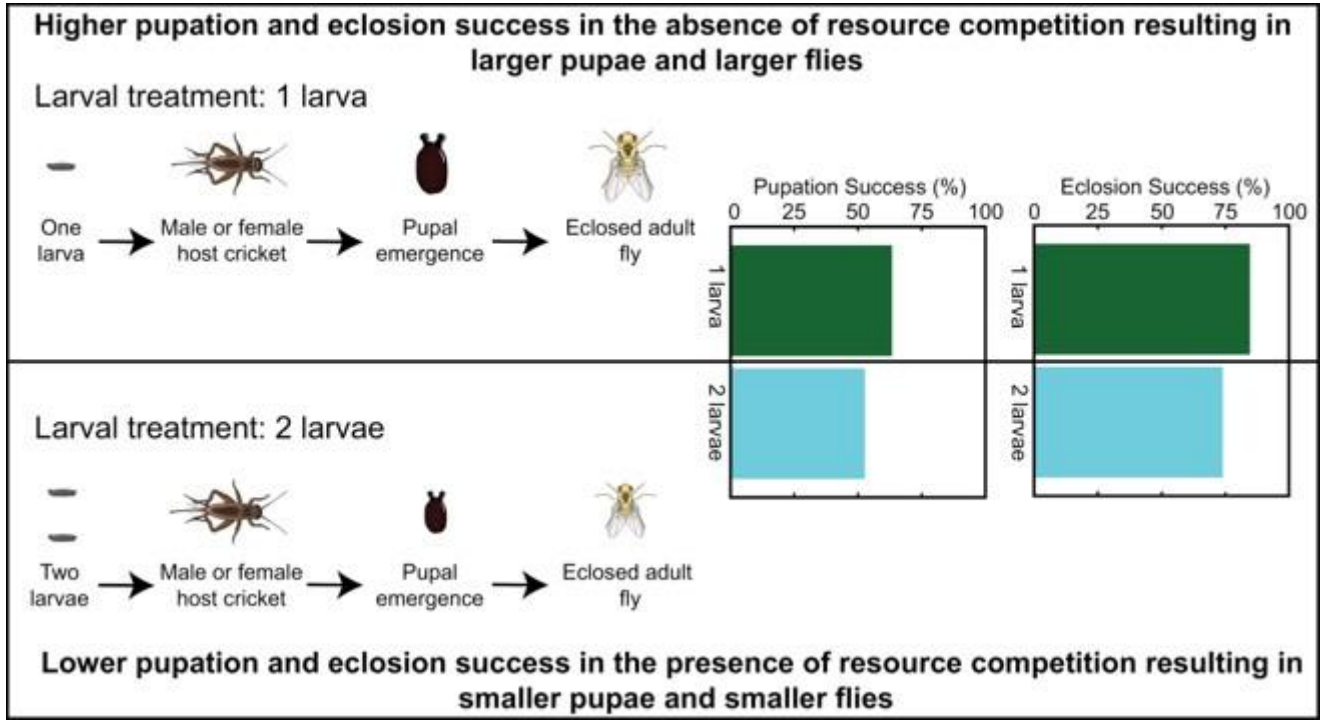

Appendix C

2024 – *Journal of the Royal Society Interface*

Paper

B. **Latham**, A. Reid, J. C. Jackson-Camargo, J. A. Williams, and J. F. Windmill, "Coupled membranes: a mechanism of frequency filtering and transmission in the field cricket ear evidenced by micro-computed tomography, laser Doppler vibrometry and finite element analysis," *Journal of the Royal Society Interface,* vol. 21, no. 214, 2024.
doi: 10.1098/rsif.2023.0779

This paper was selected by the journal as the cover image for its June 2024 issue (Volume 21, Issue 215).

JOURNAL OF THE ROYAL SOCIETY INTERFACE

THE ROYAL SOCIETY PUBLISHING

INTERFACE

royalsocietypublishing.org/journal/rsif

Research

Cite this article: Latham B, Reid A, Jackson-Camargo JC, Williams JA, Windmill JFC. 2024 Coupled membranes: a mechanism of frequency filtering and transmission in the field cricket ear evidenced by micro-computed tomography, laser Doppler vibrometry and finite element analysis. *J. R. Soc. Interface* **21**: 20230779.
https://doi.org/10.1098/rsif.2023.0779

Received: 30 December 2023
Accepted: 22 March 2024

Subject Category:
Life Sciences–Physics interface

Subject Areas:
biomechanics

Keywords:
insect ear, micro-CT, LDV, finite element analysis, auditory system, biomimetic

Author for correspondence:
Brendan Latham
e-mail: brendan.latham@strath.ac.uk

Electronic supplementary material is available online at https://doi.org/10.6084/m9.figshare.c.7159833.

THE ROYAL SOCIETY PUBLISHING

Coupled membranes: a mechanism of frequency filtering and transmission in the field cricket ear evidenced by micro-computed tomography, laser Doppler vibrometry and finite element analysis

Brendan Latham[1], Andrew Reid[1], Joseph C. Jackson-Camargo[1], Jonathan A. Williams[2] and James F. C. Windmill[1]

[1]Bioacoustics Group, Centre for Ultrasonic Engineering, Department of Electronic and Electrical Engineering, and [2]Department of Biomedical Engineering, University of Strathclyde, Glasgow, UK

BL, 0000-0003-3582-4205; AR, 0000-0003-0511-4640; JCJ-C, 0000-0001-9302-8157; JAW, 0000-0002-9828-4886; JFCW, 0000-0003-4878-349X

Many animals employ a second frequency filter beyond the initial filtering of the eardrum (or tympanal membrane). In the field cricket ear, both the filtering mechanism and the transmission path from the posterior tympanal membrane (PTM) have remained unclear. A mismatch between PTM vibrations and sensilla tuning has prompted speculations of a second filter. PTM coupling to the tracheal branches is suggested to support a transmission pathway. Here, we present three independent lines of evidence converging on the same conclusion: the existence of a series of linked membranes with distinct resonant frequencies serving both filtering and transmission functions. Micro-computed tomography (μ-CT) highlighted the 'dividing membrane (DivM)', separating the tracheal branches and connected to the PTM via the dorsal membrane of the posterior tracheal branch (DM-PTB). Thickness analysis showed the DivM to share significant thinness similarity with the PTM. Laser Doppler vibrometry indicated the first of two PTM vibrational peaks, at 6 and 14 kHz, originates not from the PTM but from the coupled DM-PTB. This result was corroborated by μ-CT-based finite element analysis. These findings clarify further the biophysical source of neuroethological pathways in what is an important model of behavioural neuroscience. Tuned microscale coupled membranes may also hold biomimetic relevance.

1. Introduction

The ear of the field cricket (family Gryllidae, subfamily Gryllinae) is notable for its remarkable sound-source localization accuracy level to that of humans [1]. It exhibits a rare instance among insects of tonotopy, with auditory neurons arranged along a low- to high-frequency gradient [2]. Approximately 70 sensory neurons [3] are individually tuned within frequency clusters, including those matching the carrier frequencies (CFs) of the calling and courtship songs [4], produced by the male's forewings [5]. Some neurons are tuned to the courtship song CF [4], between 11 and 16 kHz in *Gryllus bimaculatus* [6], while most are sharply tuned to the 4–5 kHz dominant frequency of the calling song [4,7].

The distinctive [8,9] pure-toned calling song is essential for facilitating reproduction in field crickets. Before mating, females must locate the male's position from a distance, and studies have shown this localization

behaviour is highly dependent on the CF of the conspecific calling song [1,10]. Electrophysiological recordings of individual receptors [2], the whole tympanal nerve [11] and the AN1 interneuron [12] all demonstrate acute selectivity to this frequency. This predictability in phonotactic behaviour, achieved via identifiable neural networking, has made the field cricket a valuable neuroethological model [9]. Thus, behaviour and neurophysiology are established domains in the 4–5 kHz sharp tuning of the field cricket ear. However, how the peripheral auditory anatomy causes this frequency filtering has long been acknowledged as unresolved [13–20].

The field cricket possesses two ears, one in each of the two front legs, at the proximal end of the tibia leg segment (see figure 1*a*, yellow highlight). Each ear has two tympana. The smaller and thicker anterior tympanal membrane (ATM) has been considered negligible for both reception and filtering [10,17,19], while the posterior tympanal membrane (PTM) is regarded as the primary sound receiver [10,16,19,20,22].

Unlike the ears of insects such as moths [23], the field cricket's sensory neurons are not directly attached to the tympanum. Instead, the PTM and the sensors are separated by two air-filled cavities, the tracheal branches, each with a membranous dorsal wall [18]. Auditory neurons are arranged tonotopically along the dorsal membrane of the anterior tracheal branch (DM-ATB) [2,18], where they are immersed in a lipidic fluid within a complex of structures known as the tympanal organ [18].

The field cricket anterior tracheal branch (ATB) is distinct compared to other more arboreal ensiferans: Eneopeterinae [21], Oecanthinae [24], Tettigoniidae [25] and Hagloidea [26]. Unlike these taxa, the Gryllinae ATB is not in direct contact with the ATM and is considerably smaller than the PTB (see figure 2*c*). Two small holes or 'apertures' connect the branches, the proximal aperture (PA) and the distal aperture (DA) (see figure 2 and electronic supplementary material, animation S1).

The larger PTB is more of a continuation of the leg trachea [18], part of the wider acoustic trachea connecting the two ears and two acoustic spiracles [17,27]. The spiracles are openings on either side of the thorax that provide two major sound inputs through the acoustic trachea to each ear [27]. The signal from the contralateral spiracle passes through the 'medial septum' in the middle of the animal which subjects the sound wave to an additional phase shift [28,29]. The contralateral and ipsilateral sound waves then superimpose before reaching the PTM from inside the posterior branch [14]. As such, the large tympanum is stimulated not only externally but also from a phase-shifted signal acting on its internal surface [14,30]. However, reports disagree on how these tympanal vibrations relate to the tuning of the ear to the calling song CF [14,19,21,30–32].

Several studies have reported a sharp vibrational response of the posterior tympanum close to the CF of the calling song [15,31,32]. For instance, in 1981, a distinct PTM velocity peak at 5.5 kHz was recorded [15]. A review in 2016 noted a close correspondence of this finding with the tuning curve of the tympanal nerve, and the PTM was therefore implicated as a sufficient biophysical filter determining the CF-tuning of the auditory pathway at the neural and behavioural levels [33]. Similarly, Johnstone *et al*. [31] observed a single displacement optimum at 4.0 kHz that indicated the PTM *'is mechanically tuned to a relatively narrow spectrum of frequencies*'.

A strong *direction-dependent* tuning of the PTM to the calling song CF has also been evidenced. By isolating each of the sound inputs, Michelsen *et al*. [27] calculated a significant phase shift when the calling song frequency was approached. This supported an earlier phase-shift hypothesis [13,29], whereby the internal–external phase difference exaggerates motion of the ipsilateral PTM, thus enhancing directional cues at that frequency. Experimental evidence was provided by Michelsen & Löhe [32], of a pronounced PTM peak close to the calling song CF when the sound source was presented ipsilaterally. Together, these findings suggest the PTM is indeed sharply tuned to the CF of the calling song, either from mechanical resonance and/or directional tuning.

However, other early measurements of the PTM show a CF optimum which is nonetheless too broad to match the tight tuning curves of the mechanosensory neurons [17,19]. A second frequency filter has, therefore, long been conjectured [16,17,20], and the speculated filter has even been compared to that of the mammalian cochlea [17].

More recent recordings suggest a PTM optimum as high as 11–17 kHz with broad filtering [21]. Further testing of the phase-shift hypothesis does support directional tuning [14,30] but reveals a broader response than observed by Michelsen & Löhe [32] and even at optima higher than the calling song CF [14]. The proposed second filter, situated between the posterior tympanum and the sensory neurons, has therefore received renewed support [14]. Yet the anatomy of this region is complex [3,18] and how PTM vibrations are communicated to the sensors has remained *'enigmatic*' [18].

Nevertheless, the well-known apposition of the posterior PTB wall against the large tympanum is thought to be a likely means of mechanically coupling tympanal vibrations to the tracheal branches [16,18,21,22]. The arrangement of the branches beside each other probably provides a connection from the PTM to the anterior branch supporting the neurons [21]. Moreover, the dorsal membrane of the larger branch is known to connect directly to the PTM [18]. Given this morphology, Nishino *et al*. [18] in their 2019 study propose two possible transmission routes. One involves PTM coupling to the DM-PTB affecting the fluid surrounding the sensilla, while the other involves air movement through the connecting apertures causing inflation of the ATB. It is not known whether either of these pathways is in effect [18].

As such, (i) not only is the existence of secondary filtering hypothesized, but (ii) the path of transmission also remains to be identified. Accordingly, we aimed to address both research gaps using three separate methods: micro-computed tomography (µ-CT), laser Doppler vibrometry (LDV) and finite element analysis (FEA).

Our µ-CT results revealed the presence of the 'dividing membrane' (DivM) separating the branches and linking to the PTM via the DM-PTB. Three-dimensional (3D) analysis indicated that the DivM shares significant thinness similarity with these two membranes, further suggesting its auditory functionality. LDV recordings confirmed the existence of at least two distinct PTM vibrational peaks: a natural resonance around 14 kHz and a 6 kHz peak derived externally, probably from DM-PTB tuning. The µ-CT data served as the basis for an FEA model, which supported the LDV findings and indicated a series of tuned membranes including the DivM and the DM-ATB beneath the sensors. Numerical modelling also suggested the possibility of

a membrane-mediated volume change of the ATB. We discuss how these findings contribute to understanding filtering and transmission in this remarkable auditory system.

2. Methods

2.1. Animals

Mediterranean field crickets (*Gryllus bimaculatus*, De Geer) were commercially sourced and used for µ-CT and FEA analyses (supplier: Blades Biological Ltd, UK), and as the primary subject of LDV experiments (local supplier: Pets At Home, Glasgow). In addition, the Australian species *Teleogryllus commodus* were used for LDV tests and were provided from a lab colony (courtesy of Nathan Bailey, University of St Andrews, UK) originating from wild caught females (near Moss Vale, New South Wales).

Crickets were kept in a 12 : 12 h light : dark cycle, fed ad libitum, and given egg-carton sheltering. *G. bimaculatus* were placed as adults in an incubator (OVA-Easy 190 Advance, Brinsea) at 26°C within 15 l plastic containers and fed fish-food flakes, organic wheatgerm and gel-water. *T. commodus* were bred in a temperature-controlled room at 25°C within 16 l plastic boxes, with rabbit food and water-soaked cotton pads.

The CF of the *G. bimaculatus* calling song is 4.7 kHz and that of *T. commodus* is 4.0 kHz [7]. In figures 3, 5–7, the calling song CF is represented by a thin vertical red line.

2.2. µ-CT

In identifying anatomical structures of potential auditory functionality, a *thin* cuticle over an air-filled cavity would be of especial relevance [34]. This is because thin structures have less mass and lower stiffness, giving them greater vibrational displacement and therefore greater sensitivity to acoustic waves [35].

2.2.1. Insect preparation

Insects were killed by ethyl acetate fumigation [36]. The portion of the tibia containing the ear was excised with microscissors and submerged in 1:1 alcoholic Bouin's solution [37] in an Eppendorf tube and fixed overnight at 23°C. Fixative was extracted and the specimen was washed three times in 70% ethanol for 10 min each time, before passing through an ethanol dehydration series (10 min in solution, 10 min air-drying at room temperature: 50%, 70%, 80%, 90%, 95%, and three cycles of 100%). Tibial sections were submerged in 0.3% phosphotungstic acid (PTA) stain for optimal contrast [37] and kept at 23°C for three nights. The PTA solution was removed, and the specimen was rinsed in 100% ethanol (10 min, three cycles) and then finally chemically dried by immersion in 100% hexamethyldisilazane for 2 h before air-drying at 35°C overnight [38]. Specimens were stored in 70% ethanol prior to µ-CT scanning.

2.2.2. Imaging, segmentation and thickness analysis

Tibial sections were mounted vertically on a brass sample rod and imaged in air using a Bruker SkyScan 1172 µ-CT scanner. All scans were performed with an exposure time of 1325 ms, 0.2° rotation steps for 180°, a frame averaging of 2, a current of 100 µA and without a metal filter.

Thickness measurements (figures 1*b*,*c* and 2*h*) were obtained from 12 individuals (six female, six male) scanned with an X-ray tube voltage of 48 kV and an isotropic voxel size of 0.55 µm. Membrane and air column FEA models were derived from a single representative specimen (female) scanned at 30 kV and 0.88 µm voxels (figures 5–7 and electronic supplementary material, animation S1). Projection images were reconstructed using Bruker NRecon software (v. 1.6.9.18).

The thickness relationships of the DivM with surrounding structures were quantified (figure 2*h*) within cylindrical volumes of interest (diameter 20 µm, height 55 µm) located at the midpoint of the PTM (figure 1*b*). Five structures were analysed (see figure 1*c*): the PTM, the DM-PTB, the DivM, the ventral wall of the ATB (VW-ATB) and the VW-PTB. The DM-ATB was not segmented as the membrane could not be differentiated from adhered non-DM-ATB material. The five samples were binarized by global threshold (21–255) and denoised (removal of all except largest object, in 3D). Thickness was then determined in CT Analyser (v. 1.14.10.0) using the maximal diameter sphere-fitting technique [39].

Transmission [18,29] and filtering [19] have been hypothesized to involve the air column inside the tracheal branches, rather than solid–solid tracheal coupling. As such, the air column too was segmented (figures 2*c* and 7*c*). Segmentation was performed in 3D Slicer (v. 4.11.20210226) with the threshold paint tool. The mesh was cleaned in MeshLab (v. 2021.07) before exporting as an STL file for subsequent FEA simulation.

2.3. Laser Doppler vibrometry

2.3.1. Set-up

The vibrational response of the posterior tympanum was recorded from a total of 41 *G. bimaculatus* and six *T. commodus* using a 3D LDV (MSA-100-3D, Polytec) (figure 3). To anaesthetize, animals were chilled in a freezer for 5 min at −18°C. Spiracle flaps

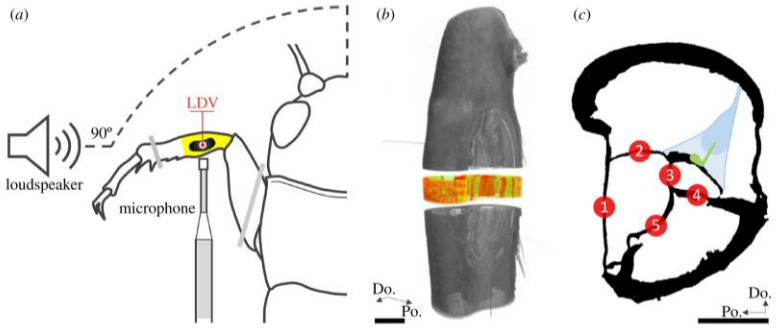

Figure 1. LDV set-up and µ-CT thickness analysis. (*a*) Schematic of LDV experimental set-up (see also electronic supplementary material, figure S2). The loudspeaker was level with the cricket 22 cm from its midline and 90° ipsilateral. The reference microphone was perpendicular to the loudspeaker within 1 cm of the ipsilateral tympanum. (*b*,*c*) Methodology employed in µ-CT 3D thickness analysis. (*b*) Volumetric visualization illustrating the approximate position of the image stack at the midpoint of the PTM from which the five cylindrical samples of diameter 20 × 55 µm were segmented. (*c*) The five structures (1–5) that were sampled and the positions in the middle of each structure from which the cylindrical segmentation was taken: 1. PTM; 2. DM-PTB; 3. DivM; 4. VW-ATB; 5. VW-PTB. The illustration in blue represents the tympanal organ and its arrangement based on the literature, e.g. [21]; green = sensory neurons. PTM, posterior tympanal membrane; DM-PTB, dorsal membrane of the posterior tracheal branch; DivM, dividing membrane; VW-ATB, ventral wall of the ATB; LDV, laser Doppler vibrometry. Scale bars: 200 µm.

were then removed with microscissors or blocked with petroleum jelly (Vaseline®). The cricket was pinned to a wax bed upon a goniometer (GN1/M, Thorlabs) attached to an aluminium platform custom-built to screw into the LDV X-Y position stage. Posterior tympana were secured facing upwards and the anterior tympana were kept free from underlying wax (see figure 1*a* and electronic supplementary material, figure S2).

The LDV sat upon a vibration isolation air table inside a semi-anechoic double-walled audiometric room (IAC Acoustics). The loudspeaker was situated level to the animal, 22 cm from the cricket's midline, at 90° azimuth, ipsilateral to the target PTM. To provide a reference signal, a 1/8″ precision pressure microphone (Type 4138 A-015, Brüel & Kjær), connected to a conditioning amplifier (Type 2690 A-0F2 NEXUS, Brüel & Kjær), was positioned perpendicular to the loudspeaker within 1 cm of the ipsilateral tympanum (figure 1a and figure S2).

2.3.2. Stimuli

LDV experiments were conducted under three acoustic conditions. All stimuli were presented at 2–20 kHz with 1600 fast Fourier transform lines and averaged over five cycles of complex averaging.

2.3.2.1. Acoustic condition 1

Pure tones (sine waves) were presented through a 5.8 cm diameter cone-diaphragm loudspeaker (VISATON FR58, 8 Ω, 120–20,000 Hz) at a linear sound pressure output of 78 dB [14] to crickets with open spiracles (flaps cut) (figure 3*a*). Single point measurements were obtained from the middle of the tympanum in 10 *G. bimaculatus* (five male, five female). Experimental duration was optimized: field crickets communicate using three songs [11], each of which has a dominant frequency between either 3–6 kHz [8] or 11–16 kHz [6]. As such, these frequency ranges were measured in 200 Hz bins; all other frequencies were binned every 1000 Hz. Results are presented as velocities (µm s^{-1}).

2.3.2.2. Acoustic condition 2

Sweeps (periodic chirps) applied through the same loudspeaker provided multipoint measurements of the whole tympanum at finer 15.625 Hz frequency bins (figure 3*b–f*). Recordings were taken from 20 *G. bimaculatus* (10 female, 10 male) and six *T. commodus* (one female, five male), with spiracles open, using a manually drawn outline of the PTM. Within the outline, a mesh of scan points was autogenerated with distances between points of app. 72 µm. To control for any nonlinearity in the loudspeaker outputs (see electronic supplementary material, figure S3), results are presented as the frequency response function (FRF) of velocity in response to sound pressure (µm s^{-1} Pa).

2.3.2.3. Acoustic condition 3

Sweep recordings were also taken with a second loudspeaker (figure 3*g*,*h*) that uses a ribbon-diaphragm technology, known as a Heil air motion transformer (ESS, 800-20,000 Hz). PTM responses were recorded from 10 *G. bimaculatus* (six female, four male) with closed spiracles and from a further 10 (six female, four male) with spiracles open. Results are presented as velocity (µm s^{-1}) alongside the mean output of the loudspeaker (dB).

2.4. Finite element analysis

2.4.1. Demonstrating coupled resonators

LDV revealed the 6 kHz peak to be a driving-force rather than the natural resonance of the tympanum, which was identified at around 14 kHz (see figure 3). To demonstrate that this experimental finding can be reproduced by the action of a mechanically coupled resonator, the PTM was simulated in COMSOL Multiphysics® (v. 6.1) *with and without* its DM-PTB coupling (see figure 4).

The PTM was represented by a 1083 × 397 µm two-dimensional (2D) ellipsoid primitive with a thickness of 8 µm. When coupled, a 240 × 1100 µm shell element was attached as the DM-PTB, 50 µm above the tympanum's major axis, and assigned a thickness of 4 µm. Coupled–uncoupled simulations were swept over the frequency domain from 1 to 20 kHz in 100 Hz steps. Instantaneous velocity was calculated from the tympanum in isolation and when coupled before conversion into real and imaginary values (µm s^{-1} Pa) for standard modal analysis.

2.4.2. Simulating the tracheal branches

Data from µ-CT and LDV supported a resonance function of the DivM and DM-PTB, respectively. These membranes were numerically modelled in COMSOL within a finite-element model of the intact system, constructed from µ-CT data (see figure 5*h-k*).

2.4.2.1. Dimensions from µ-CT

Model dimensions were taken from the 0.88 µm dataset (described in §2.2.2.). Cross-sectional µ-CT slices were segmented by binary-threshold (an example slice can be seen in figure 1*c*). The binarized images were used to outline the branches by placing vertices at the points where the tracheal walls intersect. Given the inherent irregularity of anatomical positions, traces were made on arbitrary slices by visual inspection of significant anatomical features. Outlines were made on 10 irregularly spaced images, covering the full extent of the branches. A total of 63 vertices were then connected by linear interpolation to form a wireframe mesh.

The maximal length and width of the PTM were measured from the same µ-CT dataset using a segmentation of the tympanum in 3D Slicer. The measured dimensions were then assigned as the major and minor axes of a 1083 × 397 µm ellipsoid, positioned coincident with the posterior side of the hexahedral mesh (figure 5*h–k*).

2.4.2.2. Thicknesses from µ-CT

The wireframe was converted to a shell physics model and the thicknesses from µ-CT measurements (see figure 2*h*) were assigned to corresponding elements of the model: PTM, 6.8 µm; DM-PTB, 5.2 µm; DivM, 6.2 µm; DM-ATB, 5.2 µm; non-membrane elements, 9.1 µm. The DM-ATB was given the same thickness value as its corresponding dorsal membrane of the PTB. The thicknesses of all non-membrane boundaries were assigned as the mean average of the two ventral wall thickness values (figure 2*h*).

2.4.2.3. Material properties from the literature

The material properties of the gryllid PTM and tracheal branches are unknown, and as such were here based on previous FEA modelling of the locust tympanum by Malkin *et al*. [40]. The model was made an isotropic linear-elastic solid and assigned a Poisson's ratio of 0.3 and a density of 1300 kg m^{-3}. The PTM was given a fixed boundary condition and assigned a Young's modulus of 20 MPa. All non-PTM elements were given a lower value of 2 MPa, in line with the cuticle of the cricket leg trachea known to contain the rubber-like protein resilin [41]. The model was swept over the frequency domain in steps of 100 Hz from 1 to 20 kHz. Maximum velocity of the element (µm s^{-1}) and strain energy density at the element's midpoint (J $µm^{-2}$) were calculated (figure 5). Volume change of the anterior branch has previously been proposed, albeit from aperture airflow [18]. We calculated *membrane-mediated* volumetric increase as the integral of the displacements of all ATB boundaries ($µm^3$) (figure 6).

2.4.3. The air column

The role of the PTM in effecting *pressure change* [18,29] inside the tracheal branches was investigated using the shell physics model (figure 7*a*) and applying 1 Pa pressure to the tympanum. Doing so had little effect on ATB air pressure (figure 7*b*) which indicated movement of the PTM exerts a negligible influence on internal air pressure.

A *cavity resonance* [19] was investigated using the µ-CT segmentation of the air column (figure 7*c*), which was treated as a thermoviscous pressure acoustics model. The proximal opening that leads into the PTB was the sole pressure input (given the PTM was negligible). The morphology of the tracheal branches and apertures resemble a Helmholtz resonator [42]. Transmission loss—that is, a sharp decrease in sound pressure down the air column—was considered indicative of a Helmholtz resonance and was calculated as the average pressure (Pa) below the apertures (distal) relative to that of the proximal input above (figure 7*d*).

2.5. Data analysis

Thickness results are reported as mean ± s.d. Normality was assessed using the Shapiro–Wilk test on residuals. Homogeneity of variances was tested using Levene's test. Data were assumed to be normally distributed and with homogeneity of variances, therefore a one-way analysis of variance (ANOVA) with Tukey's HSD *post-hoc* test was performed. Significance was defined as $p < 0.05$. Statistical analysis was performed in R (v. 3.6.1). Vibrometry results are reported as mean ± s.e.m. and only data points above 85% coherence were kept. FRFs were smoothed by a moving average filter of five frequency bins.

3. Results

3.1. Evidence of DivM functionality according to µ-CT 3D analysis

Thickness colour maps highlighting <10 µm cuticle in red indicated the membrane between the branches—the DivM—to be (i) within the same thickness range as the DM-PTB and PTM, and (ii) in a coupling arrangement with these membranes (figure 2*d*,*g* and electronic supplementary material, animation S1). The DivM was also conspicuous under light microscopy (figure 2*e*,*f*). Average thickness values from the subsequent 3D analysis of five segmentations (figure 1*b*,*c*) were: PTM, 6.8 ± 1.2 µm; DM-PTB, 5.2 ± 2.1 µm; DivM, 6.2 ± 1.2 µm; VW-ATB, 9.3 ± 1.6 µm; VW-PTB, 8.8 ± 2.5 µm ($n = 12$, mean ± s.d.). Statistical analysis showed the DivM to be significantly thinner than two of the five structures, the VW-ATB (***$p<0.001$) and the VW-PTB (**$p<0.01$) (figure 2*h*).

3.2. The PTM response according to LDV: evidence of DM-PTB tuning

3.2.1. Two distinct peaks in the PTM vibrational response

3.2.1.1. Acoustic condition 1

Recordings of PTM vibrations under 78 dB pure tones yielded two distinct mean-average ($n = 10$) velocity peaks, one at 5.8 kHz and the other at 13.8 kHz (see figure 3*a*). Across individuals, the position of peak 1 ranged from 5.4 to 6.0 kHz while the position of peak 2 was more variable with a range of 12.2–16.0 kHz.

3.2.1.2. Acoustic condition 2

Frequency sweeps revealed similar results: a clear mean-average ($n = 20$) peak at 6.0 kHz and another at 14.3 kHz (see figure 3*c*).

Distinct peaks were also apparent from *T. commodus*, with the first at 6.4 kHz and the second at 12.2 kHz (mean, $n = 6$) (figure 3*e*).

3.2.2. Driving-force and natural resonance identified from PTM phase

PTM phase responses revealed that, at the 6 kHz vibrational peak (figure 3*a*,*c*), the tympanum was oscillating *in-phase* relative to the wavefront of the stimulus. This can be seen in figure 3*d* (mean, $n = 20$) as the real and imaginary plots (blue and orange, respectively) trending together at the 6 kHz position.

An in-phase response is characteristic of a resonant system which remains dominated by its mass momentum, necessarily below its natural resonance peak. This means that whatever was generating the PTM peak at 6 kHz was a *driving-force* external to the tympanum itself.

The position of this driving-force matches well with the PTM vibrations from both acoustic conditions 1 and 2, as highlighted by a yellow bar (see figure 3*a*–*d*). The width of the yellow highlight corresponds to the 5.9–6.2 kHz range across individuals ($n = 20$).

In contrast, at the second vibration peak near 14 kHz (figure 3*a*,*c*), the phase of the membrane sharply diverges. This is seen in figure 3*d* (mean, $n = 20$) as the blue and orange plots trending away from each other at the 14 kHz position. This *out-of-phase* response is characteristic of the *natural resonance* of a membrane.

The position of the PTM natural resonance is highlighted by a green bar. Its considerable width corresponds to the 11.2–19.3 kHz variability between individuals ($n = 20$). For example, the specimen of figure 3*b* exhibited a PTM natural resonance at 16.2 kHz.

From *T. commodus*, the phase responses (mean, $n = 6$) of the tympana likewise indicated that peak 1 (6.4 kHz) was a driving-force, while peak 2 (12.2 kHz) was the natural resonance of the tympanum (figure 3*e*,*f*).

The mathematical theory explaining the difference between a driving-force and the PTM natural resonance is provided in electronic supplementary material, appendix S4.

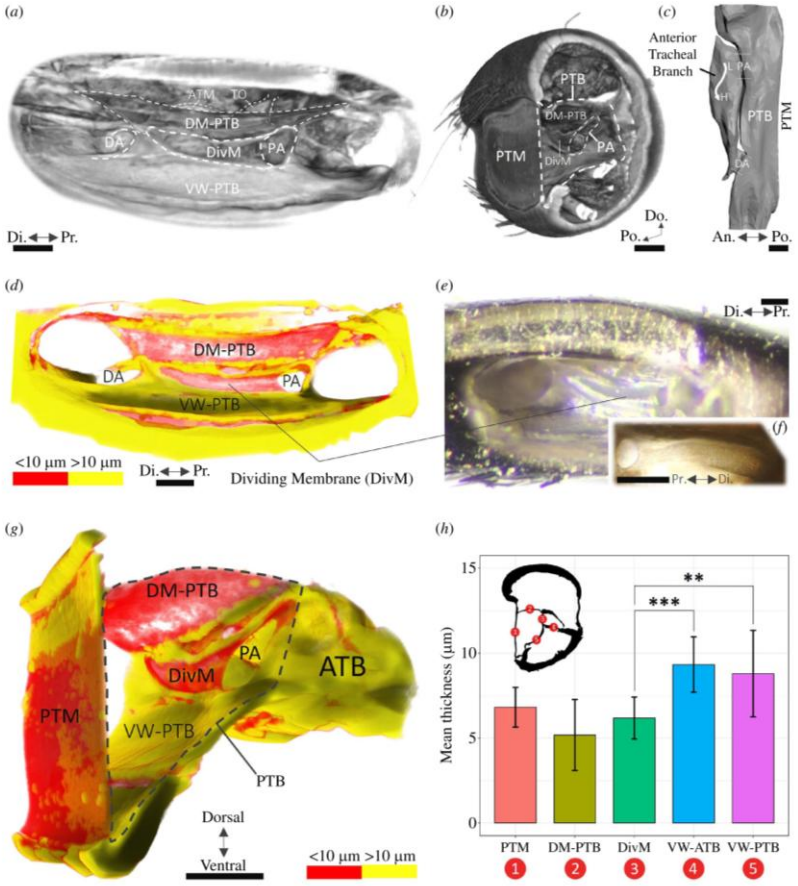

Figure 2. µ-CT visualization and 3D thickness analysis of the field cricket tracheal branches and PTM. (*a*,*b*) µ-CT volumetric visualization. (*c*) Segmentation of the air column. (*d*,*g*) Three-dimensional thickness colour maps (see also electronic supplementary material, animation S1). Cuticle below 10 µm in thickness is coloured red. (*e*,*f*) Photographs of the DivM taken under light microscopy from a left (*e*) and a right (*f*) ear. (*h*) Results of the thickness analysis of the five sampled structures (n = 12, s.d. error bars, one-way ANOVA with Tukey's HSD). Results indicate the DivM is significantly thinner than two of the structures: the VW-ATB (***p<0.001) and the VW-PTB (**p<0.01). (Only significant differences relating to the DivM are shown.) ATM, anterior tympanal membrane; TO, tympanal organ; DivM, dividing membrane; PA, proximal aperture; DA, distal aperture; DM-PTB, dorsal membrane of the posterior tracheal branch; VW-PTB, ventral wall of the PTB. Scale bars: 100 µm.

3.2.3. Effect of closing spiracles on PTM filtering

3.2.3.1. Acoustic condition 3

Conceivably, the 6 kHz driving-force was driven by the signal via the auditory spiracles. Accordingly, we measured tympanal responses with and without the spiracles blocked (see figure 3*g*). The data, however, appear considerably noisy, at least from around 6 kHz upwards.

Yet, despite the noise, the corresponding phase data at least for one individual suggested a maintained 6 kHz driving-force after the spiracles had been blocked (see figure 3*h*, yellow highlight).

Overall, the data were not deemed suitably reliable and as such the effect of closing the spiracles was largely determined from the literature (see §4).

3.2.4. PTM modal response

The PTM oscillated with a fundamental (0,1) drum mode at all frequencies. This can be seen in figure 3*i–l* in the maximal velocities of each scan point at peaks 1 and 2 for both species (see also electronic supplementary material, animation S5). This means that only one of the two observed vibrational optima can have been the natural resonance of the membrane [35].

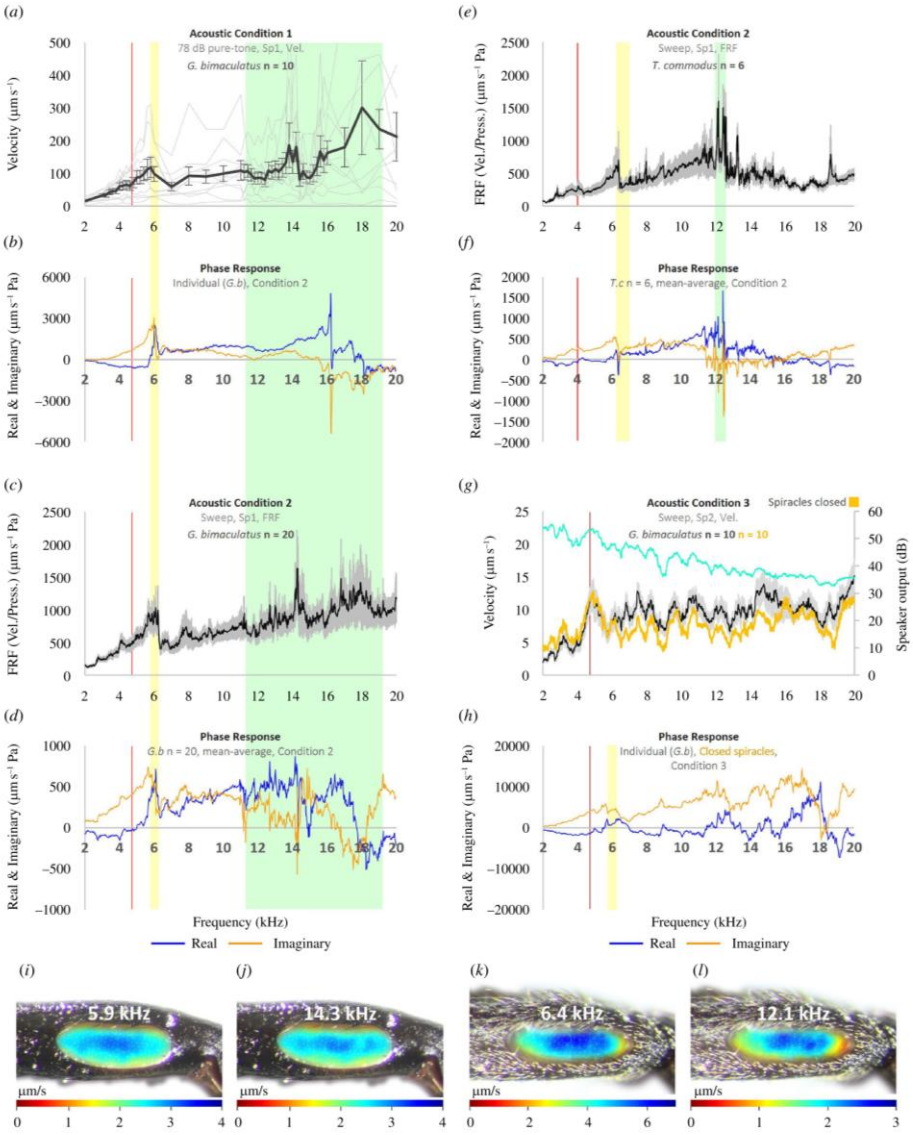

Figure 3. Responses of the field cricket PTM from LDV experiments. (*a*) Pure tone velocity recordings taken with a constant sound pressure level of 78 dB and indicating two vibrational peaks, one at 5.8 kHz and a second at 13.8 kHz ($n = 10$, mean ± s.d.). (*b–f*) Recordings from frequency sweeps (see electronic supplementary material, figure S3 for loudspeaker outputs). (*b*) The phase response of a representative tympanum showing the PTM vibrated with a driving-force at 6.0 kHz (yellow highlight) and a natural resonance at 16.2 kHz (green highlight). (*c*) Mean-average ($n = 20$, ± s.e.m.) FRF of PTM velocities in response to sound pressure, showing a vibrational optimum at 6.0 and 14.3 kHz. (*d*) Mean phase ($n = 20$, ± s.e.m.) revealing the 6.0 kHz peak was a driving-force and the 14.3 kHz peak the natural resonance of the tympanum. (*e,f*) PTM response from *T. commodus* ($n = 6$, mean ± s.e.m.) showing a driving-force peak at 6.4 kHz and the natural resonance at 12.2 kHz. (*g,h*) PTM velocities with the spiracles *open* (black, $n = 10$, mean ± s.e.m.) and *closed* (orange, $n = 10$, mean) using a ribbon-diaphragm AMT loudspeaker (loudspeaker output shown). The data were noisy, but a corresponding phase response (*h*) suggested a maintained driving-force near 6.0 kHz. (*a–h*) The widths of the yellow and green highlights correspond to the ranges in frequency positions across individuals (*G. bimaculatus*, $n = 20$; *T. commodus*, $n = 6$). (*i–l*) Maximal velocity per LDV scan point at peak 1 and 2 in *G. bimaculatus* (*i,j*) and *T. commodus* (*k,l*) showing the PTM oscillated with a drum mode at both peaks (see also electronic supplementary material, animation S5). *G.b, G. bimaculatus; T.c, T. commodus*; FRF, frequency response function; AMT, air motion transformer.

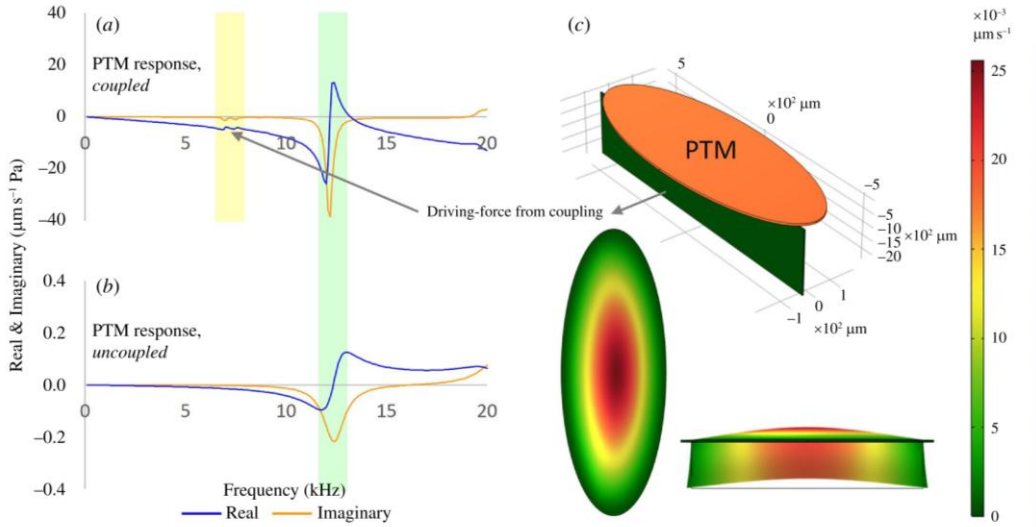

Figure 4. FEA demonstration of a coupled resonator driving the first PTM peak. (*a*,*b*) The driving-force (yellow highlight) was only evident when the PTM was coupled. (Green highlight = natural resonance of the membrane.) (*c*) FEA model in coupled configuration (external resonator in dark green).

3.2.5. Candidate driver of the driving-force

Peak 1 at 6 kHz was from a driving-force and was therefore sourced from an external driver to the PTM. The obvious candidate driver was the DM-PTB membrane, which is known from the literature [18] and our μ-CT reconstructions (e.g. figure 2*g*) to be connected to the PTM at approximately 90° on its dorsal aspect.

3.3. Coupled resonators: demonstration of LDV results from FEA

The capacity for a resonator coupled to the tympanum to drive a driving-force peak on the PTM was demonstrated by numerical modelling (see figure 4). Only when the PTM was coupled did the PTM oscillate with a driving-force (figure 4*a*, yellow highlight).

3.4. A chain of coupled membranes: FEA

The DivM was shown from μ-CT to be a candidate coupled resonator (figure 2), as was the intermediate DM-PTB from LDV experiments (figure 3). How these membranes influence the complete system, from the PTM to the ATB supporting the sensilla, was numerically modelled (figure 5).

3.4.1. Vibrational tuning of four membranes

The calculated vibrational profile of the PTM (figure 5*a*) showed robust agreement with experimental data (see figure 3*a*,*c*), in that the simulated tympanum responded with a dominant resonance at 10.7 kHz and a lower-frequency peak at 7.2 kHz.

In line with the DM-PTB functioning as the resonant driver of peak 1, the 7.2 kHz PTM peak exactly correlated with a principal sharp resonance of the DM-PTB (see figure 5*b*).

In agreement with the μ-CT investigation pointing to a DivM function, the simulated DivM vibrated with a dominant resonance at 7.0 kHz (figure 5*c*). Moreover, the DivM also exhibited a torque multiplication of the vibrational energy it received from the PTM: at the tympanum's dominant frequency position, the DivM amplified the force 34-fold (see figure 5*e*). (For a theoretical explanation of strain energy, see electronic supplementary material, appendix S4.)

At 5.1 kHz, closer to the calling song CF, the dorsal membrane of the ATB supporting the sensilla vibrated with a distinct resonance (figure 5*d*), suggesting the possibility of *successive filtering*: 10.7 kHz PTM to 7.2 kHz DM-PTB to 5.1 kHz DM-ATB.

The 5.1 kHz DM-ATB resonance was correlated with an extremely faint but nonetheless evident disturbance in PTM vibrations (see figure 5*f*, left-hand star). A possible corresponding subpeak at 4.2 kHz may have been evident in the LDV experimental recordings (figure 5*g*, left-hand star; see also figure 3*a–f*).

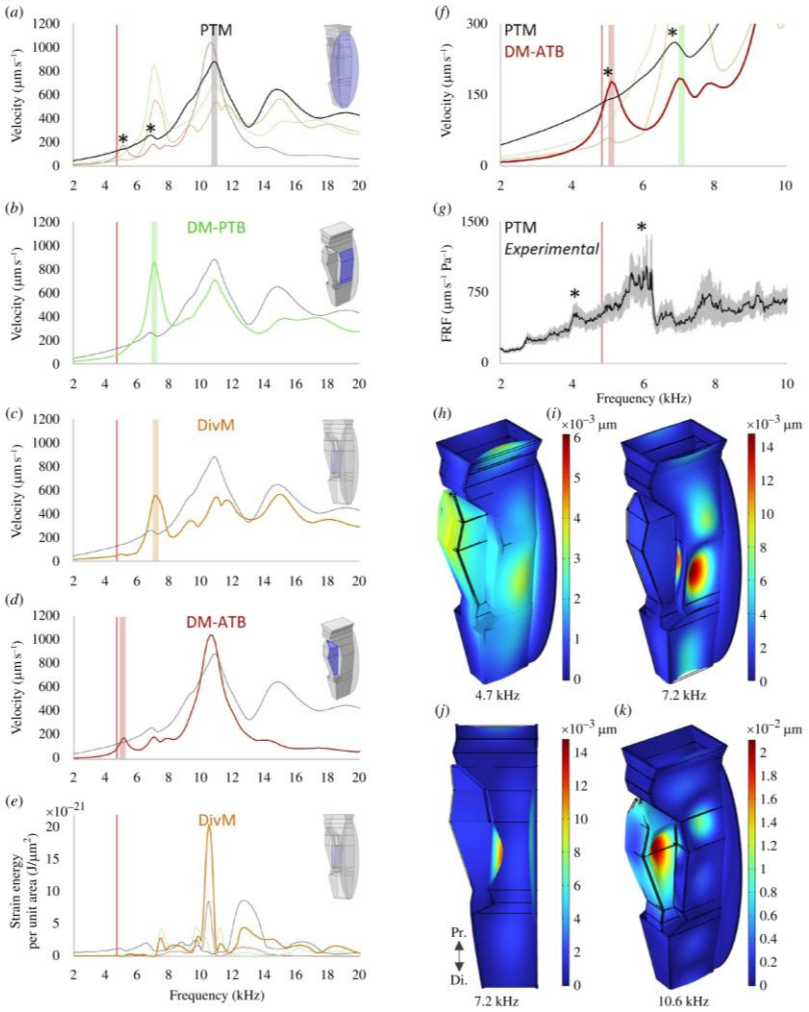

Figure 5. Vibrations of the internal membranes and PTM according to FEA. (*a*) The velocity profile of the PTM exhibited a robust match with experimental results (see figure 3) in showing a main resonance at 10.7 kHz with a lower-frequency peak at 7.2 kHz that (*b*) exactly matched the dominant resonance of the internally connected DM-PTB. (*c*) The DivM resonated with a peak velocity of 7.0 kHz. (*d*) The dorsal membrane of the ATB, which supports the sensory neurons, responded with a distinct resonance closer to the calling song CF. (*e*) The DivM effectively amplified the vibrational energy transmitted from the PTM, at the tympanum's resonant frequency. (*f*) A very slight but nonetheless evident disturbance of the PTM was directly correlated with the resonant frequency of the DM-ATB (left-hand star), (*g*) which conceivably corresponds with a possible subpeak in the LDV-recorded response. (*h–k*) The µ-CT-based FEA model used, showing boundary displacements at relevant frequencies.

3.4.2. Membrane-mediated ATB volume change

The volume of the anterior branch across frequencies was calculated. The ATB exhibited volume fluctuations from 4.8 to 10.4 kHz (see figure 6*a*). Intermediate peaks of volume increase corresponded to nulls (highlighted) at 5.1 and 7.1 kHz which matched the resonances of connected membranes: the DM-ATB, and the DivM and DM-PTB, respectively (figure 5*b–d*). The greatest increase in ATB volume occurred at 10.4 kHz, correlated with the tympanum's dominant resonance (figure 5*a*).

If functioning as a resonant membrane, the DivM appears to be well-positioned at the interface of the ATB to possibly contribute to an ATB volume change (e.g. see figure 2*g*). As such, ATB volume was calculated *with* (teal) and *without* (black) the DivM in place (figure 6*a*). Without the DivM, there was a 24.5% loss in ATB volume at the maximal peak and all peaks shifted down by approximately 600 Hz.

Figure 6*b* shows the modelled ATB at different frequencies with boundaries colour-coded according to displacements as the ATB inflated and deflated. (Note that the rest of the model is not shown and that the full model was simulated intact, *with* the DivM in place.) The ATB was in a state of relative deflation at 2 kHz but increased in volume towards 4.7 kHz, with then a slight

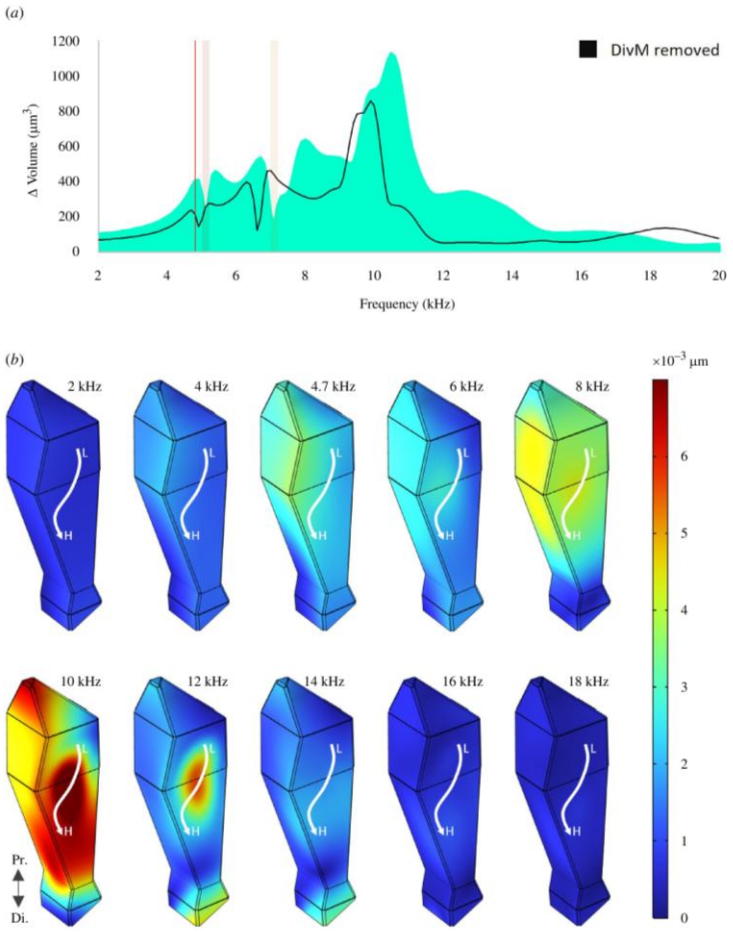

Figure 6. Membrane-mediated volume change of the ATB according to FEA. (*a*) The anterior branch inflated and deflated within a biologically relevant frequency range, between 4.8 and 10.4 kHz. The intermediate nulls were correlated with the membrane resonances (see figure 5). Removing the DivM from the system (black) reduced ATB volume by 24.5% at maximal peak and lowered all spectra by around 600 Hz. (*b*) Mosaic showing ATB boundary displacements at different frequencies. (The rest of the system, including the PTM, is not shown; the DivM was in place.) The ATB exhibited relative deflation at 2 kHz with increasing volume towards 4.7 kHz, then a slight decrease, before expanding to maximal volume around 10 kHz and then deflating towards 18 kHz. The white arrow represents the approximate positions of the low- (L) to high-frequency (H) tuned mechanoreceptors as based on Nishino *et al*. [18].

decrease, before expanding to maximal volume around 10 kHz, and then again deflating towards 18 kHz. The white arrow represents the approximate positions of the low- (L) to higher-frequency (H) tuned auditory neurons, as based on Nishino *et al*. [18].

3.5. Air column pressure and resonance according to FEA

Oscillating the PTM of the shell model (figure 7*a*) with 1 Pa pressure resulted in a less than 10% *pressure change* inside the ATB relative to that applied (see figure 7*b*), indicating PTM movement has a negligible influence on tracheal air pressure.

Using a segmentation of the air column (figure 7*c*) and the spiracular input as the sole pressure source, a *cavity resonance* (calculated as transmission loss) was not reached until 70.3 kHz (figure 7*d*), considerably higher than the spectral compositions of the calling, rivalry and courtship songs [6,7,11].

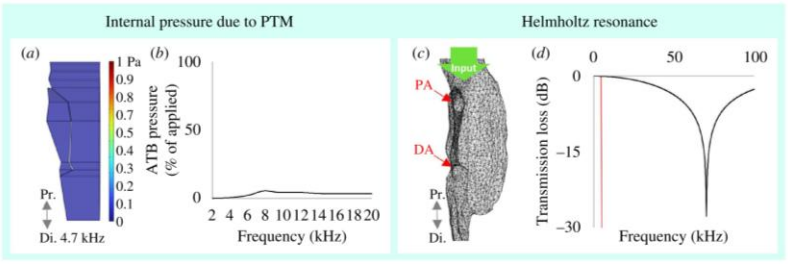

Figure 7. Tympanal driven pressure change and cavity resonance inside the tracheal branches according to FEA. (*a*,*b*) Air column pressure from stimulating the posterior tympanum with 1 Pa pressure, within (*a*) the FEA shell model. Figure shows tracheal pressure at 4.7 kHz. (*b*) Pressure inside the ATB was less than 10% of that applied from the PTM, indicating the PTM is a negligible influence on internal air pressure. (*c*) µ-CT segmentation of the air column. A sharp loss in pressure below the proximal and distal apertures (PA and DA) relative to the input pressure above (green arrow) was considered indicative of a Helmholtz resonance. (PTM was ignored.) (*d*) The air column of the tracheal branches did not resonate until 70.3 kHz, considerably above the relevant range of communication signals [6,7,11].

4. Discussion

4.1. The dividing membrane

Previous studies have proposed the existence of an additional frequency filter [14–19,33] and an unknown transmission pathway [13,16,18,19,22] behind the large tympanum of the field cricket ear. Most anatomical investigations of this region have been limited to 2D sectioned material [3,43,44], potentially restricting a comprehensive understanding of the functional anatomy. A significant advancement, however, was made in the 2019 confocal microscopy study by Nishino *et al*. [18], which included a pioneering 3D reconstruction of the ear. In our investigation, we employed µ-CT imaging to conduct 3D visualization and thickness analysis of the Gryllinae PTM and internal structures.

The 3D thickness analysis reveals a potential auditory function of the DivM structure separating the tracheal branches. This functionality is indicated by (i) its linkage to the DM-PTB and PTM membranes (figure 2*g*) and (ii) its significant thinness (figure 2*h*).

Despite its potential importance, some of the key anatomical studies on the field cricket ear do not mention the DivM [3,18,45]. In our volumetric visualizations (e.g. figure 2*a*,*b*), we too initially overlooked this structure. Its coupling and resonating potential were recognized only after applying thickness colour maps (figure 2*d*,*g*). Subsequent light microscopy (figure 2*e*,*f*), statistical analysis (figure 2*h*) and numerical modelling (figure 5*c*,*e*) further supported this observation.

Previous attention to this structure has nonetheless been applied. In detailing the field cricket tracheal branches, Friedman [46] referred to their separation by '*the thin cuticle wall*'. This thin wall was defined by Larsen *et al*. [16] as *'the partition*' and these authors further proposed an auditory function, suggesting the partition might act as a pressure difference receiver like the posterior tympanum. Although the authors acknowledge such a function is unlikely, their hypothesis shows that the DivM has been recognized as a potential resonator.

Furthermore, it has long been observed that the solid–solid connection of the PTM to adjacent tracheal branches serves as a potential transmission pathway to the sensors [16,18,21,22]. Larsen *et al*. [16] suggested that transmission from the PTM *'most likely includes the tracheal walls of the PTB and ATB*', while Schneider *et al*. [21] described the PTM-PTB-ATB arrangement as a *'coupled system*'.

Evidence of PTM–tracheal coupling supporting a transmission pathway is here presented. µ-CT thickness analysis identifies the dividing membrane as a possible resonator (figure 2). The DivM is further demonstrated from µ-CT-based modelling to amplify PTM transmission (figure 5*e*), contribute to increased ATB volume (figure 6*a*) and resonate at a distinct frequency (figure 5*c*). These findings introduce a specific pathway within tracheal coupling facilitating both transmission and filtering, from the PTM to the DivM via the DM-PTB.

4.2. Towards resolving the vibrational profile of the PTM

The posterior tympanum is the essential first link of the transmission path in the field cricket ear [10,19,20,22] and clearly functions as a frequency filter [14,15,17,19–21,30–32]. As such, any attempt to understand filtering and transmission in this system must include an understanding of the vibrational profile of this structure.

Yet the exact filtering characteristics of the PTM have remained uncertain. Previous studies have indicated a single low-frequency resonance close to the calling song CF [19,31], while others have shown two distinct peaks [15,17,20]. Tympanal tuning at the CF of the calling song has been presented as sharp [31,32] and as broad [19,30]. Most recently, a single broad resonance with an optimum above the calling song CF has been suggested [14,21].

4.2.1. Experimental findings

The LDV results presented here of the PTM vibrational response show a clear distinction between a 6 kHz peak and a second near 14 kHz (figure 3*a–d*). The presence of a low-frequency peak between 4 and 7 kHz is consistent with most studies [15,17,19,20,30–32], and the position of a second peak near 14 kHz is also in broad agreement with previous recordings [15,17,20].

The more recent finding by Lankheet *et al*. [14], of a single broad 6–8 kHz resonance, was from normalized data. Conceivably therefore, differentiation of distinct peaks may have been lost in the averaging. As for the 11–17 kHz optimum subsequently reported by Schneider *et al*. [21], this result used only one measurement below 7 kHz and therefore a 6 kHz first peak could not possibly have been recognized.

We found the tympanum oscillated at both 6 and 14 kHz with the same up-down drum mode (figure 3*i–l* and electronic supplementary material, animation S5). This result agrees with earlier observations [17,19] and means that only one of the two vibrational optima can be the natural resonance of the tympanum [35].

The natural resonance of the PTM was identifiable in the phase responses and was consistently positioned above 11 kHz (figure 3*a–d*, green highlight). In contrast, the 6 kHz peak was revealed to be the product of a driving-force, driven from an external source to the tympanum (figure 3*a–d*, yellow highlight). What then is the driver that is vibrating the tympanum at 6 kHz?

Conceivably, the 6 kHz optimum is driven by a phase-shifted signal from the auditory spiracles acting on the tympanum's internal surface. However, in figure 3*h* the 6 kHz driving-force appears maintained in an individual with *blocked* spiracles. More compelling is the study by Larsen [15] in which both spiracles of *G. bimaculatus* were blocked and yet a sharp velocity peak near 6 kHz was observed, alongside a distinct higher-frequency optimum. Together, this evidence strongly indicates that the 6 kHz peak is not driven by the spiracular inputs.

Alternatively, the driver is a mechanical resonator vibrating at its own natural resonant frequency of 6 kHz that is somehow affecting the PTM. Strikingly, Larsen [15] hypothesized such a resonator in 1981: *'… the mechanical system of the ear responds almost as if it consisted of two coupled, simple oscillators, one with a high-frequency vibration, and another with a low-frequency vibration. The identity of the two hypothetical oscillators is still obscure …'*.

Based on the 2019 anatomical study by Nishino *et al*. [18] as well as our own µ-CT results (figure 2), the obvious candidate resonator is the dorsal membrane of the posterior branch. This membrane is known to be connected to the inside surface of the tympanum (figure 2*g*).

There are at least two reasons why the properties of the DM-PTB and not the PTM may be facilitating a lower-frequency 6 kHz resonance: (i) the DM-PTB is thinner, even if not significantly so (see figure 2*h*), and a membrane even slightly thinner will resonate at a considerably lower frequency due to its flexural rigidity being proportional to the *cubed* of its thickness (see electronic supplementary material, appendix S4). (ii) The cuticle of the field cricket leg trachea is known to contain more resilin than the PTM [41], and this would be expected to lower the Young's modulus of the DM-PTB and therefore its resonant frequency.

4.2.2. Numerical modelling

The conclusion from experimental results, that the DM-PTB is driving the 6 kHz peak of the PTM, is strongly supported by the numerical modelling:

The first FEA model demonstrated the action of a coupled resonator on the PTM phase response and showed that the driving-force was only evident on the PTM when it was mechanically coupled (figure 4*a*, yellow highlight). When uncoupled, the PTM no longer vibrated with the lower-frequency peak (figure 4*b*).

The second model constructed from µ-CT data (figure 5) simulated the vibrational velocities of both the PTM (figure 5*a*) and the DM-PTB (figure 5*b*). The DM-PTB vibrated with a sharp resonance that exactly coincided with a lower-intensity peak in the PTM response.

4.2.3. The vibrational profile

Taken together, we can construct the probable profile of PTM vibrations in the field cricket: the posterior tympanum vibrates with two frequency optima, one its natural resonance of around 14 kHz, the other a 6 kHz driving-force from its coupling to the DM-PTB resonator.

4.3. Conclusions

4.3.1. Summary of key findings

Here, a coupled resonance potential of the field cricket dividing membrane is revealed by 3D µ-CT thickness analysis and corroborated by numerical modelling. LDV recordings of the PTM confirm two vibrational optima with a natural resonance around 14 kHz and a driving-force at 6 kHz probably driven by the tuning of the internally coupled DM-PTB, a conclusion supported by FEA calculations. FEA further suggests a train of successive filtering that also includes the dorsal membrane of the ATB beneath the sensilla, with the ATB subject to a possible membrane-mediated volume change. Together, these findings

indicate that in the field cricket ear both frequency filtering and transmission are performed at least in part by independently tuned mechanically coupled membranes.

4.3.2. Coupled membranes and other ensiferans

The tracheal branches of the ensiferan ear have previously been thought to function mainly to channel sound in the air column to the tympana [24]. However, in 2021, the bushcricket (Tettigoniidae) 'tracheal septum', a structure that is analogous to the field cricket dividing membrane, was shown by optical coherence tomography (OCT) to move in-phase with the PTM, thus indicating its role in mechanically coupling transmission from the PTM to the sensory neurons [47]. In the same year, an OCT study on the tree cricket (Oecanthinae) acoustic trachea revealed similar results [24]. While the morphology of the field cricket tracheal branches differs from that of these ensiferans, our findings align with these recent studies and reinforce the importance of continuing to investigate how tracheal structures mechanically transmit and filter signals from the tympana to the auditory neurons.

4.3.3. Future work

Unlike the bushcricket ear [48], the means of tonotopy in the field cricket remains undefined, although it has been suggested to involve a 'travelling wave' [33]. Applying OCT to the field cricket ear would provide direct measurements of its internal membranes. As would LDV recordings if the membranes could be exposed without compromising the system. Such measurements, especially of the DM-ATB, may elucidate a travelling wave if present.

An integral part of the field cricket's importance as a neuroethology model [9] is its frequency tuning at each stage of the auditory pathway [33]. Continuing to clarify the biophysical source of this pathway may help to contextualize our understanding of frequency filtering at the neural and behavioural levels.

Lastly, a chain of microscale coupled membranes facilitating both filtering and transmission would be noteworthy. The field cricket ear is unusually small [18] and sharply tuned to low frequencies [1], while also capable of spectral decomposition [2]. The relevance of the membranes here described to micro-electromechanical system 'MEMS' diaphragm microphones—used in today's smartphones and hearing aids [49]—is therefore apparent. Especially considering the ear of the parasitoid fly *Ormia ochracea* is also tuned to the field cricket's calling song CF [50] and has already inspired microphone patents numbering today in double figures [51].

Ethics. This work did not require ethical approval from a human subject or animal welfare committee.

Data accessibility. Data supporting this article are deposited in the University of Strathclyde data repository and openly available at [52].

Electronic supplementary material is available online at [53].

Declaration of AI use. We have not used AI-assisted technologies in creating this article.

Authors' contributions. B.L.: conceptualization, data curation, formal analysis, investigation, methodology, project administration, visualization, writing—original draft, writing—review and editing; A.R.: formal analysis, investigation, methodology, resources, supervision, validation, writing—review and editing; J.C.J.-C.: investigation, methodology, resources, supervision, validation; J.A.W.: formal analysis, investigation, methodology, validation, writing—review and editing; J.F.C.W.: funding acquisition, methodology, project administration, resources, supervision, validation, writing—review and editing.

All authors gave final approval for publication and agreed to be held accountable for the work performed therein.

Conflict of interest declaration. We declare we have no competing interests.

Funding. This work was supported by an EPSRC doctoral training partner studentship.

Acknowledgements. We are grateful to Nathan Bailey of the University of St Andrews for providing *T. commodus* crickets and to Alex Ward of the departmental workshop for manufacturing the goniometer platform.

References

1. Schöneich S, Hedwig B. 2010 Hyperacute directional hearing and phonotactic steering in the cricket (*Gryllus bimaculatus* deGeer). *PLoS One* **5**, e15141. (doi:10.1371/journal.pone.0015141)
2. Oldfield BP, Kleindienst HU, Huber F. 1986 Physiology and tonotopic organization of auditory receptors in the cricket *Gryllus bimaculatus* DeGeer. *J. Comp. Physiol. A* **159**, 457–464. (doi:10.1007/BF00604165)
3. Young D, Ball E. 1974 Structure and development of the auditory system in the prothoracic leg of the cricket *Teleogryllus commodus* (walker). Z. Zellforch. Microsk. Anat. **147**, 293–312. (doi:10.1007/BF00307466)
4. Esch H, Huber F, Wohlers DW. 1980 Primary auditory neurons in crickets: physiology and central projections. *J. Comp. Physiol.* **137**, 27–38. (doi:10.1007/BF00656914)
5. Montealegre-Z F, Jonsson T, Robert D. 2011 Sound radiation and wing mechanics in stridulating field crickets (Orthoptera: Gryllidae). *J. Exp. Biol.* **214**, 2105–2117. (doi:10.1242/jeb.056283)
6. Libersat F, Murray JA, Hoy RR. 1994 Frequency as a releaser in the courtship song of two crickets, *Gryllus bimaculatus* (de Geer) and *Teleogryllus oceanicus*: a neuroethological analysis. *J. Comp. Physiol. A* **174**, 485–494. (doi:10.1007/BF00191714)
7. Kostarakos K, Hennig MR, Römer H. 2009 Two matched filters and the evolution of mating signals in four species of cricket. *Front. Zool.* **6**, 1–12. (doi:10.1186/1742-9994-6-22)
8. Michelsen A. 1998 The tuned cricket. *News Physiol. Sci.* **13**, 32–38. (doi:10.1152/physiologyonline.1998.13.1.32)
9. Schöneich S. 2020 Neuroethology of acoustic communication in field crickets—from signal generation to song recognition in an insect brain. *Prog. Neurobiol.* **194**, 101882. (doi:10.1016/j.pneurobio.2020.101882)
10. Hill KG. 1974 Carrier frequency as a factor in phonotactic behaviour of female crickets (*Teleogryllus commodus*). *J. Comp. Physiol.* **93**, 7–18. (doi:10.1007/BF00608756)

11. Nocke H. 1972 Physiological aspects of sound communication in crickets (*Gryllus campestris* L.). *J. Comp. Physiol.* **80**, 141–162. (doi:10.1007/BF00696487)
12. Ter Hofstede HM, Schöneich S, Robillard T, Hedwig B. 2015 Evolution of a communication system by sensory exploitation of startle behavior. *Curr. Biol.* **25**, 3245–3252. (doi:10.1016/j.cub.2015.10.064)
13. Hill KG, Boyan GS. 1977 Sensitivity to frequency and direction of sound in the auditory system of crickets (Gryllidae). *J. Comp. Physiol.* **121**, 79–97. (doi:10.1007/BF00614182)
14. Lankheet MJ, Cerkvenik U, Larsen ON, van Leeuwen JL. 2017 Frequency tuning and directional sensitivity of tympanal vibrations in the field cricket *Gryllus bimaculatus*. *J. R. Soc. Interface* **14**, 20170035. (doi:10.1098/rsif.2017.0035)
15. Larsen ON. 1981 Mechanical time resolution in some insect ears: II. Impulse sound transmission in acoustic tracheal tubes. *J. Comp. Physiol.* **143**, 297–304. (doi:10.1007/BF00611165)
16. Larsen ON, Kleindienst HU, Michelsen A. 1989 Biophysical aspects of sound reception. In *Cricket behavior and Neurobiology* (eds F Huber, TE Moore, W Loher), pp. 364–390. Ithaca, NY: Cornell University Press. (doi:10.7591/9781501745904)
17. Larsen ON, Michelsen A. 1978 Biophysics of the ensiferan ear: III. The cricket ear as a four-input system. *J. Comp. Physiol.* **123**, 217–227. (doi:10.1007/BF00656874)
18. Nishino H, Domae M, Takanashi T, Okajima T. 2019 Cricket tympanal organ revisited: morphology, development and possible functions of the adult-specific chitin core beneath the anterior tympanal membrane. *Cell Tissue Res.* **377**, 193–214. (doi:10.1007/s00441-019-03000-2)
19. Paton JA, Capranica RR, Dragsten PR, Webb WW. 1977 Physical basis for auditory frequency analysis in field crickets (Gryllidae). *J. Comp. Physiol*. **119**, 221–240. (doi:10.1007/BF00656635)
20. Popov AV, Michelsen A, Lewis B. 1994 Changes in the mechanics of the cricket ear during the early days of adult life. *J. Comp. Physiol. A* **175**, 165–170. (doi:10.1007/BF00215112)
21. Schneider ES, Römer H, Robillard T, Schmidt AKD. 2017 Hearing with exceptionally thin tympana: ear morphology and tympanal membrane vibrations in eneopterine crickets. *Sci. Rep.* **7**, 15266. (doi:10.1038/s41598-017-15282-z)
22. Kleindienst HU, Wohlers DW, Larsen ON, Schmidt AKD. 1983 Tympanal membrane motion is necessary for hearing in crickets. *J. Comp. Physiol* **151**, 397–400. (doi:10.1007/BF00605455)
23. Yager DD. 1999 Structure, development, and evolution of insect auditory systems. *Microsc. Res. Tech* **47**, 380–400. (doi:10.1002/(SICI)1097-0029(19991215)47:6<380::AID-JEMT3>3.0.CO;2-P)
24. Mhatre N, Dewey JB, Quiñones PM, Mason A, Applegate BE, Oghalai JS. 2021 Reconstruction of sound driven, actively amplified and spontaneous motions within the tree cricket auditory organ. *bioRxiv* (doi:10.1101/2021.11.14.468538)
25. Veitch D, Celiker E, Aldridge S, Pulver C, Soulsbury CD, Jonsson T, Woodrow C, Montealegre-Z F. 2021 A narrow ear canal reduces sound velocity to create additional acoustic inputs in a microscale insect ear. *Proc. Natl Acad. Sci. USA* **118**, 10. (doi:10.1073/pnas.2017281118)
26. Woodrow C, Pulver C, Song H, Montealegre-Z F. 2022 Auditory mechanics in the grig (*Cyphoderris monstrosa*): tympanal travelling waves and frequency discrimination as a precursor to inner ear tonotopy. *Proc. Biol. Sci. B* **289**, 20220398. (doi:10.1098/rspb.2022.0398)
27. Michelsen A, Popov AV, Lewis B. 1994 Physics of directional hearing in the cricket *Gryllus bimaculatus*. *J. Comp. Physiol. A* **175**, 153–164. (doi:10.1007/BF00215111)
28. Wendler G, Löhe G. 1993 The role of the medial septum in the acoustic trachea of the cricket *Gryllus bimaculatus*. *J. Comp. Physiol. A* **173**, 557–564. (doi:10.1007/BF00197764)
29. Fletcher NH, Thwaites S. 1979 Acoustical analysis of the auditory system of the cricket *Teleogryllus commodus* (Walker). *J. Acoust. Soc. Am.* **66**, 350–357. (doi:10.1121/1.383668)
30. Seagraves KM, Hedwig B. 2014 Phase shifts in binaural stimuli provide directional cues for sound localisation in the field cricket *Gryllus bimaculatus*. *J. Exp. Biol*. **217**, 2390–2398. (doi:10.1242/jeb.101402)
31. Johnstone BM, Saunders JC, Johnstone JR. 1970 Tympanic membrane response in the cricket. *Nature* **227**, 625. (doi:10.1038/227625a0)
32. Michelsen A, Löhe G. 1995 Tuned directionality in cricket ears. *Nature* **375**, 639–639. (doi:10.1038/375639a0)
33. Hedwig BG. 2016 Sequential filtering processes shape feature detection in crickets: a framework for song pattern recognition. *Front. Physiol.* **7**, 46. (doi:10.3389/fphys.2016.00046)
34. Yack JE. 2004 The structure and function of auditory chordotonal organs in insects. *Microsc. Res. Tech*. **63**, 315–337. (doi:10.1002/jemt.20051)
35. Rao SS, Yap FF. 1995 *Mechanical vibrations*, pp. 75–848, vol. **4**. New York, NY: Addison-Wesley.
36. Alba-Tercedor J, Alba-Alejandre I, Vega FE. 2019 Revealing the respiratory system of the coffee berry borer (*Hypothenemus hampei*; Coleoptera: Curculionidae: Scolytinae) using micro-computed tomography. *Sci. Rep*. **9**, 17753. (doi:10.1038/s41598-019-54157-3)
37. Metscher BD. 2009 MicroCT for comparative morphology: simple staining methods allow high-contrast 3D imaging of diverse non-mineralized animal tissues. *BMC Physiol.* **9**, 1–14. (doi:10.1186/1472-6793-9-11)
38. Alba-Alejandre I, Alba-Tercedor J, Hunter WB. 2020 Anatomical study of the female reproductive system and bacteriome of *Diaphorina citri* Kuwayama, (Insecta: Hemiptera, Liviidae) using micro-computed tomography. *Sci. Rep*. **10**, 7161. (doi:10.1038/s41598-020-64132-y)
39. Van Dalen G, Koster M. 2012 *2d & 3d particle size analysis of micro-CT images*, pp. 157–171. Vlaardingen, Netherlands: Unilever Research and Development Netherlands.
40. Malkin R, McDonagh TR, Mhatre N, Scott TS, Robert D. 2014 Energy localization and frequency analysis in the locust ear. *J. R. Soc. Interface* **11**, 20130857. (doi:10.1098/rsif.2013.0857)
41. Ball EE, Cowan AN. 1978 Ultrastructural study of the development of the auditory tympana in the cricket *Teleogryllus commodus* (Walker) . *Development* **46**, 75–87. (doi:10.1242/dev.46.1.75)
42. Dogra S, Gupta A. 2022 Low-frequency noise control in ducts. In *Recent advances in computational and experimental mechanics, vol—I: select proceedings of ICRACEM 2020*, pp. 527–535. Singapore: Springer. (doi:10.1007/978-981-16-6738-1_43)
43. Michel K. 1974 Das tympanalorgan von *Gryllus bimaculatus* Degeer (saltatoria, gryllidae). *Z. Morph. Tiere* **77**, 285–315. (doi:10.1007/BF00298805)
44. Schwabe J. 1906 Beiträge zur morphologie und histologie der tympanalen sinnesapparate der orthopteren. *Zoologica* **50**, 1–154.
45. Eibl E. 1978 Morphology of the sense organs in the proximal parts of the tibiae of *Gryllus campestris* L. and *Gryllus bimaculatus* deGeer (Insecta, Ensifera). *Zoomorphologie* **89**, 185–205. (doi:10.1007/BF00993947)
46. Friedman MH. 1972 An electron microscopic study of the tympanal organ and associated structures in the foreleg tibia of the cricket, *Gryllus assimilis*. *J. Morphol*. **138**, 329–347. (doi:10.1002/jmor.1051380303)
47. Vavakou A, Scherberich J, Nowotny M, van der Heijden M. 2021 Tuned vibration modes in a miniature hearing organ: insights from the bushcricket. *Proc. Natl Acad. Sci. USA* **118**, 39. (doi:10.1073/pnas.2105234118)
48. Palghat Udayashankar A, Kössl M, Nowotny M. 2012 Tonotopically arranged traveling waves in the miniature hearing organ of bushcrickets. *PLoS One* **7**, e31008. (doi:10.1371/journal.pone.0031008)
49. Shah MA, Shah IA, Lee DG, Hur S. 2019 Design approaches of MEMS microphones for enhanced performance. *J. Sens.* **2019**, 1–26. (doi:10.1155/2019/9294528)
50. Cade W. 1975 Acoustically orienting parasitoids: fly phonotaxis to cricket song. *Science* **190**, 1312–1313. (doi:10.1126/science.190.4221.1312)

51. Zhang Y, Reid A, Windmill JFC. 2018 Insect-inspired acoustic micro-sensors. *Curr. Opin. Insect Sci.* **30**, 33–38. (doi:10.1016/j.cois.2018.09.002)
52. Latham B, Reid A, Jackson-Camargo JC, Williams JA, Windmill JFC. 2024 Data for: "Coupled membranes: a mechanism of frequency filtering and transmission in the field cricket ear evidenced by micro-computed tomography, laser Doppler vibrometry, and finite element analysis" (doi:10.15129/e03a436c-8022-4fc8-ba9e-974bf331fd42)
53. Latham B, Reid A, Jackson JC, Williams JA, Windmill JFC. 2024 Data from: Coupled membranes: a mechanism of frequency filtering and transmission in the field cricket ear evidenced by micro-computed tomography, laser Doppler Vibrometry, and finite element analysis. Figshare. (doi:10.6084/m9.figshare.c.7159833)

Appendix D

2023 – *Bioinspiration & Biomimetics*

Review Paper

L. Díaz-García, B. **Latham**, A. Reid, and J. Windmill, "Review of the applications of principles of insect hearing to microscale acoustic engineering challenges," *Bioinspiration & Biomimetics,* vol. 18, no. 5, 2023.
doi: 10.1088/1748-3190/aceb29

IOP Publishing Bioinspir. Biomim. 18 (2023) 051002 https://doi.org/10.1088/1748-3190/aceb29

Bioinspiration & Biomimetics

OPEN ACCESS

RECEIVED
31 January 2023

REVISED
23 May 2023

ACCEPTED FOR PUBLICATION
27 July 2023

PUBLISHED
14 August 2023

TOPICAL REVIEW

Review of the applications of principles of insect hearing to microscale acoustic engineering challenges

Lara Díaz-García*, Brendan Latham, Andrew Reid and James Windmill

Centre for Ultrasonic Engineering, University of Strathclyde, Glasgow, United Kingdom
* Author to whom any correspondence should be addressed.

E-mail: lara.diaz-garcia@strath.ac.uk

Keywords: bioacoustics, bioinspiration, insect hearing, acoustic sensors

Abstract

When looking for novel, simple, and energy-efficient solutions to engineering problems, nature has proved to be an incredibly valuable source of inspiration. The development of acoustic sensors has been a prolific field for bioinspired solutions. With a diverse array of evolutionary approaches to the problem of hearing at small scales (some widely different to the traditional concept of 'ear'), insects in particular have served as a starting point for several designs. From locusts to moths, through crickets and mosquitoes among many others, the mechanisms found in nature to deal with small-scale acoustic detection and the engineering solutions they have inspired are reviewed. The present article is comprised of three main sections corresponding to the principal problems faced by insects, namely frequency discrimination, which is addressed by tonotopy, whether performed by a specific organ or directly on the tympana; directionality, with solutions including diverse adaptations to tympanal structure; and detection of weak signals, through what is known as active hearing. The three aforementioned problems concern tiny animals as much as human-manufactured microphones and have therefore been widely investigated. Even though bioinspired systems may not always provide perfect performance, they are sure to give us solutions with clever use of resources and minimal post-processing, being serious contenders for the best alternative depending on the requisites of the problem.

1. Introduction

Bioinspired hearing requires a fundamentally different design paradigm. In nature, the peripheral sensory organs, the eyes, ears, or skin, are rarely passive recorders of their environment. They possess complex filtering, processing, and encoding functions that are built in to the material and structure at every level: from the atomic, through the cellular, to tissue structure, and organ structure. Such signal processing can be mechanical, such as the decomposition of sound into frequency bands that is famously performed by the mammalian cochlea [1], or the result of intercellular chemical or electrical communication [2], but a distinct characteristic is that the signal transduction and signal processing functions are integrated and inseparable. This necessity is enforced by the sparse, event-driven nature of signals transmitted to higher brain centres [3]. The signal complexity is limited to what may be encoded in the temporal pattern of a spike train [4].

In contrast, engineered sensors view transduction as a separate function. The transducer's output is a continuous in the time-domain, rather than event driven. This 'raw' signal must be appropriately filtered, encoded and efficiently transmitted in order to extract useful information. If we could borrow nature's trick of integrating this signal processing into the structure of the transducer we could unlock significant improvements in energy-efficiency, signal latency, bandwidth reduction, and device footprint. All of these areas are critical constraints on sensor networks [5], internet of things [6] and human wearable and implantable sensors [7].

Three of the most basic problems faced by animals and shared across species are the following [8–11]:

- Distinguishing conspecific communication from predator sounds.
- Localising the position of a potential prey, predator, or mate.
- Detecting weak sound signals that deteriorate as they propagate in their natural environment.

Body size compounds the complexity of these issues: sound emission and detection efficiency tend to decrease with the size of the acoustic sensor, the ability to locate sounds (and predators) when listening diminishes with diminishing space between the sensors, and that the frequency band available for communication is limited by predation and by the acoustic transmission properties of its environment [12]. The evolutionary adaptations to the physics of acoustic waves provide unique solutions to reducing the energy (and metabolic) cost of detection, to frequency decomposition, and to locating sound sources with miniscule available directional cues from the sound field. Acoustic systems at the micro-scale may draw particular inspiration from insect hearing and communication due to the constraint of insects' small body size.

Using sound to locate potential mates and to avoid predators is a common evolutionary tactic, with hearing in insects known to have evolved independently between 15 and 20 times [13]. The methods of detection can be grouped into pressure detection systems and particle velocity detection systems. In general, particle velocity detection systems are hair-like near-field, low-frequency mechano-receptors, reliant on light weight and high specific surface area in order to translate the velocity dependent viscous drag force into a detectible vibration [14]. They are often used to detect low frequency sound (less than 500 Hz) or reactive flow in the near field of an emitter, such as the mosquito antenna which is used to detect the flight disturbance from a nearby mate [15]. This paradigm has, however, been challenged recently by evidence that mosquitoes can in fact behaviourally react to sounds up to 10 m away [16]. Pressure receivers are exclusively tympanal systems, operating in the far field [17] and capable of detecting sound into the far ultrasound range [18].

Gathering inspiration from the way these problems are solved in nature has proved to be a successful path towards innovative engineering solutions. Thus, the motivation of this review is to provide a comprehensive compilation of the mechanical solutions implemented in technology that are inspired by insects and further encourage bio-inspiration as a source for innovative engineering solutions.

The body of this paper is structured in three distinct sections, each one referring to one of the three fundamental aforementioned problems. In addition, each section is divided in two subsections. The first one concerns some paradigmatic insect solutions for its corresponding problem and the second one covers engineering solutions arising from bio-inspiration of said insects.

The section 2.1 refers to spatial frequency decomposition and comprises some example cases of how insects deal with this problem and the technological solutions inspired by it. The section 3.1 verses on the direction of arrival estimation and it covers some of the most notable nature example solutions and the sensors inspired by them. Lastly, the section 4, active hearing, follows the same structure of natural examples and technology inspired by them. A section 5 finishes the manuscript.

2. Tonotopy

Frequency discrimination can be a matter of life and death for an organism. Sound communicates information. The purpose of all acoustic systems in biology is to get that information to the animal to elicit the appropriate behavioural response. One information component of sound is its frequency, and as much as the animal's survival and reproduction can depend on the organism's ability to distinguish key frequencies from its environment. Not doing so could mean a moth failing to evade the approaches of a predatory bat [19–21] or a female cricket failing to localise the position of a potential mate [22, 23].

2.1. Spatial frequency decomposition: cochlea and tympana

All ears must translate acoustic energy travelling through a medium, usually air, into mechanical motion, and then to electrical impulses. Electrical impulses are generated by neurons and, in acoustics specifically, by auditory mechanoreceptor cells, neurons with mechanically gated ion channels that require an acoustic-mechanical stimulus to fire an action potential [24]. Frequency selectivity is a difficult aspect of insect communication, since the spike train from a sensory neuron cannot encode frequency information in their signal. To have a means of discriminating frequencies, multiple such neurons must be individually tuned. A very simple ear, such as those of moths cannot passively distinguish between the frequencies of a predatory bat and the call of a potential mate, relying instead of differentiating the temporal structure of the mating call and the pulses of a bat's echolocation [25]. Individual tuning of multiple cells can be achieved by the arrangement of the neurons according to a morphological gradient. Morphological variation of a substrate—for example, some areas being thicker, thinner, wider, or narrower—in the cells' proximity can cause different points on the substrate to move differently according to the input frequency. This frequency-specific maximal displacement of the point, if coupled somehow to a sensory neuron, can in turn stimulate that neuron independently, thus tuning the cell to a single frequency. This place-based frequency decomposition is called *tonotopy*.

A second problem is that of the acoustic environment, since mating calls must compete with the potentially masking calls of other species without unnecessarily attracting the attention of predators

[26]. These mating calls are frequently pure tone signals, reflecting their reliance on resonant structures to transmit the necessary power to attract a mate as well as the need to seek unoccupied space in the locally available acoustic spectrum [27]. This places some constraints on the available communication bandwidth, since the resonant frequency is determined by the size of the radiator and, in order to transmit efficiently, the resonant structure should have a diameter approaching half of the signal wavelength [28]. There is a reproductive and survival advantage from the ability to distinguish the frequency composition of predators and competing species. In flagellar systems such as the mosquito [29], as well as some tympanal systems such as the tree cricket *Oecanthus henryi* [30] and the Noctuid moth [31], this frequency tuning is achieved by active amplification where the mechanosensory cells can produce sufficient power to drive the ear at the frequency of interest. This strategy is discussed in section 4. In this section, we discuss dispersive frequency decomposition, where sound travels and is localized to particular sites based on its frequency.

Dispersive frequency decomposition relies on a travelling wave, which is typically a flexural mode on the thin medium. The most well-known example of this is the travelling wave associated with the basilar membrane of the mammalian cochlea [32, 33]. An acoustic impulse applied to the narrow end of the wedge-shaped structure encounters a stiffness gradient. The wave shoals, increasing in amplitude whilst also slowing down until finally maximal vibration of the membrane is reached at a specific point along the membrane's length; afterwards, the wave rapidly decreases in amplitude. High-frequency stimuli terminate at a point near the narrow end, and those of lower frequency, near the wide end. Sensory neurons arranged linearly along the length of the substrate respond accordingly: a mechanoreceptor cell at a narrow region is activated only by a high frequency stimulus; a cell further along only responds to a lower frequency.

In contrast to vertebrates, among invertebrates, tonotopic systems are considerably rarer, and yet invertebrates also showcase the most diversity of system design. Moreover, invertebrate tonotopy is less understood and provides greater scope for novel discovery. Such ears can be categorised into two types, cochlea-type tonotopic systems and tympanal tonotopic systems. Both are exemplified by the bushcricket and the locust, respectively.

The bushcricket ear appears to possess the only insect cochlea yet identified [38], although some sort of cochlea analogue has been hypothesised for the cricket [39]. Bushcrickets (also known as katydids) are orthopterans, alongside crickets and grasshoppers, the latter including locusts. Their two ears (one on each of their two front legs) consist of two external tympanal membranes on either side of the leg, making four eardrums in total. Features of the bushcricket ear are reminiscent of the vertebrate peripheral auditory anatomy in terms of function. These include the tympanal plate, possibly functioning as a middle ear; and the *crista acustica*, the bushcricket's inner ear or cochlea [40] (see figure 1).

The most noticeable characteristic of the bushcricket *crista acustica* is its tapered shape and orderly arrangement of *sensilla* (figure 1(A)). The 25 or so sensory neurons are tonotopically arranged from high frequency tuned cells at the narrowest tip of the organ (up to and above around 50 kHz) to those tuned to lower frequencies its wider end (tuned from about 6 kHz) [41]. These sensors lie on a thin wall of a cuticular cavity, the anterior tracheal branch. Their dendrites project upwards dorsally, and each connects to a cap cell which is itself attached to a thin sheet that covers the entire organ, the tectorial membrane. Notably, the size gradient of these cap cells is correlated with the tonotopy. Nevertheless, the correlation is not strong enough to account for the full resolution of frequency representation. Rather, the tonotopy may require another morphological gradient such as features of the sensors themselves [35]. This arrangement appears to facilitate a travelling wave across the tectorial membrane, differentially stimulating the sensory cells according to frequency. The wave is initiated at the organ's narrow end and travels along the membrane towards the low frequency tuned sensors, terminating closer to the wider tip at low frequency impulses and closer to the point of initiation at higher frequencies [34].

The other type of tonotopic mechanism is not at all like a cochlea, and in fact has no comparison among the vertebrates. In tympanal tonotopic systems, known in the locust [37] and in the cicada [42], the tympanum, responsible for sound capture, is also responsible for frequency decomposition; both functions occur at the same substrate. This dual functionality requires the eardrums to be unusually complex, and indeed the locust tympanal membrane may be considered the most sophisticated tympanum yet identified.

Locusts have two tympana, one on each side of their abdomen. Around 70 mechanoreceptor cells attach to the underside of each tympanum, forming Müller's organ, a ganglion of *sensilla* divided into four groupings. Three of these are tuned to low-frequency bands (3.5–4, 4, and 5.5–6 kHz) and one to high frequencies (12–20 kHz) [36, 47]. Each sensory group is secured to its own specific morphologically unique tympanal feature (figure 1(C)). In addition, the locust eardrum exhibits further, larger-scale heterogeneity in the form of two parts to the tympanum, a thin membrane and a smallerthicker membrane (figure 1(D)). High-frequency mechanoreceptors attach to a point on the thin region, whereas the

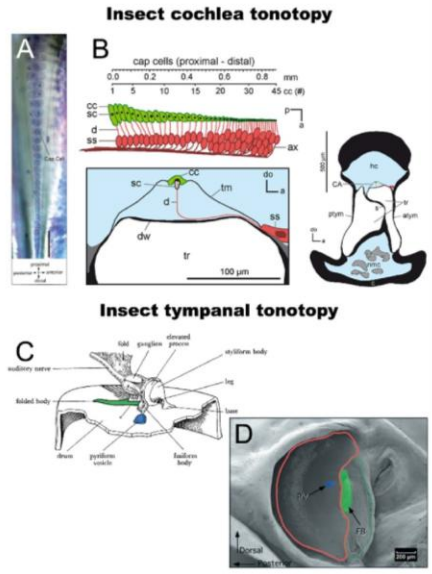

Figure 1. (A) Bushcricket crista acustica stained with methylene blue [34]. Reproduced from [34]. CC BY 4.0. (B) Anatomy of the crista acustica [35]. Used with permission of John Wiley & Sons - Books, from [35]; permission conveyed through Copyright Clearance Center, Inc. (C) Anatomy of the four locust mechanoreceptor attachment points on the underside of the tympanum [36]. Adapted to highlight the same points shown in the adjacent image, (D). Used with permission of The Royal Society (U.K.), from [36]; permission conveyed through Copyright Clearance Center, Inc. (D) SEM of the external surface of the locust tympanum [37]. Red outline: thin membrane; green outline: thick membrane; blue feature: attachment point of mechanoreceptors tuned to high frequencies; green highlight: attachment area of low frequency sensors. Used with permission of The Company of Biologists Ltd., from [37]; permission conveyed through Copyright Clearance Center, Inc.

others connect to fixtures of the much thicker membrane [37, 48]. Thus, a degree of morphological gradation is provided, enabling travelling waves. When stimulated with sound, a travelling wave is initiated in the thin membrane that maximally vibrates the tympanum at one of the four locations, depending on the stimulus frequency. At frequencies above 10 kHz, no movement of the thick membrane is detected. Rather, the travelling wave terminates at the high-frequency attachment point, rapidly attenuating when reaching the thicker cuticle. As such, there is a clear spatial frequency decomposition of high and low frequencies [37].

2.2. Bio-inspired frequency discriminating sensors

Engineered systems based on spatial frequency decomposition frequently target sub-Nyquist rate sampling as the value of their system [49]. An analogue to digital converter has a maximum sampling rate, and increasing this sampling rate lowers signal-to-noise ratios and increased power requirements [50]. A signal which is already filtered can be captured with lower sampling frequencies, and yet retain a higher effective sampling rate that can be significantly compressed by only retaining content when it is above a threshold. This strategy has been applied using electronic filter banks [51], and even converted to an output spike train to mimic the event-driven format of nerve conduction [52]. Mechanical filtering of the signal can be grouped into solutions using an array of resonators (figures 2(A) and (D)) [43, 46] or solutions using a tapered membrane [53].

Resonator arrays perhaps are the most obliquely connected to the natural inspiration, but they are simple to implement on silicon as arrays of cantilevers (figure 2(B)) [44] or clamped-clamped beams (figure 2(C)) [45]. The resonant frequency of each channel can be adjusted by changing the length of the beam; and transduction of the signal may be accomplished by piezoelectric [54, 55], triboelectric [45] or optical means [56]. While relatively easy to implement, using a beam as a method of acoustic capture is extremely inefficient for lower frequencies due to diffraction around the relatively narrow beam width. The pressure difference between the front and back sides of the cantilever is small, resulting in maximum displacements at resonance in the order of tens of nanometres [57]. The resultant electrical transduction and signal-to-noise level are also prohibitively small since the cantilevers may not rely on capacitive sensing through an electrical backplate, as in a traditional microphone, due to the impact of thin film damping on both the mechanical sensitivity of the device and the resonance frequency [58, 59]. Piezoelectric sensing can be used with the ceramic element implemented either on the upper surface with interdigitated electrodes [43], or by fabricating the cantilever as a bimorph [60]. However, both strategies produce piezoelectric charge sensitivities in the order of femto-Coulombs per nm. One strategy to overcome this limitation in micro-electromechanical system (MEMS) consists of using a thickened or disc-shaped central region in the arrays, maintaining a thin base region for the purposes of keeping a desired resonance frequency while maximising the surface area for acoustic capture (figure 2(E)) [61].

Frequency decomposition based on tapered membrane structures is closer to bio-inspired sources, consisting of a single membrane with significant acoustic dispersion to isolate the frequency bands. Such systems have two fundamental requirements: there must be a time-dependent pressure gradient along the membrane to support flexural wave propagation, and the wave velocity must change along the length of the membrane. The support of

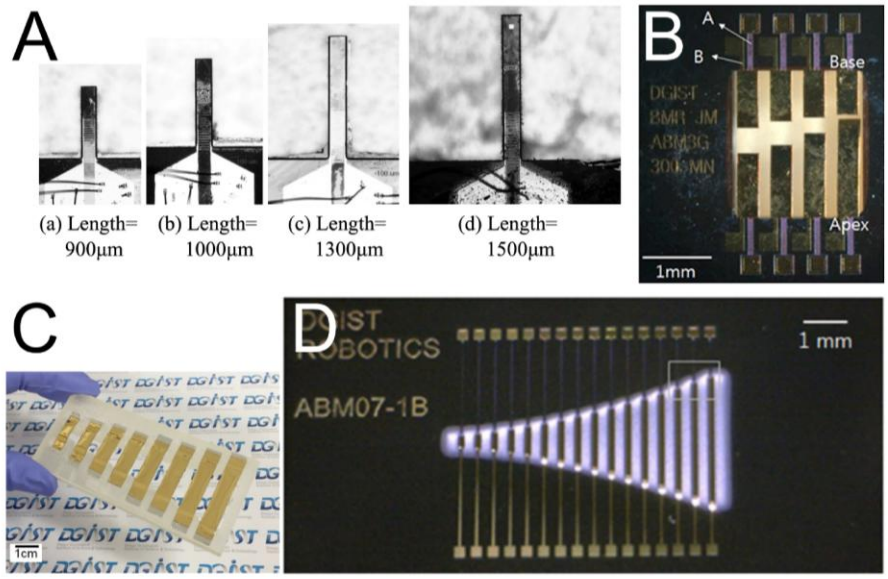

Figure 2. Array of resonator approaches to mechanical tonotopy (A) Single crystal PMN-PT cantilevers with interdigitated electrodes [43] Reproduced from [43], with permission from Springer Nature. (B) Dual sided cantilever array [44] Reproduced from [44]. CC BY 4.0. (C) Clamped-clamped array with triboelectric transduction [45]. Bottom row shows solutions to achieving desired frequency while maximising surface area for mechanical sensitivity. Used with permission of John Wiley & Sons - Books, from [45]; permission conveyed through Copyright Clearance Center, Inc. (D) Tapered clamped-clamped beam array [46]. Reproduced from [46]. © 2013 IOP Publishing. Reproduced with permission. All rights reserved.

a travelling flexural wave can be achieved by having a defined, highly localized sound input point, analogous to the oval window in the mammalian cochlea (figure 3(A)) [53, 62], or by ensuring the membrane length is between 1/6 and 1/4 of the frequency range of interest to ensure a phase difference across the membrane surface (figure 3(B)) [63, 64]. Both solutions have limitations, since restricting the sound input to a single point restrains the power that may be captured by the device, and tailoring the membrane length to the phase difference in the incoming sound wave either requires prohibitively large membranes or a highly restricted high-frequency range of interest.

The second requirement for acoustic dispersion is equally challenging to meet within the constraints of MEMS systems. The most obvious source of generating dispersion is through the tapering of the thickness of the membrane, based on an Euler–Bernoulli model of a thin plate where the bending wave speed may be given by [65]:

$$c_b = \left(\frac{Eh(x)^2\omega^2}{12\rho(1-\nu^2)} \right)^{\frac{1}{4}}$$

where ρ is the density, ω is the angular frequency, E is the Young's modulus, ν is the Poisson's ratio, and $\boldsymbol{h}(\boldsymbol{x})$ is the thickness profile. In theory, for every frequency, there is a height below which the wave speed will drop to the point where it is no longer transmitted, or at least may be assumed to be sufficiently attenuated, analogous to the acoustic black hole effect described by Mironov and Pislyakov [66]. In practice, the variation in thickness would need to be two orders of magnitude over the length in order to separate frequency bands in the acoustic range using a common MEMS material such as single-crystal silicon.

The more commonly seen model varies the width of the membrane along its length, which should not result in variation of the phase velocity [67]. Instead, such systems rely on the membrane being placed on a closed channel, or either air or some fluid medium, such as water [68] or silicon oil [64]. The variation of the velocity of fluid flow in this channel generates a variation in the velocity potential [69], and hence the local pressure on the membrane; while the depth of the fluid channel increases, the fluid loading on the membrane reduces the resonance frequency (figure 3(C)) [70]. This, in combination with the slight spatial variation of the membrane's first-order resonance peak with frequency, results in some degree of tonotopy. Despite the size of these membranes, over 5 cm in length, they have extremely low mechanical responses at the resonance of less than a micron displacement and are only able to separate a few, widely separated frequency bands with poor spatial confinement compared to examples in nature.

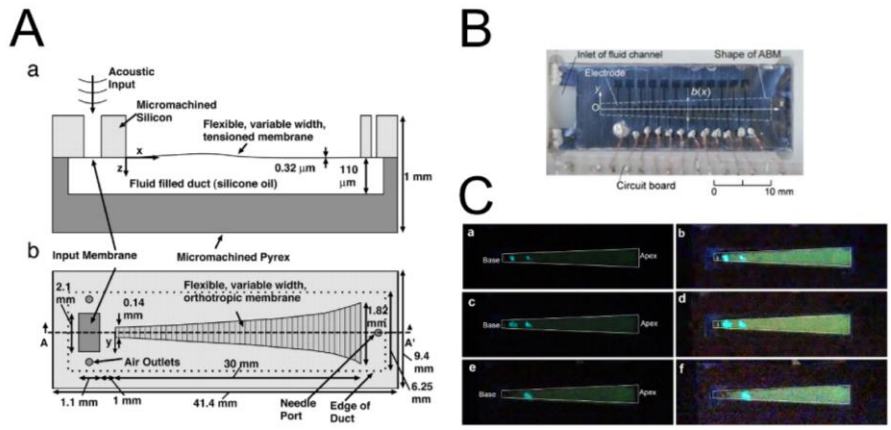

Figure 3. Continuous membrane approaches to tonotopy, which have one single graded sensing area with a localized transduction mechanism. (A) Hydromechanical model of the basilar membrane with silicon oil backing [53], [53] Copyright (2005) National Academy of Sciences, U.S.A. (B) Fluid backed tonotopic sensor using PVDF as the membrane with individual measurement points [64]. Reprinted [64], Copyright (2010), with permission from Elsevier. (C) Luminescent tapered membrane showing some frequency separation at very low frequencies (a), (b) 110 Hz; (c), (d) 80 Hz; (e), (f) 40 Hz [54]. Reproduced from [54]. CC BY 4.0.

3. Directionality

The localization of sound sources by small animals is a fundamental problem in bioacoustics. Where body size is diminutive and inter-ear distance is short, an animal cannot rely on comparison between the intensity difference or time delay of signals received at either ear. For many animals, the detection of a sound is sufficient. For example, all but one of the 10–12 independent origins of hearing in *Lepidoptera* occurred later than 65 Ma, the currently accepted date for the appearance of echolocation in bats [71]. The hearing that evolved in these moths is extremely simple, consisting of only 1–4 neurons per tympanum [72], minimum tuning over a broad frequency range [73], and limited or no directionality, yet it remains highly effective for escaping predatory bats [74]. Moths exposed to bat echolocation signals exhibit random evasive movement, diving towards the ground if in flight and freezing behaviour if running on the substrate [75]. Knowing exactly where the bat is coming from does not change the moth's response and it is not worth the evolutionary cost of developing directional hearing. For an insect on the other face of the prey-predator relationship, for parasites, or for finding the source of a conspecific mating call, it is necessary also to know the direction of the source of the sound.

Bilateral symmetry means that most animals have two ears, one for each half of their body (one notable exception is the praying mantis, which possesses only one ear [76]). Directional hearing in larger animals may be achieved by inter-aural intensity differences (IIDs), where sound shadowing from the body creates an appreciable level difference between the ears; or inter-aural time differences where the basis of comparison is the time difference of arrival between the ears. For an insect where the body length is a fraction of the wavelength of a relevant sound source, the acoustic shadow is minimal, and time differences of arrival may be measured in nanoseconds [77].

This section looks exclusively at tympanal hearing systems, as systems which have the closest analogy to the traditional microphone. Particle detection hearing systems are inherently directional, responding to the velocity vector of the sound field however such systems are far less sensitive to far-field sound and higher-frequency sound fields.

3.1. Direction of arrival estimation from tympanal structure

Ormia ochracea has undoubtedly inspired the greatest number of engineering designs which seek to mimic the unique coupling mechanism between its tympana. *O. ochracea* is a fly parasitoid of crickets, locating its host *Gryllus* by phonotaxis to the cricket's mating calls [78]. The auditory system of *O. ochracea* has long been of interest to researchers due to the uncanny accuracy with which it can locate the host call, a 5 kHz pure tone with a wavelength of over 10 times the body length of *O. ochracea* and 100 times the separation between the insect's tympana. This insect has directionality down to an accuracy of 2° in the azimuthal plane [77]. The system consists of two diaphragms mechanically connected by a bridge and pivot allowing the transfer of energy from the motion of one diaphragm to another (figures 4(A) and (D)) [79]. When the stiffness of this connecting bridge is

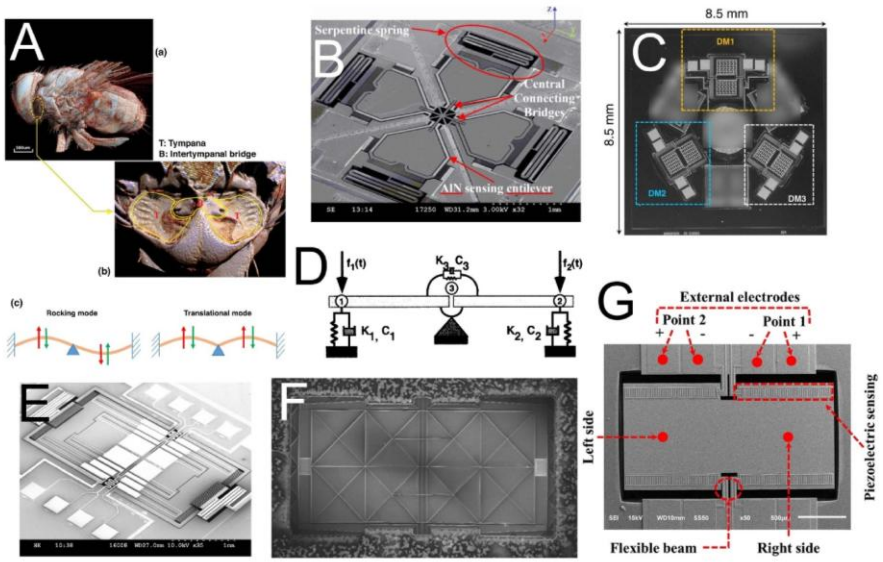

Figure 4. (A) Micro-CT images of tympanal system of *O. ochracea*. Arrays of Ormia inspired membranes [83]. Reproduced from [83]. CC BY 4.0. (B) four coupled membranes [81] © [2018] IEEE. Reprinted, with permission, from [81]. (C) Array of 3 see-saw style Ormia membranes [84]. Reproduced from [84]. CC BY 4.0. (D) Illustration of rocking and translational mode along with standard two degree of freedom model of the Ormia system [80]. Reproduced from [80], with permission from Springer Nature. SEM images of Ormia membranes targeting low acoustic frequencies using (E) silicon-on-insulator MEMS [83] Reproduced from [83]. CC BY 4.0. and (F) Silicon nitride patterning [85]. Reprinted with permission from [85]. Copyright [2009], Acoustic Society of America. (G) Transduction of membrane motion using capacitive comb sensing [86]. Reproduced from [86]. CC BY 4.0.

correctly tailored to the system, the signals from the stimulating sound wave and the linked companion diaphragm will constructively interfere with the ipsilateral sound source and destructively interfere with the contralateral sound source. The result is what was termed by Robert *et al* [80] mechanical interaural phase difference and mechanical IID which can be 40 times higher than the phase difference in the stimulating sound field. Much of the research into *Ormia*-inspired systems targets applications in hearing aids [81, 82]; however, there is an inherent conflict: the *Ormia*'s coupled ears are a resonant system and so single-frequency, while hearing aids, or teleconferencing applications require broadband sound source localization.

A potentially different tactic is employed by *Achroia grisella*. *A. grisella* is a moth of the *Pyralidae* family within the *Lepidoptera* order, known as the Lesser Wax Moth. It is less than 13 mm long and principally known as a parasite of unhealthy bee colonies, on which they deposit their eggs and on which their larvae feed. The unusual aspect of *Achroia* is the use of ultrasonic calling as a mating signal, and their use of phonotaxis rather than anemotaxis to track their preferred mate [87]. As discussed in the introduction to this section, simple hearing systems are widespread among nocturnal Lepidopters, but evidence of directional response is sparse save for some limited negative phonotaxis in Noctuids [88]. In contrast to hearing, acoustic communication in moths is rare and occurs only among isolated species and genera in the three major clades [71]. In many cases, acoustic communication is restricted to close-range courtship where directional hearing would not be critical [89]; however, *A. grisella* can transmit and track sound signals over distances over 2 m, making a sound localization capability expected. Unlike *O. ochracea*, whose acoustic perception of host crickets has probably evolved de novo, *A. grisella* already had an evolutionary ancient system for perceiving sound, and the mechanism for localization reflects an adaptation of the tympana as bat detectors to a new purpose [90, 91].

The tympana of *A. grisella* are located ventrally on the first abdominal segment (figure 5(A)). They are oval-shaped, between 500 μm and 550 μm long in the females and divided into an opaque anterior section and a transparent posterior section (figure 5(B)) [92]. These two sections of the tympana oscillate in anti-phase when there is no variation in the pressure field across the tympanum (i.e. when the sound wavefronts are planar), with a large peak in displacement near the neuronal attachment point [73, 93, 94]. This vibrational mode remains relatively stable with sound source angle until a 100 kHz sound source is located along the major axis of the

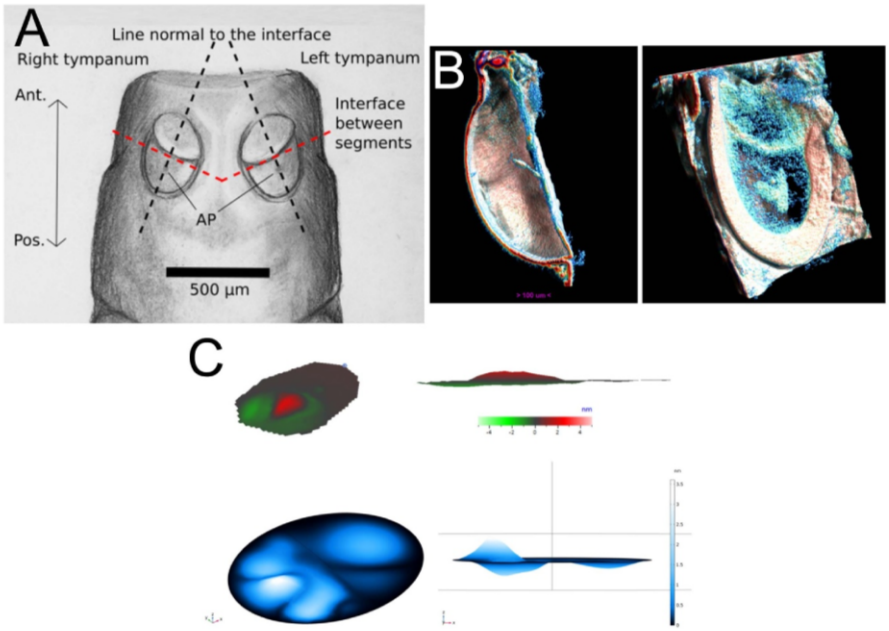

Figure 5. (A) Illustration of the ear location and orientation on the first abdominal segment of A. grisella [94]. Reproduced with permission from [94]. (B) x-ray CT voxel images of the structure of the tympanum showing the scolopale attachment point in the centre of the lower section of the tympanum [102]. © [2022] IEEE. Reprinted, with permission, from [102]. (C) Laser Doppler vibrometry measurement of A. grisella tympanal motion in response to a planar sound field and (top) and COMSOL reconstruction of the membrane (bottom) [102]. © [2022] IEEE. Reprinted, with permission, from [102].

tympanum at which point the peak in displacement near the attachment point grows sharply in magnitude [91].

3.2. Bio-inspired directional sensors

Ormia-inspired directional microphones are undoubtedly the largest class of bio-inspired hearing sensors and, consequently, have in themselves been subject to a number of dedicated reviews [83, 95]. The overwhelming direction of design has been towards a single-layer see-saw design realised in a silicon-on-insulator or related MEMS process, either as a single sensor (figures 4(E) and (F)) or an array (figures 4(B) and (C)) [85, 86, 96, 97]. This operates similarly to the *Ormiine* system, with each of the 'wings' of the device comparable to one tympanum, while the torsional stiffness of the bridge connecting the device to the substrate performs the equivalent function of the raised bridge and fulcrum in *O. ochracea*. The system is attractive to researchers as it is easily implemented in a multi-user MEMS process, and it can, with careful tailoring of the relative stiffness of the membrane wings and the torsional stiffness of the bridge, amplify directional cues in a similar manner to *O. ochracea*. This design path has several challenges which have not yet been overcome besides the inherent resonant nature of the device. The first is the signal-to-noise ratio achievable in this system. As the *Ormia*-inspired microphone relies on the interaction between the resonant modes, a traditional capacitive backplate is generally not used, at least partially because of the thin-film damping such a structure would introduce [84, 98]. Because the system works optimally at the frequency where the in-phase resonance and the out of phase resonance are the same power, increasing the bandwidth of these resonances necessarily means increasing the separation between the frequency peaks of the two modes. This has the effect of lowering the amplification of directional cues, but does broaden the frequency range over which this is possible [99]. Principally, designers avoid this issue entirely by incorporating optical [98] or capacitive comb-based sensing schemes (figure 4(G)) [97, 99]. The first of these adds significantly to the design complexity and cost, while both piezoelectric and capacitive comb-based methods in MEMS devices have low sensitivities [96, 100, 101].

The second obstacle to a good signal-to-noise ratio is more fundamental to the design—as the see-saw mechanism must be released from the periphery except at the anchor points, sound is free to diffract around the device. Since these devices are typically of a maximum size of 1 by 2 mm and the target sound field is in the acoustic range, the pressure difference across the membrane is minimal. This can

be solved by making a more direct model of *Ormia*'s hearing system, however so far all examples have been demonstrated at the mesoscale due to the complexity of fabricating a true 3D structure using lithographic methods [103, 104].

On the other hand, finite element modelling of *A. grisella*'s tympana and tests on 3D-printed models have shown that this single membrane directivity pattern can be replicated in a relatively simple stepped-thickness membrane (figure 5(C)) [102].

4. Active hearing

The third central problem for insect hearing is the inherently low energy of a propagating sound wave over the length scales that the insect can hope to capture. This problem is compounded for velocity sensing organs, such as the antenna in mosquitos and fruitflies, where the mechanism for energy capture is through the viscous drag losses in the antennal hairs [105]. In order to maximise the capture of these sounds and the transduction into neuronal signals, the mechanoreceptor neurons themselves add energy to the system, resulting in a non-linear response to sound [29]. The system is analogous to the active hearing contributions of hair cells in the cochlea; however, in insects, it can be directly observed in antennal systems. The existence of active hearing can be inferred from non-linear response characteristics in tympanal systems in insects, such as otoacoustic emissions or self-generated oscillations, in tree crickets [106] and Katydids [40]; nevertheless, the small scale of these systems and the relatively low number of congregated mechanoreceptors compared to Johnson's organ in the mosquito, make these systems harder to study.

4.1. Particle velocity sensors and active hearing

The champion species for active amplification in flagellar systems is the elephant mosquito, *Toxorhynchites brevipalpis*. The hearing organ consists of an antenna shaft which sits within a pedicel. Mechanically, it acts as a rotational spring, causing the antenna to oscillate in a rigid body motion with a resonant frequency of between 300 and 500 Hz [107]. Within the pedicel is Johnston's organ, a collection of some 16 000 mechanosensory cells arranged in a bowl shape along the base of the antenna. These consist of a scolopale rod which connects the antennal structure to the chordotonal neuron, which both senses the motion of the antenna and can inject additional energy into the antenna's oscillations [108]. If we model this system in a sound field as a passive oscillator, it can be approximated as a damped harmonic oscillator [109, 110]. Such a system will have a defined resonant frequency and a Q factor given by the ratio between resonant frequency and damping, which gives the half-power bandwidth of the resonant response.

Mosquitoes use their auditory receptors for mating purposes, detecting the acoustic signature of a female's wing beats. The female creates an extremely weak and brief sound signal, a sound particle displacement of around 3.5 nm at a distance of 10 cm [29]. As the sound intensity varies so sharply and so quickly with the change in distance between the male and the potential mate, the mosquito requires a sensor with an extremely fast temporal response. Mechanically, this would be a broadband, low Q factor, allowing the detection of higher frequency transients in the signal. Conversely, to successfully track the female, the male must filter out environmental noise for which a broadband sensor would be a poor choice and a sharply resonant, high Q factor sensor would be preferred. The antenna's frequency selectivity in passive hearing is principally determined by the resonance of the flagellum and spring base, which is well-damped and low Q factor [107]. The mosquito maximises its tracking efficiency by switching from the initial passive response to a sharply resonant response through the generation of force in the neurons at the base of the antenna [107]. These neurons fire at twice the frequency of the antenna's sound field-driven oscillation, sharpening the tuning of the resonant frequency (figure 6(A)) [111].

4.2. Bio-inspired active amplification sensors

The concept of active Q control has found applications in atomic force microscopy [112, 113] and in optical amplifiers, where it is referred to as parametric amplification. Rather than directly injecting energy, parametric amplification involves changing some property of the system with a specific phase timing, analogous to a child on a swing. In acoustic systems, the forcing mechanism is usually directly applied to either the membrane or the flagellum through electrostatic actuation, perhaps more analogous to someone pushing a swing. At root, this is a feedback system where the oscillations of the acoustic receiver are filtered through a leaky integrate and fire stage and recombined. In practice, this has meant generating a pulsed actuation signal controlled by a computational control mechanism, designed to fire in time with the oscillations of the incoming microphone signal. A MEMS microphone directly inspired by this principle was demonstrated by Guerreiro *et al* (figure 6(B)) [114, 115], using capacitive combs to inject the pulsed feedback signal. This was a unipolar signal, firing only once per oscillation of the membrane as opposed to the 2:1 mode of the mosquito [111]. The Q factor of the MEMS microphone is already high in the absence of strong damping sources such as thin film damping; however, the feedback mechanism demonstrated an increase of the Q factor from 30 to 66 with a consequent amplification of 2.19 [114].

The mechanism has also been used to lower the effective Q factor in *Ormia*-inspired devices.

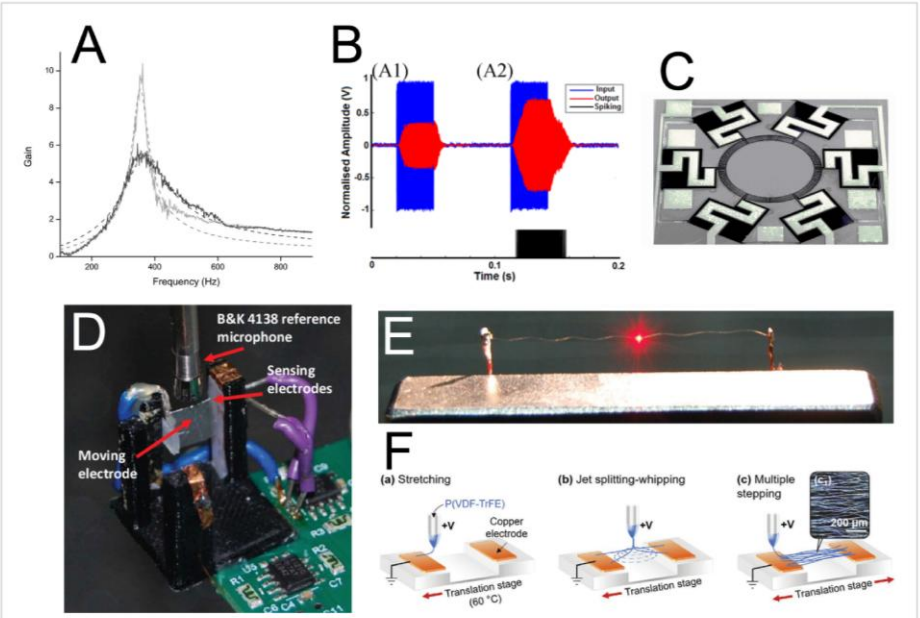

Figure 6. (A) Impact of twice frequency forcing in the mosquito antenna, changing the broadband response of the antenna into a sharp narrowband response [111]. Reprinted from [111] © 2009. Frequency forcing in a MEMS microphone using piezoelectric sensing and capacitive combs to inject the motile force, (B) resultant amplification with forcing [114], © 2018 IEEE. Reprinted, with permission, from [114]. (C) SEM of the membrane design [115]. © 2017 IEEE. Reprinted, with permission, from [115]. (D) Hair sensor microphone using electrostatic transduction [121] © 2019 IEEE. Reprinted, with permission, from [121], and (E) larger scale proof of concept of same using optical sensing [122]. Reproduced with permission from [122]. © 2018 by ASME. (F) Meshed hair sensing using electrospun PVDF [123]. Reproduced from [123]. CC BY 4.0.

As noted, MEMS devices without backplates will experience very light damping and therefore exhibit sharply resonant behaviour which can be a detriment to sound localization. The introduction of passive damping systems would increase thermal noise and reduce the microphone's fidelity. Miles *et al* [116] have demonstrated active *Q* control aimed to reduce damping, here using a proportional and differential gain and feedback scheme to an electrostatic mesh, successfully broadening the resonant response without noise gain. A similar effect can be achieved with pulse train stimulation, changing the phase timing of the pulse with respect to the diaphragm oscillations [117]. Active control over the damping in this manner relies on separate methods of measurement and feedback; for example, piezoelectric measurement of membrane motion and capacitive comb feedback [118], or laser diffraction-based measurement and actuation through a capacitive backplate [119, 120].

Particle velocity acoustic sensors are relatively rarer, with the majority of the bioinspired hair sensors being directed towards the detection of fluid flow [124], and we have few examples of hair or flagellum-based sensors that are directly mosquito inspired (for example [125]), although the claimed incorporation of active feedback appears in reality to be a simple directional response. A velocity feedback controller on a cantilever beam was demonstrated by Joyce and Tarazga [126], the device was constructed at scale being a 5 cm long aluminium beam with a resonance of 10.8 Hz. Antenna-inspired acoustic sensors should have large surface area relative to their mass (or moment of inertia) and stiffness [121, 122]. This can be achieved via sub-micron diameter thickness wires, either arranged individually (figures 6(D) and (E)) [127] or in a mesh via electrospinning (figure 6(F)) [123]. This leads to a significant challenge with signal transduction since a mechanical element that is sufficiently agile to respond to the drag forces from a sound field will also be driven more powerfully by any electrostatic or capacitive field [128]. Solutions based on electrospun meshes have the convenient electrical transduction mechanism of a piezoelectric polymer [129], in this case, P(VDF-TrFE) however, due to the random orientation of the fibres, the weak reverse piezoelectric effect and the clamped-clamped nature of the mesh the return pathway would be challenging to implement.

5. Conclusion

Insect hearing systems are diverse, but there are common sets of problems that all small animals must

deal with: size and energy. This tells us the type of problems we should be approaching with an insect-inspired solution. A system that uses a locust or bushcricket-inspired mechanical tonotopy will not outperform a well-designed digital filter in terms of frequency decomposition, but it will enable a low-power solution and reduce the data transmission needs by lowering the necessary sampling frequency. Directional sensors that make use of *Ormia* or *Achroia*-inspired directional membranes will not be more accurate than a well-spaced and sampled microphone array, but they will achieve the directionality in a fraction of the space. Only the active hearing processes are truly unique, having no digital equivalent that can change the response pattern of the sensor itself. There is great potential for this approach as we begin to consider autonomous sensors and remote 'fit-and-forget' networks for structural health monitoring, environmental monitoring or health monitoring purposes. The great difficulty thus far is in our ability to reproduce the mechanical functions of natural materials such as cuticle and resilin and to develop a reliable method of transducing the signal captured.

In summary, bio-inspired solutions are one of the most innovative and useful approaches to engineering design that prioritises energy and resource efficiency rather than the best performance possible, and have the potential to become even more so in the future as our knowledge of the principles behind biological solutions widen and our manufacturing capabilities improve.

Lara Díaz-García: Writing—Original Draft. Brendan Latham: Writing—Original Draft. Andrew Reid: Writing—Original Draft. James Windmill: Writing—Review & Editing and Supervision.

Data availability statement

No new data were created or analysed in this study.

ORCID iD

Lara Díaz-García https://orcid.org/0000-0002-0260-0312

References

[1] Robles L and Ruggero M A 2001 Mechanics of the mammalian cochlea *Physiol. Rev.* **81** 1305–52
[2] Nurse C A and Piskuric N A 2013 Signal processing at mammalian carotid body chemoreceptors *Semin. Cell Dev. Biol.* **24** 22–30
[3] Stensmyr M C, Dweck H K, Farhan A, Ibba I, Strutz A, Mukunda L, Linz J, Grabe V, Steck K and Lavista-Llanos S 2012 A conserved dedicated olfactory circuit for detecting harmful microbes in Drosophila *Cell* **151** 1345–57
[4] Strong S P, Koberle R, Van Steveninck R R D R and Bialek W 1998 Entropy and information in neural spike trains *Phys. Rev. Lett.* **80** 197
[5] Rault T, Bouabdallah A and Challal Y 2014 Energy efficiency in wireless sensor networks: a top-down survey *Comput. Netw.* **67** 104–22
[6] Yang W, Wang M, Zhang J, Zou J, Hua M, Xia T and You X 2017 Narrowband wireless access for low-power massive internet of things: a bandwidth perspective *IEEE Wirel. Commun.* **24** 138–45
[7] Jiang D, Shi B, Ouyang H, Fan Y, Wang Z L and Li Z 2020 Emerging implantable energy harvesters and self-powered implantable medical electronics *ACS Nano* **14** 6436–48
[8] Hoy R R and Fay R R 2012 *Comparative Hearing: Insects* vol 10 (Springer)
[9] Römer H 2020 Directional hearing in insects: biophysical, physiological and ecological challenges *J. Exp. Biol.* **223** jeb203224
[10] Pollack G S, Mason A C, Popper A N and Fay R R 2016 *Insect Hearing* (Springer) (https://doi.org/10.1007/978-3-319-28890-1)
[11] Robert D 2005 Directional hearing in insects *Sound Source Localization* ed A N Popper and R R Fay (Springer) pp 6–35
[12] Michelsen A 1992 Hearing and sound communication in small animals: evolutionary adaptations to the laws of physics *The Evolutionary Biology of Hearing* ed D B Webster, A N Popper and R R Fay (Springer) pp 61–77
[13] Yager D D 1999 Structure, development, and evolution of insect auditory systems *Microsc. Res. Tech.* **47** 380–400
[14] Clements A N 2013 *The Physiology of Mosquitoes* (*International Series of Monographs on Pure and Applied Biology: Zoology*) vol 17 (Pergamon) (https://doi.org/10.1016/C2013-0-07858-9)
[15] Gopfert M C, Briegel H and Robert D 1999 Mosquito hearing: sound-induced antennal vibrations in male and female Aedes aegypti *J. Exp. Biol.* **202** 2727–38
[16] Menda G, Nitzany E I, Shamble P S, Wells A, Harrington L C, Miles R N and Hoy R R 2019 The long and short of hearing in the mosquito Aedes aegypti *Curr. Biol.* **29** 709–14.e4
[17] Boyan G S 1993 Another look at insect audition: the tympanic receptors as an evolutionary specialization of the chordotonal system *J. Insect Physiol.* **39** 187–200
[18] Moir H M, Jackson J C and Windmill J F 2013 Extremely high frequency sensitivity in a 'simple'ear *Biol. Lett.* **9** 20130241
[19] Roeder K D and Treat A E 1961 The detection and evasion of bats by moths *Am. Sci.* **49** 168A—48 (available at: http://www.jstor.org/stable/27827782)
[20] Fullard J H 1988 The tuning of moth ears *Experientia* **44** 423–8
[21] Ter Hofstede H M and Ratcliffe J M 2016 Evolutionary escalation: the bat–moth arms race *J. Exp. Biol.* **219** 1589–602
[22] Popov A V, Shuvalov V F and Markovich A M 1975 Spectrum of the calling songs, phonotaxis and the auditory system in the cricket *Gryllus bimaculatus Zh. Evol. Biokhim. Fiziol.* **11** 453–60
[23] Kostarakos K, Hartbauer M and Römer H 2008 Matched filters, mate choice and the evolution of sexually selected traits *PLoS One* **3** e3005
[24] Yack J E 2004 The structure and function of auditory chordotonal organs in insects *Microsc. Res. Tech.* **63** 315–37
[25] Windmill J F C and Jackson J C 2016 ears *Insect Hearing* vol 55, ed G S Pollack, A C Mason, A N Popper and R R Fay (Springer) pp 125–57
[26] Greenfield M D 2016 Evolution of acoustic communication in insects *Insect Hearing* ed G S Pollack, A C Mason, A N Popper and R R Fay (Springer) pp 17–47
[27] Greenfield M D 2002 *Signalers and Receivers: Mechanisms and Evolution of Arthropod Communication* (Oxford University Press)
[28] Römer H 1992 Ecological constraints for the evolution of hearing and sound communication in insects *The Evolutionary Biology of Hearing* ed D B Webster, A N Popper and R R Fay (Springer) pp 79–93

[29] Gopfert M C and Robert D 2001 Active auditory mechanics in mosquitoes *Proc. R. Soc.* B **268** 333–9
[30] Mhatre N and Robert D 2013 A tympanal insect ear exploits a critical oscillator for active amplification and tuning *Curr. Biol.* **23** 1952–7
[31] Windmill J F C, Jackson J C, Tuck E J and Robert D 2006 Keeping up with bats: dynamic auditory tuning in a moth *Curr. Biol.* **16** 2418–23
[32] von Békésy G 1956 Simplified model to demonstrate the energy flow and formation of traveling waves similar to those found in the cochlea* *Proc. Natl Acad. Sci.* **42** 930–44
[33] Johnstone B M, Patuzzi R and Yates G K 1986 Basilar membrane measurements and the travelling wave *Hear. Res.* **22** 147–53
[34] Udayashankar A P, Kössl M and Nowotny M 2012 Tonotopically arranged traveling waves in the miniature hearing organ of bushcrickets *PLoS One* **7** e31008
[35] Hummel J, Kössl M and Nowotny M 2017 Morphological basis for a tonotopic design of an insect ear *J. Comp. Neurol.* **525** 2443–55
[36] Gray E G and Young J Z 1997 The fine structure of the insect ear *Phil. Trans. R. Soc.* B **243** 75–94
[37] Windmill J F C, Göpfert M C and Robert D 2005 Tympanal travelling waves in migratory locusts *J. Exp. Biol.* **208** 157–68
[38] Montealegre-Z F, Jonsson T, Robson-Brown K A, Postles M and Robert D 2012 Convergent evolution between insect and mammalian audition *Science* **338** 968–71
[39] Nishino H, Domae M, Takanashi T and Okajima T 2019 Cricket tympanal organ revisited: morphology, development and possible functions of the adult-specific chitin core beneath the anterior tympanal membrane *Cell Tissue Res.* **377** 193–214
[40] Montealegre-Z F and Robert D 2015 Biomechanics of hearing in katydids *J. Comp. Physiol.* A **201** 5–18
[41] Stölting H and Stumpner A 1998 Tonotopic organization of auditory receptors of the bushcricket Pholidoptera griseoaptera (Tettigoniidae, Decticinae) *Cell Tissue Res.* **294** 377–86
[42] Sueur J, Windmill J F C and Robert D 2006 Tuning the drum: the mechanical basis for frequency discrimination in a Mediterranean cicada *J. Exp. Biol.* **209** 4115–28
[43] Hur S, Lee S Q and Choi H S 2010 Fabrication and characterization of PMN-PT single crystal cantilever array for cochlear-like acoustic sensor *J. Mech. Sci. Technol.* **24** 181–4
[44] Jang J *et al* 2015 A microelectromechanical system artificial basilar membrane based on a piezoelectric cantilever array and its characterization using an animal model *Sci. Rep.* **5** 12447
[45] Jang J, Lee J, Jang J H and Choi H 2016 A triboelectric-based artificial basilar membrane to mimic cochlear tonotopy *Adv. Healthcare Mater.* **5** 2481–7
[46] Kim S, Song W J, Jang J, Jang J H and Choi H 2013 Mechanical frequency selectivity of an artificial basilar membrane using a beam array with narrow supports *J. Micromech. Microeng.* **23** 095018
[47] Römer H 1976 Die Informationsverarbeitung tympanaler Rezeptorelemente vonLocusta migratoria (Acrididae, Orthoptera) *J. Comp. Physiol.* **109** 101–22
[48] Stephen R O and Bennet-Clark H C 1982 The anatomical and mechanical basis of stimulation and frequency analysis in the locust ear *J. Exp. Biol.* **99** 279–314
[49] Joyce B, Dodson J and Wolfson J 2017 Beam array designs for a cochlea-inspired accelerometer for impact measurements *ASME 2017 Conf. on Smart Materials, Adaptive Structures and Intelligent Systems* (American Society of Mechanical Engineers Digital Collection) (https://doi.org/10.1115/SMASIS2017-3723)
[50] Tao S and Rusu A 2015 A power-efficient continuous-time incremental sigma-delta ADC for neural recording systems *IEEE Trans. Circuits Syst.* I **62** 1489–98
[51] Li C-h, Delbruck T and Liu S-C 2012 Real-time speaker identification using the AEREAR2 event-based silicon cochlea *2012 IEEE Int. Symp. on Circuits and Systems (ISCAS)* pp 1159–62
[52] Zai A T, Bhargava S, Mesgarani N and Liu S-C 2015 Reconstruction of audio waveforms from spike trains of artificial cochlea models *Front. Neurosci.* **9** 347
[53] White R D and Grosh K 2005 Microengineered hydromechanical cochlear model *Proc. Natl Acad. Sci.* **102** 1296–301
[54] Kim Y, Kim J-S and Kim G-W 2018 A novel frequency selectivity approach based on travelling wave propagation in mechanoluminescence basilar membrane for artificial cochlea *Sci. Rep.* **8** 12023
[55] Song W J, Jang J, Kim S and Choi H 2014 Piezoelectric performance of continuous beam and narrow supported beam arrays for artificial basilar membranes *Electron. Mater. Lett.* **10** 1011–8
[56] Bachman M, Zeng F-G, Xu T and Li G-P 2006 Micromechanical resonator array for an implantable bionic ear *Audiol. Neurotol.* **11** 95–103
[57] Zagabathuni A and Kanagaraj S 2020 Comparative analysis of mechanical characteristics of different topologies of the cantilever beam to mimic the function of the cochlea *Mater. Today* **33** 4927–32
[58] Neethu K and Suja K J 2016 Sensitivity analysis of rectangular microcantilever structure with piezoresistive detection technique using coventorware FEA *Proc. Comput. Sci.* **93** 146–52
[59] Ansari M Z, Cho C, Kim J and Bang B 2009 Comparison between deflection and vibration characteristics of rectangular and trapezoidal profile microcantilevers *Sensors* **9** 2706–18
[60] Wang H S *et al* 2021 Biomimetic and flexible piezoelectric mobile acoustic sensors with multiresonant ultrathin structures for machine learning biometrics *Sci. Adv.* **7** eabe5683
[61] Ngelayang T B, Majlis B Y and Latif R 2016 Straight bridge beams with centered diaphragm (SBBCD) design for MEMS cochlear biomodel *2016 IEEE Int. Conf. on Semiconductor Electronics (ICSE)* pp 13–16
[62] Chen F, Cohen H I, Bifano T G, Castle J, Fortin J, Kapusta C, Mountain D C, Zosuls A and Hubbard A E 2006 A hydromechanical biomimetic cochlea: experiments and models *J. Acoust. Soc. Am.* **119** 394–405
[63] Saadatzi M, Saadatzi M N and Banerjee S 2020 Modeling and fabrication of a piezoelectric artificial cochlea electrode array with longitudinal coupling *IEEE Sens. J.* **20** 11163–72
[64] Shintaku H, Nakagawa T, Kitagawa D, Tanujaya H, Kawano S and Ito J 2010 Development of piezoelectric acoustic sensor with frequency selectivity for artificial cochlea *Sens. Actuators* A **158** 183–92
[65] Karlos A, Elliott S J and Cheer J 2019 Higher-order WKB analysis of reflection from tapered elastic wedges *J. Sound Vib.* **449** 368–88
[66] Mironov M A and Pislyakov V V 2002 One-dimensional acoustic waves in retarding structures with propagation velocity tending to zero *Acoust. Phys.* **48** 347–52
[67] Hemmert W, Dürig U, Despont M, Drechsler U, Genolet G, Vettiger P and Freeman D M 2003 A life-sized, hydrodynamical, micromechanical inner ear *Biophysics of the Cochlea* (World Scientific) pp 409–16
[68] Lechner T P 1993 A hydromechanical model of the cochlea with nonlinear feedback using PVF_2 bending transducers *Hear. Res.* **66** 202–12
[69] Wittbrodt M J, Steele C R and Puria S 2004 Fluid–structure interaction in a physical model of the human cochlea *J. Acoust. Soc. Am.* **116** 2542–3
[70] Lüling H, Franosch J-M P and Leo van Hemmen J 2010 A two-dimensional cochlear fluid model based on conformal mapping *J. Acoust. Soc. Am.* **128** 3577–84
[71] Hoy R R 1992 The evolution of hearing in insects as an adaptation to predation from bats *The Evolutionary Biology*

of Hearing ed D B Webster, A N Popper and R R Fay (Springer) pp 115–29
[72] Cook M A and Scoble M J 1992 Tympanal organs of geometrid moths: a review of their morphology, function, and systematic importance *Syst. Entomol.* **17** 219–32
[73] Rodríguez R L, Schul J, Cocroft R B and Greenfield M D 2005 The contribution of tympanic transmission to fine temporal signal evaluation in an ultrasonic moth *J. Exp. Biol.* **208** 4159–65
[74] Greig E and Greenfield M D 2004 Sexual selection and predator avoidance in an acoustic moth: discriminating females take fewer risks *Behaviour* **141** 799–815
[75] Roeder K D 1962 The behaviour of free flying moths in the presence of artificial ultrasonic pulses *Anim. Behav.* **10** 300–4
[76] Yager D D and Hoy R R 1986 The cyclopean ear: a new sense for the praying mantis *Science* **231** 727–9
[77] Mason A C, Oshinsky M L and Hoy R R 2001 Hyperacute directional hearing in a microscale auditory system *Nature* **410** 686–90
[78] Walker T J 1993 Phonotaxis in femaleOrmia ochracea (Diptera: tachinidae), a parasitoid of field crickets *J. Insect Behav.* **6** 389–410
[79] Miles R N, Robert D and Hoy R R 1995 Mechanically coupled ears for directional hearing in the parasitoid fly Ormia ochracea *J. Acoust. Soc. Am.* **98** 3059–70
[80] Robert D, Miles R N and Hoy R R 1996 Directional hearing by mechanical coupling in the parasitoid fly Ormia ochracea *J. Comp. Physiol.* A **179** 29–44
[81] Zhang Y, Bauer R, Whitmer W M, Jackson J C, Windmill J F C and Uttamchandani D 2018 A MEMS microphone inspired by Ormia for spatial sound detection *2018 IEEE Micro Electro Mechanical Systems (MEMS)* pp 253–6
[82] Miles R 2017 Comparisons of the performance of commercially-available hearing aid microphones to that of the Binghamton Ormia-inspired gradient microphone *J. Acoust. Soc. Am.* **141** 3794
[83] Zhang Y, Reid A and Windmill J F C 2018 Insect-inspired acoustic micro-sensors *Curr. Opin. Insect Sci.* **30** 33–38
[84] Rahaman A and Kim B 2022 An mm-sized biomimetic directional microphone array for sound source localization in three dimensions *Microsyst. Nanoeng.* **8** 1–13
[85] Miles R N, Su Q, Cui W, Shetye M, Degertekin F L, Bicen B, Garcia C, Jones S and Hall N 2009 A low-noise differential microphone inspired by the ears of the parasitoid fly Ormia ochracea *J. Acoust. Soc. Am.* **125** 2013–26
[86] Rahaman A and Kim B 2020 Sound source localization by Ormia ochracea inspired low–noise piezoelectric MEMS directional microphone *Sci. Rep.* **10** 9545
[87] Spangler H G and Hippenmeyer C L 1988 Binaural phonotaxis in the lesser wax moth, Achroia grisella (F.) (Lepidoptera: pyralidae) *J. Insect Behav.* **1** 117–22
[88] Norman A P, Jones G and Arlettaz R 1999 Noctuid moths show neural and behavioural responses to sounds made by some bat-marking rings *Anim. Behav.* **57** 829–35
[89] Nakano R, Ishikawa Y, Tatsuki S, Surlykke A, Skals N and Takanashi T 2006 Ultrasonic courtship song in the Asian corn borer moth, Ostrinia furnacalis *Naturwissenschaften* **93** 292–6
[90] Greenfield M D and Hohendorf H 2009 Independence of sexual and anti-predator perceptual functions in an acoustic moth: implications for the receiver bias mechanism in signal evolution *Ethology* **115** 1137–49
[91] Reid A, Marin-Cudraz T, Windmill J F and Greenfield M D 2016 Evolution of directional hearing in moths via conversion of bat detection devices to asymmetric pressure gradient receivers *Proc. Natl Acad. Sci.* **113** E7740–8
[92] Hintze-Podufal C and Von Hermanni G 1996 Die Entwicklung der Tympanalorgane und ihrer invers gerichteten Skolopidien bei Wachsmotten (Lepidoptera: pyralidae: galleriinae) *Entomol. Gen.* **20** 195–201
[93] Rodríguez R L and Greenfield M D 2004 Behavioural context regulates dual function of ultrasonic hearing in lesser waxmoths: bat avoidance and pair formation *Physiol. Entomol.* **29** 159–68
[94] Reid A 2017 *Directional Hearing at the Micro-scale: Bio-inspired Sound Localization* (University of Strathclyde) (https://doi.org/10.48730/7r6d-aq98)
[95] Ishfaque A and Kim B 2018 Fly Ormia ochracea inspired MEMS directional microphone: a review *IEEE Sens. J.* **18** 1778–89
[96] Kuntzman M L, Hewa-Kasakarage N N, Rocha A, Kim D and Hall N A 2015 Micromachined in-plane pressure-gradient piezoelectric microphones *IEEE Sens. J.* **15** 1347–57
[97] Reid A, Windmill J F and Uttamchandani D 2015 Bio-inspired sound localization sensor with high directional sensitivity *Proc. Eng.* **120** 289–93
[98] Cui W, Bicen B, Hall N, Jones S A, Degertekin F L and Miles R N 2006 Optical sensing inadirectional memsmicrophone inspired by the ears of the parasitoid fly, *Ormia ochracea 19th IEEE Int. Conf. on Micro Electro Mechanical Systems* pp 614–7
[99] Kim T Y, Park S-H and Park K 2021 Development of functionally graded metamaterial using selective polymerization via digital light processing additive manufacturing *Addit. Manuf.* **47** 102254
[100] Touse M, Sinibaldi J, Simsek K, Catterlin J, Harrison S and Karunasiri G 2010 Fabrication of a microelectromechanical directional sound sensor with electronic readout using comb fingers *Appl. Phys. Lett.* **96** 173701
[101] Downey R H and Karunasiri G 2014 Reduced residual stress curvature and branched comb fingers increase sensitivity of MEMS acoustic sensor *J. Microelectromech. Syst.* **23** 417–23
[102] Díaz-García L, Reid A, Jackson-Camargo J and Windmill J F C 2022 Towards a bio-inspired acoustic sensor: Achroia grisella's ear *IEEE Sens. J.* **22** 17746–53
[103] Liu H J, Yu M and Zhang X M 2008 Biomimetic optical directional microphone with structurally coupled diaphragms *Appl. Phys. Lett.* **93** 243902
[104] Currano L J, Liu H, Gee D, Yang B and Yu M 2009 Microscale implementation of a bio-inspired acoustic localization device *Proc. SPIE* **7321** 97–104
[105] Albert J T and Kozlov A S 2016 Comparative aspects of hearing in vertebrates and insects with antennal ears *Curr. Biol.* **26** R1050–61
[106] Mhatre N, Pollack G and Mason A 2016 Stay tuned: active amplification tunes tree cricket ears to track temperature-dependent song frequency *Biol. Lett.* **12** 20160016
[107] Jackson J C and Robert D 2006 Nonlinear auditory mechanism enhances female sounds for male mosquitoes *Proc. Natl Acad. Sci. USA* **103** 16734–9
[108] Warren B, Lukashkin A N and Russell I J 2010 The dynein–tubulin motor powers active oscillations and amplification in the hearing organ of the mosquito *Proc. R. Soc.* B **277** 1761–9
[109] Avitabile D, Homer M, Champneys A R, Jackson J C and Robert D 2009 Mathematical modelling of the active hearing process in mosquitoes *J. R. Soc. Interface* **7** 105–22
[110] Windmill J F C, Jackson J C, Pook V G and Robert D 2018 Frequency doubling by active *in vivo* motility of mechanosensory neurons in the mosquito ear *R. Soc. Open Sci.* **5** 171082
[111] Jackson J C, Windmill J F C, Pook V G and Robert D 2009 Synchrony through twice-frequency forcing for sensitive and selective auditory processing *Proc. Natl Acad. Sci.* **106** 10177–82
[112] Rodríguez T R and García R 2003 Theory of Q control in atomic force microscopy *Appl. Phys. Lett.* **82** 4821–3
[113] Prakash G, Hu S, Raman A and Reifenberger R 2009 Theoretical basis of parametric-resonance-based atomic force microscopy *Phys. Rev.* B **79** 094304

[114] Guerreiro J, Reid A, Jackson J C and Windmill J F 2018 Active hearing mechanisms inspire adaptive amplification in an acoustic sensor system *IEEE Trans. Biomed. Circuits Syst.* **12** 655–64
[115] Guerreiro J, Reid A, Jackson J C and Windmill J F C 2017 Towards the development of a frequency agile MEMS acoustic sensor system *2017 IEEE SENSORS* pp 1–3
[116] Miles R N, Degertekin F L, Cui W, Su Q, Homentcovschi D and Banser F 2013 A biologically inspired silicon differential microphone with active Q control and optical sensing *Acoustical Society of America Biannual Meeting Proc. Meetings on Acoustics ICA2013* vol 19 (Acoustical Society of America) p 030031
[117] Guerreiro J, Reid A, Jackson J C and Windmill J F 2017 Bio-inspired active amplification in a MEMS microphone using feedback computation *2017 IEEE Biomedical Circuits and Systems Conf. (Biocas)* (IEEE) pp 1–4
[118] Guerreiro J, Jackson J C and Windmill J F 2017 Simple ears inspire frequency agility in an engineered acoustic sensor system *IEEE Sens. J.* **17** 7298–305
[119] Bicen B, Garcia C, Hall N A, Okandan M, Cui W, Su Q T, Miles R N and Degertekin L 2008 Diffraction based optical MEMS microphones and accelerometers with active electrostatic force feedback *J. Acoust. Soc. Am.* **123** 3230
[120] Bicen B 2010 *Micromachined Diffraction Based Optical Microphones and Intensity Probes with Electrostatic Force Feedback* (Georgia Institute of Technology) (available at: www.proquest.com/books/micromachined-diffraction-based-optical/docview/1136361303/se-2?accountid=14116)
[121] Miles R N, Farahikia M, Leahy S and Aziz A A 2019 A flow-sensing velocity microphone *2019 IEEE SENSORS* (IEEE) pp 1–4
[122] Miles R N and Zhou J 2018 Sound-induced motion of a nanoscale fiber *J. Vib. Acoust.* **140** 011009
[123] Wang W, Stipp P N, Ouaras K, Fathi S and Huang Y Y S 2020 Broad bandwidth, self-powered acoustic sensor created by dynamic near-field electrospinning of suspended, transparent piezoelectric nanofiber mesh *Small* **16** 2000581
[124] McConney M E, Schaber C F, Julian M D, Eberhardt W C, Humphrey J A, Barth F G and Tsukruk V V 2009 Surface force spectroscopic point load measurements and viscoelastic modelling of the micromechanical properties of air flow sensitive hairs of a spider (Cupiennius salei) *J. R. Soc. Interface* **6** 681–94
[125] Wang K, Gong S, Zhang Y, Yap L W and Cheng W 2022 Mosquito-inspired design of resistive antennae for ultrasensitive acoustic detection *Nanoscale* **14** 10108–17
[126] Joyce B S and Tarazaga P A 2014 Mimicking the cochlear amplifier in a cantilever beam using nonlinear velocity feedback control *Smart Mater. Struct.* **23** 075019
[127] Miles R N 2020 Effects of viscosity *Physical Approach to Engineering Acoustics* (*Mechanical Engineering*) (Springer) pp 189–231
[128] Miles R N 2018 A compliant capacitive sensor for acoustics: avoiding electrostatic forces at high bias voltages *IEEE Sens. J.* **18** 5691–8
[129] Zhou J, Li B, Liu J, Jones W E and Miles R N 2018 Highly-damped nanofiber mesh for ultrasensitive broadband acoustic flow detection *J. Micromech. Microeng.* **28** 095003